



p97/VCP regulates MRE11-dependent DNA end resection and alters cellular toxicity of ionising radiation

DPhil Thesis

Supervisors:

Prof Anne E Kiltie
Prof Kristijan Ramadan

Susan Kilgas

Green Templeton College

MRC Oxford Institute for Radiation Oncology
Department of Oncology
University of Oxford

Michaelmas Term 2021

Table of Contents

Acknowledgements **3**

Declaration **5**

Abstract **6**

List of Figures **7**

List of Tables **9**

List of Abbreviations **10**

Chapter 1: Introduction **15**

1.1. Genomic instability and cancer *15*

1.2. Radiotherapy and radiosensitisers in the treatment of cancer *16*

1.3. DNA double-strand break repair *20*
1.3.1. Non-homologous end-joining 22
1.3.2. Homologous recombination 22
1.3.3. Repair pathway choice between NHEJ and HR 23
1.2.4. Alternative-non-homologous end-joining (alt-NHEJ) 24
1.3.5. Single-strand annealing (SSA) 25
1.3.6. Role of chromatin in double-strand break repair 28

1.4. The MRE11-RAD50-NBS1 (MRN) complex *31*
1.4.1. The MRN complex structure and role in double-strand break repair 31
1.4.2. MRE11 nuclease in the regulation of repair pathway choice 38
1.4.3. MRN complex alterations in tumourigenesis 41

1.5. The role of VCP/p97 in genome stability *43*
1.5.1. p97 and the ubiquitin-proteasome system (UPS) 43
1.5.2. Regulation of ubiquitination in the DNA damage response 47
1.5.3. p97-associated co-factors 51
1.5.4. The role of p97 in the nucleus 53
1.5.5. Therapeutic applications of inhibiting the UPS 57

1.6. Aims of the Thesis *61*

Chapter 2. Materials and methods **62**

2.1. Cell lines and culture conditions *62*

2.2. Chemical treatments *62*

2.3. RNA interference *62*

2.4. Plasmid transfections *63*

2.5. Plasmid purification *63*
2.5.1. Transformation of bacteria 63
2.5.2. Maxiprep plasmid purification 64

2.6. Ionising radiation and UV laser treatment *64*

2.7. Immunofluorescence microscopy *65*
2.7.1. BrdU foci detection without denaturation 66
2.7.2. EdU detection 67

2.8. Immunohistochemistry: staining *67*

2.8.1. Immunohistochemistry: scoring 68
2.8.2. Immunohistochemistry: Human HGT1 Tissue Sections 68
2.9. Protein Analysis *69*
2.9.1. Western Blotting 69
2.9.2. Cycloheximide (CHX) chase 70
2.9.3. Cellular fractionation 70
2.9.4. Protein co-immunoprecipitation (Co-IP) 71
2.10. Reporter assays *72*
2.11. Colony formation assay *72*
2.12. Dosing of CB-5083 in vivo *73*
2.13. Xenograft model for tumour growth delay *73*
2.14. Pharmacokinetic analysis of CB-5083 concentration in plasma and different organs *74*
2.15. Statistical analysis *74*
Chapter 3: p97 and the MRE11-RAD50-NBS1 (MRN) complex: physical interaction and its functional relevance 76
3.1. p97 interacts with the MRN complex *78*
3.2. p97 is required for MRN complex turnover on chromatin upon DNA damage *80*
3.3. Dependency of the Ku complex on p97-mediated regulation of MRE11 ..... *87*
Chapter 4: p97 regulates DNA repair pathway choice through MRE11 nuclease activity 91
4.1. Inactivation of p97 causes excessive 5'-DNA end resection mediated by MRE11 nuclease activity ... 92
4.2. Inhibition of p97 causes a switch from error-free RAD51-mediated HR repair to RAD52-mediated SSA repair *109*
Chapter 5: Inactivation of p97 negatively regulates anti-resection factors and causes a delay in DNA DSB repair 117
Chapter 6: Regulation of the p97-MRE11 axis by upstream DDR kinases 131
Chapter 7: p97-mediated MRE11 regulation affects cell killing after IR *in vitro* and *in vivo* 139
7.1. Inhibition of p97 radiosensitises cancer cells in vitro *140*
7.2. p97 is more highly expressed in invasive than papillary bladder cancer *145*
7.3. The p97 inhibitor CB-5083 is well-tolerated in vivo *147*
7.4. The p97 inhibitor CB-5083 suppresses tumour growth in vivo *149*
Chapter 8: Discussion 154
8.1. p97-dependent regulation of DSB repair through MRN disassembly *156*
8.2. Post-translational modifications in the disassembly of MRN complex *157*
8.3. Potential clinical applications of targeting the p97 system in cancer therapy *158*
Chapter 9: Future work 160
Appendices 163
References 173
List of publications 198

Acknowledgements

I would like to thank my supervisors, Professor Anne Kiltie and Professor Kristijan Ramadan, for giving me the opportunity to work under their supervision. Anne, you taught me about the importance of efficiency and clarity of thinking in science. Thank you for your valuable mentorship throughout the years and for all the memories we made as a group both in and outside lab. In addition to all the lovely surprises and delicious baking you did for us, I will always remember our lab away days that were filled with joy and excitement. Thank you for being so attentive to my career goals and supporting them. Kristijan, you truly know how to inspire people with your energetic presence and passion for science. I have really enjoyed being part of your group both as a Master's and a DPhil student. I have thoroughly enjoyed having thoughtful scientific discussions and working on different exciting projects. I will always be grateful for the way you encouraged me throughout my degrees and the way you shaped me into a confident and a better scientist. Anne and Kristijan, it was a pleasure to collaborate, and I am happy it resulted in several good publications.

I would like to thank all the lab members I had the pleasure to work with. From Anne Kiltie's group - thank you Junetha, Salome, Juri, Ed, Judith, Jia-Ling and Chee. From Kristijan Ramadan's group - thank you Annamaria, Wei, Abhay, Ignacio, Sam, Shudong, John, Pauline, Cristiano, Gwennie and Ftoon. Thank you for wonderful memories and for your companionship. I am grateful to have got to know you all.

To Hannah, Charlotte, Cagla, Hala, Sovan, Shahad, Timo, Ashwin, Florian, Bill, Haonan, Sophia, Anna, Yi Chun, Anouk, Ayesha, Gabrielle and Safia – Thank you for making my years in Oxford great. Thank you for your friendship.

To my best friend Tiffany Ma – You made my years in Oxford the best years of my life so far. You were always the person to discuss exciting results and scientific ideas with. In addition to inspiring me with your intelligence, hard work and ambition, your kindness, support, and love gave me strength and made me a better person.

To my family – thank you for always having belief in me and encouraging me to take on new challenges. Thank you for your relentless support, I will always be grateful for it.

Declaration

This dissertation is submitted for the degree of Doctor of Philosophy in Oncology. I hereby declare that the work presented in this thesis is my own except where explicitly otherwise stated. I declare that this work has not been submitted for any other degree at this or any other university.

Abstract

The ubiquitin-proteasome system (UPS) is responsible for most of the protein degradation in mammalian cells which represents a particular challenge in cancer cells that commonly have heightened protein stress. The AAA+ ATPase p97 is a central component of the UPS, where it functions in concert with its co-factors to bind and unfold ubiquitinated substrates from various cellular locations, including DNA break sites. The work in this thesis demonstrates that p97 functionally interacts with one of the main DNA double-strand break (DSB) repair complexes, MRE11-RAD50-NBS1 (MRN), and influences DSB repair pathway choice by disassembling MRN from chromatin after ionising radiation (IR). Inactivation of p97 blocks MRN complex disassembly from chromatin and sites of DNA damage upon IR, which results in excessive MRE11-mediated DNA end resection, leading to defective error-free homologous recombination (HR) and upregulation of the mutagenic single-strand annealing (SSA) pathway, resulting in cancer cell radiosensitivity. Mechanistically, p97 inhibition causes radiosensitivity through MRE11 nuclease accumulation, and cancer cell survival after IR is rescued when MRE11 is inactivated in combination with p97 inhibition. Furthermore, the small molecule ATPase inhibitor of p97, CB-5083, is well-tolerated and causes tumour cell killing after IR *in vivo*. These results suggest that p97 inhibitors might be used to improve cancer radiotherapy outcomes.

List of Figures

Figure 1 Overview of DSB repair pathways. 21
Figure 2 Comparison of SSA and alt-NHEJ. 27
Figure 3 Chromatin-dependent protein assembly in DSB repair. 29
Figure 4 Functional domains of the MRE11-RAD50-NBS1 (MRN) complex proteins. 32
Figure 5 The structure of MRE11-RAD50-NBS1 (MRN) complex. 33
Figure 6 Functions of the MRN complex in DSB repair. 37
Figure 7 MRE11-mediated bidirectional processing of DSBs. 39
Figure 8 The ATPase VCP/p97 and its role in the ubiquitin-proteasome system (UPS). 44
Figure 9 The ubiquitin signalling cycle. 50
Figure 10 p97-associated co-factors. 52
Figure 11 Overview of p97/VCP functions in the cell. 53
Figure 12 Small-molecule inhibitors in the UPS. 58
Figure 13 Mass spectrometry screen of the p97 interactome after IR. 77
Figure 14 p97 interacts with the MRN complex. 79
Figure 15 MRE11 accumulates in IR-induced foci upon p97 inhibition. 81
Figure 16 RAD50 accumulates in IR-induced foci upon p97 inhibition. 82
Figure 17 MRE11 accumulates on UV-induced DNA damage sites in p97-inhibited conditions. 83
Figure 18 RAD50 accumulation on UV-induced DNA damage sites in p97-inhibited conditions. 84
Figure 19 . p97 is required for MRN turnover on chromatin upon DNA but does not affect total MRN protein levels. 86
Figure 20 p97 regulates MRE11 accumulation on DNA damage independently of Ku80. . 89
Figure 21 p97 inhibition causes excessive MRE11-mediated DNA end resection in S phase cells. 93
Figure 22 Inhibiting p97 leads to MRE11-mediated DNA hyper-resection in cells outside S phase. 95
Figure 23 BrdU foci formation in EdU-positive cells upon p97 inhibition and IR. 96
Figure 24 MRE11 endo- and exonuclease inhibitors rescue CB-5083-induced excessive ssDNA generation in S phase cells. 97
Figure 25 MRE11 endo- and exonuclease inhibitors rescue CB-5083-induced excessive ssDNA generation in cells outside S phase. 98
Figure 26 Depletion of p97 by siRNA causes excessive MRE11-mediated DNA end resection in S phase cells. 100
Figure 27 Depletion of p97 by siRNA causes excessive MRE11-mediated DNA end resection in cells outside S phase. 101
Figure 28 Depletion of p97 by siRNA causes excessive MRE11-mediated DNA end resection independently of EXO1 in S phase cells. 102
Figure 29 Depletion of p97 by siRNA causes excessive MRE11-mediated DNA end resection independently of EXO1 in cells outside S phase. 103
Figure 30 Depletion of p97 by siRNA causes excessive MRE11-mediated DNA end resection after IR independently of EXO1 in S phase cells. 104
Figure 31 Depletion of p97 by siRNA causes excessive MRE11-mediated DNA end resection after IR independently of EXO1 in cells outside S phase. 105

Figure 32 Inhibition of p97 causes nuclear RPA foci accumulation upon IR. 107
Figure 33 Inhibition of p97 leads to a decrease in phosphorylated RPA (S4/S8) foci. 108
Figure 34 p97 inhibition decreases nuclear RAD51 foci after IR. 110
Figure 35 Inhibition of p97 leads to an increase in nuclear RAD52 foci after IR. 111
Figure 36 Inactivation of p97 compromises HR-mediated repair. 113
Figure 37 Depletion of p97 compromises HR-mediated repair. 114
Figure 38 p97 inhibition increases SSA repair. 115
Figure 39 Depletion of p97 negatively regulates the anti-resection factor 53BP1 and leads to delayed DNA double-strand break repair visualised by γH2AX foci..... 118
Figure 40 Inhibition of p97 negatively regulates the anti-resection factor 53BP1 and leads to delayed DNA double-strand break repair visualised by γH2AX foci..... 119
Figure 41 Depletion of p97 negatively regulates the anti-resection factor REV7 after IR-induced DNA damage..... 121
Figure 42 The MRE11 inhibitor Mirin rescues 53BP1 recruitment defect in p97-depleted cells. 124
Figure 43 Ku80 depletion does not affect 53BP1 recruitment in p97-depleted cells. 125
Figure 44 Depletion of the p97 substrate L3MBTL1 partially rescues 53BP1 recruitment defect of p97-inactivated cells. 127
Figure 45 No additive effect on 53BP1 recruitment in L3MBTL1 and p97 co-depleted cells in combination with Mirin..... 128
Figure 46 ATM inhibition causes MRE11 accumulation on sites of DNA damage similarly to p97 inhibition. 132
Figure 47 ATR inhibition does not cause MRE11 accumulation on sites of DNA damage compared to p97 inhibition..... 133
Figure 48 DNA-PK inhibition causes MRE11 accumulation on sites of DNA damage similarly to p97 inhibition. 135
Figure 49 Inhibition of DNA-PK causes early accumulation of the DNA damage marker γH2AX and DSB repair delay after 24 hours of recovery from IR. 136
Figure 50 Determining IC10 and IC50 concentrations of CB-5083 upon 6 hours of treatment of T24 and RT112 bladder cancer cells. 141
Figure 51 CB-5083 radiosensitises T24 and RT112 bladder cancer cell lines. 142
Figure 52 MRE11 inactivation by Mirin rescues the radiosensitivity phenotype induced by CB-5083. 143
Figure 53 MRE11 inactivation by shRNA rescues the radiosensitivity phenotype induced by siRNA-mediated p97 depletion. 144
Figure 54 Cytoplasmic and nuclear expression levels of p97 in papillary and invasive bladder cancer tissue sections. 146
Figure 55 A single oral dose or IP injection of CB-5083 is well-tolerated in CD-1 nude mice. 148
Figure 56 CB-5083 radiosensitising effects in vivo. 150
Figure 57 Model of p97-mediated MRE11 removal from DNA damage and consequent regulation of DSB repair pathway choice after IR. 155
Figure 58 Related to Figure 13. Mass spectrometry screen of the MRE11 interactome. 170
Figure 59 Sub-fractionation blot of a CHX chase of the MRN complex upon p97 inhibition. 171
Figure 60 Related to Figure 55. CB-5083 effects in vivo..... 172

List of Tables

Table 1 p97 functions in the nucleus. List of p97 substrates, co-factors and associated E3 ligases with their functions in the nucleus. 55
Table 2 Table of antibodies and reagents used, their sources and catalogue numbers. . 163

List of Abbreviations

53BP1	p53 Binding Protein 1
5-FU	5-Fluorouracil
A	Alanine
AA	Amino Acid
Alt-NHEJ	Alternative-Non-Homologous End-Joining
AML	Acute Myeloid Leukaemia
ANOVA	Analysis of Variance
AP	Apurinic/apyrimidinic
APC/C	Anaphase-Promoting Complex Cyclosome
APLF	Aprataxin and PNK-Like Factor
ATCC	American Type Culture Collection
ATLD	Ataxia-Telangiectasia-Like Disorder
ATM	Ataxia-Telangiectasia Mutated
ATP	Adenosine Triphosphate
ATR	Ataxia Telangiectasia and Rad3-Related Protein
ATRIP	ATR-Interacting Protein
BCA	Bicinchoninic acid
BER	Base Excision Repair
BLM	Bloom Syndrome Protein
BP	Base Pair
BRCA	Breast Cancer Susceptibility Gene
BrdU	5-Bromo-2'-Deoxyuridine
BRCT	BRCA1 Carboxy-Terminus
BS	Bloom Syndrome
BSA	Bovine Serum Albumin
BS1	Binding Site 1
C	Cytosine
CHROMAD	Chromatin-Associated Degradation
CD4	Cluster of Differentiation 4
C. elegans	*Caenorhabditis elegans*
CB-5083	Cleave Biosciences 5083
CB-5339	Cleave Biosciences 5339
Cdc	Cell Division Cycle
CDK	Cyclin-Dependent Kinase
cDNA	Complementary DNA
CDT1	Chromatin Licensing and DNA Replication Factor 1
CHK	Checkpoint Kinase
CHX	Cycloheximide
CMG	CDC45, GINS, MCM
CPY	Carboxypeptidase Y
CRL	Cullin RING-based E3 Ligase
CtIP	C-Terminal Binding Protein 1 Interacting Protein
CUL	Cullin
CXXC	Cysteine-XX-Cysteine

D	Aspartic Acid
Da	Dalton
DAPI	4',6'Diamidino-2-Phenylindole
DDR	DNA Damage Response
ddH_2O	Double Distilled Water
DMSO	Dimethyl Sulfoxide
DNA	Deoxyribonucleic Acid
DNA2	DNA Replication Helicase/Nuclease 2
DNA-PK	DNA-Dependent Protein Kinase
$DNA\text{-}PK_{cs}$	DNA-Dependent Protein Kinase Catalytic Subunit
DNMT	DNA Methyltransferase
dNTP	Deoxyribonucleotide triphosphate
DPC	DNA-Protein Crosslink
DSB	Double Strand Break
dsDNA	Double-Stranded DNA
DSS	Disease-Specific Survival
DUB	Deubiquitinating Enzyme
DYNLL1	Dynein Light Chain Protein 1
E	Glutamic Acid
E. Coli	*Escherichia Coli*
EDTA	Ethylene Diamine Tetraacetic Acid
EdU	5-ethenyl-2'-deoxyuridine
EGFR	Epidermal Growth Factor Receptor
EGTA	Egtazic Acid
ER	Endoplasmic Reticulum
ERAD	Endoplasmic Reticulum-Associated Degradation
ERCC1	Excision Repair Cross-Complementation Group 1
ERCC4	Excision Repair Cross-Complementation Group 4
EXO1	Exonuclease 1
F	Phenylalanine
FA	Fanconi Anaemia
FACS	Fluorescence-Activated Cell Sorting
FAF1	Fas-Associated Factor 1
FBS	Fetal Bovine Serum
FDA	Food and Drug Administration
FHA	Forkhead-Associated
G	Glycine
g	Gram
GFP	Green Fluorescent Protein
Gy	Gray
HA	Haemagglutinin
H_2O_2	Hydrogen Peroxide
HDAC	Histone Deacetylase
hDNA	Heteroduplex DNA
HEK293	Human Embryonic Kidney 293
His	Histidine
HLH	Helix-Loop-Helix

HR	Homologous Recombination
HRP	Horseradish Peroxidase
h	Hour(s)
H-score	Histological score
HU	Hydroxyurea
I	Isoleucine
ICL	Inter-strand Crosslink
IHC	Immunohistochemistry
IP	Immunoprecipitation/Intraperitoneal
IR	Ionising Radiation
IRIF	Ionising-Radiation-Induced Foci
K	Lysine
KAP1	KRAB-Associated Protein-1
kDa	Kilodalton
L	Leucine
L3MBTL1	Lethal Malignant Brain Tumour Like Protein 1
LB	Luria-Bertani
LC-MS/MS	Tandem Liquid Chromatography Mass Spectrometry
LIG	Ligase
LRR	Leucine-Rick Repeat
M	Molar
MAD	Mitochondria-Associated Degradation
Mb	Megabase
MCM	Minichromosome Maintenance
MDC1	Mediator of DNA Damage Checkpoint Protein 1
Met	Methionine
MIBC	Muscle-Invasive Bladder Cancer
miRNA	MicroRNA
Min	Minute(s)
MIU	Motif Interacting with Ubiquitin
mL	Millilitre(s)
mM	Millimolar
MMEJ	Microhomology-Mediated End-Joining
MMSET	Multiple Myeloma SET Domain
MRE11	Meiotic Recombination 11
MRN	MRE11-RAD50-NBS1
mRNA	Messenger Ribonucleic Acid
MS	Mass Spectrometry
MHC-1	Major Histocompatibility Complex Class I
NBS1	Nijmegen Breakage Syndrome Protein 1
NHEJ	Non-Homologous End-Joining
nM	Nanomolar
nm	Nanometre(s)
NMIBC	Non-Muscle-Invasive Bladder Cancer
NPL4	Nuclear Protein Localisation Protein 4
ns	Not Significant
NuRD	Nucleosome Remodelling and Deacetylase

NZF	NPL4 Zinc Finger Domain
ORC	Origin Recognition Complex
ORI	Origin of Replication
PALB2	Partner and Localiser of BRCA2
PARP1/2	Poly [ADP-Ribose] Polymerase 1/2
PAXX	Paralog of XRCC4 and XLF
PBS	Phosphate-Buffered Saline
PcG	Polycomb Group
PCNA	Proliferating Cell Nuclear Antigen
PCR	Polymerase Chain Reaction
PDE6	Phosphodiesterase VI
PDX	Polystyrene Xylene
PNKP	Polynucleotide Kinase 3'-Phosphatase
Pol	Polymerase
POLQ	Polymerase Theta
PSMD	26 Proteasome Non-ATPase Regulatory Subunit
PTM	Post-translational Modification
PTIP	PAX Transcription Activation Domain Interacting Protein
PUB	PNGase (Peptide N-Glycosidase)/Ubiquitin Associated
Q	Glutamine
Rad	Radiation Sensitive
RBP1	Retinol-Binding Protein 1
REV	Reversionless
RIF1	Rap1-Interacting Factor 1
RING	Really Interesting New Gene
RIPA	Radioimmunoprecipitation Assay
RJALS	Ruijs-Aalfs Syndrome
RNA	Ribonucleic Acid
RNAP	RNA Polymerase
RNF	Ring Finger Protein
RNS	Reactive Nitrogen Species
ROS	Reactive Oxygen Species
RPA	Replication Protein A
RQC	Ribosome-Associated Quality Control
RT	Room Temperature
S Phase	Synthesis Phase
SCF	SKP, Cullin, F-Box Containing Complex
SDS	Sodium Dodecyl Sulphate
SEM	Standard Error of the Mean
SEP	After SHP1, EYC and p47
SD	Standard Deviation
S/Ser	Serine
SHP	Src Homology 2-containg Phosphatase
SILAC	Stable Isotope Labelling with Amino Acids in Cell Culture
SIM	SUMO Interacting Motif
siRNA	Short Interfering RNA
shRNA	Small Hairpin RNA

SLX	Synthetic Lethal of Unknown Function
SPRTN	SprT-like N-terminal Domain
SSA	Single-Strand Annealing
SSBs	Single Strand Breaks
ssDNA	Single-Stranded DNA
STUbL	SUMO-Targeted Ubiquitin Ligase
SUMO	Small Ubiquitin-Like Modifier
TBS	Tris-Buffered Saline
TCGA	The Cancer Genome Atlas
TFIIH	Transcription Factor II H
TLS	Translesion Synthesis
TNBC	Triple-Negative Breas Cancer
TOP	Topoisomerase
U2OS	U2-Osteosarcoma
Ub	Ubiquitin
UBC	Ubiquitin-Conjugating
UBE	Ubiquitin Conjugating Enzyme
UBL	Ubiquitin-like
UBX	Ubiquitin Regulatory X
UBXD	UBX Domain-containing protein
UBXL	Ubiquitin Regulatory X Like
UBZ	Ubiquitin-Binding Zinc Finger
UFD1	Ubiquitin Fusion Degradation Protein 1
UIM	Ubiquitin-Interacting Motif
UPR	Unfolded Protein Response
UPS	Ubiquitin-Proteasome System
UT3	UFD1-Truncation 3 Domain
UV	Ultraviolet
VBM	VCP-Binding Motif
VCP	Valosin Containing Protein
VIM	VCP Interacting Motif
VIMP	VCP-Interacting Membrane Protein
VIP	VCP-Interacting Protein
W	Tryptophan
WCE	Whole Cell Extract
WS	Werner Syndrome
WT	Wild-Type
XLF	XRCC4-Like Factor Ubiquitin Like with PHD and Ring Finger Domains
XP	Xeroderma Pigmentosum Complementation Group
XRCC	X-Ray Repair Cross Complementing
ZNF	Zinc Finger
γH2AX	Phosphorylation histone H2AX

Chapter 1: Introduction

1.1. Genomic instability and cancer

Genome instability is a hallmark of cancer, being recognised as one of the enabling factors in tumourigenesis (Hanahan and Weinberg, 2011). Cells undergoing malignant transformation display constitutive phosphorylation of various DNA damage signalling proteins such as the cell cycle regulators ATM, CHK2, p53, and the histone variant H2AX. This is thought to serve as an initial barrier to uncontrolled proliferation, which is overcome when one or more DNA damage response (DDR) pathway is deficient (Halazonetis et al., 2008). These deficiencies eventually lead to various mutations in the genome (e.g. frameshift mutations, deletions, insertions, missense and nonsense mutations) and chromosome rearrangements, such as chromosome fusions and alterations in chromosome numbers. In addition to various deficiencies in DNA repair pathways, mutations result from DNA replication stress, which leads to replication fork stalling and eventual fork collapse as a consequence of failed fork stabilisation (Zeman and Cimprich, 2014). Fork collapse can be described through the dissociation of the replisome and the formation of double-strand breaks (DSBs) (Carr et al., 2011, Zeman and Cimprich, 2014). While collapsed forks can be recovered through break-induced replication (BIR) and recombination, this can result in genetic instability, including deletions and chromosomal translocations (Anand et al., 2013, Malkova and Ira, 2013). Causes of fork stalling include: exhaustion of the available deoxyribonucleoside triphosphate (dNTP) pool, difficult to replicate regions and DNA-protein crosslinks, replication-transcription collisions that lead to RNA:DNA hybrids (R-loops), DNA damage and single-ended DSBs (seDSBs) (Kohnken et al., 2015, Zeman and Cimprich, 2014, Aguilera and Garcia-Muse, 2012). Oncogenes such as *RAS* and *MYC* cause DNA replication stress and subsequent fork collapse, which can cause cells to proceed through the cell cycle with damaged DNA, resulting in further mutations and chromosomal instability (Halazonetis et al., 2008).

Although cancer-related mutations show high inter-tumour heterogeneity, genomic profiling has enabled the identification of several “driver” mutations that can initiate tumour development (Cancer Genome Atlas Research et al., 2013, Rodriguez-Martin et al.,

2020, Jackson and Bartek, 2009). For example, mutations in a number of DDR genes are known to cause cancer predisposition syndromes: ataxia telangiectasia (AT), Nijmegen breakage syndrome (NBS), Bloom syndrome (BS), Lynch syndrome, Werner syndrome (WS) (Pearl et al., 2015), and Ruijs-Aalfs syndrome (Lessel et al., 2014).

Targeting the DDR in a context of specific DDR gene deficiencies leads to tumour cell death because deficiencies in a particular DNA repair pathway increase dependency on other alternative pathways (Bryant et al., 2005). This targeted approach is based on the phenomenon of synthetic lethality, where a deficiency in the expression of one gene alone is compatible with cell viability but a deficiency in the expression of two genes results in cell death. Perhaps the best-known example of this is the use of PARP inhibitors in cancer patients in the background of the tumour suppressor BRCA deficiency (Farmer et al., 2005, Bryant et al., 2005). Mechanisms of PARP inhibitor resistance include BRCA1/2 reversion mutations that restore the wild-type open reading frame (ORF), epigenetic modifications, DNA replication fork protection, restoration of ADP-ribosylation (PARylation), as well as the presence of combined defects in BRCA1/2 and the Shieldin complex proteins (SHLD1, SHLD2, SHLD3 and REV7), which promote non-homologous end-joining (NHEJ) and inhibit DNA end resection and homologous recombination (HR) (see Chapter 1.3.) (Li et al., 2020). Loss of function in the Shieldin complex proteins in a BRCA1/2 deficient background partially restores DNA end resection and HR, promoting PARP inhibitor resistance (Noordermeer and van Attikum, 2019, Li et al., 2020). One way of overcoming this resistance is targeting polymerase theta (Pol θ, or POLQ) in BRCA1/2 deficient cancers. Polymerase theta functions in theta-mediated end joining (TMEJ), a minority DSB repair pathway that relies on annealing of microhomologies present in 3-single-stranded DNA (ssDNA) tails, and is promoted when the majority DSB repair pathways, NHEJ and HR, are compromised (Seki et al., 2003, Carvajal-Garcia et al., 2020, Zatreanu et al., 2021).

1.2. Radiotherapy and radiosensitisers in the treatment of cancer

More than half of cancer patients receive radiotherapy as part of their treatment. Ionising radiation (IR) forms aqueous electrons and oxidising free radicals that deposit energy and cause covalent changes in the macromolecular compartments of cells. One gray (Gy) of IR

causes approximately 1,000 single-strand breaks (SSBs) and 35 double-strand breaks (DSBs) per cell (Rothkamm and Lobrich, 2003, O'Connor, 2015). The type of damage from IR can be either direct (around 33% of total damage) or indirect (around 67% of total damage). Direct damage results from the formation of organic radicals on biomolecules, whereas indirect damage is caused by free radicals, produced by the ionisation of water, generating highly reactive hydroxyl radicals (HO^{-}) that damage DNA (Alizadeh et al., 2013). The main goal of radiotherapy is to effectively target the tumour while sparing normal surrounding tissue. One way to achieve this is by fractionation therapy, where the total dose of radiation is divided into several smaller doses of radiation over a course of several days (Hellevik and Martinez-Zubiaurre, 2014). This results in better sublethal (type of damage not leading to cell death) DNA damage repair in normal cells compared to cancer cells. This phenomenon occurs because normal cells have intact DNA repair pathways and most types of cells have low proliferation rates compared to cancer cells (Spitz et al., 2019). Fractionated therapy is given in accordance with the principle of the 5R's of radiation therapy, which describes five factors that are necessary in determining the total effect of radiotherapy. These five factors are: (1) reoxygenation of cells that survive, (2) repair of sublethal damage, (3) redistribution of cells within the cell cycle, (4) repopulation of cells post-irradiation and (5) the intrinsic radiosensitivity of cells (Steel et al., 1989). When a particular dose of radiation is divided into fractionated therapy, reoxygenation and redistribution will promote overall tumour cell kill by increasing the radiation sensitivity of surviving cells. On the contrary, cells are also more likely to be repaired and repopulated due to the increased recovery time after individual doses. Therefore, the overall goal is to have fractionation schemes that maximise tumour cell kill while minimising toxicity to normal tissues, especially late-responding tissues that show injury several months/years after radiotherapy (e.g. the central nervous system, kidney, lung). Although tumour cells are considered to be early-responding, there is considerable inter-and intratumoural heterogeneity such that this is not necessarily always the case (Brown et al., 2014).

One way in which to enhance the radiosensitivity of tumour cells is to introduce specific molecules (radiosensitisers) in combination with radiotherapy that enhance damage to tumour tissue and reduce side effects to healthy tissue (Begg et al., 2011, Barazzuol et al., 2013, Reaper et al., 2011, Senra et al., 2011). The earliest strategies were based on inducing

free-radical damage by increasing oxygen delivery to the tumour using oxygen-mimicking compounds (Oronsky et al., 2011). Oxygen is a well-known radiosensitiser with high affinity for electrons and can rapidly add to free radicals, thereby producing a chain reaction of reactive radicals damaging the DNA and causing cell death. For example, nimorazole, a compound used as a radiosensitiser in head and neck cancers, contains a nitro group ($-NO_2$) that has a high electron affinity and mimics oxygen by fixing DNA damage caused by free radicals (Wang et al., 2018).

Hypoxic (low-oxygen) tumour cells are around two to three times more radioresistant than normoxic (normal oxygen concentration) cells (Harrison et al., 2002). Hypoxic tumours therefore require higher radiation doses for treatment, which is associated with increased normal tissue toxicity. By combining radiation with radiosensitising agents, the damage caused by radiation to normal surrounding tissues is lowered because tumours become more sensitive to radiation and therefore require lower doses to achieve a therapeutic effect (Rey et al., 2017).

Based on the structure of radiosensitisers, they can be broadly categorized into small-molecule chemicals, macromolecules, and nanostructures (Wang et al., 2018). Several chemical radiosensitisers have been tested in Phase I/II clinical trials and their mechanisms of function studied *in vitro* and *in vivo* (Buckley et al., 2020, Wang et al., 2018). Examples of radiosensitisers include gemcitabine (antimetabolite) (Kerr et al., 2014, Blackstock et al., 2006, Loehrer et al., 2011, Pauwels et al., 2005), 5-fluorouracil (5-FU) (antimetabolite) (Urick et al., 2011), olaparib (PARP inhibitor) (van de Ven et al., 2017), temozolomide (alkylating agent) (van Nifterik et al., 2007, Choi et al., 2014), paclitaxel and docetaxel (taxanes) (Jiang et al., 2017, Cui et al., 2014). Amongst these, the pyrimidine analogue 5-FU and the deoxycytidine analogue gemcitabine (2',2'-difuloro-2'-deoxycytidine) are classified as pseudosubstrates that are incorporated into newly synthesised DNA, leading to blocks in DNA replication and subsequent cell death (Wang et al., 2018). Additionally, histone deacetylase (HDAC) inhibitors such as the pan-HDAC inhibitor panobinostat have been shown to acts as effective radiosensitisers predominantly due to their effect on the cell cycle, DNA damage repair and apoptosis (Li and Seto, 2016, Groselj et al., 2018). Moreover, selective HDAC inhibitors such as romidepsin that acts on class I HDACs work as

effective radiosensitisers, and romidepsin has been shown to cause no exacerbation of acute or late normal tissue toxicity compared to radiation alone *in vivo* (Paillas et al., 2020).

In addition to the use of small-molecule chemicals, macromolecules such as microRNAs (miRNAs), oligonucleotides and peptides can act as radiosensitisers. MicroRNAs are a class of noncoding RNAs that regulate genes post-transcriptionally. For example, miRNA miR-205 levels have been shown to be downregulated in radioresistant breast cancer cells and miR-205 was shown to have radiosensitising effects in mouse xenograft tumour models (Zhang et al., 2014). Peptides such as antibodies targeting epidermal growth factor receptors (EGFRs) have radiosensitising effects on tumour cells by downregulating downstream mitogenic signals as well as compromising DSB repair (Huang et al., 2013).

Nanotechnology has provided further opportunities for radiosensitisation of cancer cells. Specifically, heavy-metal nanomaterials such as silver and gold particles show promise as they are able to scatter and emit energy from radiation, and they are distributed to tissues with favourable kinetics whilst showing low normal tissue toxicity (Mi et al., 2016). Additionally, nanomaterials tend to accumulate in tumour tissues compared to normal tissues (Wong et al., 2015) and are shown to impede cellular motility by destabilising the microtubule network (Tay et al., 2014).

A phenomenon whereby local radiation therapy leads to the regression of metastatic tumours is called the abscopal effect (Mole, 1953). This can be induced when radiation therapy is combined with immunotherapy, which primes cytotoxic T cells against tumour antigens, targeting both the primary tumour as well as distant metastatic sites (Twyman-Saint Victor et al., 2015, Rodriguez-Ruiz et al., 2016). For example, fractionated radiotherapy combined with immune checkpoint inhibitors against the cytotoxic T-lymphocyte-associated antigen 4 (CTLA-4) have been associated with an increased abscopal effect (Dewan et al., 2009). The immune checkpoint inhibitors PD-1/PDL-1 work on a similar principle by blocking the interaction between PD-L1 on the tumour cells with PD-1 on T cells, thereby facilitating an enhanced recognition of cancer cells by the immune system (Kim and Lee, 2021). Abscopal effects have been described in several types of

tumours such as melanoma, lymphoma, and colorectal cancer (Jin et al., 2022, Khanolkar et al., 2021, Wight et al., 2018).

Radiosensitisers influence multiple cellular pathways such as DNA repair, protein degradation and metastasis, demonstrating that there are a wide variety of potential molecular mechanisms responsible inducing radiosensitivity (Wang et al., 2018). Studying the mechanisms of radioresistance and how specific drugs radiosensitise cells will accelerate the progress of finding new and effective drugs to use in combination with radiation.

1.3. DNA double-strand break repair

DNA can be damaged by both endogenous and exogenous sources, and cells have consequently evolved specialised repair mechanisms tailored for specific lesions. Collectively, these mechanisms are part of the DNA damage response (DDR), consisting of both intra- and intercellular signalling pathways that accumulate specific repair factors leading to repair of DNA lesions (Ciccia and Elledge, 2010). DNA lesions include base damage, single-stranded DNA (ssDNA) breaks and double-stranded breaks (DSBs). Double-stranded breaks (DSBs) are regarded as the most cytotoxic because they often lead to loss of genetic information, tumourigenesis and/or cell death (Lord and Ashworth, 2012). Double-strand breaks are formed during physiological processes such as meiosis to promote accurate chromosome segregation, and during lymphocyte development as part of the V(D)J recombination events (Zhou et al., 2013). The main exogenous sources for DSBs are IR and chemotherapeutic drugs widely used in cancer therapy. Cells have two main pathways for DSB repair: non-homologous end-joining (NHEJ) and homologous recombination (HR) (Khanna and Jackson, 2001). One of the earliest signalling events in both NHEJ and HR is the phosphorylation of the histone variant H2AX (at serine 139) around DNA break sites, which acts as a recruitment platform for DDR signalling proteins, and is therefore a widely-used DNA damage marker (Lukas et al., 2011). An overview of the two main DSB repair pathways is illustrated in Figure 1.

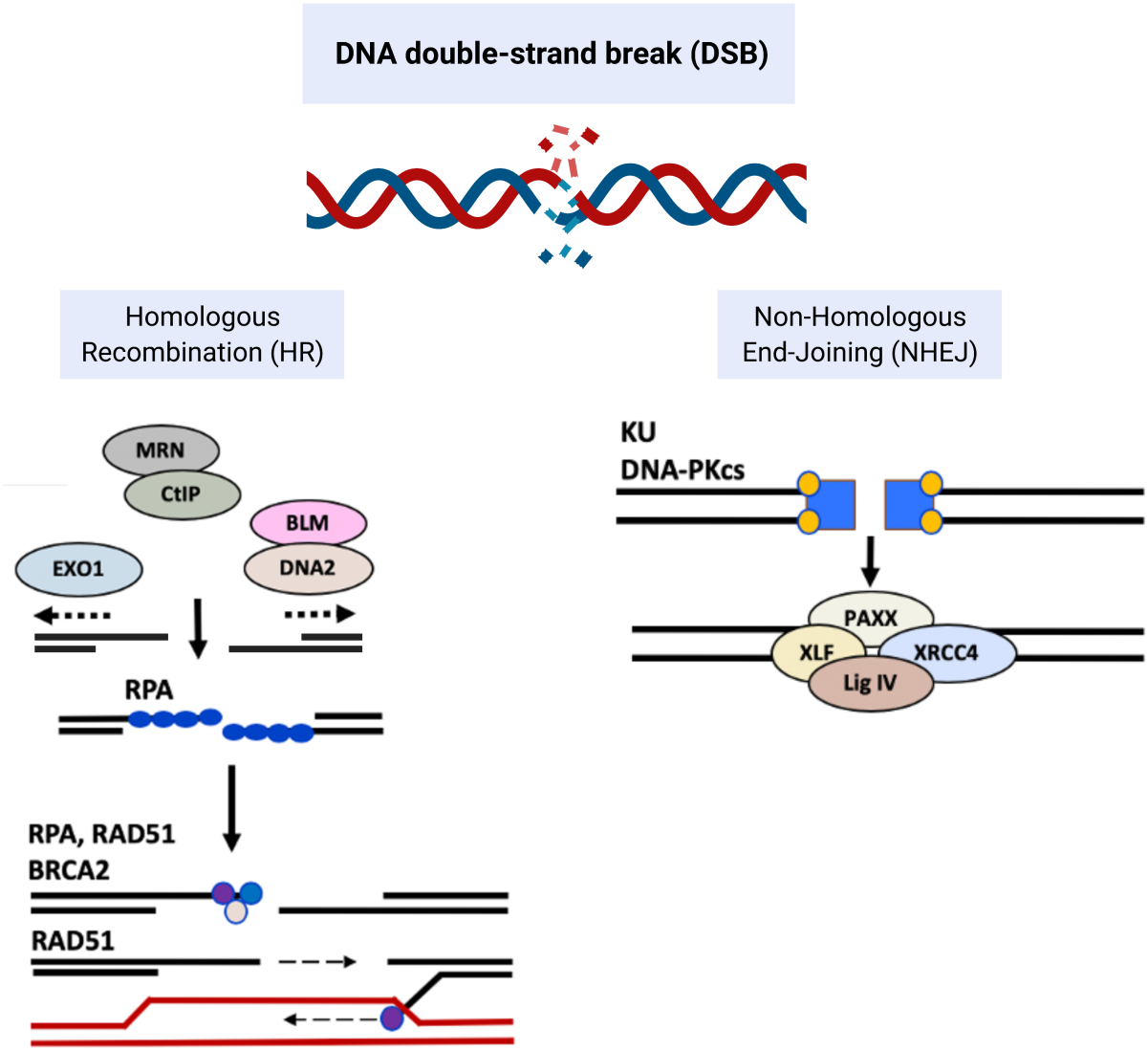


Figure 1 Overview of DSB repair pathways.
NHEJ is initiated by the Ku complex (Ku70/80), which recruits downstream mediators including the catalytic subunit of DNA-dependent protein kinase (DNA-PK_{cs}). Phosphorylation of DNA-PK_{cs} recruits the nuclease Artemis that trims broken DNA ends, and the ligation of broken DNA is mediated by DNA Ligase IV in complex with XRCC4, PAXX and XLF. HR is initiated by displacing KU from DNA ends by the MRE11-RAD50-NBS1 (MRN) complex. The nucleases MRE11 and CtIP initiate DNA end resection, which results in long-range resection by EXO1 and BLM-DNA2. Resected DNA is coated and protected by RPA, which gets replaced by RAD51. BRCA2 recruits RAD51, and the RAD51-ssDNA filament undergoes homology search and strand invasion, resulting in the formation of a D-loop with the homologous sister chromatid, eventually resulting in lesion repair. Colour coding: blue boxes in the NHEJ pathway are the KU rings, DNA-PK_{cs} is shown as yellow circles attached to KU. In HR, blue circles show individual RPA molecules on ssDNA; BRCA2 is shown as a white circle, and RAD51 molecules as purple circles. Figure adapted from (Ceccaldi et al., 2016). Figure created with Biorender.com.

1.3.1. Non-homologous end-joining

Non-homologous end-joining (NHEJ) is active throughout the cell cycle and involves joining together two broken DNA ends in a sequence-independent manner without using a homologous sister chromatid as a template, making this repair pathway relatively mutagenic (Lieber et al., 2003). The initiating event in NHEJ is the recruitment of the Ku heterodimer (Ku70/80) to each of the broken DNA ends, which acts to limit end-resection and promote the recruitment of downstream signalling proteins including the catalytic subunit of DNA-dependent protein kinase (DNA-PK_{cs}). Phosphorylation of DNA-PK_{cs} leads to recruitment of the nuclease Artemis that trims 3'-phosphogylcolate overhangs (Mari et al., 2006, Uematsu et al., 2007). DNA polymerases of the Pol X family, namely, Pol lambda (λ, or POLL) and Pol mu (μ, or POLM), fill in the resected strands. The polynucleotide kinase 3'-phosphatase (PNKP) ensures that the DNA strands are compatible for ligation by DNA Ligase IV in complex with X-ray cross-complementing protein 4 (XRCC4) and aprataxin and PNK-like factor (APLF). PNKP achieves this either by removing 3'-phosphates or phosphorylating 5'-hydroxyl groups on sugar residues of the DNA backbone (Mahajan et al., 2002, Lee et al., 2016).

1.3.2. Homologous recombination

Homologous recombination (HR) is restricted to the G2/S phase of the cell cycle, where a sister chromatid is available as a template for strand synthesis. HR is considered as an error-free way to repair DSBs and is initiated by the MRE11-RAD50-NBS1 (MRN) complex which recognises DSBs and displaces Ku70/80 from DNA ends (Lee and Paull, 2005). The nuclease MRE11 and its binding partner CtBP-interacting protein (CtIP) initiate DNA end-resection, which is a key process in determining DNA DSB repair pathway choice (Cannavo and Cejka, 2014). The DNA phosphodiester backbone is incised by MRE11's 5' endonuclease activity, creating single-strand nicks and serving as entry points for its 3'-5' exonuclease activity (Anand et al., 2016, Cejka, 2015). MRE11-dependent end resection is mediated by its co-factor CtIP (Anand et al., 2016). Some studies have suggested that CtIP has intrinsic 5' endonuclease activity (Lengsfeld et al., 2007, Makharashvili et al., 2014, Wang et al., 2014), however, the structure of CtIP is not directly related to any class of nucleases, and other studies have found no intrinsic nuclease activity for CtIP (Andres and Williams, 2017).

The generation of a 3’ overhang is required for DSBs to be repaired by HR, and further 5’-3’ exonuclease activities of Bloom syndrome protein (BLM)-EXO1 and BLM-DNA2 (BLM-DNA2) generate long ssDNA stretches, which are bound and protected by the ssDNA-binding protein replication protein A (RPA) (Yates et al., 2018). RPA interacts with the breast cancer type 2 susceptibility protein (BRCA2), which in turn is localised to DNA damage via BRCA1 and partner and localized of BRCA2 (PALB2). BRCA2 then gets displaced by RAD51 recombinase, which forms nucleofilaments with ssDNA, initiating homology search on the sister chromatid and subsequently leading to strand invasion. This results in the formation of a displacement loop (D-loop) with the homologous sister chromatid (Liu et al., 2014). This intermediate structure is known as the heteroduplex DNA (hDNA), which is resolved upon synthesis of a new strand and the subsequent removal of RAD51 from hDNA by RAD54 (Wright and Heyer, 2014). The outcome of a D-loop resolution is either a crossover (CO) or a non-crossover (NCO) event. During COs, there is reciprocal exchange of genetic information between two homologous recombining sequences. For example, DSB-induced CO events are important for chromosome segregation and the generation of genetic diversity during meiosis (Sanchez et al., 2021, Hunter, 2015). COs between homologs can lead to genome instability by causing genetic rearrangements (So et al., 2017). In contrast to COs, there is no exchange of genetic information between DNA sequences flanking the recombination sites in NCOs. However, recombining DNA molecules can still transfer genetic information locally from one DNA sequence to a homologous sequence, leading to the formation of gene conversion tracts. NCOs that occur between homologs or at ectopic sites can lead to genome instability (Sanchez et al., 2021).

1.3.3. Repair pathway choice between NHEJ and HR

The repair pathway choice between NHEJ and HR is based on the cell cycle phase and the existence of an antagonistic relationship between some of the NHEJ and HR factors. A well-known example is the antagonistic relationship between the HR protein BRCA1 and the NHEJ protein p53-binding protein 1 (53BP1) (Bunting et al., 2010, Xie et al., 2007). BRCA1 inhibits 53BP1 during G2/S phases of the cell cycle, where it excludes 53BP1 from DNA ends to initiate end-resection (Feng et al., 2015, Becker et al., 2021). Lack of BRCA1 in cells increases mutagenic NHEJ-mediated repair during S phase, and is associated with

embryonic lethality, chromosomal aberrations and tumourigenesis. However, cells lacking both BRCA1 and 53BP1 have a milder phenotype and there is a significant rescue of cell survival, clearly demonstrating the opposing roles of BRCA1 and 53BP1 in DSB repair (Bunting et al., 2010, Bouwman et al., 2010, Cao et al., 2009). Additionally, as cells enter S phase, the recruitment of BRCA1 into ionising-radiation-induced foci (IRIF) excludes 53BP1 foci to the focal periphery of nuclei, which results in a reduction of 53BP1 co-localisation at DNA damage sites. The genomic instability of BRCA1-deficient cells might therefore be the result of failing to properly exclude the anti-resection factor 53BP1 from IRIF during S phase (Chapman et al., 2012a).

1.2.4. Alternative-non-homologous end-joining (alt-NHEJ)

Alternative-NHEJ, also known as microhomology-mediated end-joining (MMEJ), is a minority DSB repair pathway that is less common than the classical NHEJ and HR. Alt-NHEJ becomes more active when NHEJ and HR are defective (Truong et al., 2013). The pathway is dependent on CtIP- and MRE11-mediated DNA end-resection, involving annealing of short 3'-overhangs of approximately 5-25 nucleotides (McVey et al., 2016). The nuclease activity of MRE11 promotes limited end-resection in alt-NHEJ, which leads to a more extensive DNA resection by EXO1 and BLM. During DNA end resection, RPA normally binds ssDNA and inhibits alt-NHEJ between microhomologies internal to the break ends, thereby promoting HR. However, when RPA binding is compromised, annealing between microhomologies increases, which promotes alt-NHEJ and decreases HR-mediated repair (Deng et al., 2014). The dependency of alt-NHEJ on DNA end-resection is further demonstrated by experiments showing that the NHEJ factor Ku70/80 is able to inhibit this pathway (Shamanna et al., 2016).

In alt-NHEJ, an error-prone DNA polymerase theta performs strand synthesis, leaving behind a specific mutational signature composed of insertions and deletions at sites of microhomology-mediated repair (Yousefzadeh and Wood, 2013). Deletion of POLQ in mouse models results in increased HR-mediated repair, evidenced by increased recombination of dysfunctional telomeres and an accumulation of RAD51 foci at DSBs. Furthermore, in the absence of functional BRCA1/2 genes, depleting POLQ significantly

decreases cell survival, which could be a potential therapeutic application for cancers deficient in HR, such as ovarian and breast adenocarcinomas (Mateos-Gomez et al., 2015).

The final DNA ligation step is performed by Ligase I (LIG1) or Ligase III (LIG3)-XRCC1 complex. PARP-1 functions together with LIG3 to catalyse alt-NHEJ and has been shown to induce chromosomal translocations in mouse cells (Audebert et al., 2004, Liang et al., 2008, Simsek et al., 2011). Using PARP inhibitors in cells deficient in HR leads to synthetic lethality, indicating that PARP-1-mediated alt-NHEJ can compensate for HR deficiency (Bryant et al., 2005, Farmer et al., 2005). In addition to PARP, polymerase theta has a necessary function in mediating alt-NHEJ in most eukaryotes (Ramsden et al., 2022), and inhibitors targeting its function have been shown to target PARP inhibitor resistance (Zatreanu et al., 2021). Additionally, PARP-1 is required for DNA end-joining in the absence of the Ku complex (Wang et al., 2006, Mansour et al., 2010, Audebert et al., 2004).

1.3.5. Single-strand annealing (SSA)

Single-strand annealing (SSA) functions to anneal long homologies of approximately 30 base pairs, leading to large deletions in the genome. Given the high density of repetitive Alu-type short interspersed elements (SINEs) in the human genome, overreliance on SSA is therefore highly mutagenic (Mansour et al., 2010). Being an alternative form of HR-mediated repair, SSA is also resection-dependent and relies on the nucleases CtIP and MRE11 (Bhargava et al., 2016, Munoz et al., 2012). When HR repair proteins such as BRCA2 or RAD51 are compromised, cells are more likely to undergo SSA by replacing RAD51-mediated homology search with mutagenic strand annealing by RAD52 (Ochs et al., 2016). When DNA end-resection increases above physiological levels, HR repair is equally compromised and cells are more likely to be repaired by SSA (Mansour et al., 2010). Conversely, proteins that limit DNA end-resection, such as the Ku complex and 53BP1, have been shown to suppress SSA. Compromised 53BP1 formation on DNA damage has similarly been shown to cause a repair pathway switch from error-free gene conversion mediated by RAD51 to mutagenic end-joining by RAD52 (Stark et al., 2004). One of the reasons why this switch happens is the antagonistic relationship between RAD52 and RAD51, where RAD51 acts as an inhibitory brake on RAD52 (Wu et al., 2008, Ivanov et al., 1996). RAD52

binds 3'-ssDNA tails and creates overhang flap sequences in the process. These flap structures are removed by the ERCC1-ERCC4 complex, whereby ERCC1 functions with XPF in a complex that is able to cleave 3'-ssDNA tails (Al-Minawi et al., 2008). Any gaps in DNA are filled in by DNA polymerases to generate ligase substrates (McVey et al., 2016). Broken DNA ends are ligated by LIG3 (Gottlich et al., 1998).

Overall, the major difference between SSA and alt-NHEJ is that extensive DNA end resection favours SSA, whereas a more limited end resection favours alt-NHEJ. Furthermore, SSA results in annealing of large sequence homologies that leads to deletions of large DNA fragments, whereas alt-NHEJ uses small homologous sequences (microhomologies) that can either lead to insertions or deletions in the genome, depending on the specifics of the repair pathway (Bhargava et al., 2016). The differences between alt-NHEJ and SSA are illustrated in Figure 2 (Ceccaldi et al., 2016).

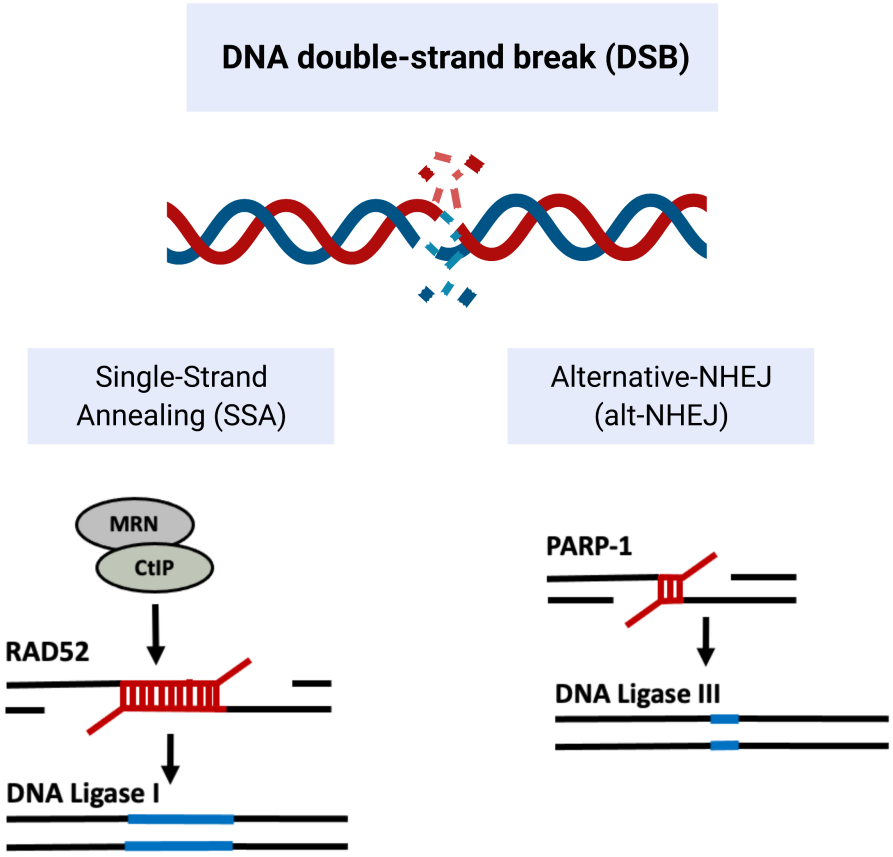


Figure 2 Comparison of SSA and alt-NHEJ.
Left: SSA is resection-dependent and anneals long homologies (around 30 base pairs), leading to large deletions in the genome. A RAD51-mediated homology search is replaced by mutagenic strand annealing by RAD52. DNA is ligated by Ligase I. Right: Alternative-NHEJ is PARP-1-dependent and relies on short resection tracts that anneal at short homologies of approximately 10 base pairs. An error-prone polymerase theta (Pol θ) then synthesises new DNA strands, resulting in a specific mutational signature of insertions and deletions at sites of microhomology-mediated repair. DNA is ligated by Ligase III. Colour coding: in alt-NHEJ and SSA, red shows the different lengths of annealing between the strands; the difference between the ligation product lengths is shown in blue for both pathways. Figure adapted from (Ceccaldi et al., 2016). Figure created with Biorender.com.

1.3.6. Role of chromatin in double-strand break repair

The formation of DSBs leads to a hierarchical recruitment of several signalling and repair proteins that form into nuclear foci (also known as ionising radiation-induced foci, or IRIF). Post-translational modifications (PTMs) of histones, such as phosphorylation, ubiquitination, methylation, and acetylation, serve to regulate and coordinate DNA damage repair by providing a recruitment platform for DNA repair factors. Furthermore, PTMs serve as a basis for signalling amplification near DSB sites. A summary of the role of chromatin in DSB repair is shown in Figure 3 (Lukas et al., 2011, Bekker-Jensen and Mailand, 2010).

Double-strand breaks are initially recognised by PARP-1, which (ADP-ribosyl)ates the amino-terminal tails of histones (Messner et al., 2010). This leads to the recruitment of chromatin remodelling complexes such as the nucleosome remodelling and deacetylase (NuRD) complex and polycomb complexes. These chromatin remodelling factors then lead to transcriptional silencing of the chromatin flanking DNA damage sites, decreasing the likelihood of collisions between RNA polymerases and DNA damage repair signalling proteins (Chou et al., 2010). The MRN complex initiates a DNA damage signalling cascade by activating the ataxia telangiectasia mutated (ATM) kinase. For the ATM signal to spread efficiently near DNA break sites, it needs to be autophosphorylated (at serine 1981); this is initiated by ATM acetylation by the phosphorylated form of histone acetyltransferase TIP60 (Sun et al., 2005). Autophosphorylated ATM then binds to the histone variant H2AX and phosphorylates it on serine 139. This phosphorylation is coupled with dephosphorylation of the neighbouring tyrosine 142 residue, which is constitutively phosphorylated in the absence of DNA damage (Cook et al., 2009). Both the phosphorylation of serine 139 and the dephosphorylation of tyrosine 142 on H2AX create binding sites for the mediator of DNA damage checkpoint protein 1 (MDC1). MDC1 binds phosphorylated H2AX (γH2AX) via its phospho-binding BRCA1 carboxy-terminus (BRCT) domain, leading to further accumulation of MDC1 and ATM through the MRN complex protein NBS1, creating a positive feedback loop whereby the γH2AX signal is amplified 0.5-2 megabases (Mb) from the DSB site (Stucki and Jackson, 2006, Jungmichel and Stucki, 2010).

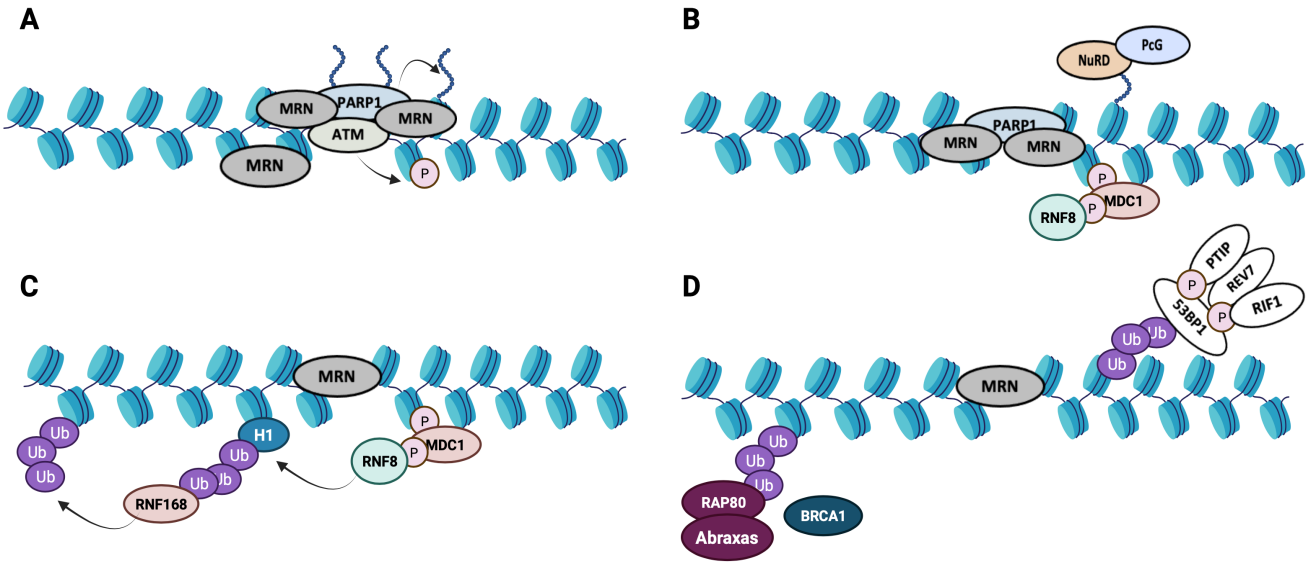


Figure 3 Chromatin-dependent protein assembly in DSB repair.
A) PARP1 ADP-ribosylates itself and nearby histones. MRN initiates a signalling cascade by ATM which phosphorylates H2AX-type histones. B) ADP-ribosylated histones recruit chromatin remodelling complexes (NuRD and PcG) involved in changing chromatin compaction near DSBs to allow access of repair factors. MDC1 is recruited to ATM-phosphorylated histone H2AX (γH2AX)**,** where it creates a positive feedback loop by recruiting more MDC1 and ATM. The E3 ligase RNF8 is recruited to damage by MDC1. C) RNF8 ubiquitinates (marked as "Ub") histone H1 (marked as "H1"), which results in RNF168 accumulation. D) RNF168 ubiquitinates H2AX-type histones, which leads to the recruitment of 53BP1 that is phosphorylated by ATM and binds to PTIP, REV7 and RIF1. This creates a complex of anti-resection proteins promoting NHEJ-mediated repair. Ubiquitinated histone-binding proteins also recruit RAP80 and its binding partner Abraxas, which further recruits the HR protein BRCA1. Figure adapted from (Schwertman et al., 2016). **Abbreviations**: PcG, polycomb-group protein; NuRD, nucleosome remodelling deacetylase; PTIP, PAX transcription activation domain interacting protein. Figure was created with Biorender.com.

Ubiquitination of histones and DNA repair factors is one of the main PTMs occurring at DSB sites. It is commonly associated with providing a recruitment platform for downstream signalling proteins, which depends on lysine 63 (K63)-mediated ubiquitination events. The main E3 ligases involved in the synthesis of these ubiquitin chains are RNF8 and RNF168 (Mailand et al., 2007, Doil et al., 2009, Stewart et al., 2009). RNF8, a RING-domain ubiquitin ligase, is recruited to DSBs via its forkhead-associated (FHA) domain, which recognises ATM-mediated phosphorylation sites in MDC1, and initiates ubiquitination on histones (Mailand et al., 2007). Another RING-domain ubiquitin ligase, RNF168, then recognises and amplifies the existing ubiquitin chains generated by RNF8 (Leung et al., 2014). The endpoint of the K63-linked ubiquitination cascade is the recruitment of chromatin-associated repair proteins such as 53BP1, RAP1-interacting factor 1 (RIF1), BRCA1-RAP80 complex and PAX transcription activation domain interacting protein (PTIP), all of which have a direct effect on DSB repair pathway choice by influencing the extent of DNA end resection (Wu et al., 2009, Fradet-Turcotte et al., 2013, Escribano-Diaz et al., 2013).

Small ubiquitin-related modifier (SUMO) chains and chromatin methylation cooperate with ubiquitination to promote retention of repair factors on DNA damage. For example, cooperation between ubiquitination and methylation of histone H4 lysine 20 (H4K20) by multiple myeloma SET domain (MMSET) methyltransferase leads to 53BP1 retention, which inhibits DNA end resection and HR (Pei et al., 2011). Additionally, the formation of mixed ubiquitin-SUMO chains by the SUMO-targeted ubiquitin ligase RNF4 is responsible for MDC1 and RPA retention, and promotes RAD51 loading at DSBs (Yin et al., 2012).

1.4. The MRE11-RAD50-NBS1 (MRN) complex

1.4.1. The MRN complex structure and role in double-strand break repair

The MRE11-RAD50-NBS1 (MRN) complex is a highly conserved structure with orthologues of RAD50 and MRE11 in eubacteria, archaea and eukaryotes, which shows that both RAD50 and MRE11 have the same specificity and function across different domains of life. However, the NBS1 subunit is less conserved and is confined to eukaryotes. A schematic representation of human MRN complex proteins is shown in Figure 4. The MRN complex has central functions in chromosomal and telomere maintenance, DSB repair, and sister chromatid association (Haber, 1998, Bressan et al., 1999, Yamaguchi-Iwai et al., 1999, Hartsuiker et al., 2001). To physically link two sister chromatids during HR, and broken DNA ends during NHEJ, the MRN complex needs to bind two DNA substrates (Hopfner et al., 2002). This is achieved by the flexible globular structure of MRN, as illustrated in Figure 5.

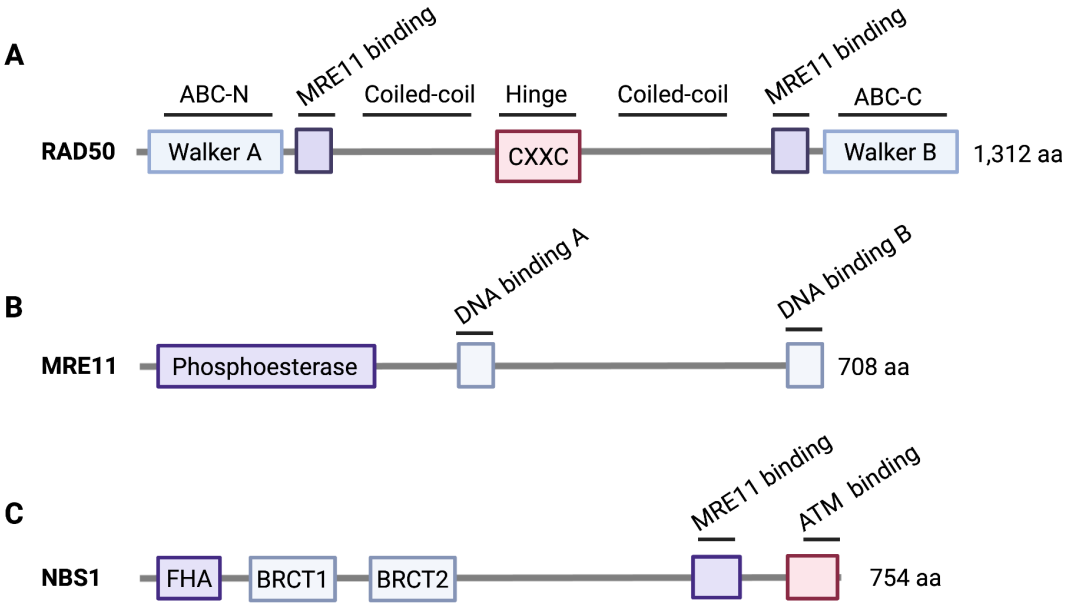


Figure 4 Functional domains of the MRE11-RAD50-NBS1 (MRN) complex proteins.
A) RAD50 contains two ATP binding domains (labelled ABC N-term and C-term). The N-terminal and C-terminal ATP-binding domains include Walker A and B domains, respectively. RAD50 has two MRE11 binding domains adjacent to ABC domains. The long heptad repeats that form coiled-coil domains are separated by a hinge region containing cysteine-XX-cysteine (CXXC) motif that binds zinc ions. B) MRE11 contains an N-terminal nuclease domain (phosphoesterase domain), which overlaps with RAD50 and NBS1 binding domains. MRE11 has two separate DNA binding domains (marked as "DNA binding A" and "DNA binding B"). C) NBS1 contains an N-terminal FHA domain and two consecutive BRCT domains. Its MRE11 and ATM interaction domains are located near the C-terminus. Figure adapted from (Assenmacher and Hopfner, 2004). Figure was created with Biorender.com.

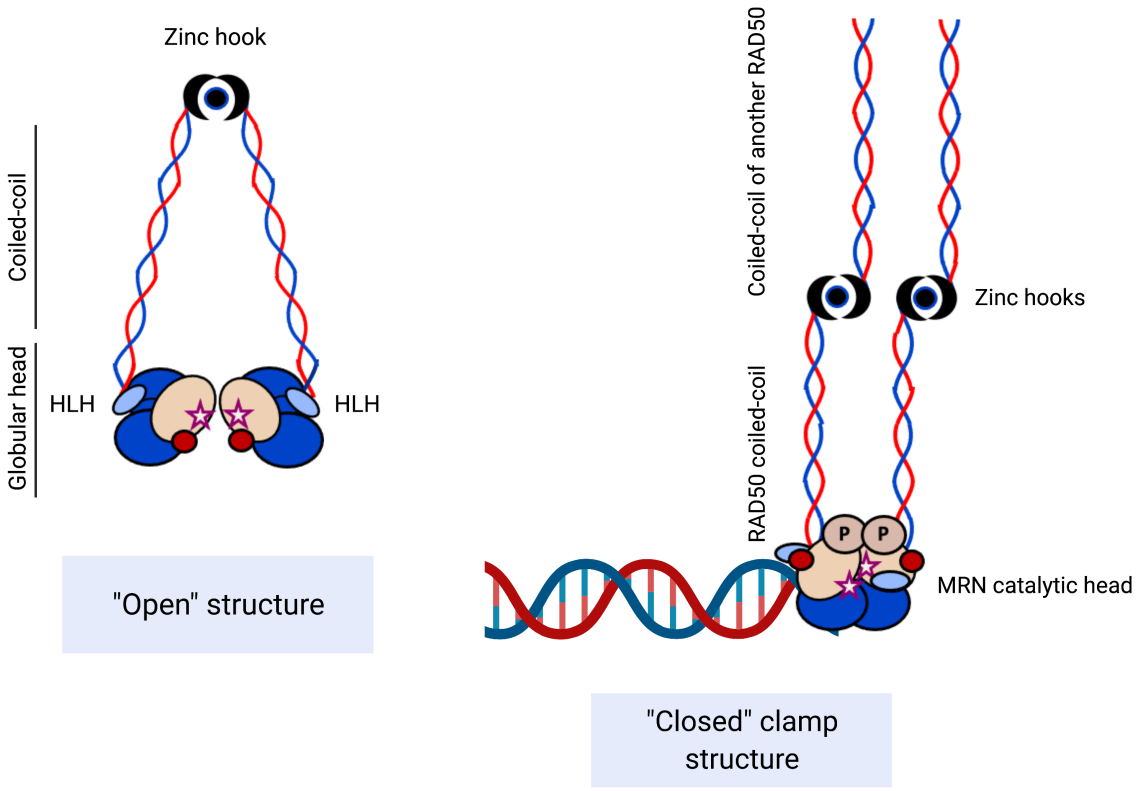


Figure 5 The structure of MRE11-RAD50-NBS1 (MRN) complex.
Left: RAD50 dimer (in dark blue) has a globular head domain and coiled-coil domains that end as zinc hooks as indicated in the figure. The MRE11 dimer (in beige) is shown with its helix-loop-helix motifs (HLH) that bind two RAD50 coiled-coil domains. Nuclease sites are shown as star shapes. NBS1 (in red) binds to MRE11. The structure is shown in its "open" form without ATP molecules bound to the complex. Right: The same complex as on the left, but in its "closed" ATP-bound form, which causes DSB processing by the globular catalytic head domain. DNA-bridging activities of the complex are shown as two separate RAD50 molecules interacting via zinc hooks. Figure adapted from (Lammens et al., 2011, Assenmacher and Hopfner, 2004).

RAD50 is an ABC-type ATPase with long heptad repeats (structural motifs that consist of a group of seven repeating amino acids). The heptad repeats of RAD50 fold into antiparallel coiled-coil domains, bridging the N-terminal Walker A and the C-terminal Walker B motifs into close proximity (Hopfner et al., 2002). At the apex of the coiled-coil domain lies a conserved Cysteine-X-X-Cysteine motif (CXXC, where X stands for any amino acid), which dimerises via cysteine residues in the presence of zinc ions. This dimerisation event allows the MRN complex to encircle the DNA and link sister chromatids in HR, and to bridge DNA ends during NHEJ (Myler et al., 2017). Additionally, the flexible coiled-coil domains of RAD50 are responsible for the MRN complex retention on DNA, where it recognises and processes blocked and misfolded DNA ends (Lammens et al., 2011). For example, the Ku complex is present throughout the cell cycle and physically blocks other proteins from binding to DNA ends. The MRN complex removes Ku from DNA ends to coordinate DSB repair, allowing other downstream proteins to access the DNA. Truncation of the RAD50 coiled-coil domains and its zinc hook prevents the complex from encircling the DNA, thereby compromising DSB repair and leading to chromosomal instability (Myler et al., 2017).

MRE11 has both ssDNA endonuclease and 3'-5' exonuclease activities able to resect misfolded and blocked DNA ends in a bi-directional manner, where MRE11 endonuclease activity at first makes incisions into dsDNA up to 300 bases away from the break site, after which MRE11 exonuclease resects towards the broken ends in a 3'-5' direction together with the EXD2 nuclease (Keeney et al., 1997, Neale et al., 2005, Shibata et al., 2014, Broderick et al., 2016, Garcia et al., 2011). CtIP functions as a co-factor for MRE11 and its phosphorylation at T847 is necessary to promote MRE11's endonuclease activity (Anand et al., 2016). The MRE11 dimer and the two nucleotide-binding domains (NBDs) of RAD50 form the "catalytic head" of the MRN protein complex, which have DNA binding and nuclease activities. The C-terminal helix-loop-helix (HLH) motifs of MRE11 dimer bind to the coiled-coil domains of two RAD50 molecules near the ATPase domains. Binding of ATP to RAD50 subunits induces a conformational change in the HLH domain of MRE11 and the RAD50 coiled-coil domain, which leads to a formation of a clamp structure with high DNA-binding activity (Hopfner et al., 2002, Lammens et al., 2011). When the CXXC motif of

RAD50 is mutated, the interaction between MRE11 and RAD50 is disrupted, which compromises DNA repair efficiency (Hopfner et al., 2002).

In *S. cerevisiae* (budding yeast), MRE11 nuclease deficiency can in certain conditions be bypassed, particularly in the absence of the Ku complex or bulky adducts at DNA ends (Mimitou and Symington, 2010, Moreau et al., 1999, Foster et al., 2011). In contrast, *Schizosaccharomyces pombe* (fission yeast) and higher eukaryotes depend on functional MRE11 nuclease activity and CtIP for viability (Buis et al., 2008, Langerak et al., 2011, Sartori et al., 2007). For example, MRE11 nuclease deficiency causes early embryonic lethality in mice, and MRE11 nuclease deficient cell lines display sensitivity to IR (Buis et al., 2008). Furthermore, MRE11 nuclease and CtIP deficiency causes sensitivity to topoisomerase inhibitors in several organisms (Deng et al., 2005, Hartsuiker et al., 2009, Huertas and Jackson, 2009, Nakamura et al., 2010, Hoa et al., 2016), thereby illustrating their importance in the maintenance of genomic stability. Additionally, all the known ATLD mutations do not reside in the conserved MRE11 nuclease regions, further supporting the importance of MRE11 nuclease activity in organismal survival (Stracker et al., 2004). Finally, in addition to MRE11 nuclease deficiency being embryonic lethal in mice, null mutations of the MRN complex components is lethal in vertebrates, demonstrating that the whole complex has essential functions in maintaining genomic stability (Xiao and Weaver, 1997, Luo et al., 1999, Zhu et al., 2001).

The NBS1 subunit does not have any catalytic or DNA-binding activities, however it is essential for conformational changes within the complex, targeting MRN to chromatin during DNA replication and recombination (Myler et al., 2017; Difilippantonio et al., 2005). It has been demonstrated that both budding yeast and human cells require NBS1 (or Xrs2 in yeast) for nuclear localisation of both MRE11 and RAD50 (Cerosaletti et al., 2006, Kim et al., 2017, Cerosaletti and Concannon, 2004, Desai-Mehta et al., 2001). The C-terminus of NBS1 contains separate motifs that mediate a direct interaction with MRE11 (Desai-Mehta et al., 2001, You et al., 2005). Enforced MRE11 nuclear localisation in budding yeast partially overcomes the defective nuclear function of MRE11 in Xrs2 mutants (Oh et al., 2016, Tsukamoto et al., 2005, Kim et al., 2017). In contrast, enforced MRE11 nuclear localisation cannot restore the nuclear localisation of RAD50 in NBS1 deficient cells (Kim et

al., 2017). NBS1 associates with the Walker A and B domains of RAD50, directly interacting with the MRE11-RAD50 tetramer. It binds MRE11 through the MRE11-interacting region in its C-terminus that is required to promote the endonuclease activity of MRE11 on blocked DNA ends and hairpin structures by sensing CtIP phosphorylation and stimulating the rate of RAD50 ATP hydrolysis (Anand et al., 2019).

NBS1 signals the presence of DSBs to the cell cycle checkpoint machinery by activating the ATM kinase via its C-terminal domain. NBS1 is necessary and sufficient for conversion of ATM into active monomers even in the absence of DNA (Dupre et al., 2006). However, to ensure a strict regulatory process whereby neither DNA or the MRN complex alone is sufficient to fully activate ATM, the MRN complex controls ATM activation in two independent steps: (1) a DNA-dependent step, where MRN tethers broken DNA ends to increase the local concentration of DNA breaks in order to activate ATM, and (2) a DNA-independent step, where NBS1 interacts with ATM-specific HEAT repeats, promoting autophosphorylation of ATM (Buis et al., 2008).

Activated ATM then phosphorylates the histone variant H2AX on serine 139 to form γH2AX, which leads to the recruitment of MDC1, the MRN complex and other protein complexes to chromatin flanking DSBs. This essentially divides the MRN complex into two separate compartments during DSB repair (Berkovich et al., 2007, Lee and Paull, 2005) (Figure 6): the chromatin compartment, dependent on MDC1 recruitment, and the H2AX-independent DNA compartment (Stucki and Jackson, 2006, Bekker-Jensen et al., 2006). In the chromatin compartment, MRN participates in the recruitment of downstream DDR signalling proteins. In the DNA compartment, MRN functions to remove blocked DNA ends and resect dsDNA to regulate repair pathway choice (Xie et al., 2009). For example, MRE11 with CtIP nuclease are required for alt-NHEJ repair upon IR-induced DSBs in G1 phase of the cell cycle. This subset of damage causes DSBs to localise to heterochromatic DNA regions in an ATM-dependent manner (Riballo et al., 2004, Goodarzi et al., 2008). However, inhibition of topoisomerase II by etoposide directs the DSB repair pathway towards NHEJ and is repaired independently of ATM. In summary, the MRN complex has different functions and outcomes depending on whether it is located on MDC1-modified chromatin

or on DNA. However, there is an intricate coordinated crosstalk between chromatin and DNA during DSB repair (Quennet et al., 2011).

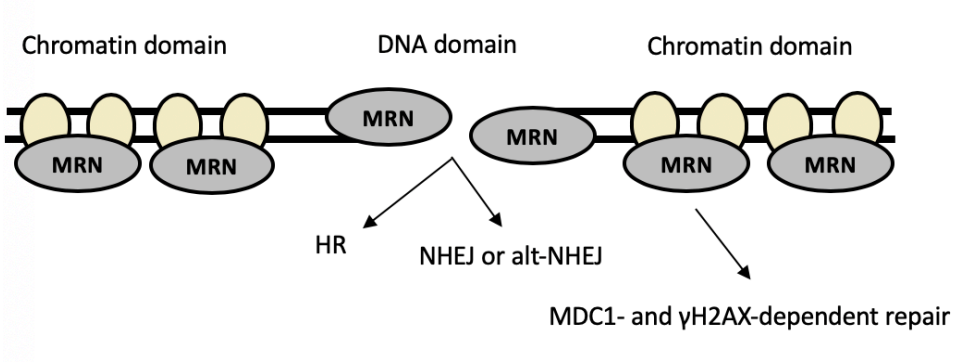


Figure 6 Functions of the MRN complex in DSB repair.
MRN exists in either the H2AX-dependent chromatin compartment or the H2AX-independent DNA compartment. In the chromatin fraction, its activities are MDC1-dependent and involve the activation of the ATM kinase in DDR. In the DNA domain, MRE11's endo- and exonuclease activities resect DNA ends for either HR or NHEJ/alt-NHEJ. The chromatin domain includes histones depicted as light yellow circles. Adapted from (Xie et al., 2007).

1.4.2. MRE11 nuclease in the regulation of repair pathway choice

MRE11 has both 5'-endonuclease and 3'-5' exonuclease activities, and CtIP is its essential co-factor required to stimulate MRE11's 5'-endonuclease activity (Lee and Paull, 2005, Nicolette et al., 2010). DNA DSB repair by HR requires the exposure of 3'- ssDNA, which is created by 5'-3' exonuclease activity. However, as MRE11 has the opposite exonuclease polarity (3'-5' exonuclease activity), the MRN complex does not directly lead to the generation of 3'-ssDNA. Rather, MRE11 endonuclease activity nicks the DNA from multiple positions in a 5'-3' direction, generating several entry sites for substrates with exonuclease activity (Anand et al., 2016, Cejka, 2015, Garcia et al., 2011), which can be broadly categorised into two groups: (1) DNA2 nuclease and BLM helicase function to resect DNA in an ATP-dependent manner. The MRN complex induces resection by recruiting BLM to DNA ends; (2) EXO1 nuclease and BLM helicase stimulate end resection. Although biochemical evidence indicates that EXO1 can function independently of BLM, BLM helicase stimulates EXO1 by increasing EXO1 affinity and processivity (Nimonkar et al., 2011, Nicolette et al., 2010, Gravel et al., 2008). The exonuclease activity of MRE11 resects towards the DSB in a 3'-5' direction, whereas the 5'-3' exonucleases BLM/WRN-EXO1 and/or BLM/WRN-DNA2 resect away from the break. The resulting product is a resected 3'-overhang, which is bound by RPA (Garcia et al., 2011, Mimitou and Symington, 2008, Zhu et al., 2008). MRE11 exonuclease efficiently targets dsDNA substrates with blunt or recessed 3' ends (Paull and Gellert, 1998, Connelly et al., 1999, Herdendorf et al., 2011, Trujillo et al., 1998, Trujillo and Sung, 2001). The endonuclease activity of MRE11 cleaves blocked DNA ends (such as the Ku heterodimer, or Spo11 meiotic recombinase in budding yeast) as well as DNA hairpin substrates (Anand et al., 2016, Cannavo and Cejka, 2014, Deshpande et al., 2016, Reginato et al., 2017, Trujillo and Sung, 2001, Paull and Gellert, 1999, Paull, 2018). The type of protein block on DNA ends does not seem to be relevant for MRE11's endonucleolytic activity, because its activity is stimulated also when DNA ends are labelled with streptavidin bound to biotin on DNA ends (Anand et al., 2016, Deshpande et al., 2016). The current working model for bidirectional processing of DSBs by MRE11 and EXO1 is indicated in Figure 7 (Garcia et al., 2011).

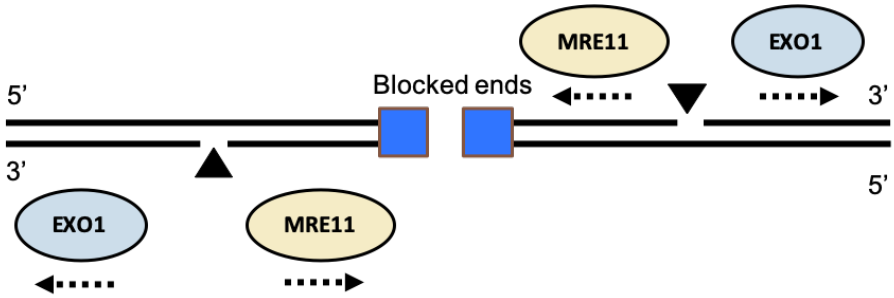


Figure 7 MRE11-mediated bidirectional processing of DSBs.
In the presence of blocked DSB ends (depicted as blue squares), MRE11 endonuclease activity nicks DNA flanking the DSB ends from multiple sites away from the break (here indicated as black triangles), which creates initiation sites for other nucleases (e.g. EXO1, BLM-DNA2). This allows bidirectional resection to take place, where MRE11 resects towards the break in a 3'-5' direction, and EXO/BLM-DN2 resect away from the break in a 5'-3' direction. This process creates long 3'-ssDNA stretches that can then be used in HR repair. The direction of MRE11 and EXO1 activities are shown as dashed arrows. Figure adapted from (Garcia et al., 2011).

MRE11 has been demonstrated to nick the DNA strand from multiple positions up to 300 base pairs (bp) away from the break site (Garcia et al., 2011). Furthermore, inhibiting the endonuclease activity of MRE11 shows a stronger resection defect than inhibiting its exonuclease activity, indicating that the initial endonucleolytic processing of DNA ends creates necessary substrates for the entry of subsequent exonuclease complexes (Garcia et al., 2011, Jazayeri et al., 2008). Indeed, it has been shown that in addition to the 5'-3' BLM-EXO1 and/or BLM-DNA2 exonucleases, MRN complex interacts with exonuclease 3'-5' domain containing 2 (EXD2) co-factor to promote efficient 3'-5' MRE11-mediated exonuclease activity. This is required for efficient DNA end resection, recruitment of RPA and HR-mediated error-free DNA repair (Nimonkar et al., 2011, Shibata et al., 2014, Broderick et al., 2016). EXD2 accelerates MRE11's 3'-5'-mediated DNA end resection, promoting faster generation of ssDNA that serves as a better substrate for downstream 5'-3' long-range exonucleases. Ultimately, efficient generation of ssDNA is required to suppress unscheduled DNA resection events which would otherwise lead to deleterious error-prone DNA repair events (Broderick et al., 2016).

Several studies have demonstrated the importance of balancing MRE11-mediated DNA end resection in the regulation of repair pathway choice (Broderick et al., 2016, Jachimowicz et al., 2019, He et al., 2018). When MRE11 nuclease activities are not adequately regulated, DNA end resection could either be insufficient or excessive, both of which compromise error-free DSB repair. Over-accumulation of MRE11 has been shown to lead to degradation of nascent DNA strands and genome instability syndromes (Hashimoto et al., 2010, Schlacher et al., 2011, Ray Chaudhuri et al., 2016). For example, UBQLN4, a regulator of protein degradation in cells, binds to ubiquitinated form of MRE11 and removes it from chromatin to favour NHEJ repair. UBQLN4-mutated cells show increased DNA end resection, and therefore more HR-mediated repair, which can be reversed using the MRE11 complex inhibitor Mirin. This shows that MRE11 accumulation on chromatin in UBQLN4-mutated cells is responsible for increased end-resection and a subsequent switch from NHEJ-mediated repair to HR-mediated repair (Jachimowicz et al., 2019).

Another example of MRE11-mediated regulation of DSB repair pathway choice is its association with the dynein light chain protein 1 (DYNLL1). DYNLL1 limits nucleolytic processing of DNA by interacting with the MRN complex, binding directly to MRE11 to limit its nuclease activity. Loss of DYNLL1 in BRCA1-mutant cells enables long-range DNA end resection, thereby restoring HR efficiency and inducing PARP inhibitor resistance (He et al., 2018). The anti-resection proteins 53BP1 and the shieldin complex proteins are also involved in counteracting MRE11-mediated nucleolytic activity, favouring NHEJ-mediated repair over HR (Gupta et al., 2018, Dev et al., 2018). Furthermore, DYNLL1 interacts with 53BP1 to limit MRE11 nuclease activity, demonstrating that there is an effective crosstalk between different branches of DDR proteins in the coordination of repair pathway choice (Lo et al., 2005).

The accurate coordination of MRE11-mediated nucleolytic DNA degradation also requires control mechanisms which prevent its binding to DNA or chromatin when DSB repair is completed to avoid degradation of nascent DNA strands. Appropriate levels of C1QBP protein are necessary to bind to MRE11 and inhibit its 3’-5’ exonuclease activity. C1QBP stabilises MRE11 upon DNA damage repair completion by establishing a repressive MRE11-RAD50-C1QBP (MRC) complex (Bai et al., 2019). Upon DNA damage, the MRC complex is

dissociated by ATM-mediated phosphorylation of MRE11 on Serine 676/678 (Kijas et al., 2015, Bai et al., 2019). Inhibiting C1QBP leads to tumour regression with chemotherapy in breast cancer xenograft tumour models (Bai et al., 2019).

In addition to regulating the balance between NHEJ and HR, the extent of DNA end resection also regulates whether cells are repaired by classical or alternative repair pathways. For example, when ssDNA levels accumulate above physiological levels, cells are more likely to be repaired by a mutagenic SSA pathway instead of the error-free HR pathway (Duursma et al., 2013). For example, silencing 53BP1 or exhausting its capacity to bind damaged chromatin compromises RAD51-mediated HR repair and increases mutagenic RAD52-mediated SSA. This demonstrates that 53BP1 not only acts as an anti-resection factor favouring NHEJ but is also required to control the fidelity of HR-mediated repair (Ochs et al., 2016). Overall, the above-mentioned examples of regulating MRE11-mediated nuclease activities demonstrate the importance of balancing the level of DNA end resection for efficient repair of DSBs. Therefore, it is not surprising that dysregulation of the MRN complex is common in different cancers (Bian et al., 2019).

1.4.3. MRN complex alterations in tumourigenesis

The importance of the MRN complex in DSB repair is demonstrated in ataxia telangiectasia-like disorder (ATLD) (Taylor et al., 2004, Palmeri et al., 2013, Fievet et al., 2019, Alsbeih et al., 2008) and Nijmegen breakage syndrome (NBS) (Digweed and Sperling, 2004), characterised by hypomorphic mutations in MRE11 and NBS1, respectively. Cells from ATLD and NBS patients are hypersensitive to IR, display chromosomal instability and defective DNA repair. Additionally, RAD50 has been reported to be mutated in NBS (Waltes et al., 2009). Alteration in the MRN complex expression levels are present in cancer-prone disorders, indicating that MRN function could be linked to tumourigenesis. Recent findings also demonstrate that MRN and CtIP are required for the resolution of RNA-DNA hybrids (i.e. R-loops) in mammals, and R-loop mediated genomic instability is common in tumourigenesis (Chang et al., 2019, Makharashvili et al., 2018, Kotsantis et al., 2016).

Accumulating evidence demonstrates that the MRN complex has tumour-suppressive functions. For example, germline variants of the MRN complex genes are linked to the development of breast cancer (Damiola et al., 2014, Heikkinen et al., 2006), and MRE11 complex dysfunction in triple-negative breast cancer (TNBC) is associated with increased ATR and PARP inhibitor sensitivity. Additionally, breast cancer tumourigenesis models in mice expressing a hypomorphic MRE11 allele ($MRE11^{ATLD}$) display chromosomal instability, inability to resolve R-loops and an overall increase in oncogene-induced DNA damage (Fagan-Solis et al., 2020).

Somatic MRN complex mutations in tumours are infrequent (Zehir et al., 2017), although reduced MRN protein complex expression levels have been observed in breast, ovarian, colorectal and bladder cancers (Bartkova et al., 2008, Brandt et al., 2017, Choudhury et al., 2010, Situ et al., 2019, Zaki et al., 2014). In muscle-invasive bladder cancer, high MRE11 expression levels were shown to have significantly better disease-specific survival after radiotherapy compared to patients who received cystectomy (Choudhury et al., 2010), whereas low expression of MRE11 in gastric cancer is associated with good response to chemotherapy and surgical resection (Altan et al., 2016). These observations demonstrate the importance of context-specific cellular responses in understanding how MRN complex expression levels affect the outcome of cancer therapies. It is therefore not only important to understand the role of individual complex components in tumourigenesis, but to also develop standards of measuring and evaluating the whole MRN complex. Overall, studies on MRN in tumourigenesis demonstrate the importance of the complex in tumour suppression and protection against genomic instability (Bian et al., 2019).

1.5. The role of VCP/p97 in genome stability

1.5.1. p97 and the ubiquitin-proteasome system (UPS)

p97 (VCP in metazoans or Cdc48 in lower eukaryotes) is an evolutionarily conserved AAA-type ATPase that is a central component of the ubiquitin-proteasome system (UPS). p97 uses energy from ATP hydrolysis to extract ubiquitinated substrates from a variety of cellular compartments, leading to target substrate recycling or degradation by the proteasome (Vaz et al., 2013) (Figure 8). The most studied role of p97 is in the endoplasmic reticulum-associated degradation (ERAD) pathway (van den Boom and Meyer, 2018), however, it also has central roles in protein quality control in mitochondria-associated degradation (MAD) (Taylor and Rutter, 2011), endosomal trafficking (Ramanathan and Ye, 2012), ribosome-associated quality control (RQC) (Verma et al., 2013) and chromatin-associated degradation (CHROMAD) (Franz et al., 2016, Ramadan et al., 2007).

In ERAD, p97 is involved in protein retrotranslocation, which is the process of transporting misfolded proteins back into the cytosol to be degraded by the proteasome. It associates with proteins of the retrotranslocation complex such as Derlin-1/2 proteins (Lilley and Ploegh, 2005), the ERAD-associated E3 ubiquitin ligase HRD1 (Bays et al., 2001) and the VCP-interacting membrane protein (VIMP) (Ye et al., 2004). These proteins are necessary in bringing p97 to its substrates during ERAD. Amongst the first characterised p97 ERAD substrates was the aberrant form of the yeast carboxypeptidase Y (CPY) protein (Ye et al., 2001). Cdc48 (homologous to human p97) was found to be involved in the removal of this protein from the ER (Ye et al., 2001). Additionally, p97 interacts with ER-attached cluster of differentiation 4 (CD4) and major histocompatibility complex class I (MHC-1) proteins involved in the immune response, and is involved in their retro-translocation into the cytosol where they are degraded by the proteasome (Ye et al., 2003, Ye et al., 2001, Sasset et al., 2015). p97-mediated extraction of CD4 and MHC-1 is dependent on its co-factor complex Ufd1-Npl4 (Ye et al., 2001, Magadan et al., 2010, Ye et al., 2003). This pathway is exploited by viruses, where viral proteins target newly synthesised MHC-1 or CD4 proteins to be degraded in the cytosol (Binette et al., 2007).

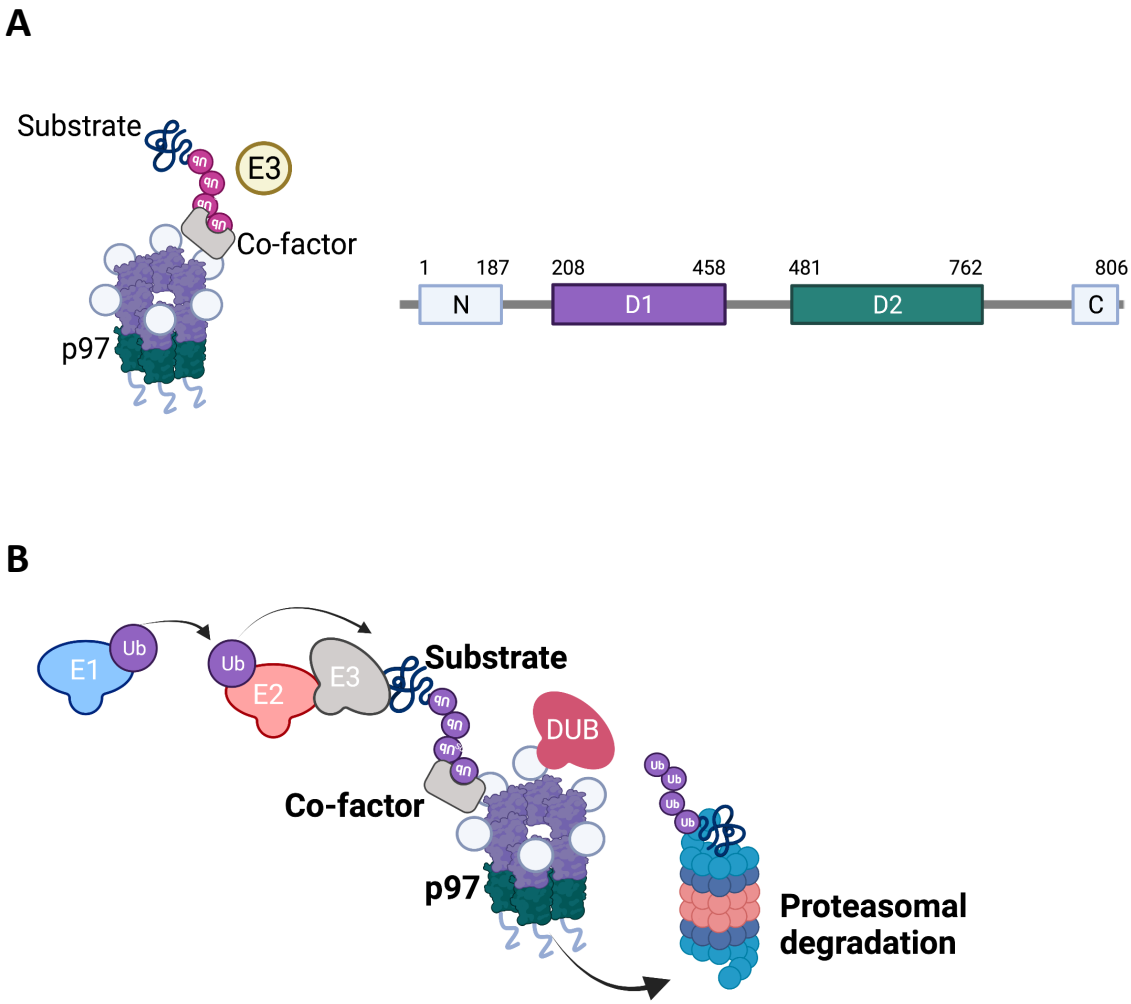


Figure 8 The ATPase VCP/p97 and its role in the ubiquitin-proteasome system (UPS). (A) Structure of p97. Each subunit consists of an N-terminal globular domain and two ATPase domains (D1 and D2), which form a hexameric barrel-like structure. Substrates are moved through the pore in the centre of the protein. Amino acid residues for each domain are indicated. (B) Model for p97 function in the cell. Substrates are ubiquitinated (marked as Ub) by a variety of ubiquitinating enzymes (E1 activating, E2 conjugating and E3 ligases). p97 recognises ubiquitinated substrates with the aid of its co-factors. Using energy from ATP hydrolysis, p97 structurally remodels its substrates, which can lead to their proteasomal degradation. Ubiquitinated substrates are deubiquitinated by deubiquitinating enzymes (DUBs). Adapted from. (van den Boom and Meyer, 2018). Figure created with Biordender.com.

In CHROMAD, p97 releases ubiquitinated substrates from chromatin during DSB repair (Dantuma et al., 2014). Extraction of nuclear p97 substrates has an impact on DSB repair pathway choice, whereby the removal of certain substrates from chromatin direct repair towards HR, whereas extraction of others promote NHEJ (van den Boom et al., 2016, Singh et al., 2019, Acs et al., 2011). Repair pathway choice is determined by various p97 subcomplexes and co-factors. For example, p97 and the Ataxin-3 deubiquitinase promotes RNF8 extraction from chromatin after IR, which promotes the NHEJ and suppresses HR (Singh et al., 2019). Additionally, p97 interactions with its co-factor complex Ufd1-Npl4 have been shown to promote HR-dependent repair by regulating the extraction of substrates associated with NHEJ (e.g. Npl4-mediated Ku80 extraction upon DSB induction) (van den Boom et al., 2016). p97 is also shown to be involved in the extraction of trapped PARP1 from chromatin, mediated by PIAS4 SUMOylation and RNF4-dependent ubiquitination. In this context, p97 is specifically recruited to trapped and modified PARP1 by the Ufd1 co-factor, which ultimately results in PARP1 removal from chromatin (Krastev et al., 2022). Finally, ongoing research and unpublished data from Prof Kristijan Ramadan's lab has shown that the p97 co-factor UBXD8 is recruited to DNA damage sites where it regulates MRE11 accumulation upon IR-induced DNA damage. Overall, the above-mentioned examples illustrate that it is the specificity of various p97 related co-factors and subcomplexes that regulate repair outcomes. As p97 has over 40 associated co-factors, there is considerable complexity in the coordination of different repair substrates, and delineating specific repair complexes and their cellular contexts in relation to p97 is a topic of ongoing extensive research. By controlling the repair pathway outcome, p97 has an important function in bridging the UPS with the DDR.

In MAD, p97 and the Ufd1-Npl4 co-factor complex is involved in the extraction of misfolded proteins from the mitochondrial outer membrane (MOM). The complex is recruited to the surface of mitochondria, where it aids with the clearance of damaged mitochondria by mitophagy (Hemion et al., 2014).

In the RQC pathway, p97 functions to extract defective nascent polypeptides that emerge from the ribosome, directing these peptides to the proteasome (Brandman et al., 2012). Depletion of p97 or its co-factor complex Ufd1-Npl4 causes ubiquitinated polypeptides to accumulate in complex with the ribosome (Verma et al., 2013).

p97 functions in endosomal trafficking by participating in receptor-mediated endocytosis (Kirchner et al., 2013), where it interacts with clathrin proteins, which are important structural components in the formation of coated pits on the inner surface of the plasma membrane of cells (Pleasure et al., 1993). Although the exact mechanism of p97 function in endosomal trafficking is still largely unexplored, its inactivation delays lysosome fusion with an endosome, thereby preventing the hydrolysis of endocytosed material (Ramanathan and Ye, 2012, Meyer et al., 2012).

Within these protein quality control pathways, p97 functions with specific co-factors that enable it to execute such diverse roles within a variety of cellular pathways. The co-factors associated with p97 are also part of the UPS, and function by bridging p97 to ubiquitinated substrates via their p97 interaction domains and ubiquitin-binding domains (UBDs) (Ramanathan and Ye, 2012).

As demonstrated by the above examples of the different kinds of roles of p97 in the cell, the UPS is the major protein degradation pathway in the cytoplasm and nucleus of eukaryotic organisms, and therefore necessary for maintaining protein homeostasis within cells (Hershko and Ciechanover, 1998). Under physiological conditions, protein homeostasis is appropriately maintained by balancing recycling and degradation events. Misfolded and aggregated proteins are effectively removed to avoid cellular stress from the accumulation of dysfunctional proteins. In contrast, most cancer cells are under constant protein stress from higher levels of protein translation from activated oncogenes as well as higher mutation rates resulting in the accumulation of misfolded and aggregated proteins (Guang et al., 2019, Deshaies, 2014). In addition, cancer cells have altered copy numbers of chromosomes (aneuploidy), which can add to the proteotoxic stress phenotype by increasing the expression of misfolded and/or mutated proteins (Deshaies, 2014). Therefore, several cancers have upregulated the components of the UPS as a survival

mechanism, making cancer cells sensitive to disruptions within the UPS pathway (Williams et al., 2008a, Torres et al., 2010). Additionally, the UPS represents over 19% of mutated cancer driver genes in common cancers such as breast, lung, and ovarian cancers (Tokheim et al., 2021). These data suggest that inhibiting components of the UPS would be more toxic to cancer cells than normal cells. The proteasome inhibitor bortezomib provided the first evidence for this concept, demonstrating that inhibition of the UPS causes cancer cell death while mostly sparing normal cells (Shen et al., 2013). Bortezomib is currently used in the treatment of multiple myeloma (Hideshima et al., 2005), non-Hodgkin's lymphoma and mantle cell lymphoma (Goy et al., 2005, O'Connor et al., 2005, Richardson et al., 2005).

In many cases, the proteasome is unable to degrade ubiquitinated substrates without the aid of p97, which functions to unfold these substrates in a way that they can be threaded into the catalytic core of the proteasome (Franz et al., 2014, Meyer et al., 2012, Heidelberger et al., 2018). For example, p97-dependent misfolded protein retrotranslocation to the cytosol in ERAD brings substrates to the proteasome to be degraded (Ye et al., 2001). When p97 function is disrupted, ERAD substrates accumulate, triggering the unfolded protein response (UPR), an evolutionarily conserved response to protein misfolding, which leads to the activation of several target genes (Hollien and Weissman, 2006). Cancer cells have evolved mechanisms to survive these stress conditions (Grootjans et al., 2016), so understanding the role of p97 within the UPS and UPR might allow us to appropriately target this for cancer therapy. If ERAD is not reversed, UPR will promote apoptosis (Walter and Ron, 2011).

1.5.2. Regulation of ubiquitination in the DNA damage response

Ubiquitination is the main mediator of p97 activity and has a central role in UPS-mediated protein homeostasis (Jackson and Durocher, 2013). Regulation of ubiquitination in the DDR is also necessary for the maintenance of genomic stability (Jackson and Durocher, 2013, Mailand et al., 2007).

Ubiquitin is a 76-amino acid protein that is attached to specific substrates to form branched, linear, homogenous, and mixed chains. Substrates can be mono-, multi-mono-

or polyubiquitinated. Depending on the specific chain topology, the ubiquitination signal can have different cellular outcomes. For example, lysine 63 (K63)-linked chains usually regulate protein-protein interactions and act as recruitment platforms, whereas K11- and K48-linked chains are regarded as proteasomal degradation signals (Swatek et al., 2019). The attachment of ubiquitin onto target proteins consists of a three-step enzymatic cascade (Figure 9): ubiquitin-activating enzyme (E1s) binds to the C-terminal part of ubiquitin in an ATP-dependent manner. Ubiquitin-conjugating enzyme (E2s) then binds ubiquitin, and together with an E3 ligase transfers ubiquitin onto target proteins, forming an isopeptide linkage between the amino group of the lysine residue in a target protein and the C-terminal part of ubiquitin (Komander and Rape, 2012). The ubiquitin code is complex and involves various enzymes: two E1 activating enzymes, over 35 E2 conjugating enzymes and over 600 E3 ligases (Swatek et al., 2019).

Ubiquitination is recognised by specific reader proteins containing specialised ubiquitin-binding domains (UBDs), and there are more than 20 different types of UBDs characterised so far. Commonly known UBDs in the DDR are the ubiquitin-binding zinc-finger (UBZ), ubiquitin-interacting motif (UIM), and motif interacting with ubiquitin (MIU) domains (Dikic et al., 2009). For example, one of the well-characterised p97 co-factor complexes in the DDR, the Ufd1-Npl4 complex, mediates its interaction with p97 via the UBD in Npl4. This interaction leads to the extraction of DDR substrates marked with K48-linked ubiquitin, directing these substrates to the proteasome to be degraded (Meerang et al., 2011). Additionally, p97 removes K48-linked Ku80 subunit (van den Boom et al., 2016), the polycomb protein lethal (3) malignant brain tumour like protein 1 (L3MBTL1) (Acs et al., 2011), and KRAB-associated protein-1 (KAP1) (Kuo et al., 2016) to coordinate DSB repair pathway choice.

In addition to the ubiquitin chain-forming enzymes, there are over 100 deubiquitinating enzymes (DUBs) that remove ubiquitin from its substrates, providing reversibility and flexibility to the ubiquitin system. DUBs are divided into six families consisting of either cysteine proteases or metalloproteases (Mevissen and Komander, 2017). For example, the DUB Ataxin-3 forms a protein complex with p97 and the E3 ligase RNF8 to regulate ubiquitination in DSB repair (Singh et al., 2019). To ensure tight regulation of ubiquitination

in the nucleus, DUBs are themselves post-translationally modified by ubiquitin, and degraded once they have completed their specific functions (Meray and Lansbury, 2007).

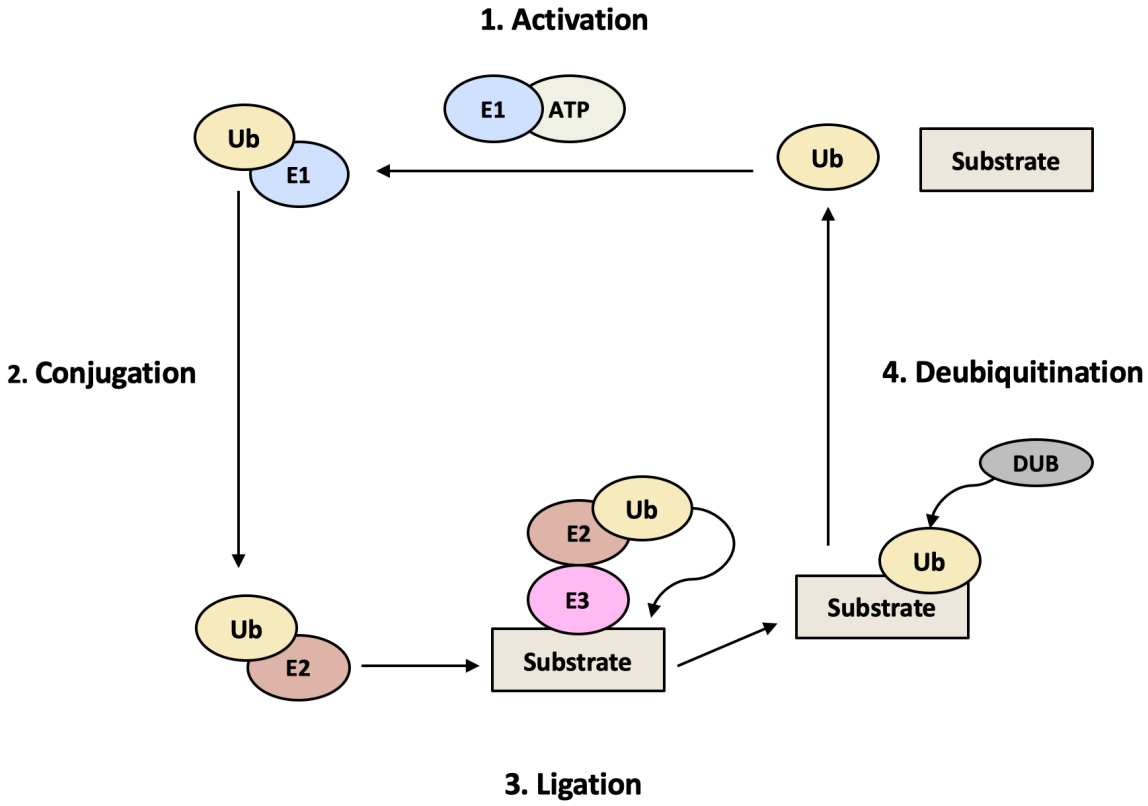


Figure 9 The ubiquitin signalling cycle.
The ubiquitin system is under the control of E1 activating, E2 conjugating and E3 ligase enzymes that are involved in the attachment of ubiquitin onto target substrates. First, E1 conjugating enzyme binds the C-terminus of ubiquitin in an ATP-dependent manner. Then, E2 conjugating enzyme and E3 ligase transfer ubiquitin onto target substrates, which can either be monoubiquitinated or polyubiquitinated. Ubiquitination is a reversible process and deubiquitinating enzymes (DUBs) are involved in reversing ubiquitination. Figure adapted from (Schwertman et al., 2016).

1.5.3. p97-associated co-factors

The multiple roles of p97 are determined by its binding partners that target p97 to the correct substrate in different cellular locations. There are around 40 known p97-associated co-factors, with the largest group containing ubiquitin regulatory X (UBX) and UBX-like (UBXL) domains (Buchberger et al., 2015, Alexandru et al., 2008). The ubiquitin-like domains bind to the N-terminus of p97 and have high sequence similarity to ubiquitin (Walters et al., 2002). Other domains mediating binding to p97 are the VCP-interacting protein (VIP) motif, the SHP motif, VCP-binding motif (VBM), the peptide N-glycanase/ubiquitin-associated (PNGase/PUB) domain, and the ubiquitin-binding domain (UBD) (Figure 10) (Yeung et al., 2008).

Three mutually exclusive p97 core complexes exist that bind to a set of different accessory proteins: the $p97^{-Ufd1\text{-}Npl4}$, $p97^{-UBXD1}$ and the $p97^{-p47}$ complex (Figure 10). The Ufd1-Npl4 co-factor complex is involved in proteasome-dependent functions: RQC (Brandman et al., 2012), ERAD (Brodsky, 2012), and CHROMAD (van den Boom and Meyer, 2018). Its functions in CHROMAD reduce protein-induced chromatin stress (PICHROS). UBXD1 and p47 have proteasome-independent functions and are involved in ubiquitin-dependent vesicular trafficking and membrane fusion, respectively (Buchberger et al., 2015). The three core complexes contain more than one p97 N-terminal binding site and can thereby occupy several N-terminal subunits at any given time (Schuberth and Buchberger, 2008).

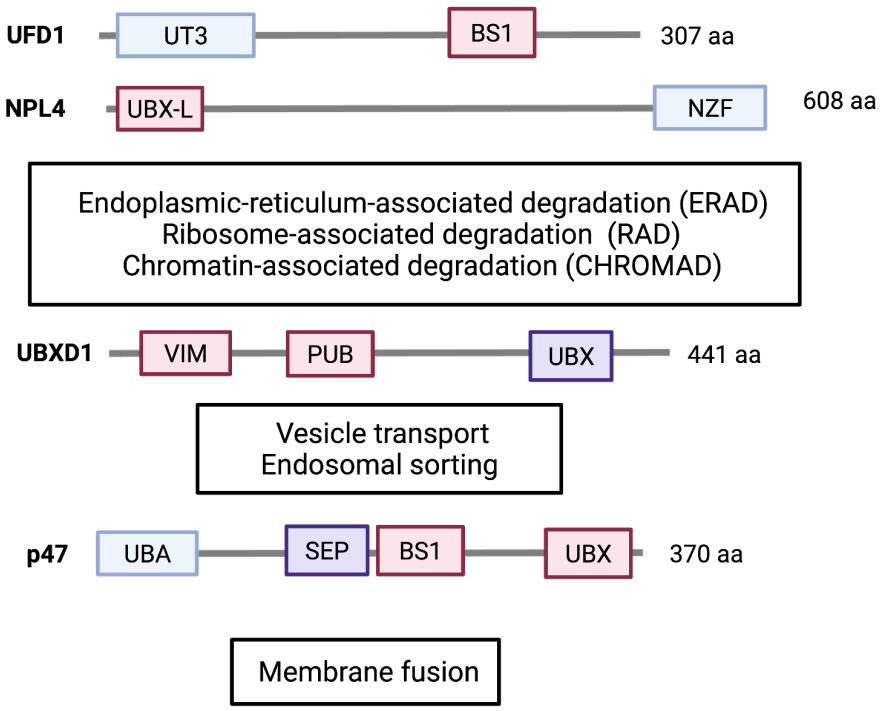


Figure 10 p97-associated co-factors.
Domains of the p97 core complex co-factors Ufd1-Npl4, p47, and UBXD1. Their main functions are illustrated below the protein domains. The binding domains of p97 include the UBX or UBX-like domain (UBX-L), or short motifs such as VIM, which bind to the N-terminus of p97. PUB domain binds the C-terminus part of p97 (indicated on UBXD1). Ubiquitin-binding domains (UBA, NZF) are also shown. The amino acid length is indicated next to each domain structure. UT3, Ufd1 truncation 3 domain; NZF, Npl4 zinc finger domain; VIM, VCP-interacting motif; PUB, N-glycanase/ubiquitin-associated domain; SEP, after shp1, eyc and p47; BS1, binding site 1. Figure adapted from (Meyer et al., 2012). Figure was created with Biorender.com.

1.5.4. The role of p97 in the nucleus

As previously mentioned, p97 has several roles in the cell where it regulates protein homeostasis both within the cytoplasm and in the nucleus (Figure 11). Nuclear functions of p97 include DNA replication, transcription, mitosis, and DNA repair. Inhibition of p97 reduces clonogenic survival in several cancer cell lines as well as suppressing tumour growth in mouse xenograft models by causing proteotoxic stress and impairing DSB repair in cancer cells (Anderson et al., 2015, Le Moigne et al., 2017, Zhou et al., 2015, Kilgas et al., 2021).

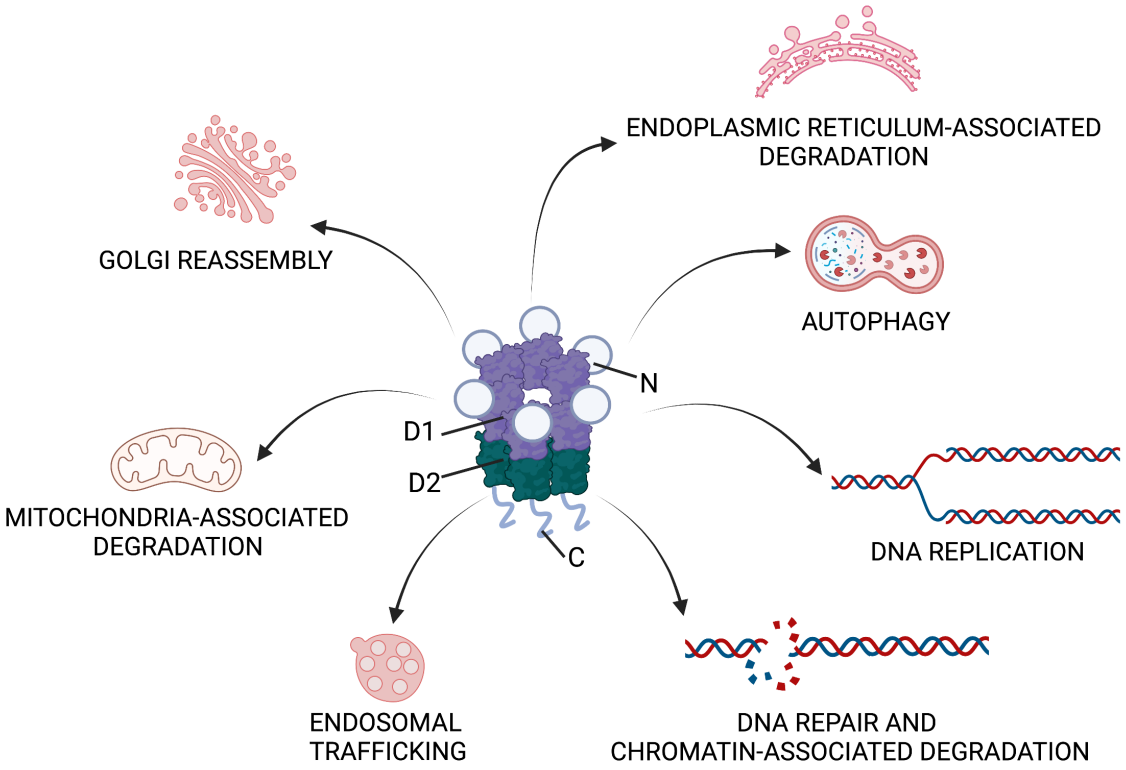


Figure 11 Overview of p97/VCP functions in the cell.
p97 has several functions both in the cytoplasm and the nucleus. The N-terminus, D1 and D2 ATPase domains and C-terminus of p97 are also shown. Figure created with Biorender.com.

Furthermore, p97 is physically recruited to DSB sites, and depletion of p97 radiosensitises cancer cells (Meerang et al., 2011, Kilgas et al., 2021, Singh et al., 2019). p97 is involved in both NHEJ-mediated repair and HR. Its role in repair pathway choice is dependent on cell cycle and the available co-factors for the removal of ubiquitinated substrates after DNA damage. For example, p97 removes ubiquitinated Ku80, thus promoting HR over NHEJ as the Ku complex is inhibitory for long-range end resection (van den Boom et al., 2016). Similarly, L3MBTL1 is a p97 substrate involved in the regulation of NHEJ. It is a polycomb group (PcG) protein involved in chromatin remodelling, and under physiological conditions recognises the histone mark H4K20me2 (dimethylated lysine 20 of histone 4), which prevents 53BP1 recruitment to DNA lesions. Upon DNA damage induction, L3MBTL1 is ubiquitinated and targeted for proteasomal degradation via the $p97^{\text{-Ufd1-Npl4}}$ complex. This process then enables the recruitment of 53BP1, thereby promoting NHEJ (Acs et al., 2011, Gurvich et al., 2010). Furthermore, p97 directly interacts with ubiquitinated DNA-PK_{cs}, and the depletion of p97 in cancer cell lines results in an overall decrease in NHEJ efficiency (Jiang et al., 2013, Torrecilla et al., 2017). Also, the p97-Ataxin 3 complex removes the ubiquitin ligase RNF8 from chromatin after IR, which promotes NHEJ-mediated repair. This occurs because RNF8-dependent linker histone H1 ubiquitination is necessary for the recruitment of downstream RNF168 that is involved in spreading ubiquitination to surrounding H2A-type histones that then serves as a recruitment platform for the anti-resection protein 53BP1. In the absence of p97, RNF8 accumulates on chromatin and disrupts the timely recruitment of RNF168, which leads to compromised NHEJ efficiency as well as radiosensitising BRCA2 deficient cancer cells (Singh et al., 2019). These results illustrate the importance of understanding the specific cellular context in which p97 mediates its role in coordinating DSB repair pathway choice. A list of well-known p97 nuclear substrates, associated co-factors and E3 ligases are provided in Table 1 below.

Table 1 p97 functions in the nucleus. List of p97 substrates, co-factors and associated E3 ligases with their functions in the nucleus.
*BRCA1 and WRN interact with p97, however it is unknown whether these proteins are p97 substrates or just interaction partners. Table adapted from (Ramadan, 2012).

Substrates	Co-factors	E3 ligases	Associated pathways	References
Aurora B	Ufd1-Npl4	Cullin-3	Mitosis	(Ramadan et al., 2007) (Dobrynin et al., 2011)
L3MBTL1	Ufd1-Npl4	Unknown	DSB repair	(Acs et al., 2011)
Ku80	Ufd1-Npl4	Unknown	DSB repair	(van den Boom et al., 2016)
MRN complex (MRE11 subunit)	Unknown	Unknown	DSB repair	(Kilgas et al., 2021)
***BRCA1 (?)**	BRCA1	HERC1	DSB repair	(Zhang et al., 2000) (Wu et al., 2010)
CDT1	Ufd1-Npl4	Cullin-4	DNA replication / repair	(Franz et al., 2011) (Raman et al., 2011)
SET8	Ufd1-Npl4	Cullin-4	UV-induced lesions	(Raman et al., 2011)
***WRN (?)**	Unknown	Unknown	DNA replication / repair	(Indig et al., 2004)
Rbp1	Ufd1-Npl4 UBXD7 UBXD9	Cullin-3	UV-induced lesions	(Verma et al., 2011)
Mcm7	Ufd1-Npl4	Cullin-2	DNA replication	(Maric et al., 2014) (Moreno et al., 2014)
Unmodified and SUMO1-modified TOP1	TEX264	Unknown	DNA replication	(Fielden et al., 2020)
Unidentified K48-linked substrates	ATX3	RNF8	DSB repair	(Singh et al., 2019)

In addition to regulating NHEJ, p97 functions in HR-mediated repair. Depletion of the p97-Ufd1-Npl4 complex impairs DNA end-resection, disrupting the downstream recruitment of phosphorylated RPA, BRCA1 and RAD51, leading to a decrease in HR repair (van den Boom et al., 2016, Singh et al., 2019). One of the reasons why RPA, BRCA1 and RAD51 are not effectively recruited in p97-depleted conditions is the upstream accumulation of ubiquitinated substrates (e.g. the Ku complex) that are not effectively removed. The removal of Ku70/80 is dependent on the cell cycle, and p97-mediated extraction of K48-linked Ku80 is confined to the G2/S phase of the cell cycle. The removal of Ku80 by p97 leads to increased DNA end resection, the level of which is an important determinant of DSB repair pathway choice (van den Boom et al., 2016, Ismail et al., 2015, Feng and Chen, 2012). Furthermore, p97 is involved in the removal of phosphorylated KAP1 during G2/S phase, which leads to the recruitment of BRCA1 and RAD51, further promoting HR repair (Kuo et al., 2016). Finally, p97 controls DSB repair pathway choice by regulating the MRN complex accumulation on chromatin upon IR (Kilgas et al., 2021). Inactivation of p97 in combination with IR leads to MRE11 retention on chromatin, excessive 5'-DNA end resection, impaired homologous recombination (HR) and reliance on mutagenic single-strand annealing (SSA) for DSB repair. This process radiosensitises cancer cells and impairs tumour growth in mouse xenografts upon ionising radiation (IR) (Kilgas et al., 2021).

p97 is also an essential factor in mitosis, DNA replication and transcription (Torrecilla et al., 2017). It regulates mitosis by extracting the mitotic kinase Aurora B from chromatin, and this function is conserved from *C. elegans* to humans (Ramadan et al., 2007, Sasagawa et al., 2012, Dobrynin et al., 2011). DNA replication processes, p97 functions with its co-factor Fas-associated factor 1 (FAF1) in the removal of the replication-licensing factor CDT1, which is necessary for replication fork firing (Franz et al., 2016, Raman et al., 2011). Furthermore, SprT-like- N-terminal Domain (SPRTN) functions as a p97 co-factor in DNA replication, including in error-free translesion synthesis (TLS) during replication stress, where SPRTN removes DNA polymerase delta (Pol δ), promoting the recruitment of polymerase eta (Pol η) and facilitating its removal beyond DNA lesions (Davis et al., 2012, Kim et al., 2013, Machida et al., 2012). p97 is also involved in replication termination, where it removes the minichromosome maintenance protein 7 (MCM7) independently of the proteasome (Maric et al., 2014, Moreno et al., 2014). In the Fanconi anaemia (FA) repair pathway, p97

disassembles the Cdc45-MCM2-7-GINS (CMG) helicase complex, thereby promoting interstrand crosslink (ICL) repair (Fullbright et al., 2016). Furthermore, p97 degrades RNA polymerase II in response to UV-induced DNA damage. RNA polymerase II is ubiquitinated by the E3 ligase cullin-3 (CUL3), which recruits the $p97^{-Ufd1-Npl4}$ complex together with the co-factors UBXD7 and UBXD9. p97 then removes the largest RNA polymerase II subunit, retinol-binding protein 1 (RBP1), which leads to dismantling of the whole complex.

1.5.5. Therapeutic applications of inhibiting the UPS

Cancer cells often display aneuploidy, which is caused by error rates in chromosome segregation, leading to chromosomal instability and an abnormal number of chromosomes (Williams et al., 2008a, Torres et al., 2010). Aneuploidy is one of the causes of proteotoxic stress in cancer cells, as these extra chromosomes produce proteins which are often mutated, misfolded and which form aggregates. This inherent difference between normal cells and tumour cells has been exploited in the development of drugs targeting protein homeostasis in cancer cells (Deshaies, 2014).

The first drug targeting the UPS to be taken into the clinic was the proteasome inhibitor bortezomib, used in the treatment of multiple myeloma, B-cell non-Hodgkin's lymphoma and mantle cell lymphoma (Hideshima et al., 2005, Goy et al., 2005, O'Connor, 2015). Similarly, several UPS-targeting cancer drugs are currently in clinical trials, including inhibitors against ubiquitinating and deubiquitinating enzymes (Edelmann et al., 2011). (Figure 12). The small molecule p97 ATPase inhibitors, CB-5083 and CB-5339, work on the principle of increasing proteotoxic stress in cancer cells, eventually causing cancer cell death while sparing normal tissues (Anderson et al., 2015). For example, as opposed to cancer cells, inhibiting p97 in primary rat hepatocytes (Acharya et al., 2011) and mouse skeletal muscle cells (Piccirillo and Goldberg, 2012) did not induce apoptosis. A number of inhibitors of p97 ATPase activity have been reported (Le Moigne et al., 2017, Zhou et al., 2015, Chou et al., 2013, Magnaghi et al., 2013, Wang et al., 2008, Bursavich et al., 2010, Sasazawa et al., 2012, Yi et al., 2012, Ikeda et al., 2014). The reversible ATP competitive inhibitor DBeQ (IC50 of 1.5 µM) was identified as the first selective inhibitor of p97 D1 and

D2 ATPase activity. It was followed by the generation of more potent and specific competitive inhibitors, namely ML240 (IC50 of 100 nM) and ML241 (IC50 of 100 nM), that are both derivatives of DBeQ, targeting the D2 ATPase domain of p97 (Deshaies, 2014, Chou et al., 2013). Similar to DBeQ, the reversible allosteric p97 inhibitor NMS873 inhibits both the UPS and autophagy pathway, but is much more potent towards cancer cells with an IC50 of around 30 nM compared to 1.5 µM in DBeQ (Deshaies, 2014).

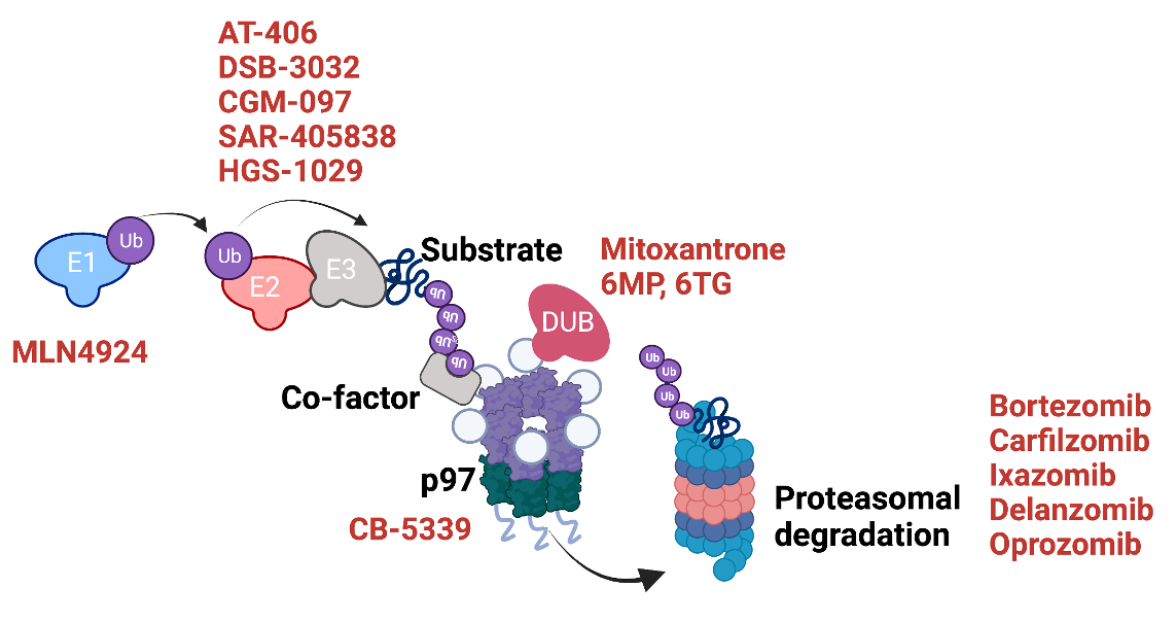


Figure 12 Small-molecule inhibitors in the UPS.
Several different classes of UPS-targeting drugs have been developed – drugs inhibiting E1, E2 and E3 ligases, DUBs, the p97 system as well as the proteasome. The proteasomal degradation drugs Bortezomib and Carfilzomib are FDA approved, and the p97 ATPase inhibitor CB-5339 has just recently entered Phase I (Edelmann et al., 2011). Figure created with Biorender.com.

One of the ATPase competitive p97 inhibitors, CB-5083, was taken into phase I clinical trials in 2015 (https://clinicaltrials.gov trial numbers NCT02243917 and NCT0223598) for the treatment of advanced solid tumours and multiple myeloma, sponsored by Cleave Biosciences (Tang et al., 2019). Unfortunately, due to off-target effects with phosphodiesterase VI (PDE6), a regulator of phototransduction cascade in the eye, the clinical trials had to be terminated due to eye toxicity (Arshavsky et al., 2002, Roux et al., 2021, Tang et al., 2019). CB-5083 is a reversible ATP competitive inhibitor that specifically targets the D2 ATPase domain of p97. It is also a derivative of DBeQ, but with a much higher potency (IC50 of 11 nM) and selectivity (Ye et al., 2017). It has been demonstrated to have tumour-suppressive functions across a variety of solid tumour models (Anderson et al., 2015). When comparing its activity to the proteasome inhibitors bortezomib and carfilzomib, CB-5083 is effective in several solid tumour models, while the proteasome inhibitors have only limited efficacy in solid tumours (Huang et al., 2014). This could be due to the specific pharmacology of bortezomib and carfilzomib, or due to a cellular homeostatic mechanism that triggers a compensatory response to inhibiting the proteasome (Deshaies, 2014). Furthermore, CB-5083 causes predominantly nuclear accumulation of K48-linked ubiquitin chains, whereas bortezomib leads to the accumulation ubiquitinated proteins primarily in the cytoplasm (Anderson et al., 2015). Additionally, CB-5083-induced K48-linked ubiquitination at a higher molecular weight compared to bortezomib. These data show that inhibiting p97 directly affects not only the ERAD pathway but also the nuclear protein degradation pathway. The nuclear effects of CB-5083 could be the reason why p97 inhibition is an effective anti-cancer agent as it directly impairs DNA repair protein signalling pathways in cancer cells (Anderson et al., 2015, Tang et al., 2019). Finally, when comparing the plasma levels of CB-5083 and bortezomib inhibitors, CB-5083 showed sustained exposure of drug in the plasma compared to proteasome inhibitors, which might be one of the reasons why CB-5083 has superior solid tumour activity (Anderson et al., 2015).

After the clinical trials with CB-5083 were terminated, Cleave Biosciences developed a second-generation CB-5083 analog, CB-5339, with 15-fold less activity on human PDE6 in biochemical assays and around 30 times less maximum concentration on rat retinas than CB-5083 (Roux et al., 2021). CB-5339 has a comparable sensitivity and potency to CB-5083

in a panel of over 100 cell lines, but higher bioavailability than CB-5083 (Roux et al., 2021). An *in vivo* p97 small hairpin RNA (shRNA) screen of 16 human cancers showed that acute myeloid leukaemia (AML) is the most responsive cancer type to p97 inactivation (Roux et al., 2021). In addition to inducing global UPR and inhibiting UPS, CB-5339 functions in the DDR by decreasing the activation of the ATM kinase and its downstream targets BRCA1, SMC1 and KAP1. These cellular effects were further demonstrated *in vivo* in a patient-derived xenograft (PDX) of AML mouse model, showing that CB-5339 causes a decrease in bone marrow leukaemic infiltration and increased overall survival of AML mice (Roux et al., 2021). Due to the promising effects *in vivo*, CB-5339 was taken into Phase I clinical trials (https://clinicaltrials.gov trial number NCT0437264) for the treatment of advanced solid tumours and lymphomas. Overall, despite p97's pleiotropic effects in cells, the development of CB-5083 and CB-5339 has demonstrated that p97 is an effective cancer target and can be utilised to develop inhibitors with high specificity and potency for the treatment of both haematological malignancies as well as solid tumours (Roux et al., 2021, Anderson et al., 2015).

1.6. Aims of the Thesis

Understanding the complex cellular processes occurring after IR-induced DSBs is fundamental for the identification of new druggable targets in cancer therapy. The ATPase p97 has emerged as one of the important proteins regulating DSB repair upon IR. Perhaps the best-known role of p97 is in the regulation of protein homeostasis, particularly in the ERAD pathway. This thesis focused on understanding the functions of p97 in the regulation of DSB repair pathway choice, specifically in combination with IR. Previous proteomics work in the lab identified that p97 interacts with one of the main DNA DSB sensors and repair protein complexes, the MRE11-RAD50-NBS1 (MRN) complex, which is one of the central protein complexes in DSB repair. These preliminary findings provided the basis for this thesis.

The aim of this DPhil thesis was to understand the functional relevance of the interaction between p97 and the MRN complex, specifically looking at how p97 inactivation affects the MRN complex levels on chromatin and on DNA upon IR. The resulting effects on downstream DDR signalling proteins were studied, specifically in the context of NHEJ, HR and SSA DSB repair pathways. The thesis set out to identify how p97 regulates DSB repair pathway choice through regulating the MRN complex and focused on MRE11 nuclease activity regulation on DNA and chromatin as well as the consequences of this on the extent of DNA end-resection. Finally, the potential radiosensitising effects of p97 inactivation were studied in cells using the small molecule inhibitor of p97 CB-5083 or siRNA-mediated depletion of p97, and the extent to which the radiosensitisation depends on MRE11 regulation were also investigated. The underlying hypothesis of the thesis is that p97 is involved in the disassembly of MRE11 from chromatin and DNA damage sites upon IR, and inactivation of p97 therefore causes excessive MRE11 accumulation, DNA end resection and a change of DSB repair pathway choice from error-free repair to mutagenic repair, leading to radiosensitisation of cancer cells.

Chapter 2. Materials and methods

2.1. Cell lines and culture conditions

Human T24 and RT112 cell lines were obtained from the German Collection of Microorganisms and Cell Cultures (DSMZ). HEK293 and HeLa cells were obtained from the American Type Culture Collection (ATCC). All cell lines were grown in complete medium supplemented with 10% FBS without antibiotics. T24 cells were grown in McCoy's 5A medium (Thermo Fisher Scientific; Cat# 16600082), HEK293 and HeLa cells were grown in Dulbecco's Modified Eagle's medium (DMEM; Gibco; Cat#11965084), and RT112 cells were grown in RPMI-1640 medium (Sigma; Cat# R8758-6X500ML). DR-GFP U2OS cells were kindly provided by Dr Sovan Sarkar, University of Oxford, and grown in complete DMEM supplemented with 3 μg/mL puromycin (Thermo Fisher Scientific; Cat# A1113802). SA-GFP U2OS cells were provided by Pavel Janscak, University of Zurich, and grown under the same conditions as DR-GFP U2OS cells. All cell lines were maintained at 37°C in a 5% CO_2 humidified incubator. All cells used in experiments tested mycoplasma negative.

2.2. Chemical treatments

Cells were treated with the following reagents: 10 μM BrdU (Sigma; Cat#B5002) and 10 μM Edu (Sigma; Cat#C1042) for 24 hours and 20 minutes, respectively; 10 μM CB-5083 (MCE; Cat#HY-12861) for at least 2 hours, 500 μM hydroxyurea (Sigma; Cat#H8627) for 1 hour, and 100 μM Mirin (Sigma; Cat#M9948), 100 μM PFM01 (Tocris; Cat#6222) and 100 μM PFM39 (Sigma; #SML1839) for 3 hours. Concentrations of PFM01 and PFM39 were chosen according to previously published data (Shibata et al., 2014). For clonogenic survival assays, CB-5083 and Mirin were applied for 6 hours and 24 hours, respectively.

2.3. RNA interference

Cells were seeded in antibiotic-free medium to achieve approximately 50-70% confluence on the day of transfection. Cells were transfected using Lipofectamine RNAiMAX (Thermo Fisher Scientific; Cat#13778075) according to the manufacturer's instructions. Briefly, for 6-well plates: A) 100 μL Opti-MEM (Thermo Fisher Scientific; Cat# 11058021) was mixed

with 1.25 µL RNAimax and B) 100 µL Opti-MEM was mixed with an appropriate concentration of siRNA (10-40 nM final concentration). Mix A and B were incubated at RT for 5 minutes, then gently mixed and incubated for 15 minutes at RT. Then, 400 µL of cell culture medium supplemented with FBS was added to mix AB. Medium from 6-well plates was removed and all 600 µL of the transfection mix was added to each well in a drop-wise manner. Cells were incubated with this mix for 6 hours at 37°C, then topped up with 1.4 mL of normal medium in each well. For larger plates, the transfection reagents were scaled up according to the surface area of the plates.

2.4. Plasmid transfections

Cells were seeded to be around 70% confluent at the time of transfection. Cells were transfected using Lipofectamine 3000 (Thermo Fisher; Cat#L3000008) according to the manufacturer's instructions. Briefly, for 6-well plate transfections: A) 125 µL Opti-MEM was mixed with 5 µL Lipofectamine 3000 reagent and B) 125 µL Opti-MEM was mixed with appropriate plasmid DNA and 10 µL P3000 reagent. Mix A and B were incubated for 5 minutes at RT, then combined and incubated for another 15 minutes at RT. The transfection mix was added to the cells in a drop-wise manner and cells were incubated at 37°C for 48-72 hours.

2.5. Plasmid purification

2.5.1. Transformation of bacteria

Aliquots of DH5α chemically-competent *Escherichia coli* (Thermo Fisher; Cat# 18263012) were thawed on ice. One microlitre of the required plasmid was mixed with 50 µL of bacterial slurry and incubated on ice for 30 minutes. The plasmid was introduced to bacterial cells by heat shock in a 42°C water bath for 90 seconds. Transformed bacteria were recovered on ice for 5 minutes and transferred to a bacterial shaker (New Brunswick Scientific) in 250 µL SOC outgrowth medium (NEB; Cat# B9020S) in selective antibiotics at 37°C and 250 rpm for 1 hour. Bacteria were then plated onto agar plates (Sigma; Cat# L5542) in selective antibiotics and grown overnight in a bacterial incubator at 37°C (Binder). On the following day, single colonies were picked for amplification in 5 mL Luria-Bertani

(LB; Sigma; Cat# L3022) medium with appropriate antibiotics and incubated in a bacterial shaker (37°C, 250 rpm) overnight.

2.5.2. Maxiprep plasmid purification

Maxipreps were performed according to the manufacturer's instructions (QIAGEN; cat#12162). The overnight bacterial culture from Chapter 2.5.1 was centrifuged at 6000 x g for 15 minutes at 4°C and bacterial pellets were resuspended in 10 mL Buffer P1 (50 mM Tris-HCl, 10 mM EDTA, 100 µg/mL RNase A, pH 8.0). Bacteria were lysed by adding Buffer P2 (200 mM NaOH, 1% SDS w/v) and gently mixing by inverting 4-6 times before incubation at RT for 5 minutes. Ten mililitres of chilled Buffer P3 (3.0 M potassium acetate, pH 5.5) was then added followed by immediate mixing by vigorous inversion 4-6 times, followed by incubation on ice for 20 minutes. Meanwhile, a QIAGEN-tip 500 was equilibrated by allowing buffer QBT (750 mM NaCl; 50 mM MOPS, pH 7.0; 15% isopropanol (v/v); 0.15% Triton X-100 (v/v)) to enter the column by gravity flow. Cell lysate was then poured into a 50 mL syringe body and the separated supernatant was injected into a clean 50 mL tube using a plunger. The supernatant was then added to the equilibrated QIAGEN-tip 500 and allowed to enter the resin by gravity flow. The QIAGEN-tip was then washed twice with 30 mL Buffer QC (1.0 M NaCl; 50 mM MOPS, pH 7.0; 15% isopropanol (v/v)). The DNA was eluted with 15 mL buffer QF (1.25 M NaCl; 50 mM Tris-HCl, pH 8.5; 15% isopropanol) and precipitated by adding 10.5 mL RT isopropanol. The solution was centrifuged at 6000 x g for 1 hour at 4°C. The supernatant was carefully removed by decanting. The DNA pellet was washed with 5 mL of RT 70% ethanol and centrifuged again at 6000 x g for 20 minutes at 4°C. Ethanol was then carefully decanted, the DNA pellet was air-dried for 5 minutes at RT and dissolved again in a suitable volume of TE buffer (10 mM Tris-HCl pH 8.0; 1 mM EDTA). Plasmid yield was measured using a NanoDrop Spectrophotometer (Thermo Fisher; Cat# ND-ONE-W).

2.6. Ionising radiation and UV laser treatment

Cells were irradiated in complete medium at a dose rate of 1.5 Gy/min using a Gamma-Service Medical GmbH GSR D1 irradiator. For UV-A laser micro-irradiation, cells were pre-treated with 10 µg/mL Hoechst (Sigma-Aldrich; Cat# 23491-45-4) for 20 minutes before

UV, and micro-irradiated using an in-house UV-A pulsed Q-switched Nd:YAG laser system (MiniliteTM II) with a wavelength of 355 nm. The laser was connected to a Nikon TE2000 microscope under a 10X objective. The laser pulse was manually controlled, and a single pulse duration was 5 nanoseconds (ns). Reproducibility of laser energy pulses was monitored using an in-house pyroelectric power detector (Scitec PE08) and a CFQ-1520 quartz coverslip. Laser energy was adjusted to be 10 µJ across the laser line. Cells were recovered for indicated times and collected for analysis. For immunofluorescence microscopy, cells were cultured on 9 mm No. 1 cover glasses (VWR; Cat#631-0169).

Cells were line-micro-irradiated using a built in-house UV-laser system based around a UV-A (355 nm) Q-switched Nd:YAG laser (MiniliteTM II) that produced pulses of 5 ns duration. Laser energy pulse–pulse reproducibility was monitored by an in-house energy sensor based around pyroelectric (Scitec PEO8) sensor and a CFQ- 1520 quartz coverslip pick off. Laser energy on the sample was adjusted on the laser's variable attenuator to be typically (10 J across the line.

2.7. Immunofluorescence microscopy

Depending on the specific antibodies used, cells were either permeabilised with 0.25% Triton X-100 in 1X PBS for 10 minutes at room temperature (RT), or soluble proteins were extracted with a pre-extraction buffer on ice for 2-5 minutes (25 mM HEPES (pH 7.4), 50 mM NaCl, 1 mM EDTA, 3 mM $MgCl_2$, 300 mM sucrose, and 0.5% Triton X-100). Cells were fixed with 4% ice cold formaldehyde solution in PBS for 10 minutes at RT, washed with PBS (Gibco; Cat#10010023) and blocked for 1 hour at RT with 5% BSA in PBS (alternatively, samples were blocked overnight at 4°C). Samples were incubated with primary and Alexa Fluor 488 and 568 secondary antibodies in 2.5% BSA in PBS solution for 1 hour in the dark at RT. Coverslips were washed three times for 5 minutes between each antibody incubation and mounted on microscopy slides using DAPI mounting reagent (Invitrogen; Cat#P36962).

IR-induced foci and UV-induced laser stripes were imaged with either a Nikon Ni-E epifluorescent microscope under a 60X objective or a Zeiss 710 confocal microscope using a 63X objective. All images were analysed using Fiji image processing software. UV-induced

laser stripes were analysed by measuring the mean intensity at the site of DNA damage (co-localised with γH2AX signal) and subtracting the mean nuclear background intensity. All laser measurements were normalised to the earliest time point in control cells to allow comparison between independent experiments. For ionising radiation-induced foci (IRIF) with Zeiss 710 confocal microscopy, the original CZI file format was used to analyse foci on Fiji software. Nuclei were outlined in the DAPI channel and the number of nuclear foci in the channel of interest was determined by dividing the raw intensity ("RawIntDen") by the maximum ("Max") gray value.

Phospho-histone H2AX (S139) was used as a DNA damage marker across several microscopy experiments throughout the thesis. Two different phospho-histone H2AX (S139) antibodies were used: mouse monoclonal (Millipore; Cat# 2739172) and rabbit polyclonal (Cell Signaling; Cat# 2577). For 53BP1, MRE11 (Figures 15 and 17), phospho-RPA32 (S4/S8), and RPA70 staining, mouse monoclonal antibody (Millipore; Cat# 2739172) was used. For MRE11 (Figures 20, 46, 47, 48), RAD50, and REV7 staining, rabbit polyclonal (Cell Signaling; Cat# 2577) antibody was used. Some inconsistencies seen in phospho-histone H2AX (Ser139) staining intensities could have arisen due to antibody species differences. Additionally, these images were taken at separate times and processed using different threshold settings on Fiji. Furthermore, two different confocal microscopes (Zeiss 710 and Zeiss 780) were used for imaging across the thesis, which operate on the same principles but could account for some staining intensity differences, especially in Figures 15, 16 and 32. The specific primary and secondary antibodies used for IF are indicated in Appendices, Table 2.

2.7.1. BrdU foci detection without denaturation

Cells cultured on 9 mm No. 1 cover glasses (VWR; Cat#631-0169) were incubated with 10 µM BrdU for 24 hours to visualise single-stranded DNA (ssDNA). Cells were either treated with 20 nM sip97 and 20 nM siMRE11 24 hours prior to adding BrdU, or 10 µM CB-5083 and 100 µM Mirin for the last 2 and 3 hours, respectively. Ten micromolar of EdU was added in the last 20 minutes of the experiment to mark cells in S phase. Five hundred micromolar of hydroxyurea (HU) was added in the last hour of the experiment as a positive

control for ssDNA foci formation in S phase. Soluble proteins were then extracted, cells were fixed and BrdU foci were visualised according to the immunofluorescence microscopy methods outlined above.

2.7.2. EdU detection

Cells were labelled with 10 µM EdU 20 minutes prior to extracting soluble proteins and fixing the cells. Cells were then blocked for 1 hour at RT in 5% BSA/PBS solution and S-phase cells were stained using Click chemistry according to the manufacturer's instructions (Invitrogen). Plates were incubated for 30 minutes at RT in the dark. Each well was then washed with PBS before proceeding to immunofluorescence antibody incubations.

2.8. Immunohistochemistry: staining

Samples were incubated at 50°C for 20 minutes. Deparaffinisation in xylene (Thermo Fisher Scientific; Cat#1330-20-7) was performed twice for 3 minutes each, followed by rehydration for 3 minutes each through graded ethanol: 100% (twice), 70% (once) and 50% (once). Slides were rinsed in dH_2O for 1 minute. Antigen retrieval was done in citrate buffer (10 mM citric acid, 0.05% v/v Tween-20; pH 6.0) for 7 minutes by heating in a microwave. Samples were allowed to cool, rinsed in dH_2O and washed twice with PBS. Tissue sections were blocked in endogenous peroxidase by incubating for 20 minutes at RT with 3% H_2O_2 (Thermo Fisher; cat# 7722-84-1). Samples were then avidin-blocked (Vector Labs; SP-2001) for 15 minutes at RT, biotin- blocked for 15 minutes (Vector Labs; SP-2001) and blocked with normal goat serum (Agilent; Cat#X090710-8) in 3% BSA in PBS at a 1:10 dilution. Between blocking steps, samples were washed three times with PBS for 3 minutes each. Primary antibody was diluted in 3% BSA in PBS and incubated overnight at 4°C. Samples were washed and incubated with biotinylated secondary antibody for 15 minutes at RT, washed twice and incubated with avidin solution for further 15 minutes. Samples were washed and stained with DAB (Vector Labs; Cat# SK-4100) for 2 minutes. DAB was removed by washing with water, and samples were counterstained with filtered Harris' haematoxylin (Sigma-Aldrich; Cat#HHS32-1L) for 15 seconds at RT. Excess stain was removed by rinsing in water and samples were dipped in 1% acid alcohol (1% concentrated

HCl in 70% ethanol). Blueing of haematoxylin was done by dipping slides in Scott's tap water (42 mM $NaHCO_3$, 166 mM $MgSO_4$) and 0.5% lithium-carbonate (Sigma-Aldrich; Cat#554-13-2) for 10 times each. Tissue was washed under tap water and dehydration was carried out with graded ethanol for 3 minutes each: 50% (once), 70% (once) and 100% (twice). Samples were mounted with dibutyl phthalate polystyrene xylene (DPX) (Sigma-Aldrich; Cat#1005790500). The specific primary and secondary antibodies used for IHC are indicated in Appendices, Table 2.

2.8.1. Immunohistochemistry: scoring

Stained tissue was scanned using 40X magnification with the Aperio ScanScope™ CS2 scanner (Leica Biosystems) and images were captured using Leica Aperio Image Scope software. Tissue was outlined on H&E sections by Dr Lisa Browning, Consultant Histopathologist (LB), John Radcliffe Hospital, Oxford. Each area was captured by taking images at 40X magnification and scored by assessing both the intensity and the percent area positive for each image. The staining intensity was determined using the following score range: 0 (negative), 1+ (weak), 2+ (moderate), 3+ (strong). Nuclear and cytoplasmic staining was assessed by myself and Prof Anne Kiltie independently. Both scorers used reference images with typical scoring values to determine the intensity of each area, and an overall consensus score was determined by taking the most commonly occurring intensity and the mean value of percentage of cancer cells stained.

2.8.2. Immunohistochemistry: Human HGT1 Tissue Sections

Tumour samples of high-grade stage T1 (into lamina propria) non-muscle invasive bladder cancer (HGT1) were identified in the Oxford Radcliffe Biobank. Twenty-seven cases obtained between the years 2009-2015 were used under the appropriate ethical approval (South Central Oxford REC C 09/H0606/5+5). Out of the 27 cases, eight patients underwent radical cystectomy and muscle-invasive disease was found in the resection specimen of one patient post-cystectomy (pT2). Two patients had disease progression following bladder biopsy for disease recurrence in 2013 and 2015.

2.9. Protein Analysis

2.9.1. Western Blotting

Cells were lysed using RIPA lysis buffer (Thermo Fisher; Cat# 89901) supplemented with freshly added protease (Thermo Fisher; Cat# A32955) and phosphatase (Thermo Fisher; Cat#12821650) inhibitors. Cells were sonicated for 10-15 cycles, 30 seconds on and 30 seconds off in a 4°C water bath (SUB Aqua 2 Plus; Grant). Lysed cells were centrifuged at 20,000 x g for 10 minutes at 4°C. Supernatant was removed and protein was quantified with the BCA assay (Thermo Fisher; Cat# 23225) and Omega software (BMG Labtech). Protein samples were then prepared in Laemmli buffer and boiled at 95°C for 5 minutes. In general, around 30 µg of protein was loaded onto gels per sample. Protein was run on 4-20% SDS-PAGE precast gels (Bio-Rad; Cat#4561096) in 1X Running Buffer (Bio-Rad; Cat# 1610772) at 100 V for approximately 1.5 hours. Protein samples were then transferred onto a nitrocellulose membrane (Thermo Fisher Scientific; Cat# 88018) using Bio-Rad turbo transfer (Cat# 10026938) kit with 1X Transfer Buffer (200 mL BioRad Transfer buffer, cat#, 100 mL ethanol and 800 mL dH_2O) for 10 minutes at 20 V. Nitrocellulose membranes were then blocked in LI-COR blocking buffer (Cat# 927-70001) for 1 hour at RT on a rocker (Stuart). Membranes were incubated in primary antibody in LICOR antibody diluent (Cat# 927-75001) overnight at 4°C on a rocker, then washed 3 times for 10 minutes each with PBS-T (PBS and 0.005% w/v Tween-20). Membranes were then incubated in a suitable secondary antibody in LICOR antibody diluent for 1 hour at RT on a rocker, then washed again 3 times for 10 minutes each, and imaged using LI-COR imaging system (Odyssey).

Alternatively, samples were transferred to a nitrocellulose membrane (Thermo Fisher Scientific; Cat# 88018) using Mini Trans-Blot Electrophoretic Transfer Cell (Bio-Rad; Cat# 1703930). Briefly, the gel sandwich was assembled according to the manufacturer's instructions (BioRad; Cat# 1703930) and transfer was performed at 100 V for 1 hour in an ice-cold transfer buffer (1x Tris/Glycine buffer; 20 % methanol; 0.025 % SDS). Nitrocellulose membranes were then blocked in 5% skimmed milk (Sigma-Aldrich; Cat# 70166) in 1X TBS-T solution for 1 hour at RT. Membranes were then washed 5 times for 5 minutes each before an overnight incubation at 4 °C in an appropriate antibody dilution buffer (3% BSA/TBS-T). After overnight incubation, membranes washed 3 times for 10 minutes each

with 1X TBS-T at RT and incubated with a relevant HRP secondary antibody solution (2.5% skimmed milk in TBST). Membranes were washed 3 times for 10 minutes each and visualised using SuperSignal™ West Pico PLUS Chemiluminescent Substrate (Thermo Fisher Scientific; Cat# 34579) after a 5-minute incubation at RT in the dark). Signal was detected using the ChemiDOc MP system (BioRad). The specific primary and secondary antibodies used are indicated in Appendices, Table 2.

2.9.2. Cycloheximide (CHX) chase

For cycloheximide chase experiments, cells were treated with specific inhibitors (10 µM CB-5083) or siRNA (48 prior to CHX administration). For each time point, excluding the 0-hour time point, 0.1 mg/mL CHX (Sigma-Aldrich; Cat# C1988) was added to culture dishes and cells were either immediately irradiated (10 Gy) or not. Cells were allowed to recover over time (3 hours, 6 hours, and 9 hours), after which cells were collected by washing twice with ice-cold PBS and centrifuged at 900 x g for 5 minutes at 4°C. Cell pellets were then resuspended in freezing medium (10% DMSO and 90% FBS) and frozen at -80°C until the following day for cellular fractionation.

2.9.3. Cellular fractionation

T24, HEK293 and HeLa cells were trypsinised and washed twice with ice-cold PBS by gentle resuspension and centrifugation at 900 x g at 4°C. Firstly, the cytoplasmic fraction was isolated from cells with buffer A (10 mM HEPES, 10 mM KCl, 0.34 M sucrose, 10% glycerol; pH 7.5) supplemented with fresh protease and phosphatase inhibitors, 20 mM N-Ethylmaleimide (NEM) and 0.1% Triton X-100. Buffer was carefully mixed by tapping Eppendorf tubes containing sample and not mixing the sample with a pipette tip. Samples were centrifuged at 350 x g for 5 minutes at 4°C. Supernatant was collected into a new tube (soluble fraction: cytoplasmic and nuclear). Cell pellets were washed twice more with buffer A (without Triton X-100, but with inhibitors and NEM). Samples were once again centrifuged at 350 x g for 5 minutes and supernatant discarded. Nuclei were ruptured to release the nucleoplasm using hypotonic buffer B (5 mM HEPES, 3 mM EDTA, 0.2 mM EGTA; pH 8.0) with freshly supplemented inhibitors and NEM. Samples were mixed by gently tapping Eppendorf tubes and kept on ice for 20 minutes. Then, samples were centrifuged

at 1700 x g for 5 minutes at 4°C. Supernatant was separated from the rest of the samples into clean Eppendorf tubes. Samples were washed twice again with buffer B, leaving samples on ice for 10 minutes between each wash step, and centrifuged at 500 x g for 5 minutes at 4°C. The pellet (chromatin) was washed twice with benzonase buffer (25 mM Tris-HCl, pH 8.0, 20 mM NaCl, 2 mM KCl and 5 mM $MgCl_2$). The first wash contained inhibitors and N-Ethylmaleimide (NEM; Sigma-Aldrich; Cat# EE3876-25G), whereas the second wash had no inhibitors or NEM in the buffer. Samples were centrifuged at 5000 x g for 5 minutes at 4°C and digested with benzonase (500 U/ml) (Millipore; Cat# 71205) and RNase (25 U/µL) (Thermo Fisher Scientific; #Cat EN0531) in a shaker set to 1000 rpm at 4°C. Digested chromatin was then centrifuged at 20,000 x g for 10 minutes and the pellet was stored at -80°C. Chromatin pellets were then lysed in RIPA buffer containing protease and phosphatase inhibitors and NEM. Cells were lysed by sonication (20 cycles: 30 seconds on, 30 seconds off). Protein concentrations were measured using the BCA assay. For chromatin samples, approximately 15-20 µg of protein was loaded onto SDS-PAGE gels for Western Blotting. Details of the chemicals used in the buffers can be found in Appendices, Table 2.

2.9.4. Protein co-immunoprecipitation (Co-IP)

Cells were transfected with the plasmid of interest using Lipofectamine 3000 as per manufacturer's protocol (Thermo Fisher; Cat#L3000008). After a 48-hour transfection, cells were trypsinised, washed twice with ice-cold PBS and centrifuged at 700 x g for 5 minutes at 4°C. Cells were then fractionated and chromatin was isolated as previously outlined. Digested chromatin was centrifuged at 20,000 x g for 10 minutes at 4°C. Supernatant was collected into a separate Eppendorf and diluted three times with IP lysis buffer (50 mM Tris-HCl, 150 mM NaCl, 1 mM EDTA, 0.5-1% Triton X-100, pH 8.0) containing protease and phosphatase inhibitors and 20 mM NEM. Samples were incubated using Pierce anti-HA magnetic beads (Thermo Fisher; Cat# 88836) at 4°C on a rotating wheel at 15 rpm for at least 2 hours. Before incubation step, beads were washed with IP lysis buffer 3 times for 10 minutes each at 4°C on a rotating wheel at 15 rpm. IP lysates were loaded onto washed beads (20 µL beads per sample), and 10% of the lysate was used as input sample. Supernatant was removed using a magnetic rack (Thermo Fisher Scientific; #12321D). Proteins were eluted by boiling samples in 2X Laemmli buffer for 10 minutes at 95°C. Eluted

proteins were analysed by Western Blotting. Details of the chemicals used in the buffers can be found in Appendices, Table 2.

2.10. Reporter assays

To measure homologous recombination (HR) efficiency, U2OS DR-GFP cells were seeded in 6-well plates to be approximately 50-70% confluent the following day. Cells were either treated with siControl, sip97 or siRAD51 for 48 hours, and transfected with 3 µg of I-SceI plasmid (gift from Dr Tim Humphrey, University of Oxford) using Lipofectamine 3000 (Thermo Fisher; Cat# L3000008) as previously outlined. The U2OS DR-GFP stable cells contained a GFP gene with an I-SceI cutting site, and a GFP fragment with truncated 3' and 5' termini. Repair of I-SceI-induced DSBs by HR led to the formation of GFP positive cells (refer to Figure 36 schematic). Cells were recovered in complete medium without antibiotics for at least 24 hours after treatment, and GFP-positive cells were measured using BD FACS DIVA software. Raw FACS data were gated for GFP expressing cells and analysed using FlowJo V10 software. The percentage of GFP positive cells in each condition was normalised to the I-SceI expressing positive control sample using Excel. For single-strand annealing (SSA) efficiency, U2OS SA-GFP reporter cells were transfected, treated, and analysed identically to the HR assay. The U2OS SA-GFP reporter construct contained a 5' fragment of the GFP gene and a 3' fragment of the GFP with an I-SceI cutting site. Repair of I-SceI-induced DSBs by SSA resulted in the formation of GFP positive cells that were analysed by FACS DIVA software as for U2OS DR-GFP cells (refer to Figure 38 schematic).

2.11. Colony formation assay

T24 and RT112 cells were seeded in 10 cm dishes at appropriate densities across three technical replicates. All drugs used for clonogenic assays were dissolved in DMSO. Cells were either treated with DMSO control, CB-5083 (6-hour treatment), or Mirin (24-hour treatment) over a range of concentrations to determine the IC10 and IC50 of the drugs (where IC10 marks the drug concentration at which 90% of cells survived, and IC50 represents the concentration at which 50% of cells survived). For radiosensitivity assays, cells were either treated with DMSO control, CB-5083, Mirin, or in combination (Mirin applied in the first 24 hours, and CB-5083 applied in the last 6 hours) at IC10 and IC50

concentrations prior to irradiation with 0, 2, 4 and 6 Gy. Cells were cultured for 8-12 days to allow colonies to form. Colonies were fixed and stained with 0.5% crystal violet powder (Sigma; Cat# 548-62-9) in dH_2O and 20% methanol (Thermo Fisher Scientific; Cat# 67-56-1) for approximately 5 minutes. Colony numbers were checked under a light microscope and colonies below 50 cells were excluded. The number of colonies in each dish was determined using a GelCount colony counter (Oxford Optronix). Plating efficiency was determined by dividing the number of colonies counted per dish by the number of cells seeded. The surviving fraction of cells was determined by normalising the number of colonies in each condition to the non-irradiated control.

2.12. Dosing of CB-5083 *in vivo*

For oral gavage, 6 CD1-nude mice were randomised into 3 groups, and CB-5083 was given as a single dose:

Group 1: Two mice given 25 mg/kg.

Group 2: Two mice given 50 mg/kg.

Group 3: Two mice given 100 mg/kg.

For intraperitoneal injections, 5 CD1-nude mice were randomised into 2 groups, and CB-5083 was given as a single dose:

Group 1: Two mice given 25 mg/kg.

Group 2: Three mice given 50 mg/kg.

The mice were monitored for a week and their body weights and general well-being evaluated daily.

2.13. Xenograft model for tumour growth delay

Animal experiments were conducted by Dr Salome Paillas (Prof Anne E Kiltie group) in accordance with United Kingdom Home Office Guidelines for animal testing and research and approved by the University of Oxford Animal Welfare and Ethical Review Body (AWERB) under University of Oxford project licences PPL P4B738A3B and P8484EDAE. Susan Kilgas helped with experiments and data analysis. All experiments are in accordance with the ARRIVE guidelines (Kilkenny et al., 2012). Flank RT112 bladder cancer xenografts

were established subcutaneously in 6-to 7-week-old female CD-1 nude mice by injecting 5×10^6 cells in Matrigel (1:2 ratio of Matrigel to cells suspended in ice-cold PBS) in a final volume of 100 µL. Before the start of the experiment, mice were randomised to four experimental groups using the "random" function (RAND) on Excel: control (n=8; no treatment), 25 mg/kg CB-5083 (n=8; diluted in 5% DMSO, 0.5% methyl cellulose and 1% Tween-80 in ddH_2O) via intraperitoneal injection (IP), IR only (n=8; 6 Gy, single fraction) using a Gulmay-320 cabinet irradiator, and IR combined with CB-5083 (n=8), where the drug was administered 6 hours prior to IR. Group sizes were determined by G*Power analysis software to detect large effect sizes. Mice received treatment when their tumour size reached 50 mm^3. Tumour volume was monitored 3 times per week using manual callipers and calculated using the following formula: width x height x length x [π/6]. Kaplan-Meier survival analysis was used to measure the time to treble tumour volume. Mice were weighed before the start of experiment and regularly three times a week. Up to 6 mice were kept in each individually ventilated cage (IVCs).

2.14. Pharmacokinetic analysis of CB-5083 concentration in plasma and different organs

Four CD-1 nude mice bearing RT112 xenografts were treated with 25 mg/kg CB-5083 via IP injection for 6 hours once the tumour volume reached 50 mm^3. Plasma, tumour, kidney, liver, and bladder were collected by Dr Salome Paillas, University of Oxford, to determine the concentration of CB-5083 (µM) by high performance liquid chromatography (HPLC) analysis (HPLC analysis was performed by Dr Lisa Folkes and Alix Hampson, University of Oxford).

2.15. Statistical analysis

Statistical analysis was carried out using GraphPad Prism. All data represent three independent biological repeats unless stated otherwise. Data distribution was determined by running a normality test. When comparing two groups, Student's t-test was used for normally distributed data and Mann-Whitney test for non-normally distributed data. One-way ANOVA was used to measure tumour growth *in vivo,* and two-way ANOVA was used

to measure clonogenic cell survival after IR. When comparing three or more non-normally distributed groups, Kruskal-Wallis test with Dunn's multiple comparisons was used. Asterisks represent the following: *P<0.05, **P<0.01, ***P<0.001, ****p<0.0001; NS, not significant.

Chapter 3: p97 and the MRE11-RAD50-NBS1 (MRN) complex: physical interaction and its functional relevance

p97 has several substrate specific co-factors, and various p97 substrates have been described in DNA damage response. Among them are the NHEJ factor Ku70/80 and chromatin remodeling proteins L3MBTL1 and KAP1 (van den Boom et al., 2016, Acs et al., 2011, Kuo et al., 2016). However, many of p97's co-factors containing the UBX domain are functionally poorly characterised (Meerang et al., 2011) and therefore the biochemical mechanisms of p97's functions in DNA repair still need to be explored. To identify relevant substrates for p97 in the DDR, Prof Kristijan Ramadan's lab previously conducted a triplex SILAC-based mass spectrometry experiment, where they treated cells with IR and overexpressed a dominant-negative p97-EQ mutant (Figure 13 A and B). This EQ mutant lacks ATP hydrolysis activity, but can bind ubiquitinated substrates, thereby causing substrate "trapping" without their degradation (Ye et al., 2003, Meerang et al., 2011, Ritz et al., 2011). HEK293 cells were treated with 10 Gy IR and recovered either 30 minutes (early recovery) or 8 hours (late recovery), and fractionated into cytosol, nucleosol and chromatin. Different fractions were then immunoprecipitated and samples were sent for mass spectrometry analysis. An increase in the interaction between the MRN complex and p97 was observed over 8 hours of recovery from IR in both the nucleosol and chromatin fractions (Figure 13 B) (unpublished data).

A reciprocal mass spectrometry screen was performed by Prof Anne Kiltie's group (PRIDE dataset identifier: PXD016279), where HA-tagged MRE11 was overexpressed in T24 bladder cancer cells and its interactome was studied. The screen validated previous SILAC-based mass spectrometry results, demonstrating that p97 interacts with MRE11. Furthermore, the number of p97 peptides in the complex with MRE11 resembled RAD50 and NBS1, which are part of the MRN core complex (Appendices: Figure 58).

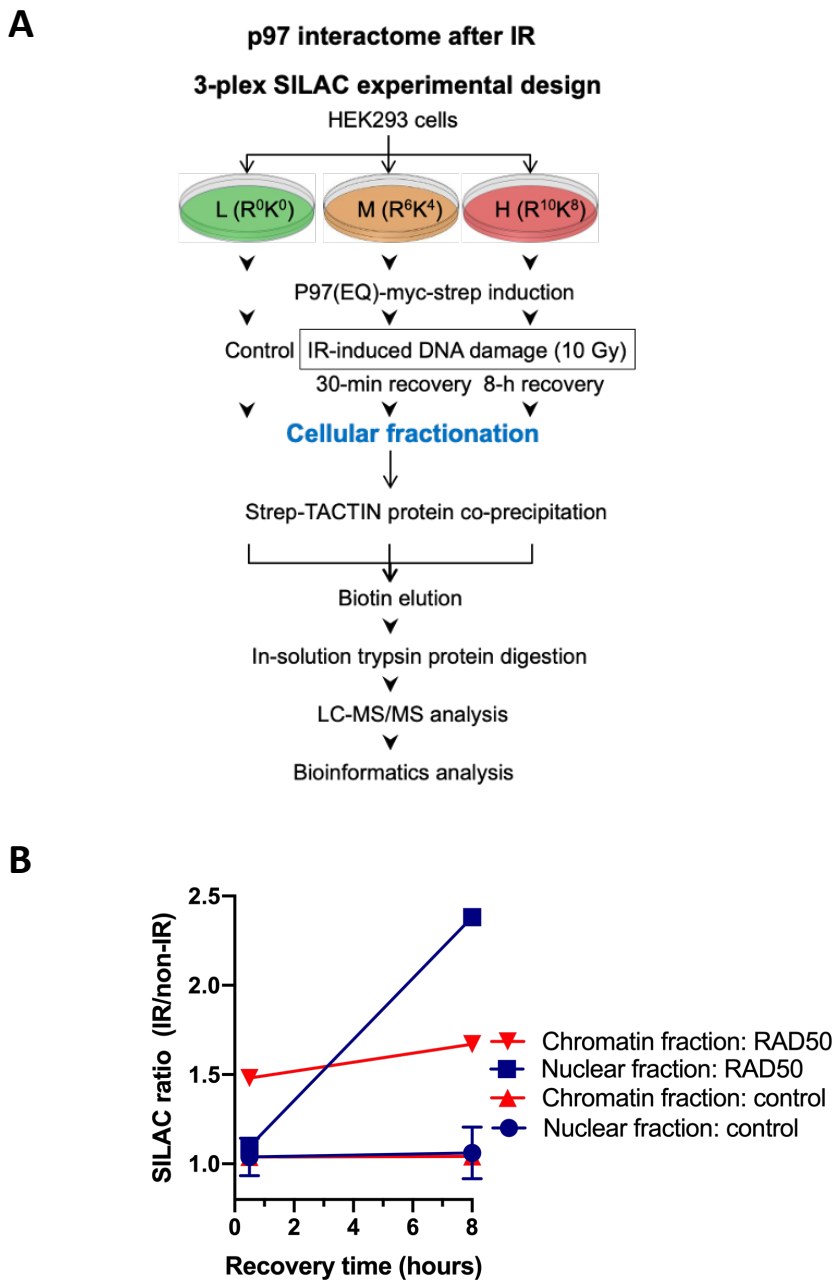


Figure 13 Mass spectrometry screen of the p97 interactome after IR.
A) Schematic overview of the SILAC-based mass spectrometry screen to identify p97 interaction partners after 10 Gy IR. HEK293 cells were irradiated, recovered over 8 hours, and fractionated into cytoplasmic, nuclear soluble, and chromatin (insoluble) compartments. **B)** SILAC ratios of p97 and RAD50 interaction on chromatin and in nuclear fraction after 8 hours of recovery from 10 Gy IR. SILAC ratio: ratio of irradiated cells to non-irradiated control cells. Control cells: coverage of all proteins detected +/- SEM. For nuclear soluble fraction, N=306 at 30 minutes and N=302 at 8 hours. For chromatin, N=1029 at 30 minutes and N=1026 at 8 hours. "N" represents the total number of proteins identified with SILAC ratios. These data were created and analysed by Dr Ignacio Torrecilla from Prof Kristijan Ramadan's group.

3.1. p97 interacts with the MRN complex

The above-mentioned mass spectrometry screens provided the preliminary data for this thesis. In order to biochemically confirm these results, the interaction between p97 and the MRN complex was studied by co-immunoprecipitation of p97 and the MRN complex components in the chromatin fraction of MRE11-overexpressed T24 cells upon 10 Gy IR (Figure 14 A). Overexpressed MRE11 was pulled down with a haemagglutinin (HA) tag and was shown to interact with the MRN complex components RAD50 and NBS1 as well as p97 both in the presence or absence of DNA damage by 10 Gy IR. These results were confirmed in a p97-EQ mutant overexpressed system, which demonstrated an interaction between p97 and the MRN complex components as well as in an endogenous system, where p97 was pulled down with all MRN complex components (Kilgas et al., 2021). Similarly, the interaction between p97 and the MRN complex was present regardless of IR-induced DNA damage. Furthermore, efficient subcellular fractionation was confirmed by running cytoplasmic, nuclear soluble and chromatin fractions of the MRN complex on the same gel (Appendices: Figure 59A) (Kilgas et al., 2021). Overall, the data confirm the results from mass spectrometry screens that p97 interacts with the MRN complex. As p97 removes DNA repair substrates from chromatin, it was hypothesised that p97 is involved in the disassembly of the MRN complex from chromatin and DNA damage sites, specifically in the context of DNA damaging IR.

A

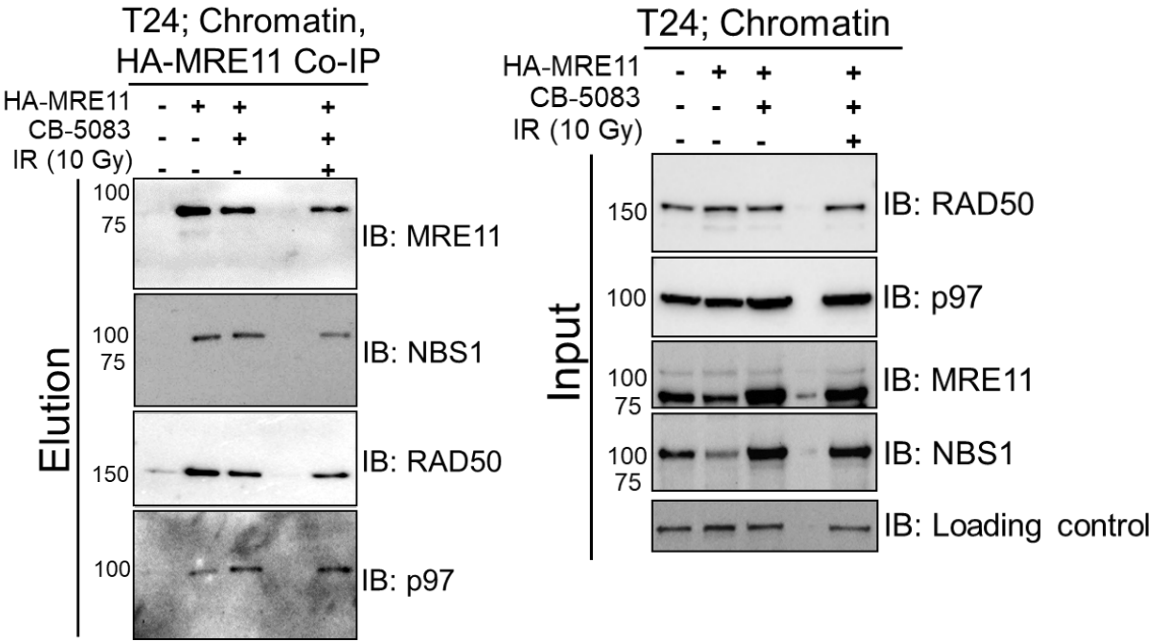


Figure 14 p97 interacts with the MRN complex.
Immunoprecipitation of HA-MRE11 overexpressed T24 cells demonstrating an interaction between p97 and the MRN complex components. Cells were fractionated, and HA-tagged MRE11 was pulled down in either DMSO- or CB-5083-treated (10 µM) conditions after 10 Gy IR; n=2 independent experiments. Input samples are shown on the right. Unspecific bands from the IP were used as loading control. Samples were treated with benzonase (500 U/mL) at 4°C until the DNA was digested.

3.2. p97 is required for MRN complex turnover on chromatin upon DNA damage

Inhibiting or depleting p97 activity has been previously shown to cause global accumulation of polyubiquitinated substrates in the cell, which results in the substrates not being effectively removed from their cellular locations (Meerang et al., 2011, Ramadan, 2012, van den Boom et al., 2016). To understand how p97 affects the MRN complex retention on chromatin and DNA damage upon IR, MRE11 and RAD50 nuclear foci accumulation was measured upon 2 Gy IR and over 8 hours of recovery in p97-inhibited T24 cells. Treatment with 10 μM CB-5083, a reversible competitive D2 ATPase inhibitor of p97, caused MRE11 (Figure 15 A and B) and RAD50 (Figure 16 A and B) to accumulate in IR-induced foci (IRIF) over 8 hours after damage induction compared to DMSO control conditions. These results were validated using UV-A laser micro-irradiation experiments, which creates quantifiable localised DNA damage within cell nuclei. For UV laser DNA damage, cells were pre-sensitised with Hoechst (10 μg/mL) for 15-20 minutes before DNA damage induction. Similarly, UV-A laser damage caused MRE11 and RAD50 to accumulate on micro-irradiated sites in p97 inhibitor treated T24 cells over 8 hours after DNA damage induction, characterised by increased intensity at the sites of DNA damage compared to DMSO control (Figure 17 A and B; Figure 18 A and B). Cells were recovered up to 8 hours in these experiments, however, further monitoring of MRE11 and RAD50 clearance from DNA damage sites would be needed to study the kinetics of cell recovery after UV-A laser damage. For this, live cell imaging would be the most accurate way of determining the kinetics of both MRE11 and RAD50 recruitment as well as their removal from DNA damage sites.

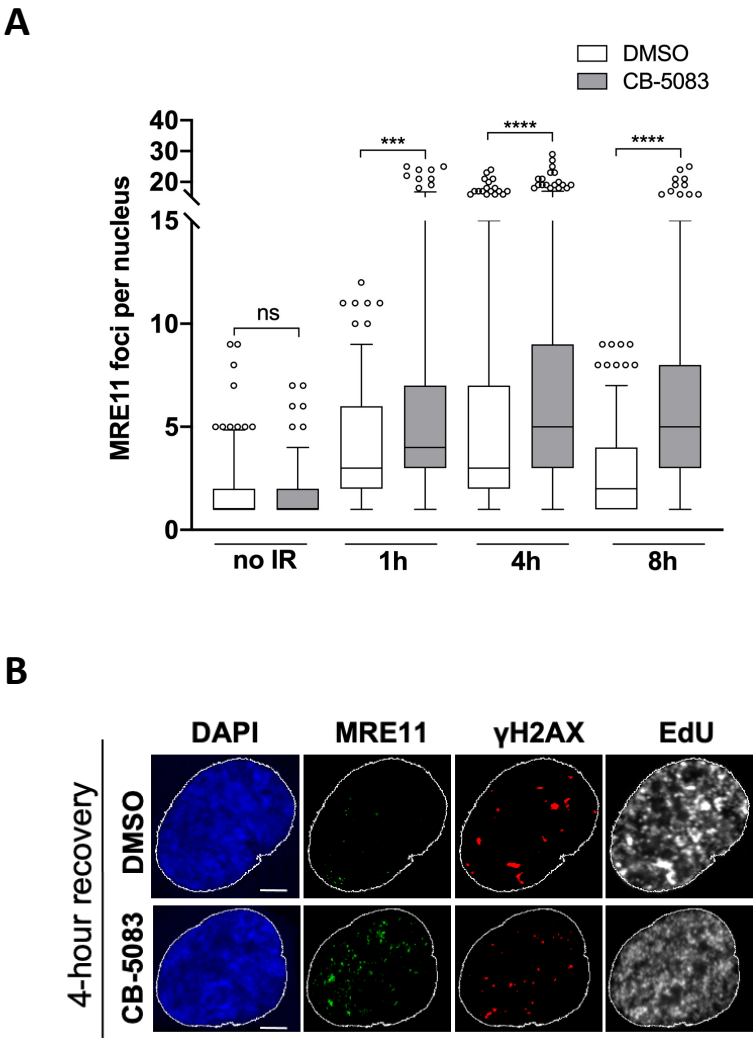


Figure 15 MRE11 accumulates in IR-induced foci upon p97 inhibition.
A) Number of MRE11 nuclear foci in T24 cells over 8 hours of recovery after 2 Gy IR and +/- 10 µM CB-5083 treatment. Data is presented as a box-and-whisker plot with interquartile range. Values beyond the 5th and 95th percentiles are shown as individual points; n=3 independent experiments. At least 60 individual cells were counted per repeat and condition. Statistical analysis: Mann-Whitney test. NS, not significant ($p>0.05$); *** $p\leq0.001$; **** $p\leq0.0001$. **B)** Representative images showing MRE11 foci accumulation in CB-5083-treated conditions compared to DMSO control. EdU is a marker of S phase (only S phase cells were analysed). γH2AX is used as a marker of DNA damage and DAPI is a nuclear marker. The staining for γH2AX differs from Figure 16, which could be due to using a different species of γH2AX antibody for these set of experiments (Millipore; #2739172; mouse monoclonal). Please refer to Methods chapter 2.7. for further information. Scale bar: 5 µm.

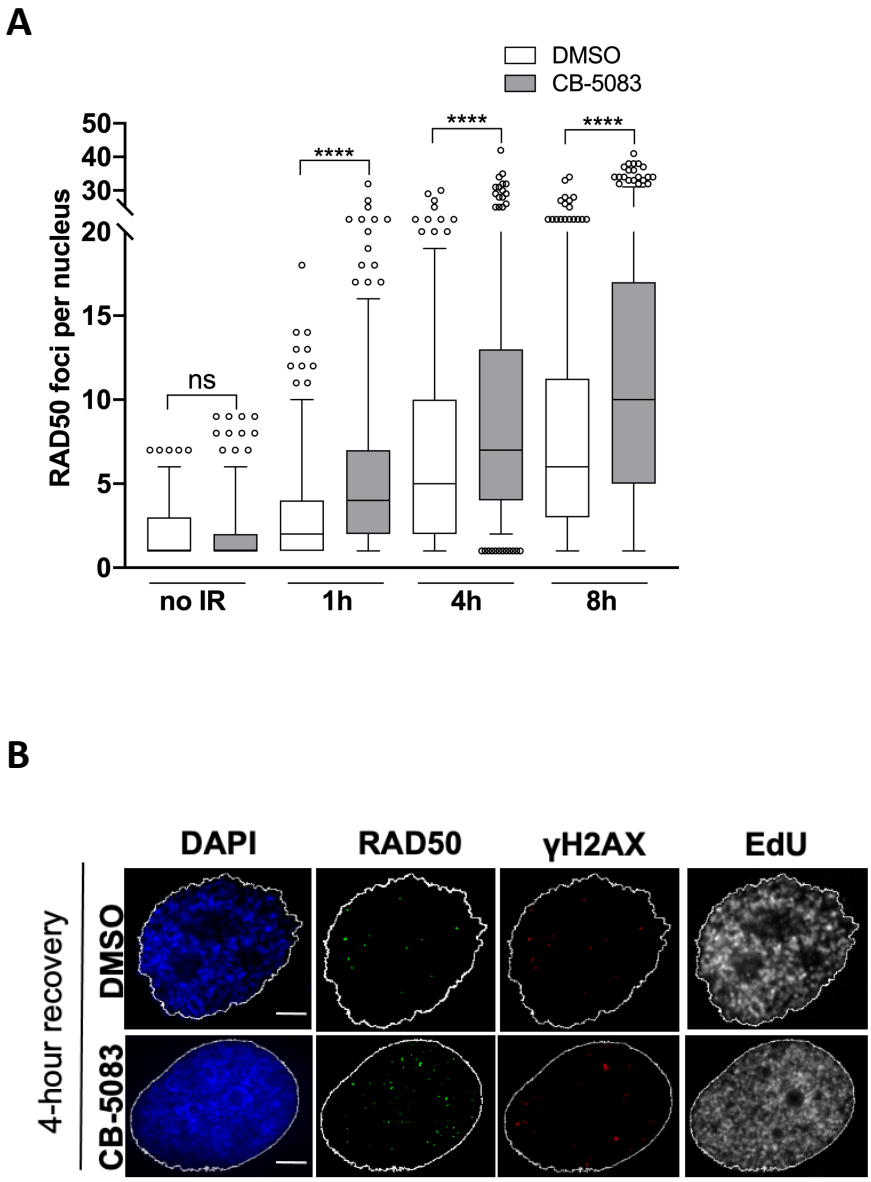


Figure 16 RAD50 accumulates in IR-induced foci upon p97 inhibition.
A) Number of RAD50 nuclear foci in T24 cells over 8 hours of recovery after 2 Gy IR and +/- 10 µM CB-5083 treatment. Data is presented as a box-and-whisker plot with interquartile range. Values beyond the 5th and 95th percentiles are shown as individual points; n=3 independent experiments. At least 60 individual cells were counted per repeat and condition. Statistical analysis: Mann-Whitney test. NS, not significant ($p>0.05$); **** $p\leq0.0001$ **B)** Representative images of RAD50 nuclear foci in CB-5083-treated conditions compared to untreated control cells. Only S phase cells were counted (EdU positive). γH2AX marks DNA damage and DAPI marks individual nuclei. The staining for γH2AX differs from Figure 15, which could be due to using a different species of γH2AX antibody for these set of experiments (Cell Signaling; #2577; rabbit polyclonal). Please refer to Methods chapter 2.7. for further information. Scale bar: 5 µm.

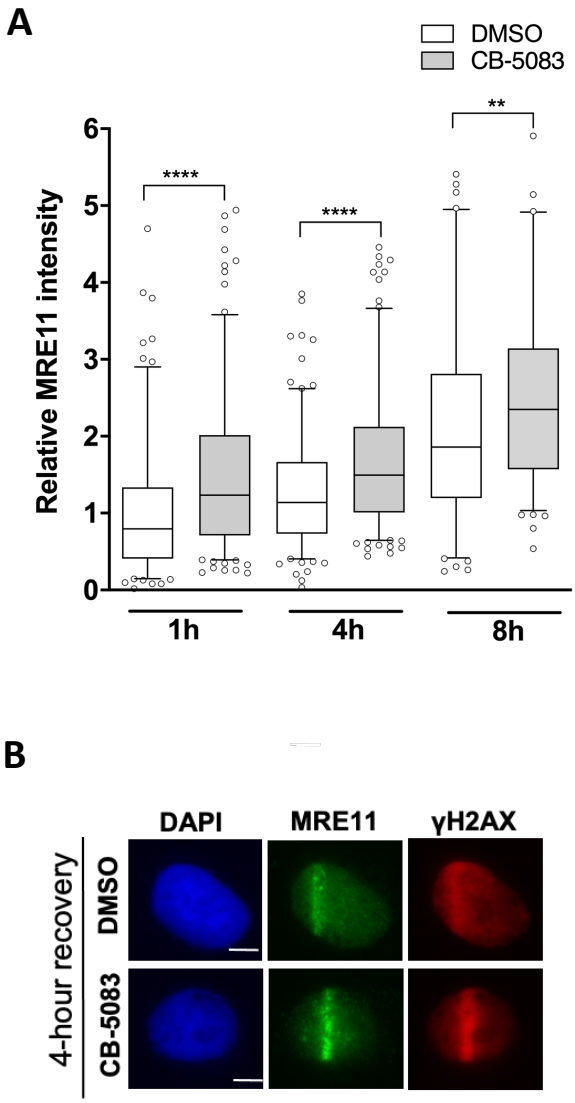


Figure 17 MRE11 accumulates on UV-induced DNA damage sites in p97-inhibited conditions.

A) Relative intensity of MRE11 on UV-A pulsed laser-induced (wavelength 355 nm; 5 ns pulse length) DNA damage sites in T24 cells upon 10 µM CB-5083 or DMSO control conditions and 8 hours of recovery. MRE11 intensity was quantified by normalising its intensity on DNA damage sites to the intensity at the earliest time point in DMSO control. Cells were pre-sensitised with Hoechst (10 µg/mL). Laser was connected to a Nikon TE2000 microscope with a 10X objective, and energy was adjusted to be approximately 10 µJ across the laser line. Data is shown as a box and whiskers plot. Values above 5th and 95th percentiles are shown as individual data points; n=3 for 1-hour and 4-hour recovery; n=2 for 8-hour recovery. At least 60 individual cells were counted per repeat and condition. Statistical analysis: Mann-Whitney test. ** $p<0.01$; **** $p\leq0.0001$. **B)** Representative images showing MRE11 accumulation upon p97 inhibition compared to DMSO control. Scale bar: 5 µm.

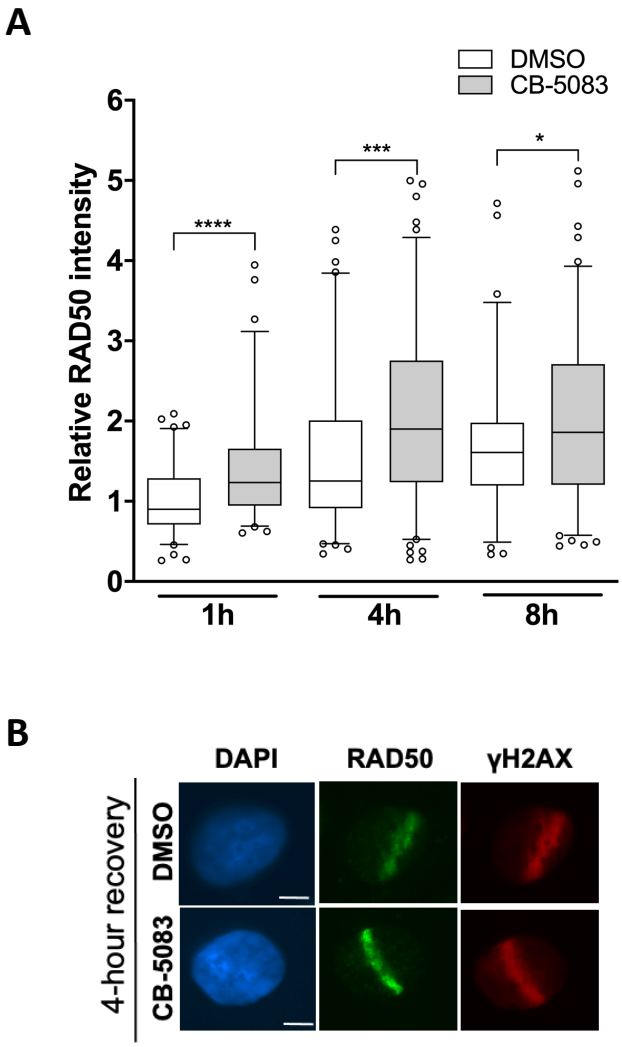


Figure 18 RAD50 accumulation on UV-induced DNA damage sites in p97-inhibited conditions.

A) Relative intensity of RAD50 on UV-A pulsed laser-induced (wavelength 355 nm; 5 ns pulse length) DNA damage sites in T24 cells upon 10 µM CB-5083 or DMSO control conditions and 8 hours of recovery. Cells were pre-sensitised with Hoechst (10 µg/mL). Laser was connected to a Nikon TE2000 microscope with a 10X objective, and energy was adjusted to be approximately 10 µJ across the laser line. Data is presented as a box and whiskers plot, where values above 5th and 95th percentiles are shown as individual points; n=3 for 1-hour and 4-hour recovery; n=2 for 8-hour recovery. At least 60 individual cells were counted per repeat and condition. Statistical analysis: Mann-Whitney test. * p≤0.05; *** p≤0.001; **** p≤0.0001. **B)** Representative images of RAD50 accumulation in CB-5083-treated conditions compared to DMSO control. Scale bar: 5 µm.

To study whether the MRN complex degradation is disrupted in p97-inactivated conditions, the MRN complex turnover was biochemically analysed by cycloheximide (CHX) chase assay in both soluble and chromatin fractions upon 10 Gy IR. CHX inhibits protein translation and causes degradation of the available protein pool over time under non-treated conditions. Inactivation of p97 either by the inhibitor CB-5083 (Figure 19 A) or by silencing p97 with siRNA (sip97) (Figure 19 B) blocked the disassembly of MRN from chromatin in T24 cells. These results were further confirmed in HeLa cells, where inhibition of p97 caused chromatin accumulation of all MRN complex components after IR and CHX (Kilgas et al., 2021). When observing the MRN protein complex levels in whole cell lysates upon p97 inhibition and IR, there was no overall increase in total protein levels (Figure 19 C). The MRN complex retention on chromatin was further confirmed with a CHX assay using a doxycycline (DOX)-inducible p97-EQ substrate trapping mutant, in which p97 can bind its substrates but is unable to process them (Kilgas et al., 2021). To confirm that p97 inactivation leads to chromatin-specific MRN complex retention, both chromatin and cytoplasm/nucleoplasm fractions were run on the same gel, and MRN complex retention was only observed in chromatin fraction upon p97 inactivation, compared to the nucleosol and cytosol fractions (Appendices: Figure 59 A) (Kilgas et al., 2021). Finally, the relative distribution of EdU-positive and -negative cells was analysed by immunofluorescence microscopy in p97 inhibited and DMSO control conditions in T24 cells (Figure 19 D) to understand whether there are any general differences in S phase distribution between p97 inactivated and control cells. No significant differences in S phase distribution were observed across three independent repeats. In the future, it would be important to test general cell cycle distribution effects upon p97 inhibition in T24 cells, and to perform cycloheximide assays with synchronised cells to make sure that any differences observed in protein stability and amount are not due to changes in the cell cycle. In summary, these results demonstrate that p97 regulates MRN complex disassembly from chromatin, and inactivating p97 either by p97 inhibition or siRNA-mediated depletion causes MRN complex retention on chromatin after IR, especially for the MRE11 nuclease.

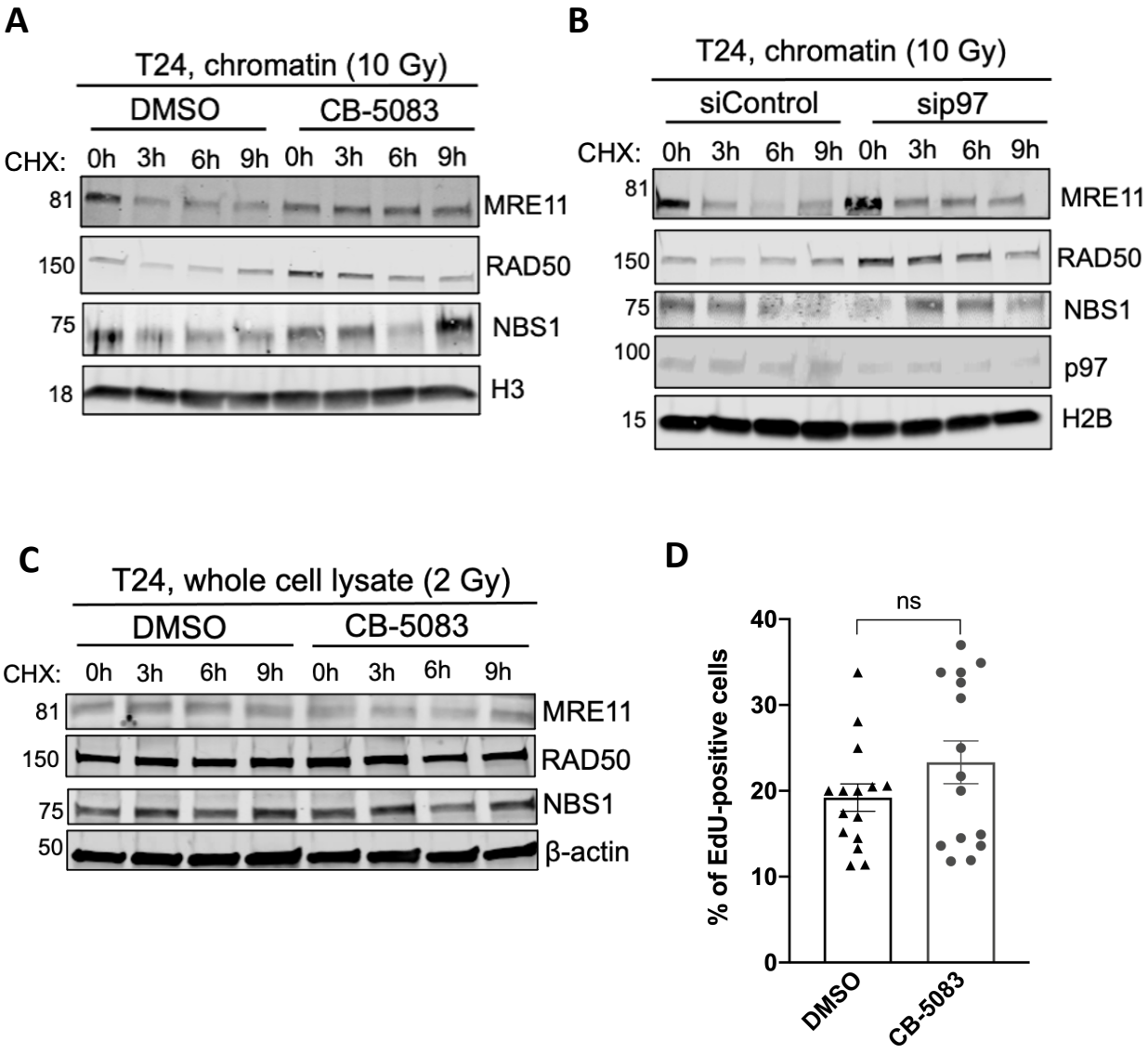


Figure 19 . p97 is required for MRN turnover on chromatin upon DNA but does not affect total MRN protein levels.

A) Inhibition of p97 by 10 µM CB-5083 in T24 cells treated with 10 Gy IR leads to MRN complex retention on chromatin upon cycloheximide (CHX; 9 h). Histone H3 is loading control; n=3 independent experiments. Unexpected NBS1 sample degradation was observed in CB-5083-treated conditions at 6 hours upon CHX treatment. This could have been due to inefficient sample sonication or residual protease activities. **B)** Knockdown of p97 by siRNA (10 nM; over 48 hours) stabilises MRN on chromatin upon 10 Gy IR and over 9 h CHX treatment in T24 cells. Histone H2B is loading control. Data is representative of n=2 independent experiments. **C)** Total protein levels of the MRN complex upon CHX treatment (9 h), p97 inhibition and 2 Gy IR in T24 cells. Beta-actin is loading control. Data is representative of n=3 independent experiments. D) Percentage of EdU-positive cells in p97 inhibited and control conditions does not significantly differ. At least 240 cells were counted per repeat and condition across n=3 independent experiments. Statistical analysis: Mann-Whitney test. NS, not significant. Individual data points are shown indicating the percentage score per image analysed.

3.3. Dependency of the Ku complex on p97-mediated regulation of MRE11

It has been shown that p97-mediated Ku70/80 heterodimer disassembly from DNA break sites is needed for resumption of HR-mediated DSB repair (van den Boom et al., 2016). The Ku complex is acting upstream of MRE11 and stimulates NHEJ repair while blocking HR repair (van den Boom et al., 2016). Therefore, this could suggest that p97-mediated MRE11 regulation is an indirect effect over the Ku complex. To study whether this is the case, MRE11 accumulation on DNA damage sites after IR was studied in both Ku- and p97-depleted conditions. Depletion of Ku80 by siRNA, which causes depletion of the whole Ku70/80 complex (van den Boom et al., 2016, Nussenzweig et al., 1996, Fink et al., 2010), did not affect MRE11 accumulation on DNA damage, and combined depletion of Ku80 and p97 did not further affect p97-mediated MRE11 accumulation, demonstrating that p97 regulates MRE11 independently of Ku70/80 (Figure 20 A and B). Depletion of p97 and Ku80 were confirmed by Western Blotting (Figure 20 C).

It has been demonstrated that the absence of Ku increases the efficiency of DNA end resection (Zhou et al., 2014), which is in line with the antagonistic function between NHEJ and HR (Chapman et al., 2012b). However, the data from Figure 20 shows that depletion of Ku80 did not result in increased MRE11 accumulation on DNA damage sites upon IR compared to control-depleted cells. This suggests that the absence of the Ku complex might not directly cause MRE11 accumulation above normal levels, but instead increase the efficiency of resection mediated by downstream long-range EXO1/BLM-DNA2. However, the specific activities and dependencies of different nucleases in the context of Ku depletion should be studied further in the future to draw any conclusions. In addition, MRE11 activity is stimulated by the presence of Ku-bound DSB ends, where MRE11 acts to remove Ku. Therefore, it would be interesting to compare what effect does Ku depletion versus overexpression have on MRE11 accumulation on DNA damage in these conditions (Myler et al., 2017). Overall, the results from this chapter demonstrate that p97 functionally interacts with the MRN complex and is involved in the removal of the complex from chromatin and from sites of DNA damage after IR and UV laser micro-irradiation. Inactivation of p97 causes MRN to accumulate on chromatin due to it not being efficiently degraded, suggesting that p97 could be involved in the disassembly of the MRN complex

on DNA damage sites. Protein disassembly is controlled by ubiquitination and previous studies have shown that MRE11 is ubiquitinated, however it is unknown which ubiquitin ligases and specific co-factors are involved in the process. Ubiquitination of MRE11 determines its stability on chromatin and thereby regulates DNA repair pathway choice (Jachimowicz et al., 2019, Nicholson et al., 2017). ‘

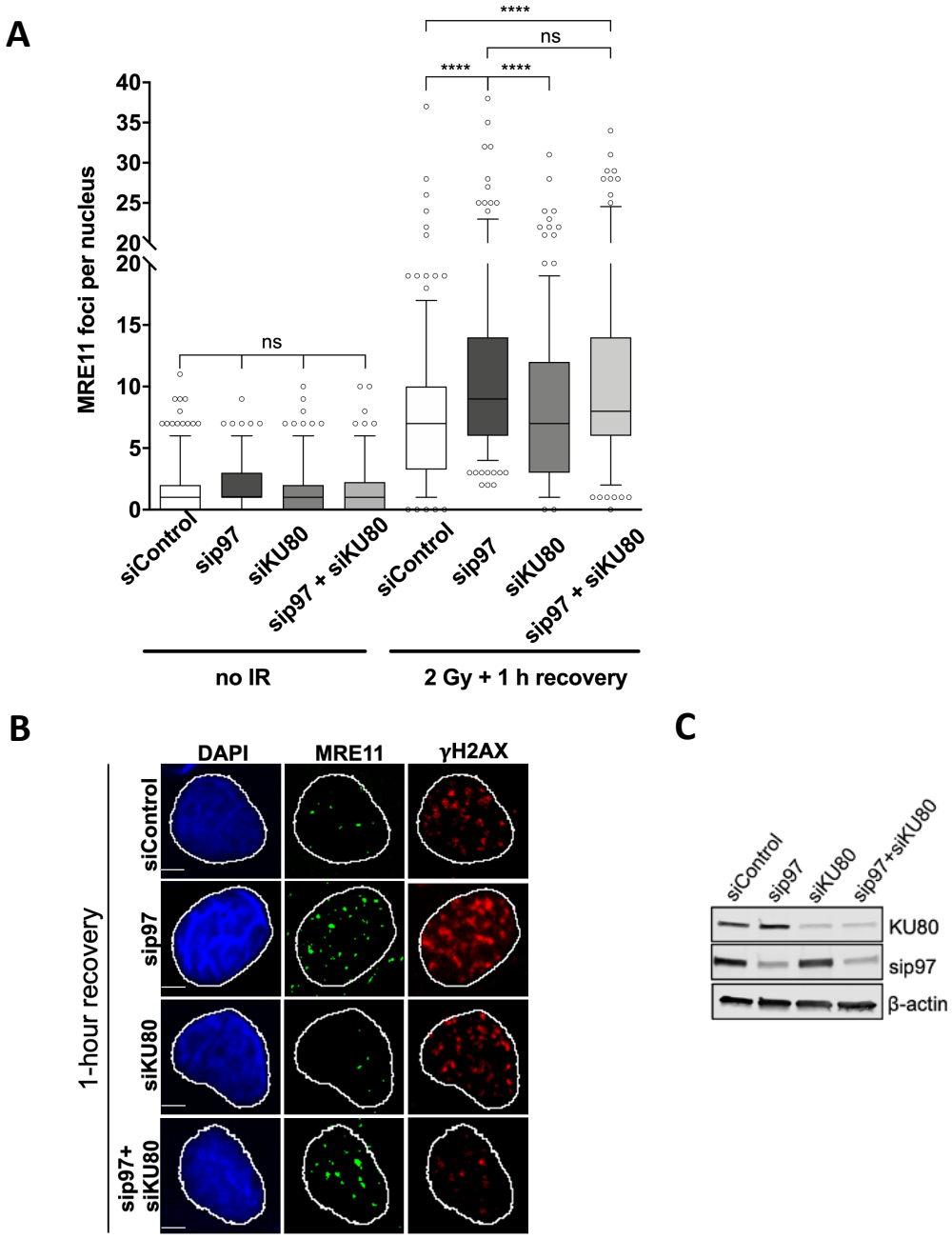


Figure 20 p97 regulates MRE11 accumulation on DNA damage independently of Ku80. **A)** Number of MRE11 nuclear foci in T24 cells over 1 hour of recovery after 2 Gy IR in p97- and Ku80-depleted conditions. Data is presented as a box-and-whisker plot with interquartile range. Values beyond the 5th and 95th percentiles are shown as individual points; n=3 independent experiments. At least 60 individual cells were counted per repeat and condition. Statistical analysis: Mann-Whitney test. NS, not significant ($p>0.05$); **** $p\leq0.0001$ **B)** Representative images of the number of MRE11 foci after 1 hour of recovery from 2 Gy IR in p97- and Ku80-depleted T24 cells. Scale bar: 5 µm. **C)** Western Blot showing knockdown of p97 and Ku80. Beta-actin is loading control.

With regards to the findings from this chapter, MRN could be one of p97's substrates, where p97 recognises ubiquitinated components of the complex. It is known that p97/Cdc48 unfolds proteins by a threading mechanism, where substrates are threaded through its central pore (Twomey et al., 2019, Bodnar and Rapoport, 2017, van den Boom et al., 2021, Ji et al., 2021), but it is not yet fully understood how various substrates that function in different cellular pathways are recognised and inserted into the p97/Cdc48 pore. For example, substrate loop insertion into the p97 central pore can be coupled with recognition of an internal site in the substrate. This mechanism has been recently demonstrated for p97 and its co-factor p37, where p97 binds an internal recognition site (IRS) of inhibitor-3 (I3) protein in complex with protein phosphatase-1 (PP1). Binding to the IRS initiates substrate threading into p97's central pore to release PP1 from its inhibitory protein I3 (van den Boom et al., 2021). Alternatively, studies on the mechanisms Cdc48 substrate processing have demonstrated that Cdc48 is able to directly bind ubiquitin chains rather than the attached substrate, where the ATPase pulls on the initiator ubiquitin and moves it through the central pore, leading to ubiquitin chain unfolding. Once Cdc48 reaches the substrate, it can translocate and unfold the substrate (Ji et al., 2021). In future studies, it would be interesting to determine whether p97 recognises the MRN complex through ubiquitination or through specific p97 subcomplexes. There are no known p97 binding domains in any of the MRN complex components, and therefore it could be possible that the substrate is either recognised through ubiquitin chains, or alternatively being bridged to p97 through specific co-factors able to bind the MRN complex components. It would be important to first determine which MRN complex components are ubiquitinated. Then, an unbiased approach such as mass spectrometry of the MRN complex interaction partners upon DNA damage induction could be done to identify potential E3 ligases and p97 co-factors involved in the MRN complex disassembly. The results could then be validated by various biochemical methods such as immunoprecipitation, protein stability assays, and proximity ligation assays (PLAs).

Chapter 4: p97 regulates DNA repair pathway choice through MRE11 nuclease activity

It has been previously shown that p97 regulates DNA DSB repair pathway choice through its various DDR substrates and that depletion of p97 leads to defective NHEJ- as well as HR-mediated repair (Meerang et al., 2011). The HR defect in p97-depleted conditions is thought to be caused by the Ku complex accumulation on DSBs (van den Boom et al., 2016), whereas the defect in NHEJ occurs due to compromised 53BP1 recruitment (Acs et al., 2011). One of the major DSB repair pathway choice determinants is the level of DNA end resection. For example, when levels of ssDNA exceed a certain threshold, there is a switch from RAD51-mediated HR repair to mutagenic RAD52-mediated SSA repair. This has been shown to occur due to compromised 53BP1 function (Ochs et al., 2016), which in itself is an anti-resection protein that balances DNA end-resection and inhibits ssDNA formation outside the G2/S phase. One of the mechanisms by which 53BP1 controls end resection is by inhibiting the formation RAD51 foci (Ghezraoui et al., 2018). Where 53BP1 is compromised and DNA end resection is hyperactive, RAD51 foci formation decreases whereas RAD52 foci formation increases (Ochs et al., 2016). This happens because RAD51 and RAD52 counteract each other, and RAD51 usually exerts an inhibitory brake on RAD52 (Ceccaldi et al., 2016). Results from the previous chapter showed that inhibiting or silencing p97 by siRNA leads to MRE11 accumulation on chromatin and IR-induced DNA lesions. Since one of the major determinants of DNA DSB repair pathway choice is the level of MRE11-mediated end resection (Nakamura et al., 2019, Jachimowicz et al., 2019, He et al., 2018, Bai et al., 2019), this chapter focuses on the functional relevance of MRE11 accumulation on DNA damage sites upon p97 inactivation by studying its effects on DNA end resection and subsequent DSB repair pathway choice.

4.1. Inactivation of p97 causes excessive 5'-DNA end resection mediated by MRE11 nuclease activity

The formation of single-stranded DNA (ssDNA) was studied in the absence of p97 by BrdU assay under native conditions. This assay allows to visualise ssDNA foci by treating cells with BrdU for 24 hours and using a BrdU antibody to detect BrdU foci by immunofluorescence microscopy (Caron et al., 2019). T24 cells were treated with 10 µM BrdU for 24 hours and briefly labelled with EdU to mark S phase cells (Figure 21 A). Inhibition of p97 led to an increase in DNA end resection (measured by the number of BrdU foci) in S phase (EdU positive) cells compared to DMSO control (Figure 21 B and C). The increased ssDNA phenotype was almost completely rescued back to control levels when cells were treated with the MRE11 complex inhibitor Mirin, indicating that the increased number of ssDNA foci were mostly caused by MRE11 accumulation upon p97 inhibition. Hydroxyurea (HU) was used as a positive control as it induces replication stress in S phase cells that leads to increased ssDNA formation.

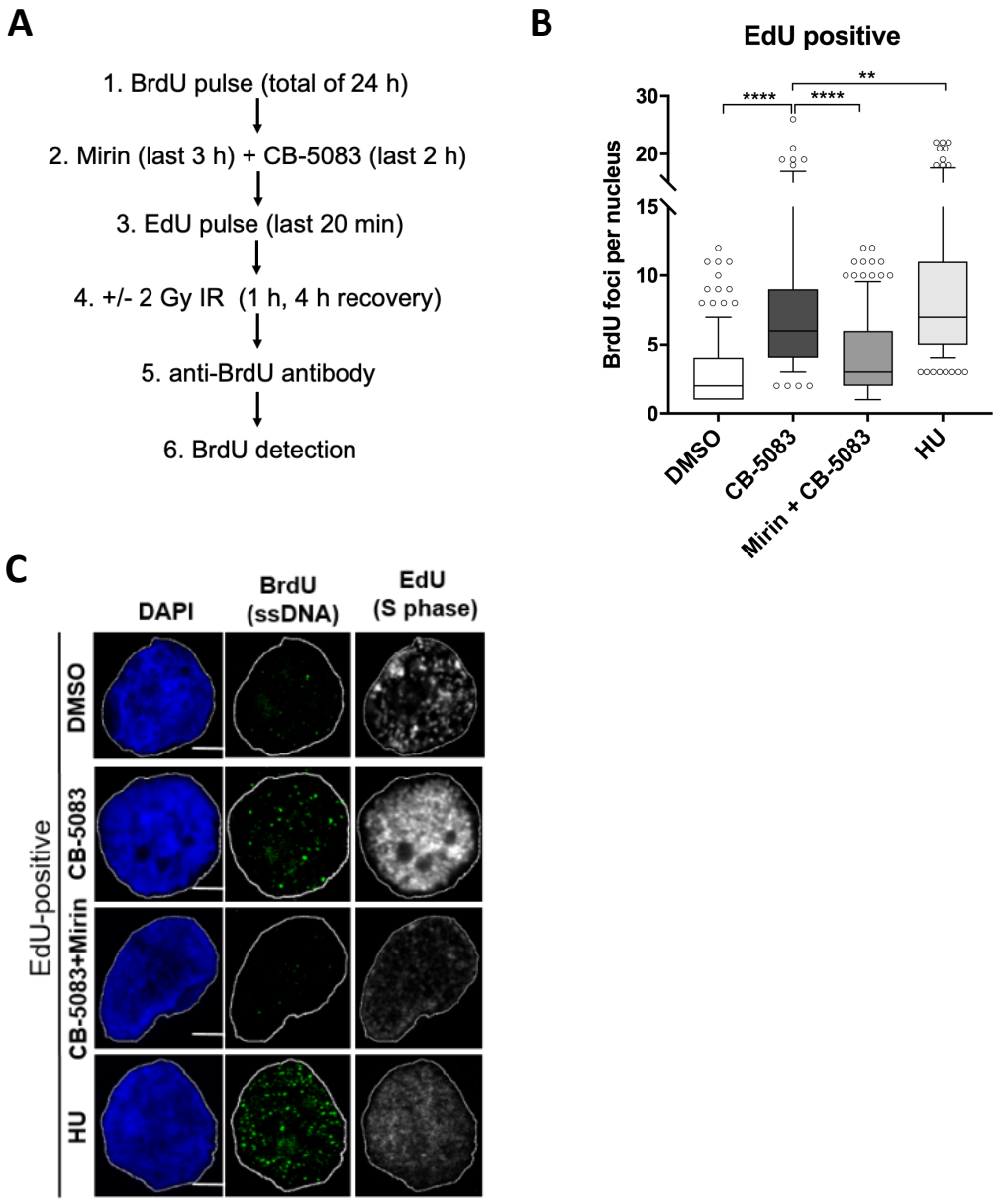


Figure 21 p97 inhibition causes excessive MRE11-mediated DNA end resection in S phase cells.

A) Non-denaturing BrdU assay experimental design. **B)** Number of EdU-positive (S phase) BrdU foci in CB-508- and Mirin-treated T24 cells. Mirin reverses the ssDNA phenotype in p97-inhibited cells. Hydroxyurea (HU) serves as a positive control. Data is presented as a box-and-whisker plot with interquartile range. Values beyond the 5th and 95th percentiles are shown as individual data points. At least 60 cells were counted per repeat and condition. The data is representative of 3 biological repeats. Statistical analysis: Kruskal-Wallis test with Dunn's multiple comparisons. ** $p<0.01$; **** $p\leq0.0001$ **C)** Representative images. Scale bar: 5 µm.

In addition to MRE11-mediated nuclease activity in S phase, MRE11 also functions in G1 as part of the alternative-NHEJ pathway, which results in the annealing of microhomologies in the genome (Shibata et al., 2017). Therefore, ssDNA foci formation was studied also in EdU-negative cells. Inhibition of p97 in cells outside S phase led to an increase in ssDNA foci similarly to cells in S phase, which was reversed to near control levels upon addition of Mirin to CB-5083-treated cells (Figure 22 A and B). HU-treated cells were used as a negative control, as HU induces replication stress and therefore its effects are restricted to cells in S phase. As expected, ssDNA did not form outside S phase in HU-treated cells. To further confirm these results and study how IR-induced damage might affect the formation of ssDNA in p97-inhibited conditions, a BrdU assay was done in the presence of IR (2 Gy) in S phase cells, which also showed that p97 inhibition causes increased formation of ssDNA foci that is reversed when MRE11 is simultaneously inhibited (Figure 23 A and B). As expected, in Figure 23A and B, there is also a general increase in the number of BrdU foci from non-irradiated to irradiated cells in control conditions. However, no further increase of BrdU foci was observed in control cells between 1 hour and 4 hours after IR. One of the potential reasons could be that a proportion of control cells recovered from irradiation between 1 hour and 4 hours after DNA damage, and the radiation dose used was relatively low (2 Gy). Furthermore, similar phenotypes were observed using specific MRE11 exo- and endonuclease inhibitors in both S phase (Figure 24 A and B) and in cells outside S phase (Figure 25 A and B). These results indicate that the effects observed with Mirin in combination with CB-5083 are not simply due to off-target effects of Mirin treatment.

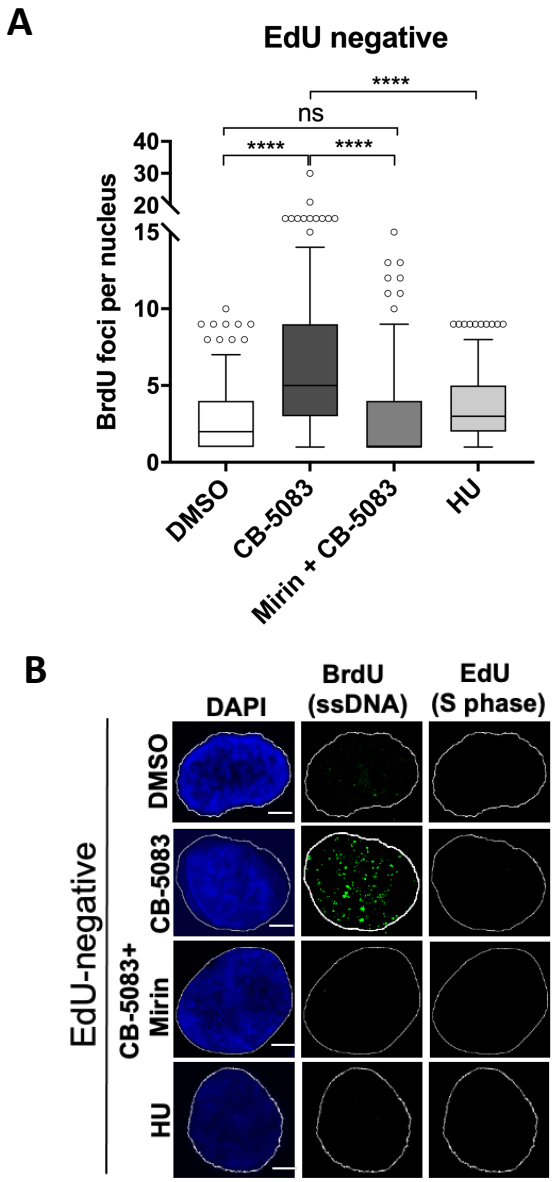


Figure 22 Inhibiting p97 leads to MRE11-mediated DNA hyper-resection in cells outside S phase.

A) EdU-negative (non-S-phase) BrdU foci in CB-508- and Mirin-treated T24 cells. Hydroxyurea (HU) and DMSO serve as negative controls. Data is presented as a box-and-whisker plot showing interquartile range. Values beyond the 5th and 95th percentiles are shown as individual data points. At least 60 cells were counted per repeat and condition. The data is representative of 3 biological repeats. Statistical analysis: Kruskal-Wallis test with Dunn's multiple comparisons. NS, not significant; **** p≤0.0001 **B)** Representative images. Scale bar: 5 µm.

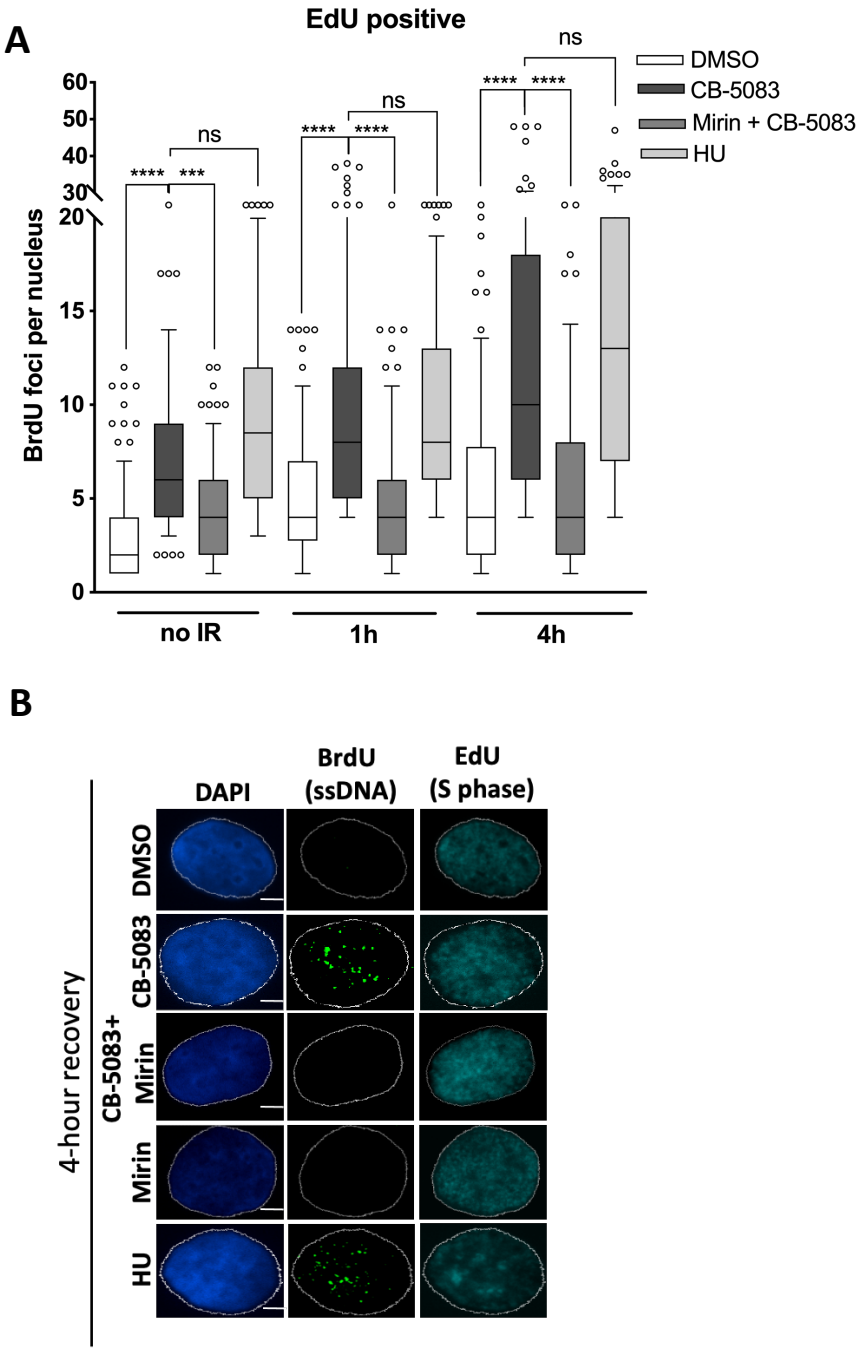


Figure 23 BrdU foci formation in EdU-positive cells upon p97 inhibition and IR.
A) Number of BrdU foci in EdU-positive CB-5083-treated T24 cells (+/- 2 Gy IR and 1 h and 4 h recovery). Data is presented as box-and-whisker plot with interquartile range and 5th-95th percentiles. Values beyond 5th and 95th percentiles are plotted as individual points. At least 60 individual cells were counted per repeat and condition. The data is representative of 3 biological repeats. Statistical analysis: Kruskal-Wallis test with Dunn's multiple comparisons. NS, not significant; **** p≤0.0001 **B)** Representative images after 4 hours of IR are shown. Scale bar: 5 µm.

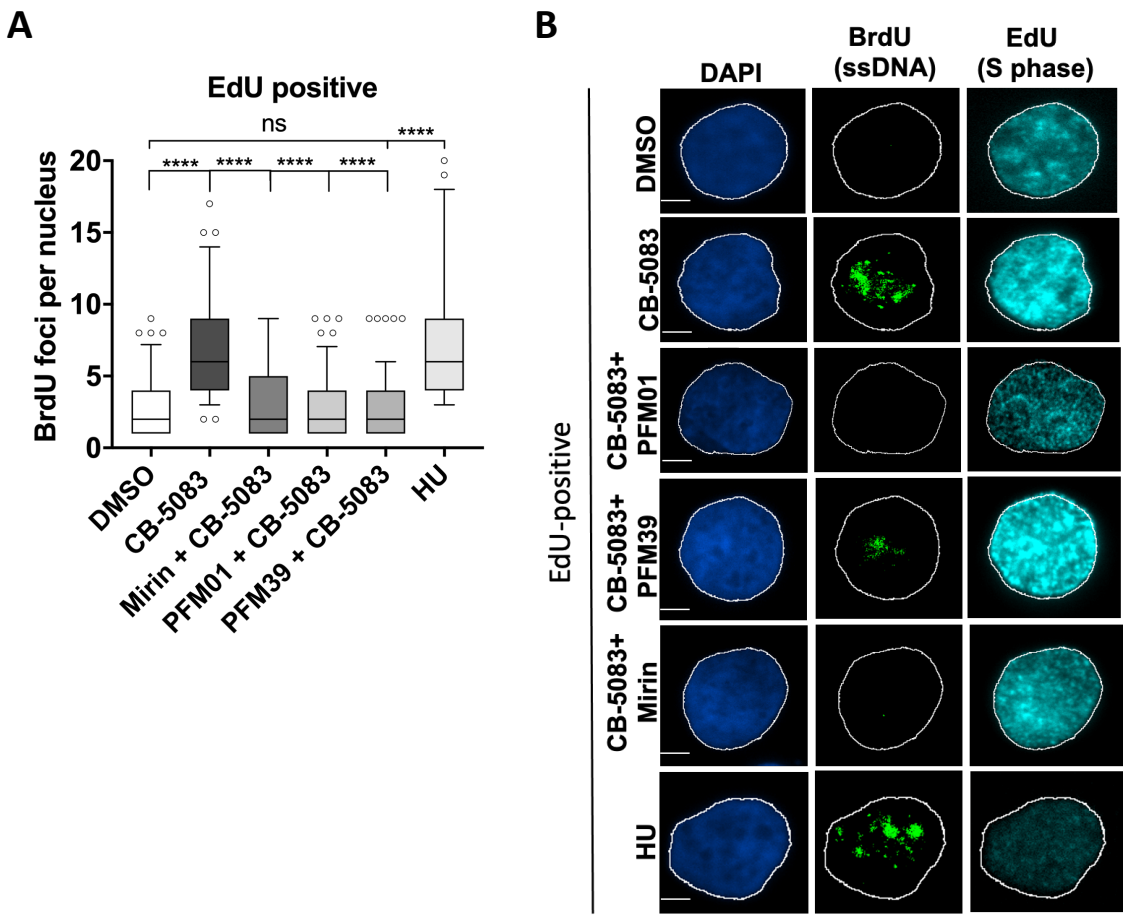


Figure 24 MRE11 endo- and exonuclease inhibitors rescue CB-5083-induced excessive ssDNA generation in S phase cells.

A) Number of BrdU foci in EdU-positive T24 cells after treatment with CB-5083 in combination with specific MRE11 inhibitors: MRE11 complex inhibitor Mirin; the endonuclease inhibitor PFM01; the exonuclease inhibitor PFM39. Hydroxyurea (HU) serves as a positive control. Data is shown as box-and-whiskers plot with interquartile range and 5th-95th percentiles. Values beyond 5th and 95th percentiles are plotted as individual data points. At least 60 individual cells were counted per repeat and condition. The data is representative of 2 independent biological experiments. Statistical analysis: Kruskal-Wallis test with Dunn's multiple comparisons. NS, not significant; **** p≤0.0001.
B) Representative images are shown. Scale bar: 5 µm.

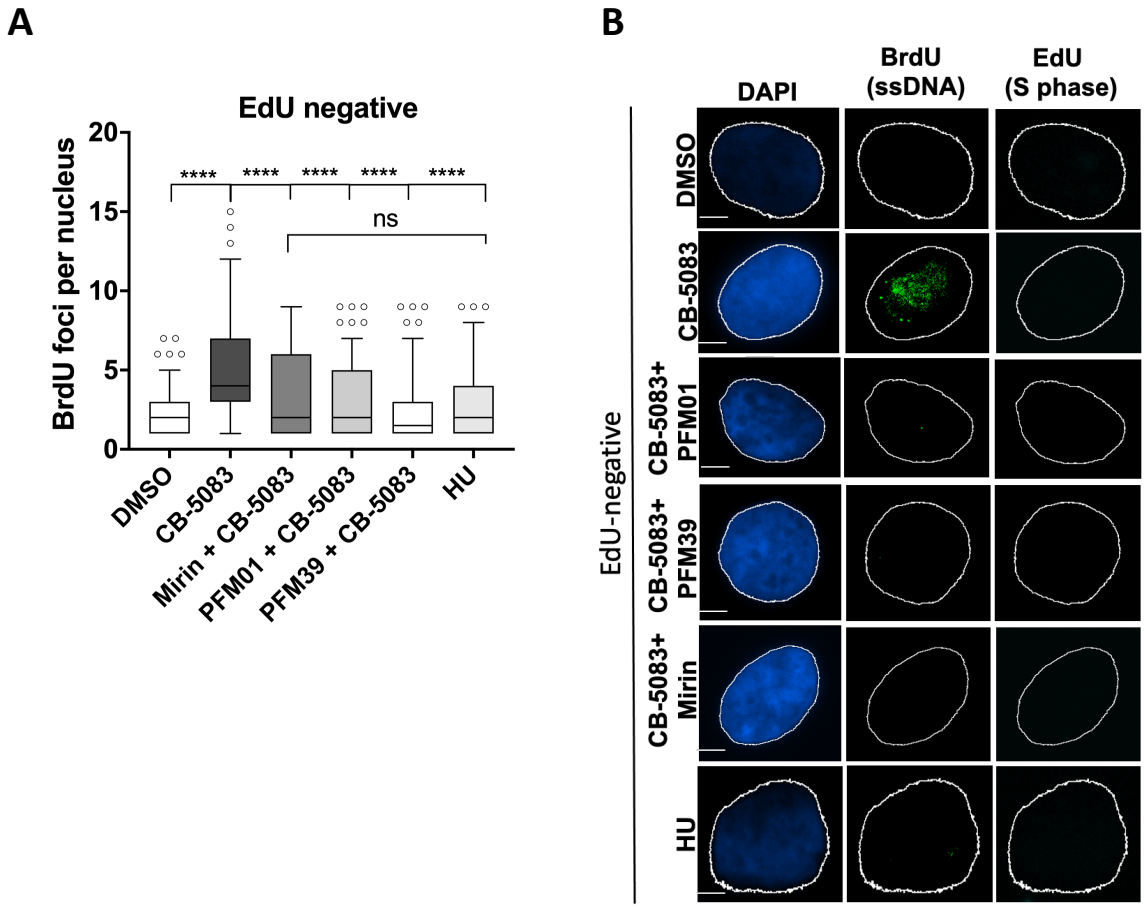


Figure 25 MRE11 endo- and exonuclease inhibitors rescue CB-5083-induced excessive ssDNA generation in cells outside S phase.

A) Number of BrdU foci in EdU-negative T24 cells after treatment with CB-5083 in combination with specific MRE11 inhibitors: MRE11 complex inhibitor Mirin; the endonuclease inhibitor PFM01; the exonuclease inhibitor PFM39. Hydroxyurea (HU) serves as a negative control. Data is shown as box-and-whiskers plot with interquartile range and 5th-95th percentiles. Values beyond 5th and 95th percentiles are plotted as individual data points. At least 60 individual cells were counted per repeat and condition. The data is representative of 2 independent biological experiments. Statistical analysis: Kruskal-Wallis test with Dunn's multiple comparisons. NS, not significant; **** p≤0.0001.
B) Representative images are shown. Scale bar: 5 µm.

To confirm that the phenotypes seen with p97 inhibition also hold true when p97 is depleted by siRNA, T24 cells were either treated with sip97, siMRE11, or both, and ssDNA accumulation was studied in EdU-positive (Figure 26 A-C) and -negative cells (Figure 27 A and B), similarly to p97 and MRE11 inhibited conditions. Treatment of cells with siRNA against p97 caused ssDNA foci accumulation similarly to p97-inhibited conditions, which was rescued upon co-depletion of MRE11, confirming the specificity of the results seen with inhibitors.

To further prove that the increased ssDNA foci formation is due to MRE11 nuclease activities and not due to off-target effects of p97 and MRE11 inhibitors, the BrdU assay was repeated upon depletion of the EXO1 nuclease, a nuclease acting downstream of MRE11 that is involved in long-range DNA resection away from the break sites (in 5'-3' direction) (Ceccaldi et al., 2016, Garcia et al., 2011). For this, cells were depleted of p97, MRE11 or EXO1 by siRNA, and ssDNA generation was monitored either with or without IR in both EdU-positive (Figure 28 A-C; Figure 30 A and B) and EdU-negative (Figure 29 A and B; Figure 31 A and B) T24 cells. For IR-induced DNA damage, cells were recovered over 1 hour or 8 hours after 2 Gy IR (Figure 30 A and B; Figure 31 A and B).

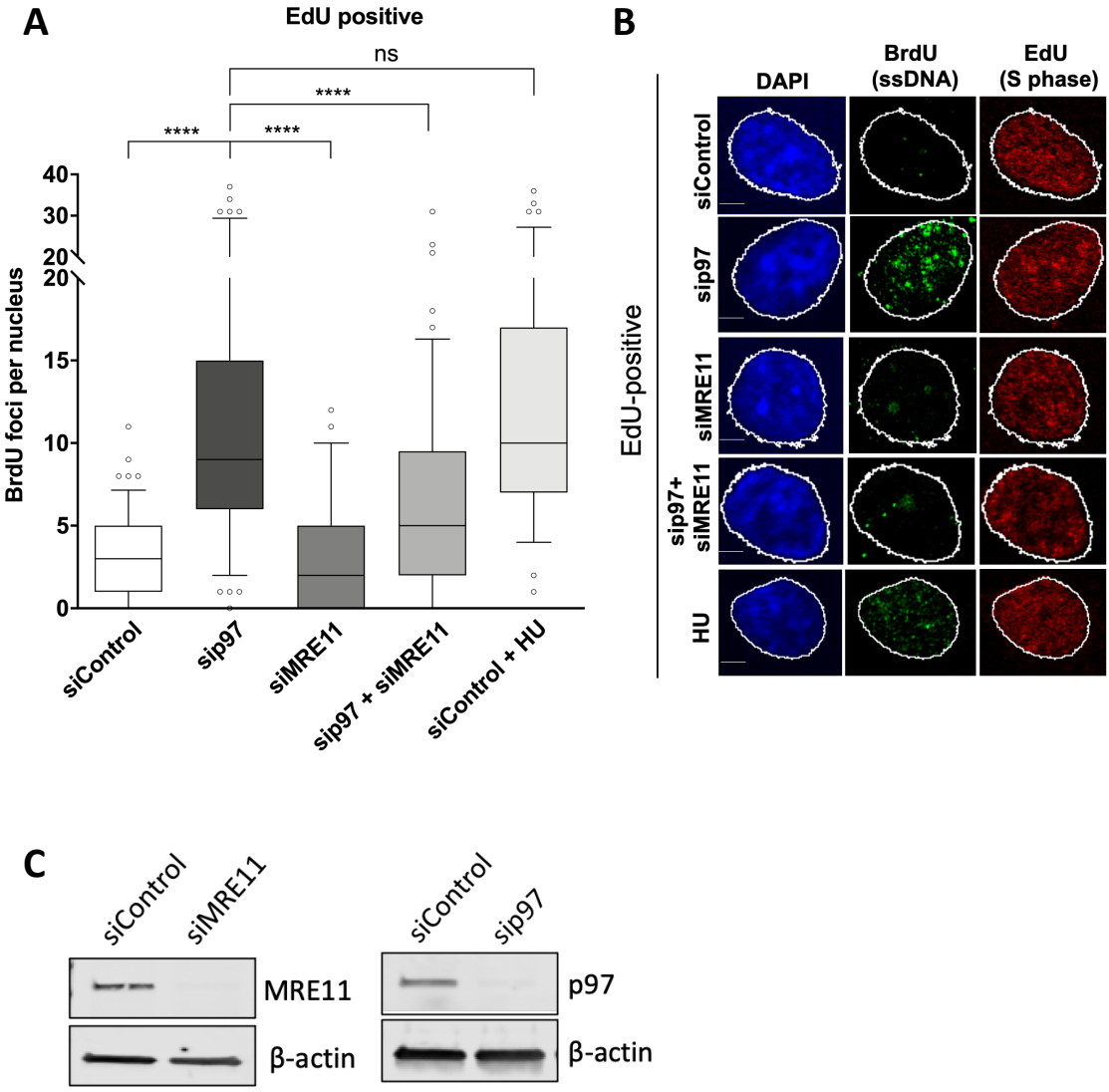


Figure 26 Depletion of p97 by siRNA causes excessive MRE11-mediated DNA end resection in S phase cells.

A) Number of BrdU foci in EdU-positive T24 cells after siRNA-mediated p97 depletion, or in combination with siRNA-mediated MRE11 depletion. Hydroxyurea (HU) serves as a positive control. Data is shown as box-and-whiskers plot with interquartile range and 5th-95th percentiles. Values beyond 5th and 95th percentiles are plotted as individual data points. At least 60 individual cells were counted per repeat and condition. The data is representative of 2 independent biological experiments. Statistical analysis: Kruskal-Wallis test with Dunn's multiple comparisons. NS, not significant; **** p≤0.0001. **B)** Representative images are shown. Scale bar: 5 µm. **C)** Western Blots confirming knockdown of MRE11 and p97. Beta-actin is loading control.

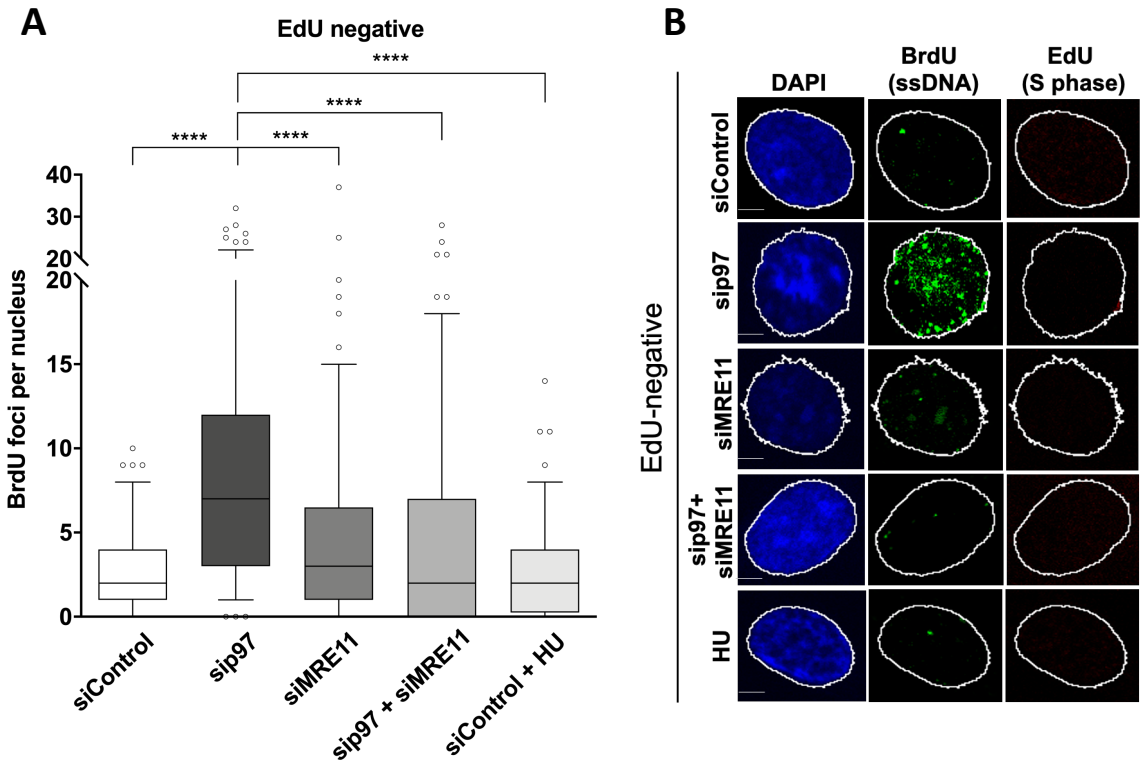


Figure 27 Depletion of p97 by siRNA causes excessive MRE11-mediated DNA end resection in cells outside S phase.

A) Number of BrdU foci in EdU-negative T24 cells after siRNA-mediated p97 depletion (10 nM; 48 hours), or in combination with siRNA-mediated MRE11 depletion (10 nM; 48 hours). Hydroxyurea (HU) serves as a negative control. Data is shown as box-and-whiskers plot with interquartile range and 5th-95th percentiles. Values beyond 5th and 95th percentiles are plotted as individual data points. At least 60 individual cells were counted per repeat and condition. The data is representative of 2 independent biological experiments. Statistical analysis: Kruskal-Wallis test with Dunn's multiple comparisons. NS, not significant; **** p≤0.0001. **B)** Representative images are shown. Scale bar: 5 µm.

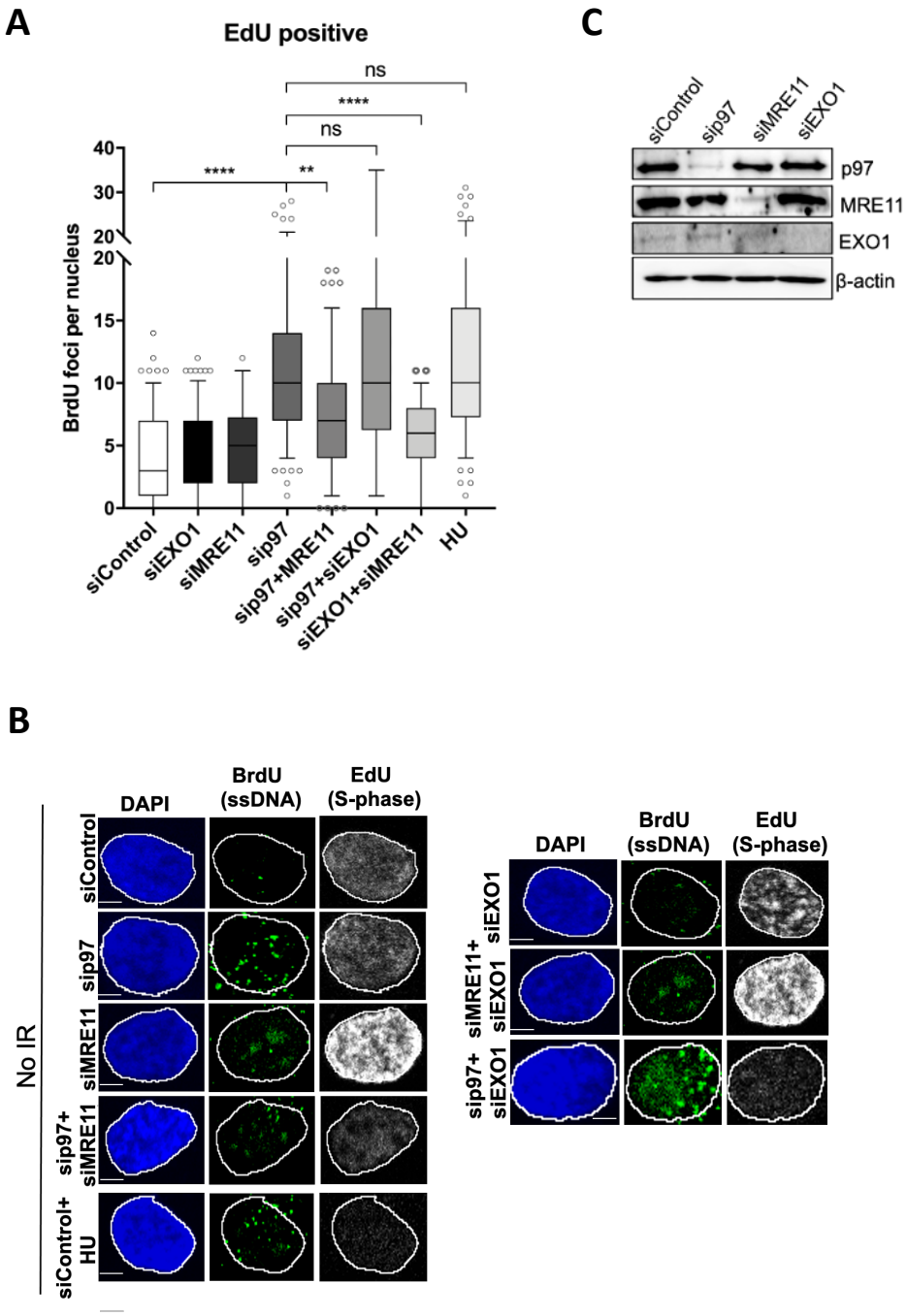


Figure 28 Depletion of p97 by siRNA causes excessive MRE11-mediated DNA end resection independently of EXO1 in S phase cells.

A) Number of BrdU foci in EdU-positive T24 cells after p97, MRE11 and EXO1 depletion. Hydroxyurea (HU) serves as a positive control. Data is shown as box-and-whiskers plot with interquartile range and 5th-95th percentiles. Values beyond 5th and 95th percentiles are plotted as individual data points. At least 60 individual cells were counted per repeat and condition; n=3 independent experiments. Statistical analysis: Kruskal-Wallis test with Dunn's multiple comparisons. NS, not significant; ** $p<0.01$; **** $p\leq0.0001$. **B)** Representative images are shown. Scale bar: 5 µm. **C)** Western Blot confirming depletion of p97, MRE11 and EXO1. Beta-actin is loading control.

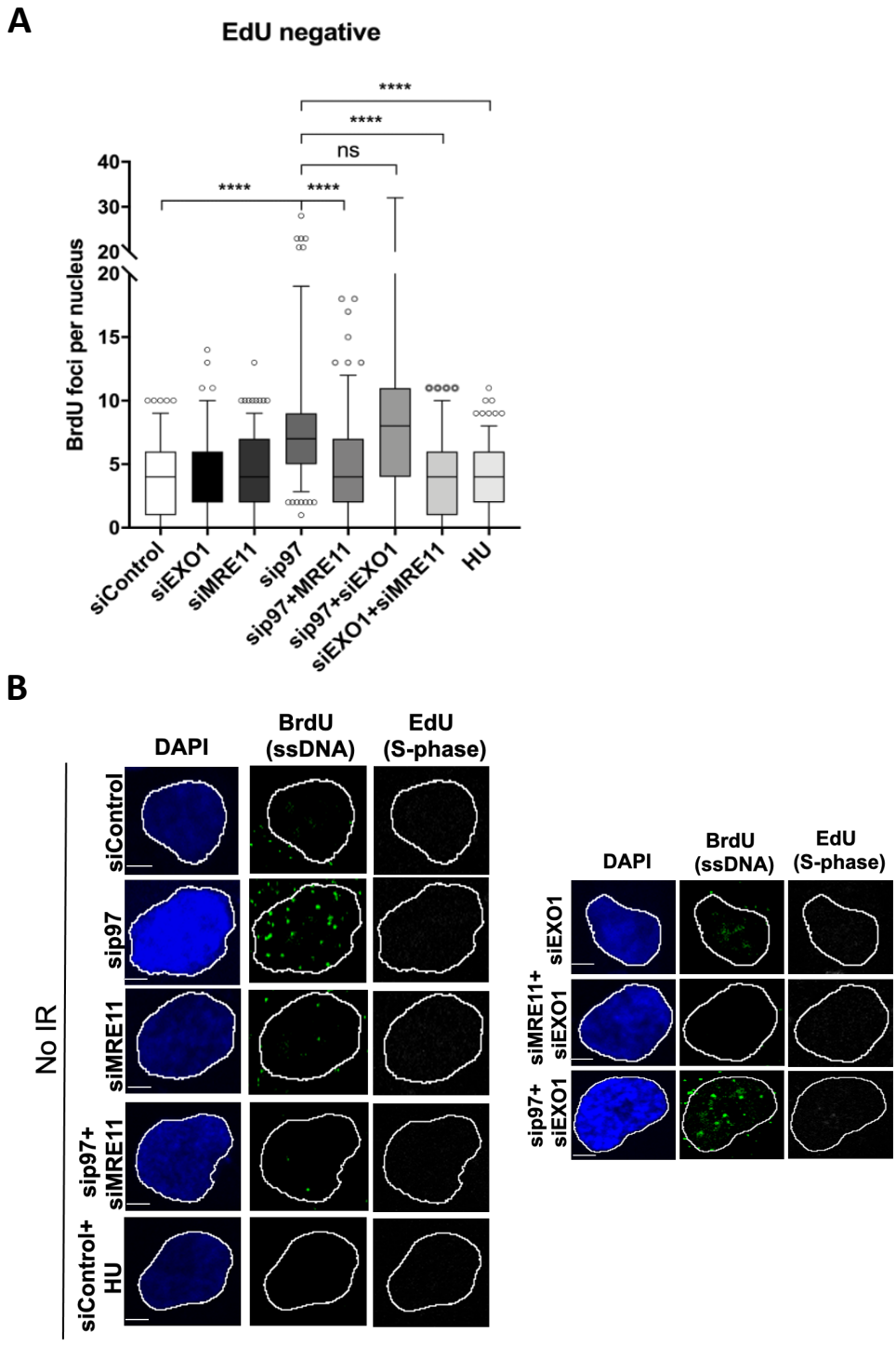


Figure 29 Depletion of p97 by siRNA causes excessive MRE11-mediated DNA end resection independently of EXO1 in cells outside S phase.

A) Number of BrdU foci in EdU-negative T24 cells after p97, MRE11 and EXO1 depletion. Hydroxyurea (HU) serves as a negative control. Data is shown as box-and-whiskers plot with interquartile range and 5th-95th percentiles. Values beyond 5th and 95th percentiles are plotted as individual data points. At least 60 individual cells were counted per repeat and condition; n=3 independent experiments. Statistical analysis: Kruskal-Wallis test with Dunn's multiple comparisons. NS, not significant; **** p≤0.0001. **B)** Representative images are shown. Scale bar: 5 µm.

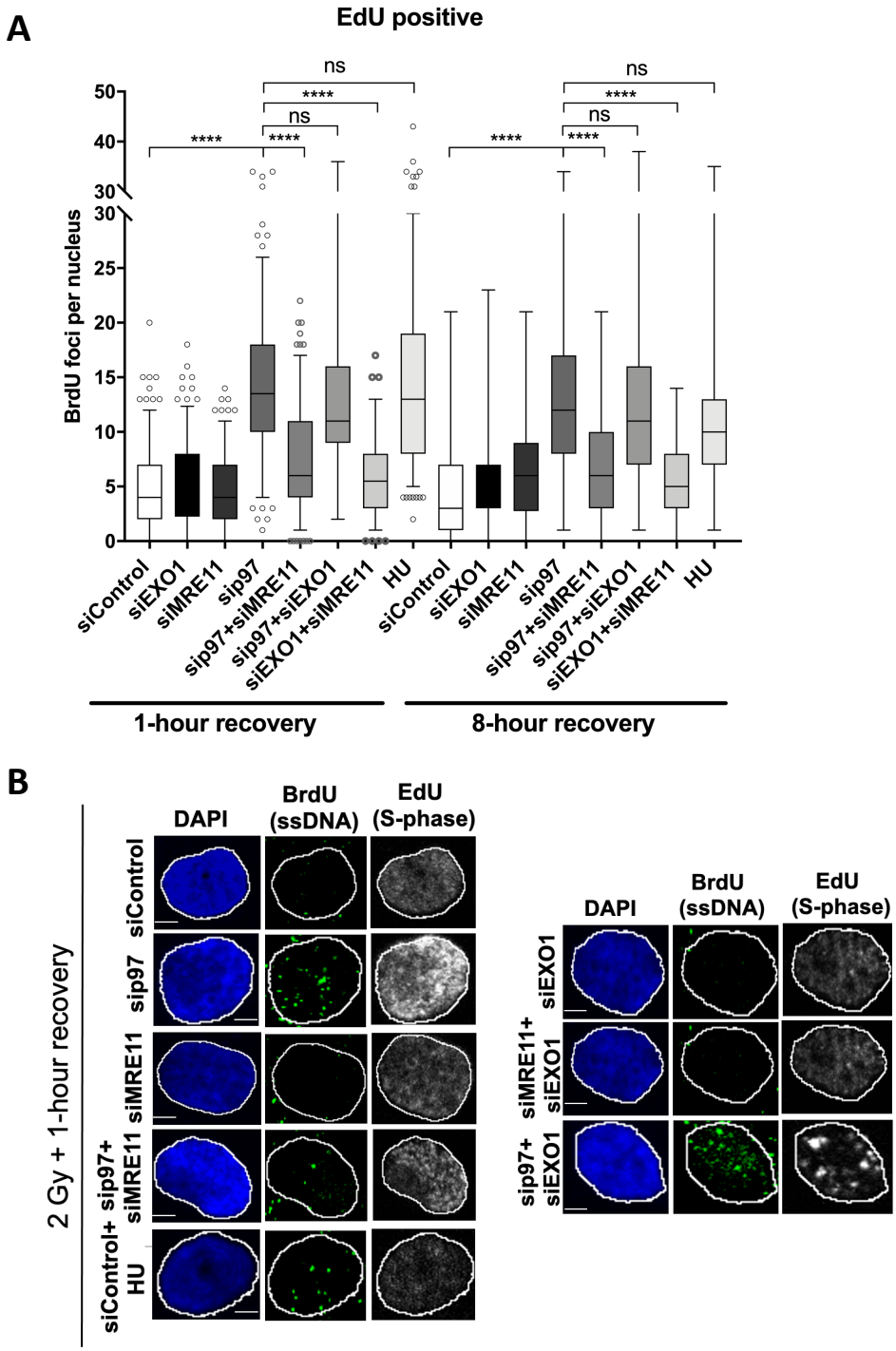


Figure 30 Depletion of p97 by siRNA causes excessive MRE11-mediated DNA end resection after IR independently of EXO1 in S phase cells.

A) Number of BrdU foci in EdU-positive T24 cells after p97, MRE11 and EXO1 depletion. Cells were irradiated at 2 Gy and recovered over 8 hours. Hydroxyurea (HU) serves as a positive control. Data is shown as box-and-whiskers plot with interquartile range and 5th-95th percentiles. Values beyond 5th and 95th percentiles are plotted as individual data points. At least 60 individual cells were counted per repeat and condition; n=3 independent experiments. Statistical analysis: Kruskal-Wallis test with Dunn's multiple comparisons. NS, not significant; ** p<0.01; *** p≤0.001; **** p≤0.0001. **B)** Representative images are shown. Scale bar: 5 µm.

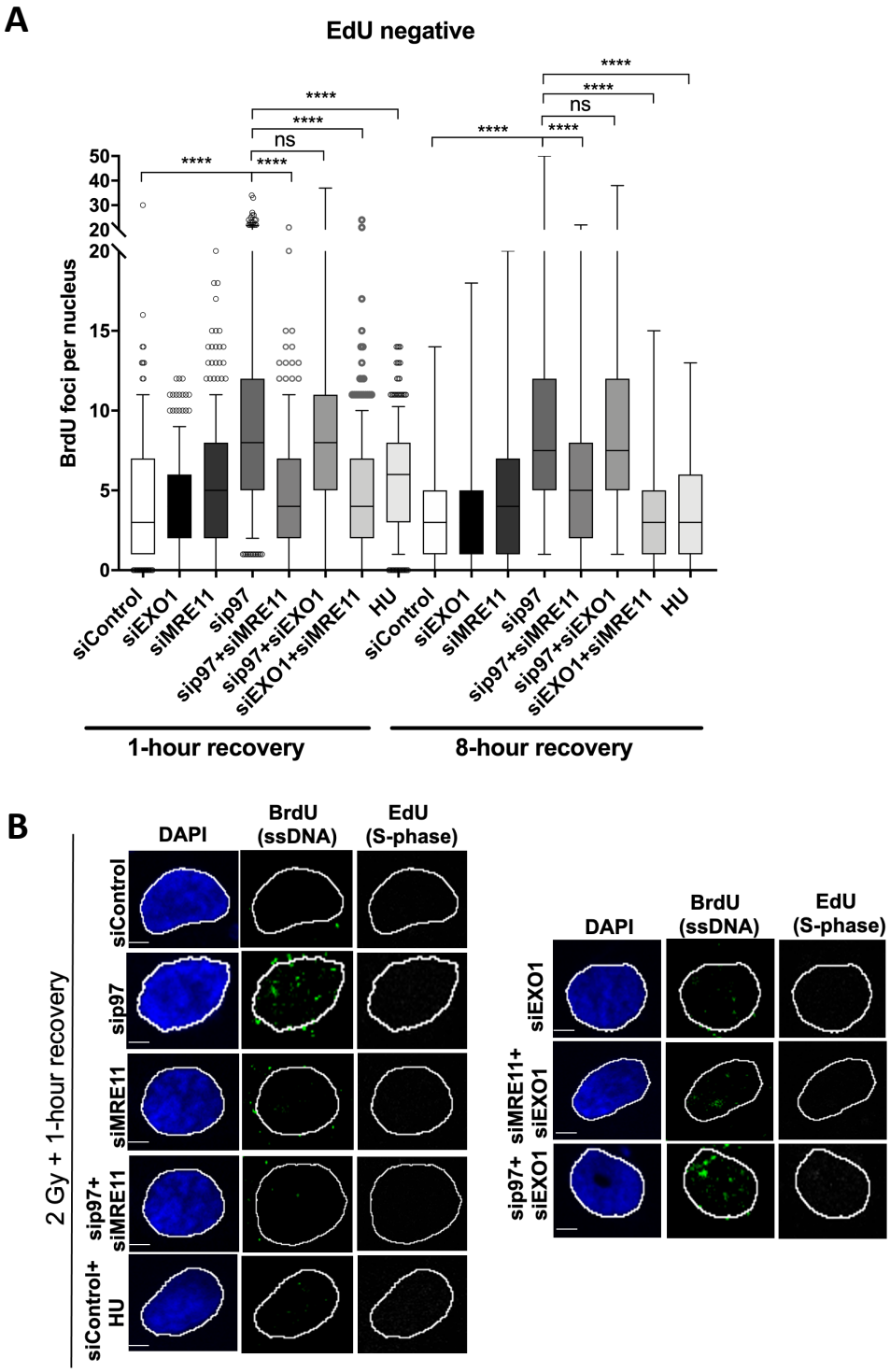


Figure 31 Depletion of p97 by siRNA causes excessive MRE11-mediated DNA end resection after IR independently of EXO1 in cells outside S phase.

A) Number of BrdU foci in EdU-negative T24 cells after p97, MRE11 and EXO1 depletion. Cells were irradiated at 2 Gy and recovered over 8 hours. Hydroxyurea (HU) serves as a negative control. Data is shown as box-and-whiskers plot with interquartile range and 5th-95th percentiles. Values beyond 5th and 95th percentiles are plotted as individual data points. At least 60 individual cells were counted per repeat and condition; n=3 independent experiments. Statistical analysis: Kruskal-Wallis test with Dunn's multiple comparisons. NS, not significant; * $p<0.05$; *** $p\leq0.001$; **** $p\leq0.0001$. **B)** Representative images are shown. Scale bar: 5 µm.

Single-stranded DNA is coated and protected by the ssDNA-binding protein RPA (Nimonkar et al., 2011, Chen and Wold, 2014), which is therefore used as a readout of end resection. The number of nuclear RPA foci were determined in T24 cells upon 2 Gy IR and over an 8-hour recovery period in CB-5083- or DMSO control-treated cells. Inhibiting p97 caused an increase in total nuclear RPA foci number over 8 hours compared to control cells, which agrees with the results using the BrdU assay (Figure 32 A and B). Only S phase cells were quantified to exclude variations from cell cycle changes.

It has been reported that phosphorylation of RPA can negatively regulate BLM helicase and DNA end resection by establishing a negative feedback loop between resection initiation and termination (Soniat et al., 2019). Therefore, it was investigated whether phosphorylation of RPA is inhibited in the absence of p97, as p97 inhibition was shown to cause DNA hyper-resection. Phosphorylated RPA (at serine 4/serine 8) levels were studied after 2 Gy IR and p97 inhibition by 10 µM CB-5083 in S phase T24 cells. As expected, phosphorylated RPA did not accumulate to the same extent as total RPA. Fewer overall nuclear foci were formed in CB-5083-treated conditions after IR compared to DMSO-treated conditions (Figure 33 A and B). These results further support the previous findings and are in line with recent literature on RPA phosphorylation and DNA end resection control.

The effect of MRE11-dependent ssDNA accumulation upon p97 inactivation was shown to be independent of EXO1 nuclease activity in the specific BrdU assay used here. It is possible, however, that the phenotype observed in these conditions is dependent on another long-range resection pathway, specifically the DNA2-BLM-mediated pathway. It has been shown that the MRN complex promotes DNA2 exonuclease activities by recruiting BLM to DNA ends, which is needed for DNA2 exonuclease function (Nimonkar et al., 2011). Furthermore, EXO1 activity is stimulated by BLM (Nimonkar et al., 2008). Therefore, it would be useful to study both the DNA2 and BLM dependency on MRE11-mediated excessive end resection in p97 inactivated conditions. Overall, these results indicate that the absence of p97 causes excessive 5'-DNA end resection mediated by MRE11 nuclease, which is caused by the accumulation of MRE11 on chromatin and DNA damage sites.

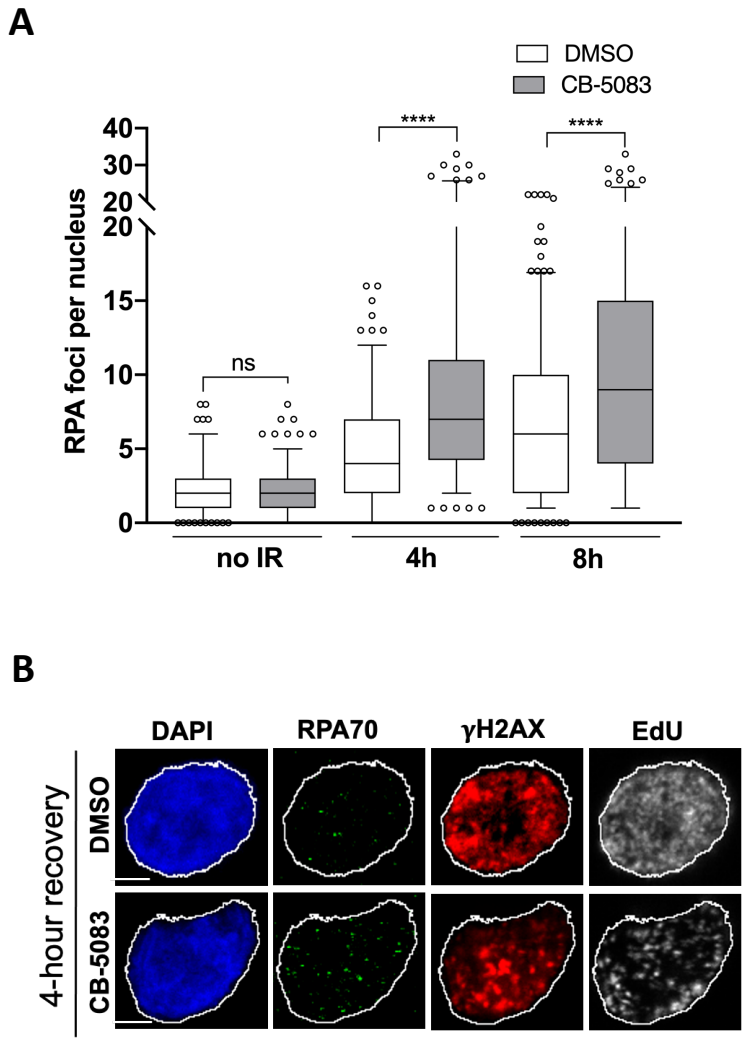


Figure 32 Inhibition of p97 causes nuclear RPA foci accumulation upon IR.
A) Number of EdU-positive RPA70 foci over 8 hours of recovery from 2 Gy IR in DMSO- or CB-5083-treated T24 cells. Data is presented as a box-and-whiskers plot, and values beyond the 5th and 95th percentiles are shown as individual data points. Statistical analysis: Mann-Whitney test. At least 60 individual cells were counted per repeat and condition; n=3 independent experiments. NS, not significant; **** p≤0.0001 **B)** Representative images shown at 4 hours after IR. The staining for γH2AX differs from Figure 15 and 16, as these images were taken on another confocal microscope (Zeiss 780 instead of Zeiss 710). Furthermore, these experiments were conducted at separate times and analysed on Fiji using different threshold settings than for Figures 15 and 16. Please refer to Methods chapter 2.7. for further information. Scale bar: 5 µm.

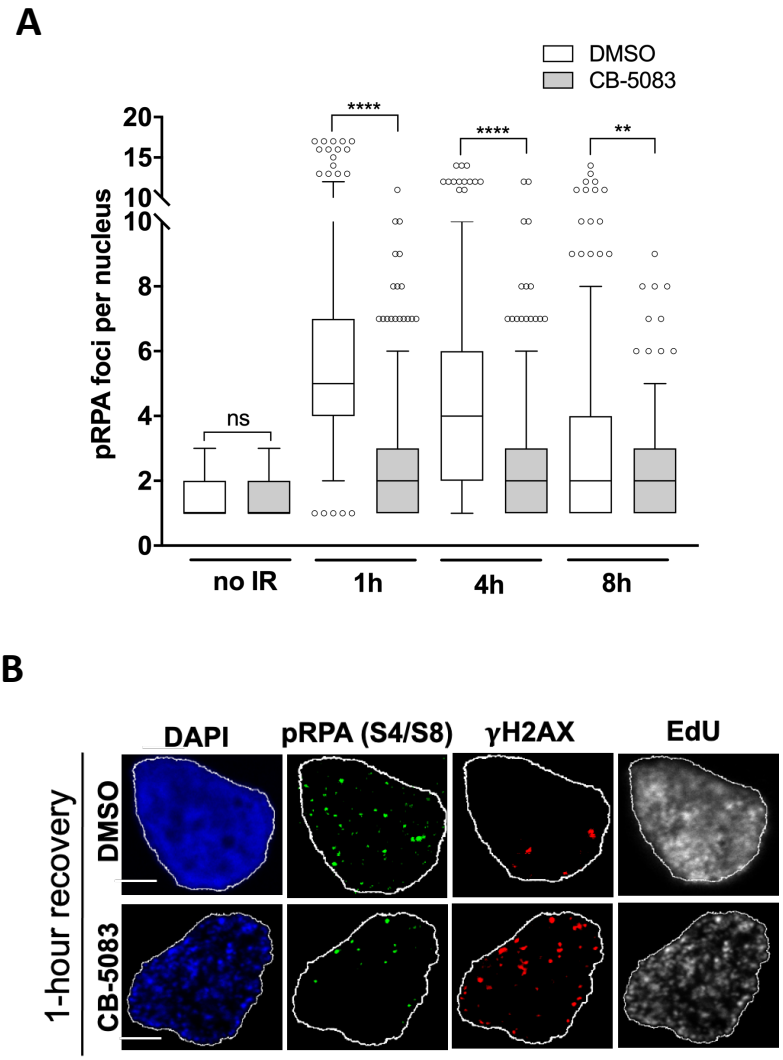


Figure 33 Inhibition of p97 leads to a decrease in phosphorylated RPA (S4/S8) foci.
A) Number of phosphorylated RPA (S4/S8) nuclear foci after 2 Gy IR in DMSO- and CB-5083-treated conditions. The graph shows a box-and-whiskers plot with interquartile range. Values beyond 5th and 95th percentiles are plotted as individual values. At least 60 individual cells were counted per repeat and condition; n=3 independent experiments. Statistical analysis: Mann-Whitney test. NS, not significant; ** p≤0.01; **** p≤.0001. **B)** Representative images after 1 hour of 2 Gy IR. Scale bar: 5 µm.

4.2. Inhibition of p97 causes a switch from error-free RAD51-mediated HR repair to RAD52-mediated SSA repair

Since the balance of DNA end resection is mediated by a balance between RAD51- and RAD52-mediated repair (Ceccaldi et al., 2016, Ochs et al., 2016), it was next studied whether there is a switch from RAD51-mediated repair to RAD52-mediated repair in p97-inhibited conditions by analysing the number of RAD51 and RAD52 nuclear foci after 2 Gy IR and treatment with CB-5083. Compared to DMSO control cells, p97 inhibition caused a decrease in the formation of RAD51 nuclear foci over 8 hours of recovery from IR (Figure 34 A and B), whereas an opposite trend was observed with RAD52 foci, which was shown to increase upon CB-5083 treatment (Figure 35 A and B). In summary, these results demonstrate that p97 inhibition leads to defective RAD51 recruitment to DNA damage sites, whereas RAD52 recruitment is upregulated.

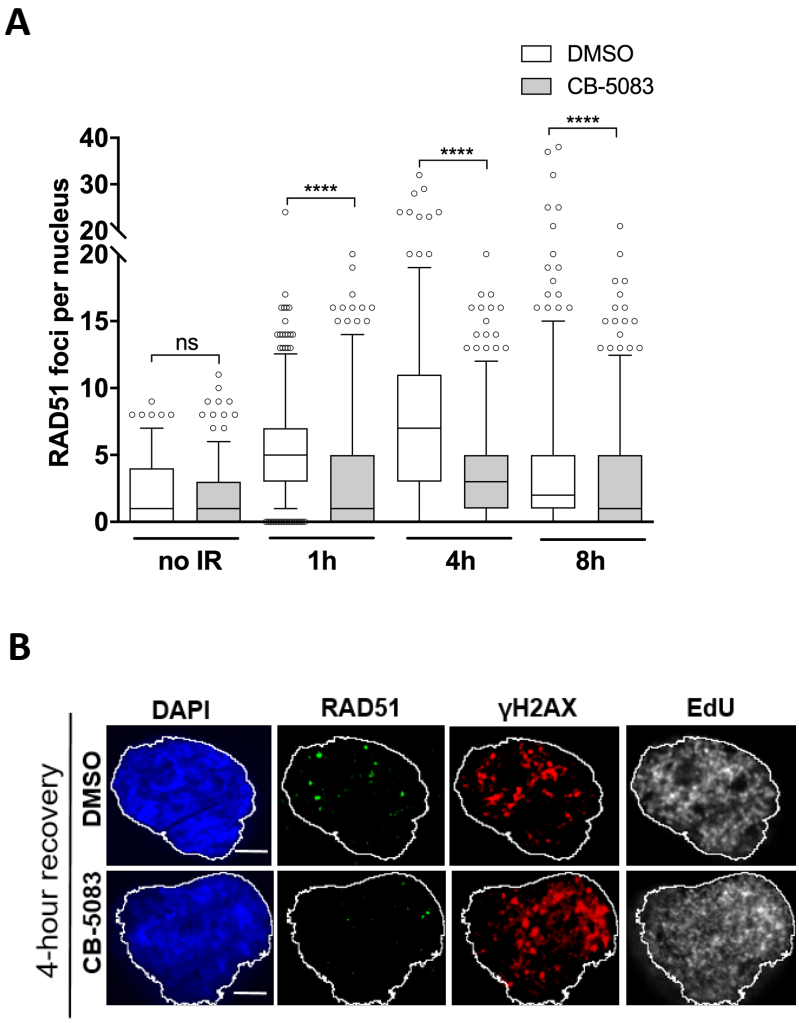


Figure 34 p97 inhibition decreases nuclear RAD51 foci after IR.
A) The number of RAD51 foci among EdU-positive T24 cells after 2 Gy IR and CB-5083 treatment. The graph is a box-and-whiskers plot with 5th and 95th percentiles. Values beyond these percentiles are shown as individual data points. At least 60 individual cells were counted per repeat and condition; n=3 independent experiments. Statistical test: Mann-Whitney test. NS, not significant; **** p≤.0001.
B) Representative images after 4 hours of recovery from 2 Gy IR. Scale bar: 5 µm.

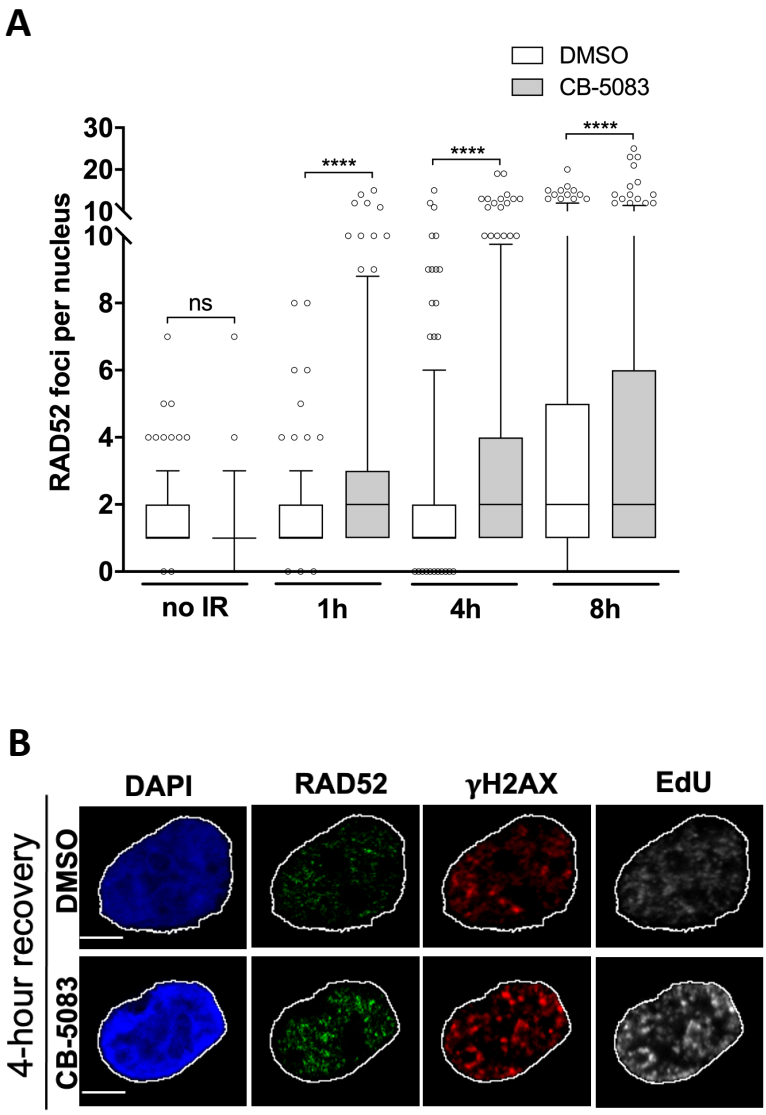


Figure 35 Inhibition of p97 leads to an increase in nuclear RAD52 foci after IR. **A)** RAD52 foci in EdU-positive T24 cells upon 2 Gy IR and CB-5083 treatment. The graph shows a box-and-whiskers plot with interquartile range. Values beyond 5th and 95th percentiles are plotted as individual points. At least 60 individual cells were counted per repeat and condition; n=3 independent experiments. Statistical test: Mann-Whitney test. NS, not significant; **** p≤.0001. **B)** Representative images after 4 hours of recovery from 2 Gy IR. Scale bar: 5 µm.

RAD51 is commonly used as a readout of HR-mediated repair and RAD52 is a marker for mutagenic SSA (Ochs et al., 2016, Bhargava et al., 2016), suggesting that there is an upregulation of mutagenic RAD52-mediated SSA in cells with inhibited p97 function. Another possibility would be that RAD52 is a direct target of p97. However, data from the SILAC-based MS screen of the p97 interactome after IR (related to Figure 13; unpublished data from Prof Kristijan Ramadan's lab) did not identify RAD52 as a potential p97 interaction partner. RAD52 was also absent in another recently conducted label-free quantification (LFQ) MS screen of the p97 interactome in our lab (unpublished). Furthermore, data from an independent MS-based proteomic screen characterising p97 interaction partners with or without the p97 inhibitor NMS873 did not identify RAD52 in the screen (Xue et al., 2016). To demonstrate that RAD52 is not a direct target of p97, MRE11 could be overexpressed to see whether cells show an increase in IR-induced RAD52 foci. Alternatively, targeting the Shieldin complex components or 53BP1 should lead to an increase in RAD52 foci.

Next, to measure DSB repair pathway choice quantitatively, direct-repeat (DR) HR and SSA GFP-based reporter assays were used. Specific DSBs were created by expressing I-SceI nuclease in the DR-GFP (HR repair) and SA-GFP (SSA repair) U2OS constructs. Inhibition of p97 by CB-5083 (10 μM) caused approximately a 40% decrease in HR-mediated repair efficiency compared to the I-SceI-treated positive control cells which were normalised to 100% (Figure 36 A-D), demonstrating that p97 is needed for efficient HR as previously published (Meerang et al., 2011, Singh et al., 2019, van den Boom et al., 2016). RAD51 knockdown by siRNA was used as a control affecting the HR pathway. These results were confirmed by siRNA depletion of p97 (Figure 37 A-C), which caused around a 60% decrease in HR-mediated repair. On the contrary, inhibiting p97 with CB-5083 (10 μM) increased SSA repair capacity for around 30% compared to I-SceI-treated positive control (* $p<0.05$) (Figure 38 A-D). Inactivation of RAD52 by siRNA-mediated knockdown was used as a control for decreased SSA. Overall, these results confirm that SSA-mediated repair becomes more active in an HR-deficient background in p97 inactivated cells.

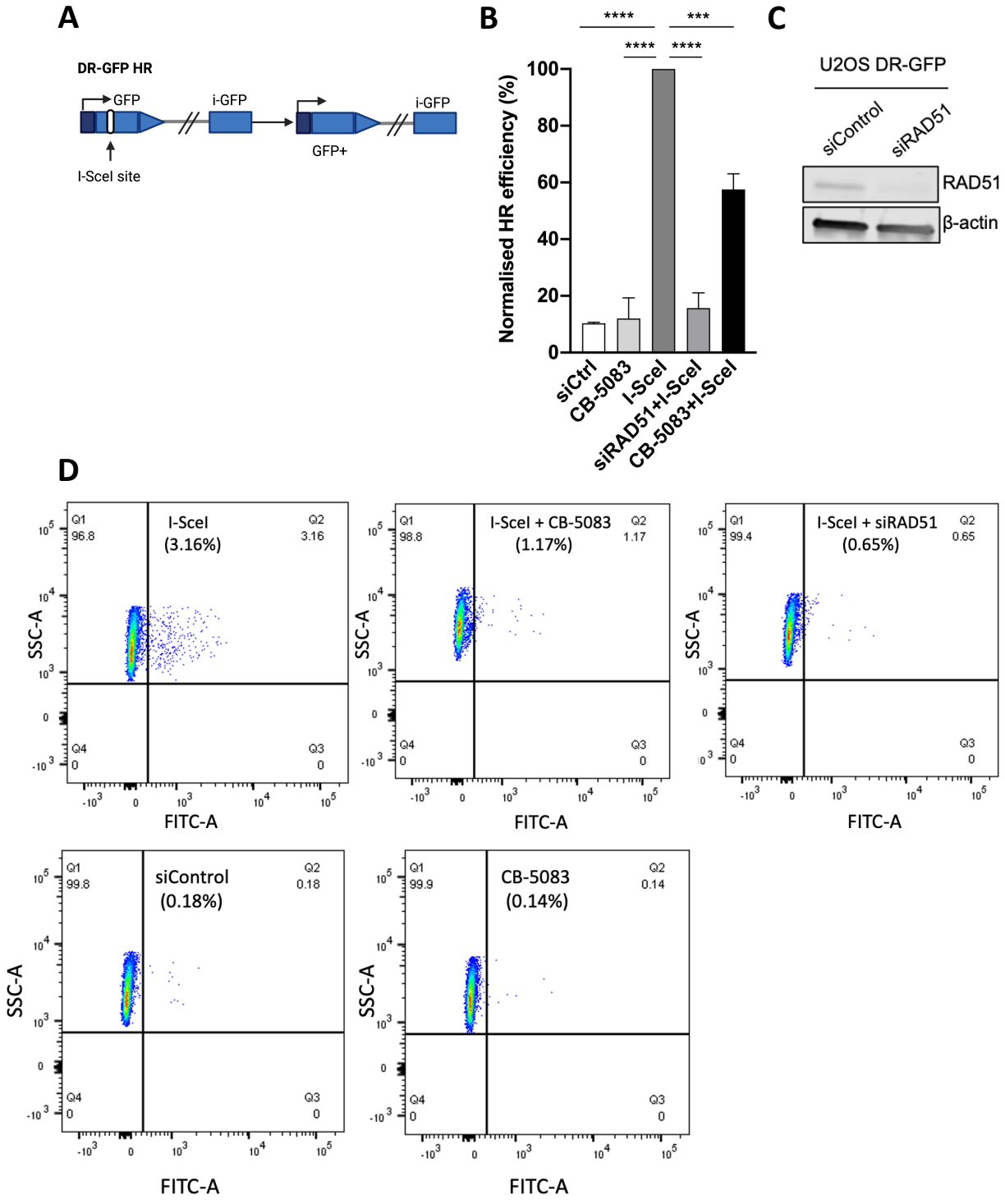


Figure 36 Inactivation of p97 compromises HR-mediated repair.

A) I-SceI-based DR-GFP construct used to measure HR repair efficiency. **B)** U2OS DR-GFP cells were treated with CB-5083 for 6 hours and transfected with I-SceI plasmid overnight to induce DNA breaks. HR repair was measured by FACS where GFP positivity is a readout of HR efficiency. Data is normalised to I-SceI positive control. RAD51 knockdown serves as an internal control that shows a decrease in HR compared to the positive control I-SceI. Statistical analysis: one-way ANOVA with Dunnett's multiple comparisons. *** p≤0.001; **** p≤0.0001; n=3 independent experiments. **C)** Western blots showing RAD51 and p97 knockdown efficiency. Beta actin serves as a positive control. **D)** An example of raw FACS data from a single experiment. The percentage of GFP-positive cells are indicated in brackets. FITC-A shows forward scatter area and SSC-A shows side scatter area. At least 10,000 events were acquired per experiment per condition.

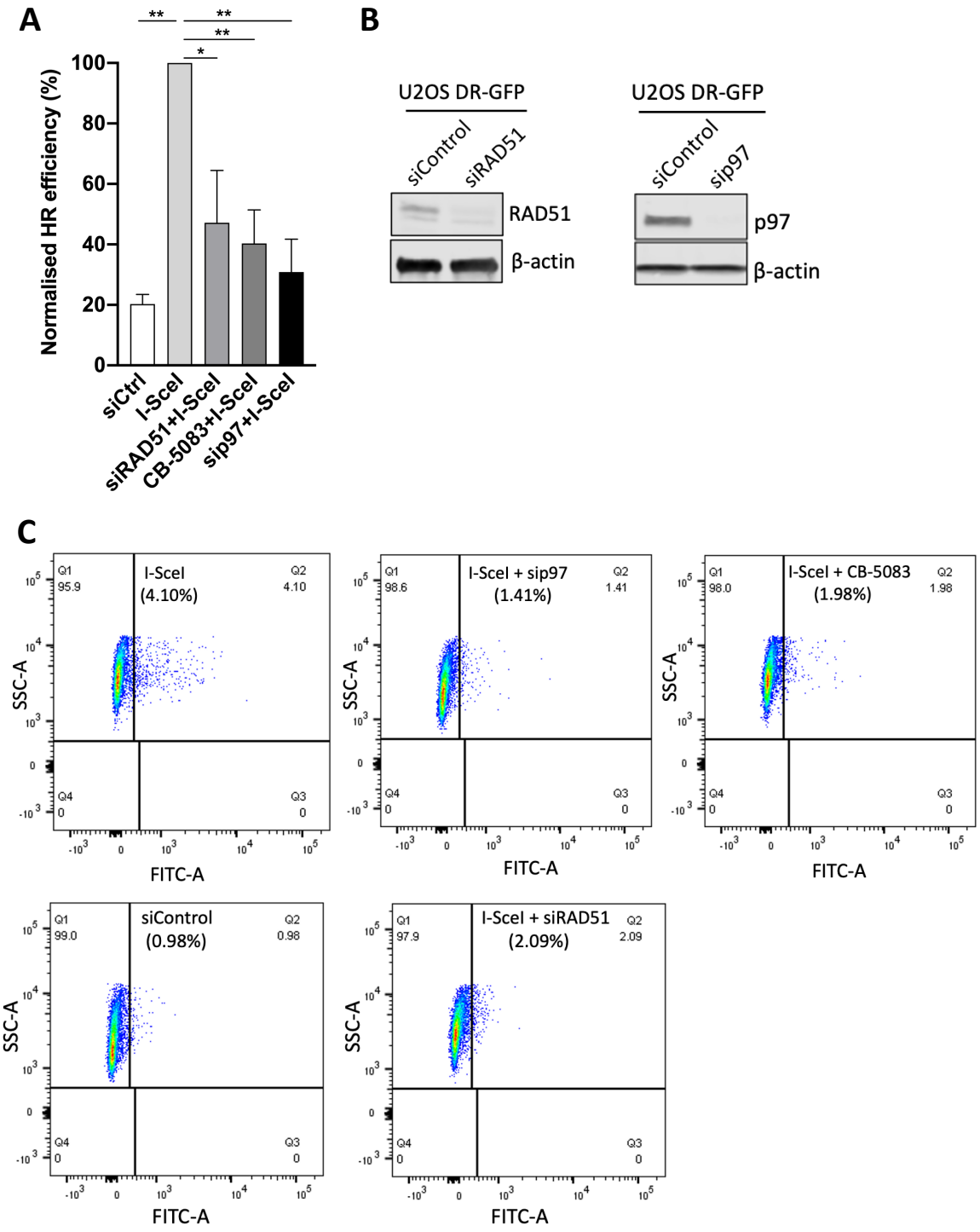


Figure 37 Depletion of p97 compromises HR-mediated repair.
A) U2OS DR-GFP cells were transfected with I-SceI plasmid to induce double-strand breaks. Cells were treated with CB-5083 for 6 hours or siRNA against p97 (10 nM; 48 hours), and HR repair was monitored by measuring GFP positive cells. RAD51 knockdown serves as an internal control that shows a decrease in HR compared to the positive control I-SceI. Statistical analysis: one-way ANOVA with Dunnett's multiple comparisons. * p≤0.05; ** p≤0.01; n=3 independent experiments. **B)** Western blots showing RAD51 and p97 knockdown efficiency. Beta actin serves as a positive control. **C)** An example of raw FACS data from a single experiment. The percentage of GFP-positive cells are indicated in brackets. FITC-A shows forward scatter area and SSC-A shows side scatter area. At least 10,000 events were acquired per experiment per condition.

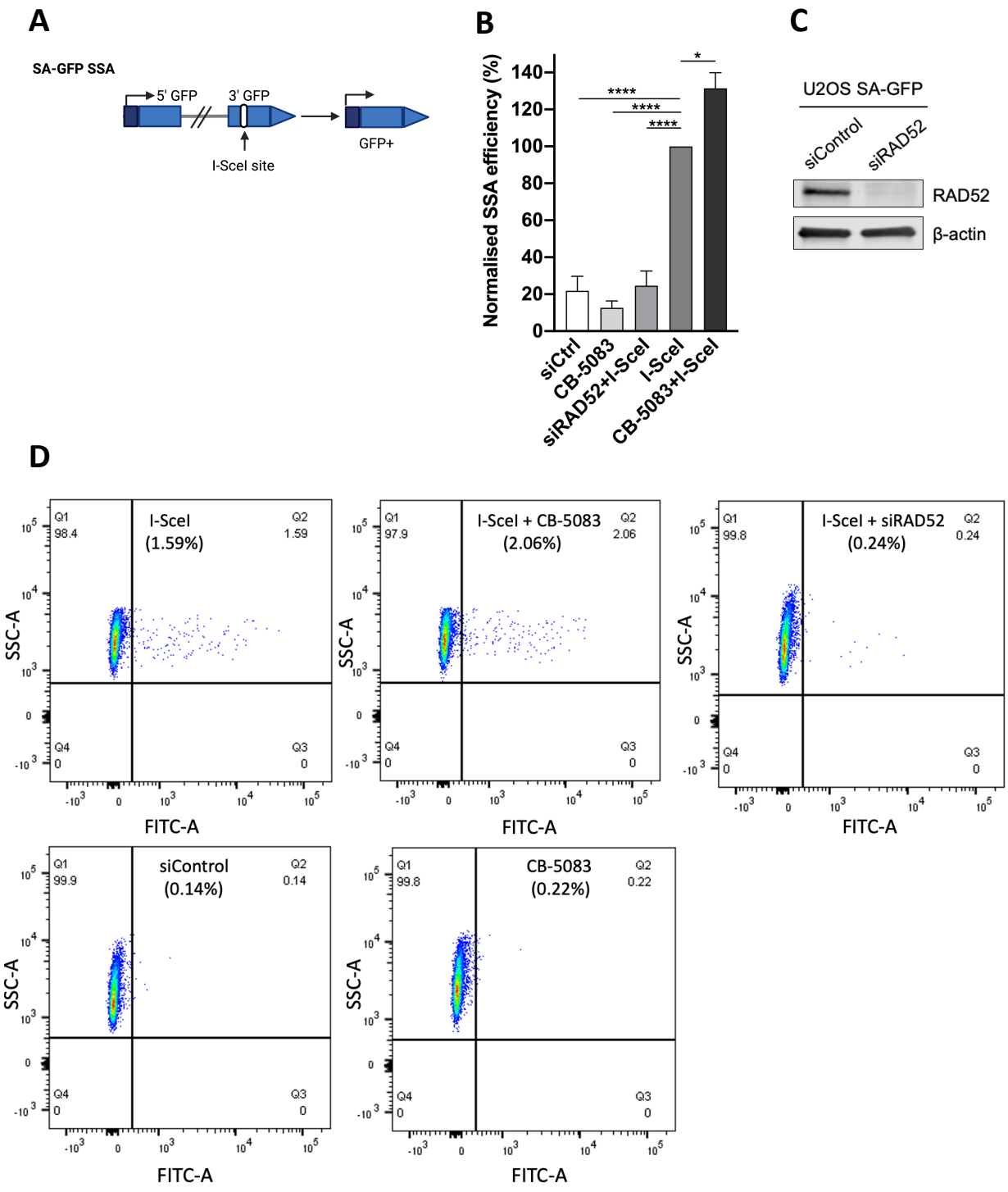


Figure 38 p97 inhibition increases SSA repair.

A) I-SceI-based SA-GFP construct used to measure SSA repair efficiency. **B)** U2OS SA-GFP cells were treated as in Figure 36, apart from using RAD52 knockdown as an internal control for SSA repair efficiency. GFP positive cells were measured by FACS and indicate that SSA is actively taking place. Results were normalised to I-SceI-transfected cells that serve as positive control; n=4 independent experiments. Statistical analysis: one-way ANOVA with Dunnett's multiple comparisons: * p≤0.05; **** p≤0.0001. **C)** Western blot showing knockdown of RAD52. Beta actin is used as loading control. **D)** An example of raw FACS data from a single experiment. The percentage of GFP-positive cells are indicated in brackets. FITC-A shows forward scatter area and SSC-A shows side scatter area. At least 10,000 events were acquired per experiment per condition.

Overall, the results from this chapter demonstrate that p97 inhibition or siRNA depletion causes the formation of excessive ssDNA foci, which is dependent on MRE11-mediated end resection and independent of the downstream long-range nuclease EXO1. Nevertheless, considering that MRE11 resection is responsible for a relatively short-range resection up to a couple of hundred bases (Garcia et al., 2011, Daley et al., 2015), it is possible that the MRE11-mediated end resection phenotype by BrdU assay is dependent on another long-range resection pathway, such as the DNA2-BLM pathway. Therefore, in future work it would be important to also determine the dependency of this phenotype on DNA2-BLM-mediated resection. Inhibition of p97 leads to an overall HR defect by decreasing RAD51 recruitment to IR-induced DNA damage, whereas there was an upregulation of RAD52 foci, indicating a change from HR-mediated repair to SSA-mediated repair. These results were quantitatively confirmed by assessing HR and SSA efficiency by FACS-based GFP reporter assays, showing HR defects both with p97 inhibition and depletion, and a subsequent increase in SSA-mediated repair. Furthermore, pathway choice between HR and SSA depends on the interaction between BRCA1 and PALB2, and mutations in either of these factors disrupting this interaction promotes SSA over HR (Anantha et al., 2017). Previously, research from our lab demonstrated that in addition to defective recruitment of 53BP1, depletion of p97 impairs the recruitment of BRCA1 to sites of DNA damage (Singh et al., 2019), supporting the observations that p97 inactivation leads to a defective/dysregulated HR pathway.

Other ways in which this system could be studied is to use fluorescently labelled DNA in combination with WT MRE11, WT p97 or p97-EQ mutant (defective in ATP hydrolysis), and study whether DNA end-resection is excessively taking place with a p97 substrate trapping mutant (ATPase deficient but binds and traps its substrates). Alternatively, DNA combing assay could be used to label BrdU under native conditions to visualise ssDNA fibers which could be quantified in both control and p97-inhibited conditions. Furthermore, more quantitative PCR (qPCR)-based methods can be used to measure single-stranded DNA (ssDNA) after p97 inactivation. To prove the specificity of MRE11 nuclease activities in this system, MRE11 nuclease deficient mutants could be created to study MRE11 in a more controlled manner compared to using inhibitors and siRNA depletion, which might have pleiotropic and off-target effects.

Chapter 5: Inactivation of p97 negatively regulates anti-resection factors and causes a delay in DNA DSB repair

Data from previous chapters demonstrated that inactivation of p97 either by inhibitors or siRNA-mediated depletion causes HR defects most likely caused by excessive MRE11-mediated nuclease activity and DNA end resection. Next, it was studied whether chemical inhibition of p97 with CB-5083 or siRNA-mediated depletion in combination with IR-induced DNA would cause sustained DNA damage, resulting in unrepairable DSBs and radiosensitisation. To better understand how the balance between resection factors and anti-resection factors in the context of p97 inactivation leads to DNA damage repair delay, the dynamics of two well-recognised DNA damage markers were studied after IR: 53BP1 and γH2AX. The number of 53BP1 and γH2AX nuclear foci were quantified after 2 Gy IR and repair was monitored over 24 hours of recovery in p97 siRNA-depleted cells (Figure 39 A-D). In line with previously published data, 53BP1 foci formation was significantly impaired in p97-depleted cells (Acs et al., 2011) at both time points (30 minutes and 4 hours) before 24-hour recovery (Figure 39 A and C).

In addition to being a marker for DSBs, 53BP1 is one of the core anti-resection DNA repair factors promoting NHEJ over resection-dependent HR (Ghezraoui et al., 2018), and functions by counteracting DNA end resection by limiting access of nucleases to DNA ends (Ghezraoui et al., 2018, Dev et al., 2018), which supports the observations that p97 depletion creates a hyper-resection phenotype in cells, and this most likely counteracts the NHEJ-promoting anti-resection factors. Interestingly, despite the initial recruitment defect of 53BP1 to sites of IR-induced foci in p97 depleted cells, 53BP1 was more persistent on DNA damage at 24 hours of recovery from IR in p97 depleted cells, compared to DMSO control cells. This could be due to persistence of DNA damage and a general ´DNA damage repair delay. To confirm this, the number of γH2AX nuclear foci were quantified after 2 Gy IR and 24 hours of recovery (Figure 39 B-D). There was a significant DNA DSB repair delay at 24 hours in p97 depleted cells, measured by significantly increased γH2AX foci compared to control, whereas there were no significant changes in γH2AX foci at earlier time points. These results were further confirmed using the p97 small molecule inhibitor CB-5083 (10 μM), which phenocopied the results of siRNA-mediated depletion of p97 (Figure 40 A-C).

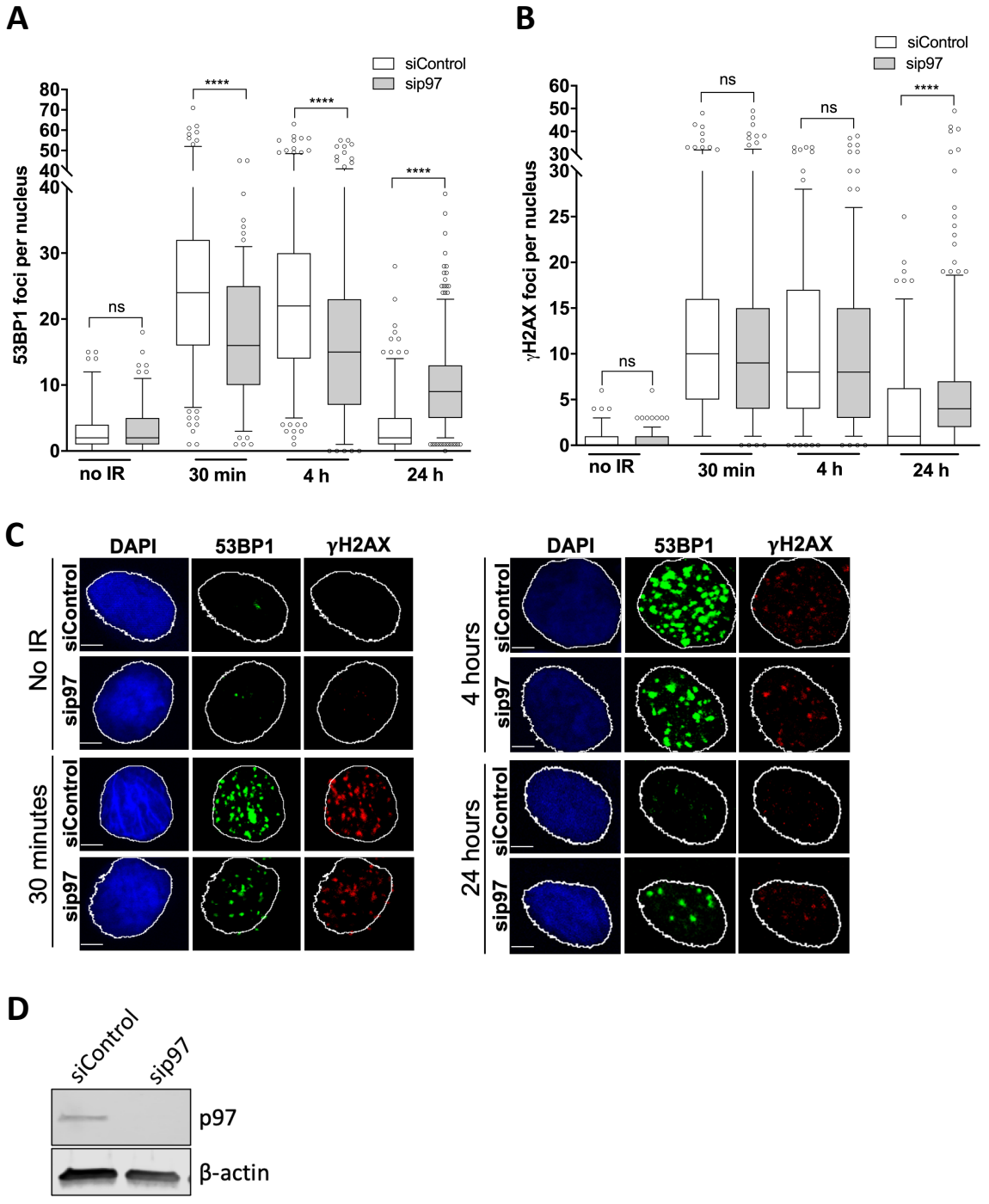


Figure 39 Depletion of p97 negatively regulates the anti-resection factor 53BP1 and leads to delayed DNA double-strand break repair visualised by γH2AX foci.

A) Number of 53BP1 and (**B**) γH2AX nuclear foci over 24 hours in p97 siRNA-depleted T24 cells after 2 Gy IR. Graphs in A) and B) are presented as box-and-whiskers plot with interquartile ranges. Data beyond the 5th and 95th percentiles is shown as individual points. At least 60 individual cells were counted per repeat and condition; n=3 independent experiments. Statistical analysis: Mann-Whitney test. NS, not significant; **** p≤0.0001. **C)** Representative images of 53BP1 and γH2AX foci at each time point over a 24-hour recovery period. Scale bar: 5 µm. **D)** Western blot showing knockdown of p97. Beta actin is used as loading control.

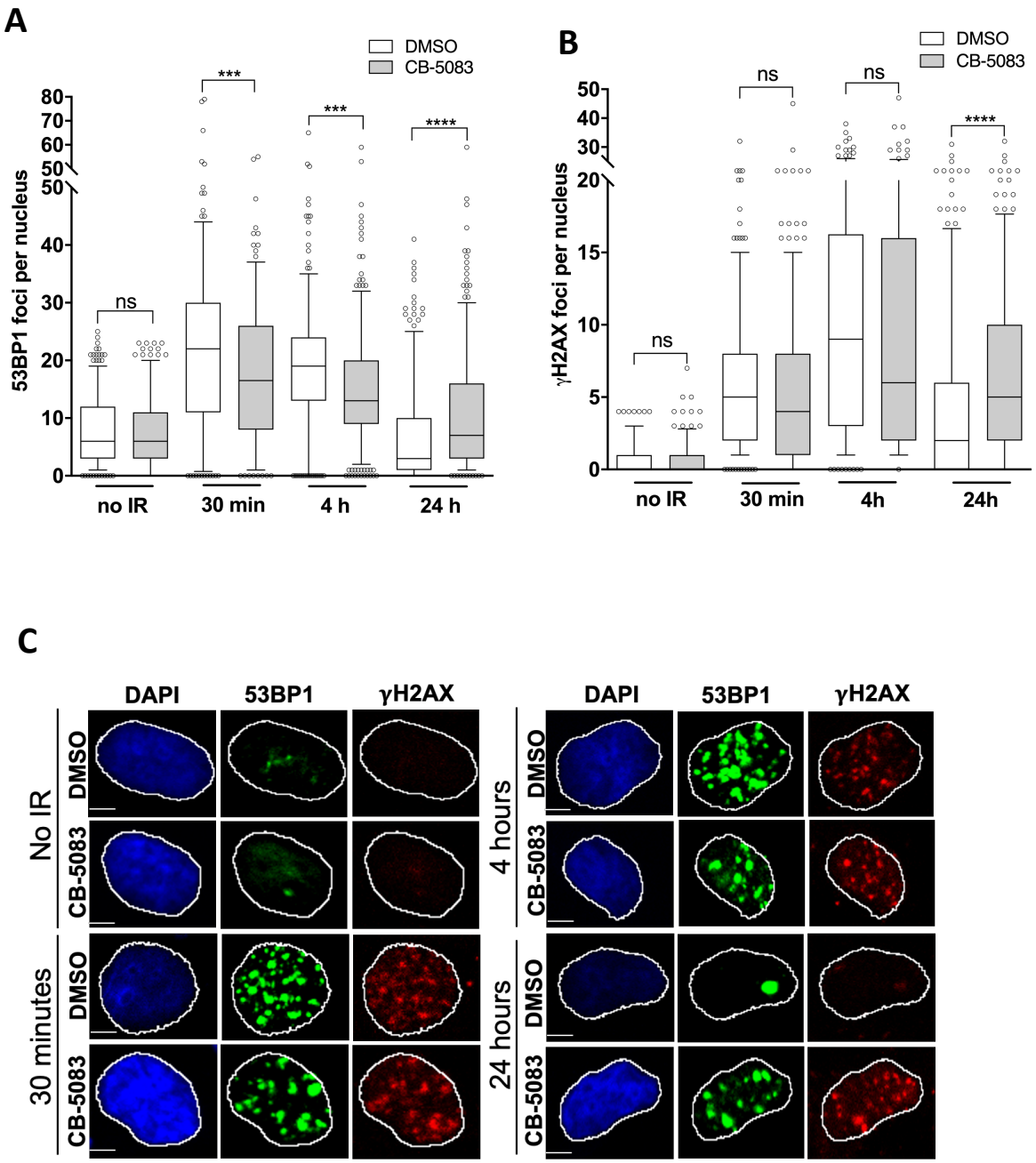


Figure 40 Inhibition of p97 negatively regulates the anti-resection factor 53BP1 and leads to delayed DNA double-strand break repair visualised by γH2AX foci.
A) Number of 53BP1 and (**B**) γH2AX nuclear foci over 24 hours in CB-5083-treated T24 cells after 2 Gy IR. Graphs in A) and B) are presented as box-and-whiskers plot with interquartile ranges. Data beyond the 5th and 95th percentiles is shown as individual points. At least 60 individual cells were counted per repeat and condition; n=3 independent experiments. Statistical analysis: Mann-Whitney test. NS, not significant; *** p≤0.001; **** p≤0.0001. **C)** Representative images of 53BP1 and γH2AX foci at each time point over a 24-hour recovery period. Scale bar: 5 µm.

Additionally, it was investigated whether there is a similar recruitment defect in other anti-resection factors that promote NHEJ over HR and act in complex with 53BP1. Specifically, DNA damage recruitment of REV7, a Shieldin complex component, was studied after 2 Gy IR and over 24 hours of recovery. Depletion of p97 caused a similar recruitment defect of REV7 to IRIF as 53BP1, where REV7 recruitment was defective in p97 depleted conditions at 4 hours post-IR but increased after 24 hours of recovery (Figure 41 A-C). These results confirm previous observations that at 24 hours after IR, there is persistent DNA damage and significantly more γH2AX foci.

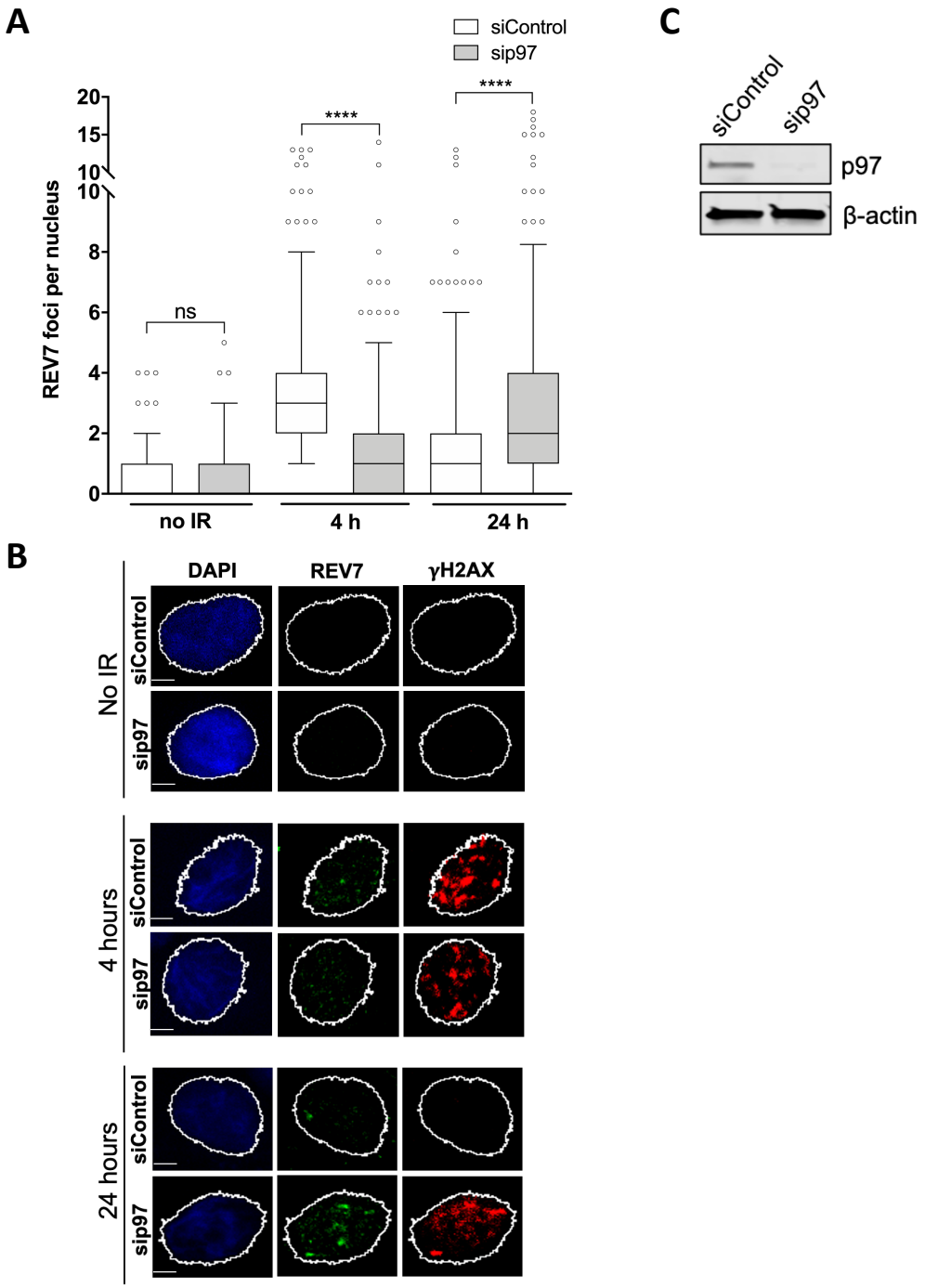


Figure 41 Depletion of p97 negatively regulates the anti-resection factor REV7 after IR-induced DNA damage.

A) Number of REV7 nuclear foci over 24 hours in p97-depleted T24 cells after 2 Gy IR. Graph is presented as box-and-whiskers plot with interquartile ranges. Data beyond the 5th and 95th percentiles is shown as individual points. At least 50 individual cells were counted per repeat and condition; n=3 independent experiments. Statistical analysis: Mann-Whitney test. NS, not significant; **** p≤0.0001. **B)** Representative images of REV7 foci at each time point over a 24-hour recovery period. Scale bar: 5 µm. **C)** Western Blot showing knockdown of p97. Beta-actin is loading control.

Knowing from previous results that p97 inactivation results in a 53BP1 and REV7 recruitment defect to IR-induced foci, and that decreased recruitment of 53BP1 and REV7 to DNA damage sites can create a permissive environment for DNA end resection, it was next determined whether 53BP1 recruitment defect can be rescued in combination of p97 depletion and MRE11 inhibition by Mirin in T24 cells. Mirin-treated cells were able to completely rescue defective 53BP1 recruitment seen in p97-depleted cells after IR-induced DNA damage (Figure 42 A-C). This indicates that MRE11 accumulation and subsequent DNA end resection poses a barrier to the NHEJ factor 53BP1 when p97 is inactive. To further understand whether 53BP1 recruitment defect to IRIF in p97-inactivated cells is an indirect effect or a result of MRE11 accumulation, 53BP1 recruitment was studied in the context of Ku80 and L3MBTL1 depletion by siRNA. Both Ku80 and L3MBTL1 are p97 substrates upstream of 53BP1 and the Shieldin complex (including REV7) (Acs et al., 2011, van den Boom et al., 2016). Depletion of Ku80 had no effect on the 53BP1 recruitment defect in p97-depleted cells (Figure 43 A-C), indicating that p97 regulates 53BP1 recruitment independently of Ku.

In figure 43 B, similarly to the representative image in Figure 20, combined depletion of p97 and Ku80 shows less γH2AX nuclear foci than each of the individual knockdowns. Although not in the scope of this thesis, the decrease in the number of γH2AX seemed to be consistent in between experiments and biological repeats. In order to confirm whether a combined depletion of p97 and Ku80 does indeed result in the formation of less γH2AX foci upon IR compared to control and individual knockdowns, the number of γH2AX foci should be quantified across three independent repeats and the results statistically analysed. However, it has been shown that inactivation of p97 decreases ATM activation, and activated ATM phosphorylates histone H2AX at Ser139 residue to form γH2AX that propagates DNA damage signalling and retains factors involved in DSB repair (Stiff et al., 2004, Roux et al., 2021, Savic et al., 2009). Depletion of p97 on its own might not be enough to cause a significant decrease in γH2AX foci formation, however the simultaneous depletion of the Ku complex could further influence this as Ku is bound by DNA-PKcs, and DNA-PKcs directly phosphorylate H2AX at Ser139 redundantly to ATM (Stiff et al., 2004). Therefore, simultaneous defects in ATM activation and DNA-PKcs activation could significantly influence the formation of γH2AX after IR. Further studies need to determine

the relationship between p97, the Ku complex, and γH2AX signalling upon DNA damage, and whether the decreased γH2AX foci observed is mostly through ATM and DNA-PK_{cs} signalling, or due to some other factors resulting from p97 and Ku co-depletion, such as heterochromatin formation/chromatin compaction, which is also known to influence γH2AX foci formation (Kim et al., 2007).

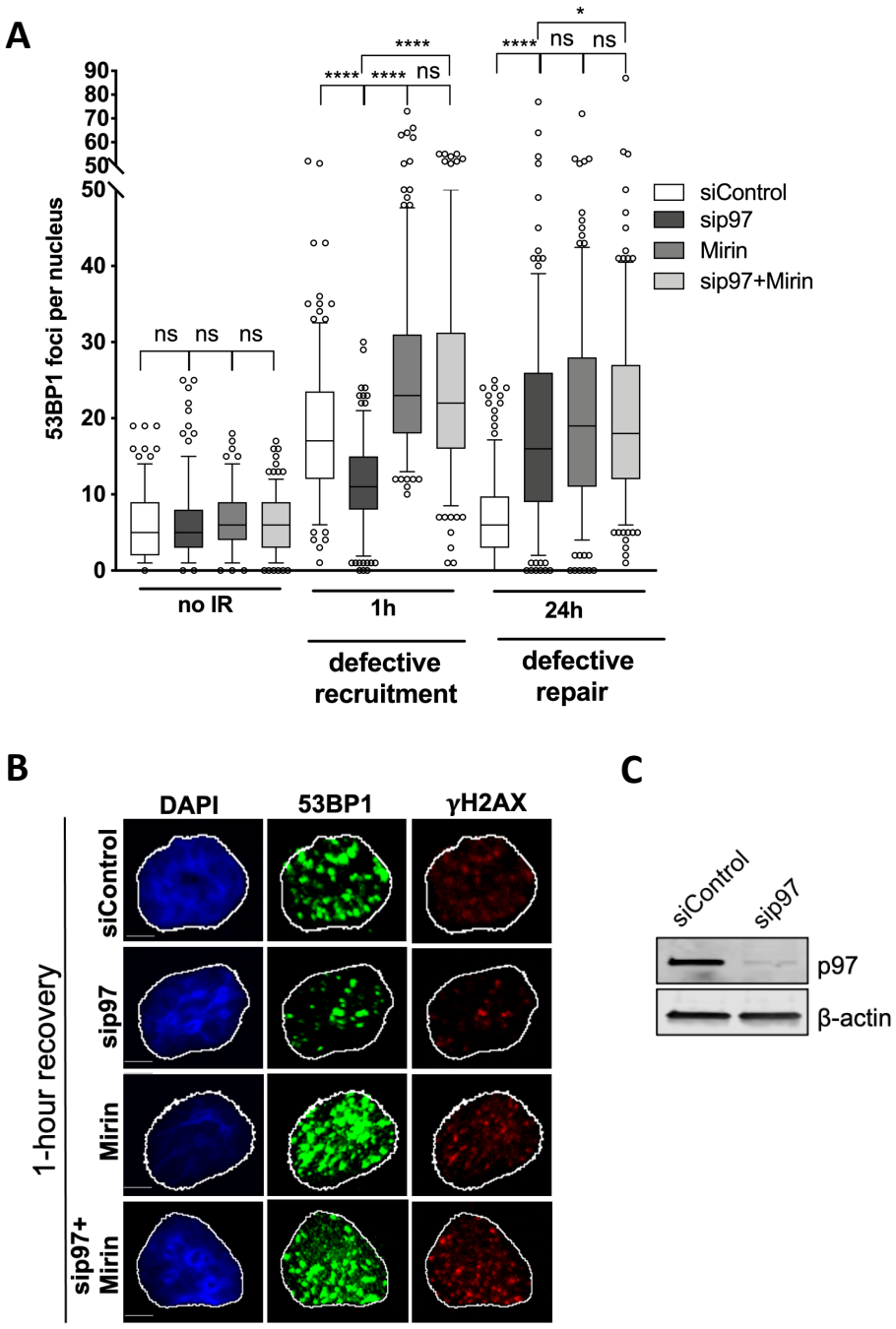


Figure 42 The MRE11 inhibitor Mirin rescues 53BP1 recruitment defect in p97-depleted cells.

A) Number of 53BP1 nuclear foci at 1 hour and 24 hours of recovery in p97-depleted and Mirin-treated T24 cells after 2 Gy IR. Graph is presented as box-and-whiskers plot with interquartile ranges. Data beyond the 5th and 95th percentiles is shown as individual points. At least 60 individual cells were counted per repeat and condition; n=3 independent experiments. Statistical analysis: Mann-Whitney test. NS, not significant; * p≤0.05; **** p≤0.0001. **B)** Representative images of 53BP1 foci at 1 hour of recovery from 2 Gy IR. Scale bar: 5 µm. **C)** Western Blot showing knockdown of p97. Beta-actin is loading control.

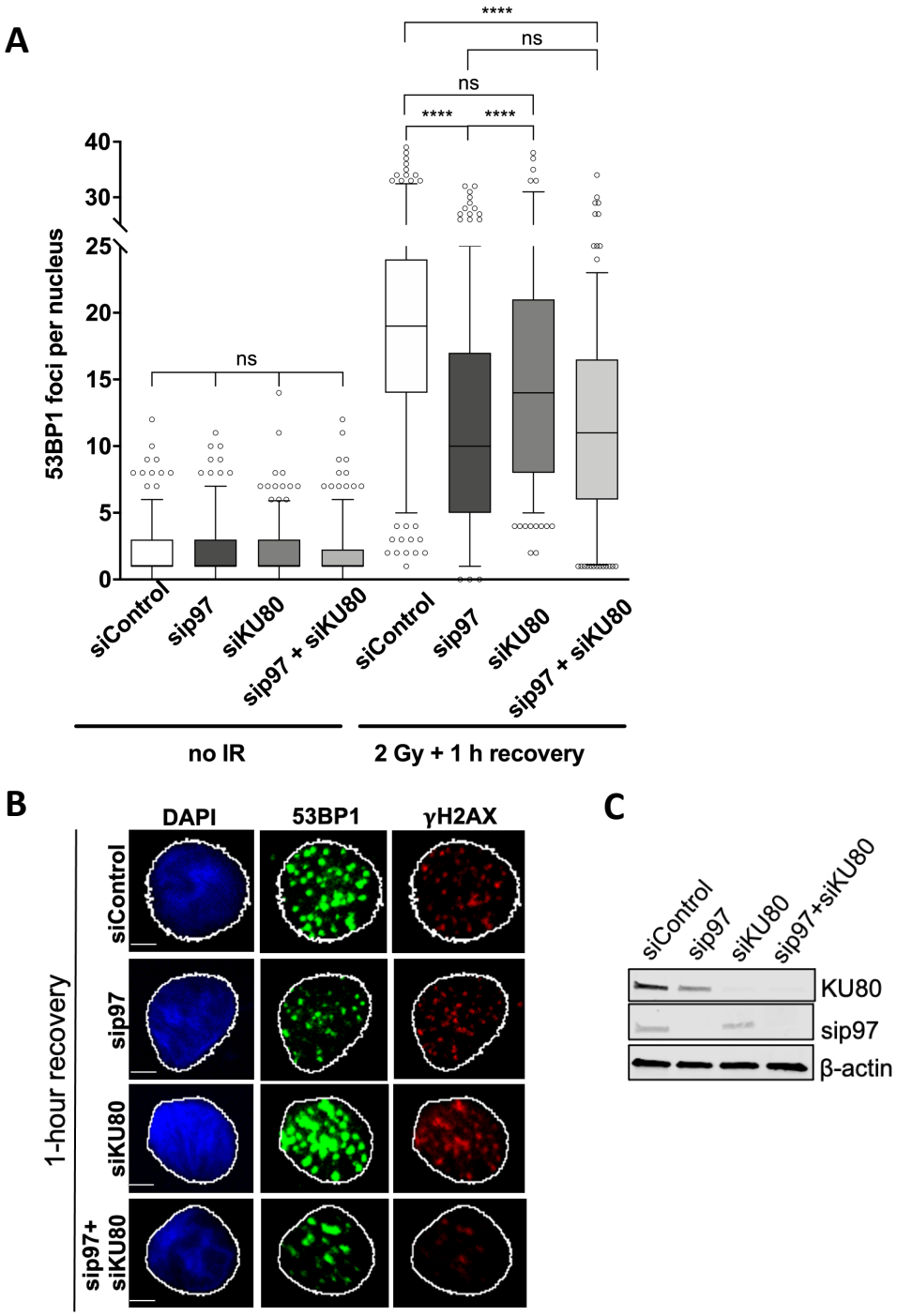


Figure 43 Ku80 depletion does not affect 53BP1 recruitment in p97-depleted cells.
A) Number of 53BP1 nuclear foci at 1 hour of recovery in Ku80- and p97-depleted T24 cells after 2 Gy IR. Graph is presented as box-and-whiskers plot with interquartile ranges. Data beyond the 5th and 95th percentiles is shown as individual points. At least 60 individual cells were counted per repeat and condition; n=3 independent experiments. Statistical analysis: Mann-Whitney test. NS, not significant; **** p≤0.0001. **B)** Representative images of 53BP1 foci at 1 hour of recovery from 2 Gy IR. Scale bar: 5 µm. **C)** Western Blot showing knockdown of p97 and Ku80. Beta-actin is loading control.

Another factor regulating 53BP1 recruitment to DSB sites is the PcG chromatin remodeller L3MBTL1, which is also a substrate for p97. Removal of L3MBTL1 by p97 has been shown to promote 53BP1 recruitment to methylated histone H4 (Acs et al., 2011). A partial rescue of 53BP1 foci recruitment to IRIF was observed in p97 and L3MBTL1 co-depleted T24 cells after 2 Gy IR (Figure 44 A-C), suggesting that p97-mediated extraction of L3MBTL1 is not the only mechanism determining downstream 53BP1 recruitment, and that there are most likely other p97 substrates regulating 53BP1 recruitment to DSBs. These data were validated with another siRNA sequence against L3MBTL1, showing that this is not due to an off-target effect of the siRNA (Figure 45 A-C). Furthermore, these results demonstrated that when MRE11 was inhibited by Mirin and combined with L3MBTL1 depletion, there was no additive effect on 53BP1 recruitment in p97-depleted cells after IR (Figure 45 A-C).

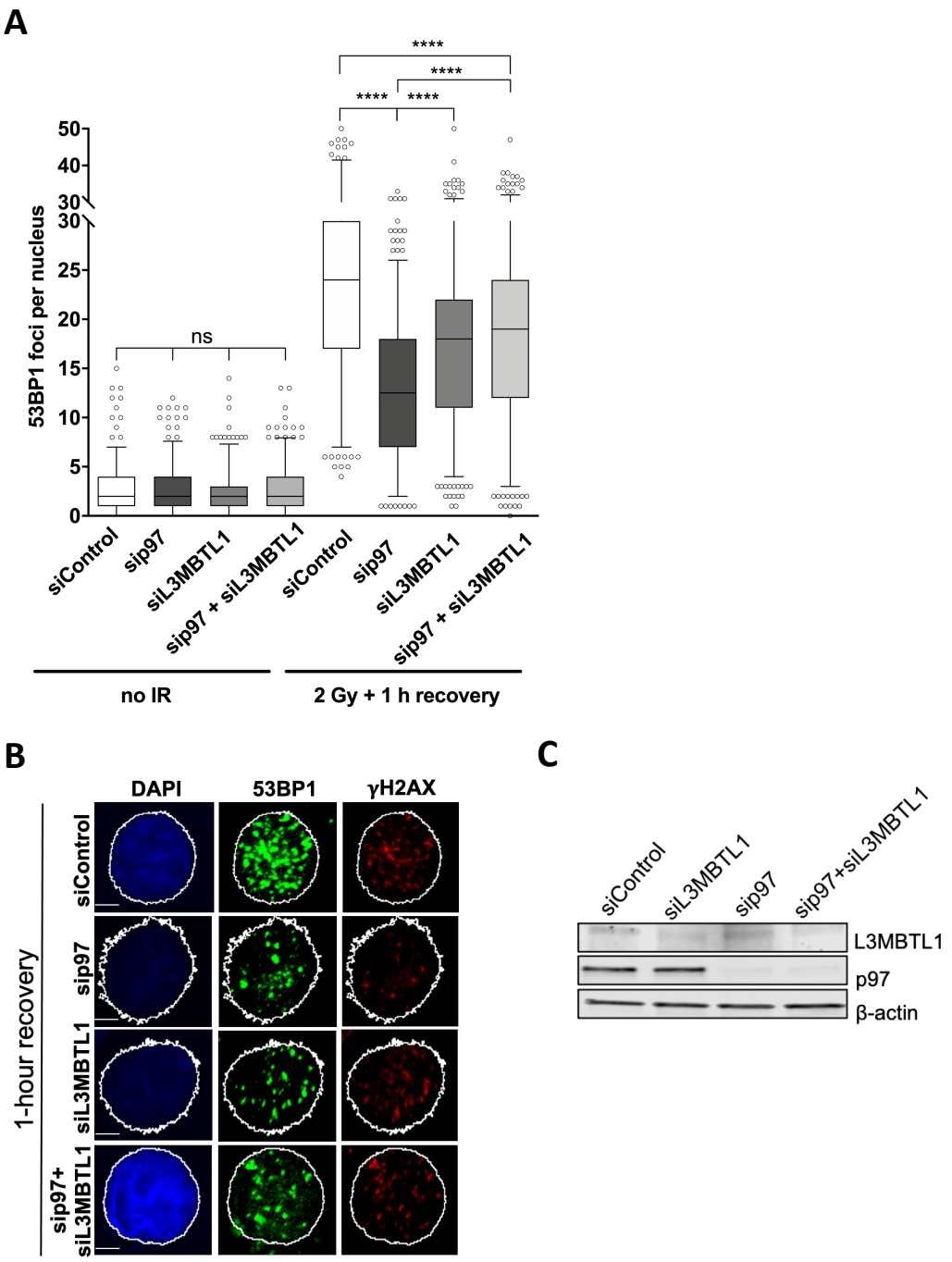


Figure 44 Depletion of the p97 substrate L3MBTL1 partially rescues 53BP1 recruitment defect of p97-inactivated cells.

A) Number of 53BP1 nuclear foci at 1 hour of recovery in L3MBTL1- and p97-depleted T24 cells after 2 Gy IR. Graph is presented as box-and-whiskers plot with interquartile ranges. Data beyond the 5th and 95th percentiles is shown as individual points. At least 60 individual cells were counted per repeat and condition; n=3 independent experiments. Statistical analysis: Mann-Whitney test. NS, not significant; **** p≤0.0001. **B)** Representative images of 53BP1 foci at 1 hour of recovery from 2 Gy IR. Scale bar: 5 µm. **C)** Western Blot showing knockdown of p97 and L3MBTL1. Beta-actin is loading control.

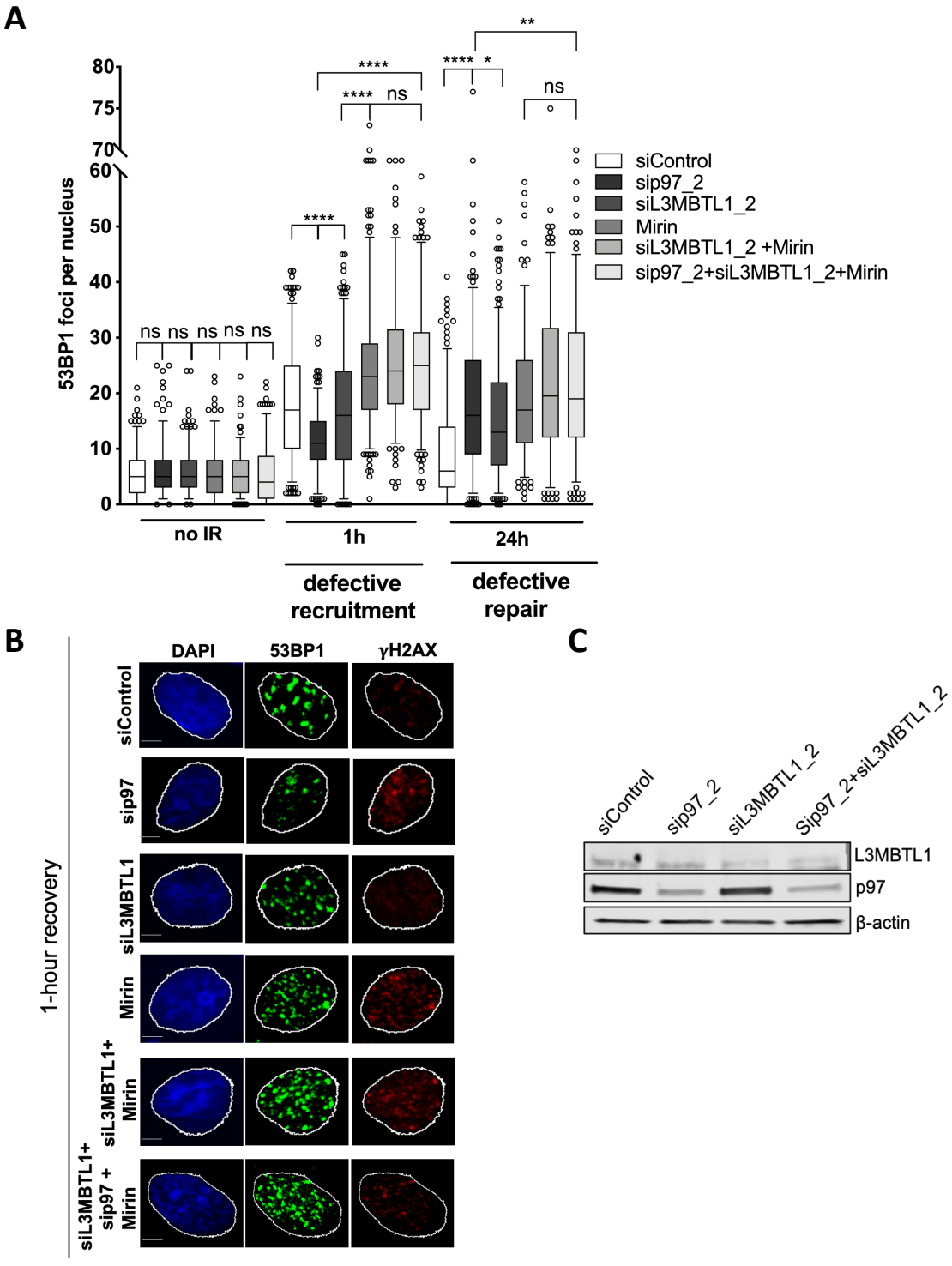


Figure 45 No additive effect on 53BP1 recruitment in L3MBTL1 and p97 co-depleted cells in combination with Mirin.

A) Number of 53BP1 nuclear foci at 1 hour and 24 hours of recovery in L3MBTL1- and p97-depleted T24 cells (+/- Mirin) after 2 Gy IR. Graph is presented as box-and-whiskers plot with interquartile ranges. Data beyond the 5th and 95th percentiles is shown as individual points. At least 60 individual cells were counted per repeat and condition; n=3 independent experiments. Statistical analysis: Mann-Whitney test. NS, not significant; * p≤0.05; ** p<0.01; **** p≤0.0001. **B)** Representative images of 53BP1 foci at 1 hour of recovery from 2 Gy IR. Scale bar: 5 µm. **C)** Western Blot showing knockdown of p97 and L3MBTL1. Beta-actin is loading control.

In summary, the results from this chapter show that p97 regulates 53BP1 recruitment to DNA damage upon IR, and its inactivation leads to a delay in DSB repair. When putting this in the context of the previous chapter (referring to Figures 36-38), which demonstrated that p97 inactivation causes increased SSA efficiency and decreased HR, these results might at first seem surprising as HR has a relatively slower repair kinetics (Shibata et al., 2011, Taleei et al., 2011). However, SSA is a minority DSB repair pathway and occurs at limited sites in the genome where appropriate direct repeat sequences are available for annealing (around 30 base pairs long) (Bhargava et al., 2016). Furthermore, SSA is unable to fully compensate for HR or NHEJ, and often occurs when DSB ends have undergone extensive end resection that are unable to be resolved by HR or alt-EJ (Bhargava et al., 2016), therefore explaining why having SSA repair pathway as a dominant repair pathway choice might be inefficient. For example, when there is limited recruitment of 53BP1 to sites of DNA damage, such as observed upon p97 inactivation in combination with IR, excessive resection takes place and exhausts the available pool of RAD51. These conditions promote SSA over HR, and 53BP1 therefore has been shown to promote the fidelity of DSB repair (Ochs et al., 2016).

Overall, results from this chapter showed that p97 regulates 53BP1 recruitment partially through L3MBTL1 removal and independently of the Ku complex. 53BP1 recruitment to DSBs is largely restored in p97-depleted cells upon MRE11 complex inactivation. These data suggest that decreased recruitment of the anti-resection NHEJ-associated factors 53BP1 and REV7 to IRIF in p97-depleted cells creates a permissive environment for excessive DNA end resection. The full restoration of the number of 53BP1 foci after IR in p97-inactivated cells by Mirin or siRNA-mediated MRE11 depletion demonstrates that MRE11 accumulation at DSBs blocks 53BP1 access to DNA damage sites. However, data from previous MS screens done in Prof Kristijan Ramadan (unpublished data) and Prof Anne Kiltie labs (PRIDE dataset identifier: PXD016279) indicates that p97 interacts with the MRN complex, and that MRE11 is a direct target of p97 (Kilgas et al., 2021). Furthermore, this hypothesis is supported by immunoprecipitation experiments which demonstrated in both an endogenous and MRE11 and p97 overexpressed systems that p97 functionally interacts with MRE11. Additionally, CHX chase assays done both in T24 and HeLa cells upon p97-inhibited and -depleted conditions as well as in an overexpressed p97-EQ mutant substrate

trapping conditions show that p97 inactivation leads to MRE11 accumulation on chromatin after IR-induced DNA damage (Kilgas et al., 2021). Unpublished work from Prof Kristijan Ramadan's lab is currently in progress of showing that UBXD8 is a specific adaptor and p97 co-factor in bridging MRE11 and p97. Despite these encouraging data, it would be important to perform *in vitro* reconstitution experiments with ubiquitinated MRE11 and p97 with its potential bridging co-factor in order to confirm that p97 directly binds MRE11. Altogether, these findings demonstrate that p97-mediated regulation of MRE11 levels at DSBs is an independent process of the previously demonstrated p97-Ku complex axis in the regulation of DSB repair pathway choice (van den Boom et al., 2016).

Chapter 6: Regulation of the p97-MRE11 axis by upstream DDR kinases

Protein phosphorylation often acts as a recruitment signal for downstream ubiquitination, which then controls the timely removal and disassembly of DDR proteins from DNA damage sites (Hunter, 2007). To further understand how upstream DDR kinases affect MRE11 accumulation on DNA damage, the effects of chemical inhibition of the three DDR kinases ATM, ATR, and DNA-PK were studied on MRE11 accumulation upon IR-induced DNA damage.

Treatment of T24 cells with the ATM kinase inhibitor KU-55933 (Figure 46 A and B) led to nuclear MRE11 foci accumulation after 1-hour recovery from 2 Gy IR when compared to DMSO control. When ATM-inhibition was combined with p97-inhibition, there was no further accumulation of MRE11, indicating that p97 is acting in the same DDR signalling axis as ATM. Western Blots confirmed successful inhibition of the ATM pathway by phospho-ATM (S1981) and phospho-CHK2 (Thr68) inactivation (Figure 46 C). To determine whether a similar phenotype is also observed in ATR-inhibited conditions, T24 cells were treated with the ATR inhibitor AZD6738, and MRE11 accumulation on DNA damage sites was measured after 2 Gy IR and 1 hour of recovery. There was no significant change in MRE11 accumulation in AZD6738-treated cells from control-treated cells (Figure 47 A-C). Furthermore, there was no significant further change in MRE11 accumulation where ATR and p97 inhibitors were combined, compared to p97 inhibition alone. This suggests an ATM-dependent and ATR-independent regulation of MRE11 accumulation upon p97 inhibition on IR-induced DNA damage sites. Western Blots confirmed inactivation of ATR pathway upon AZD6738 treatment by measuring CHK1 phosphorylation (S345) after DNA damage (Figure 47 C).

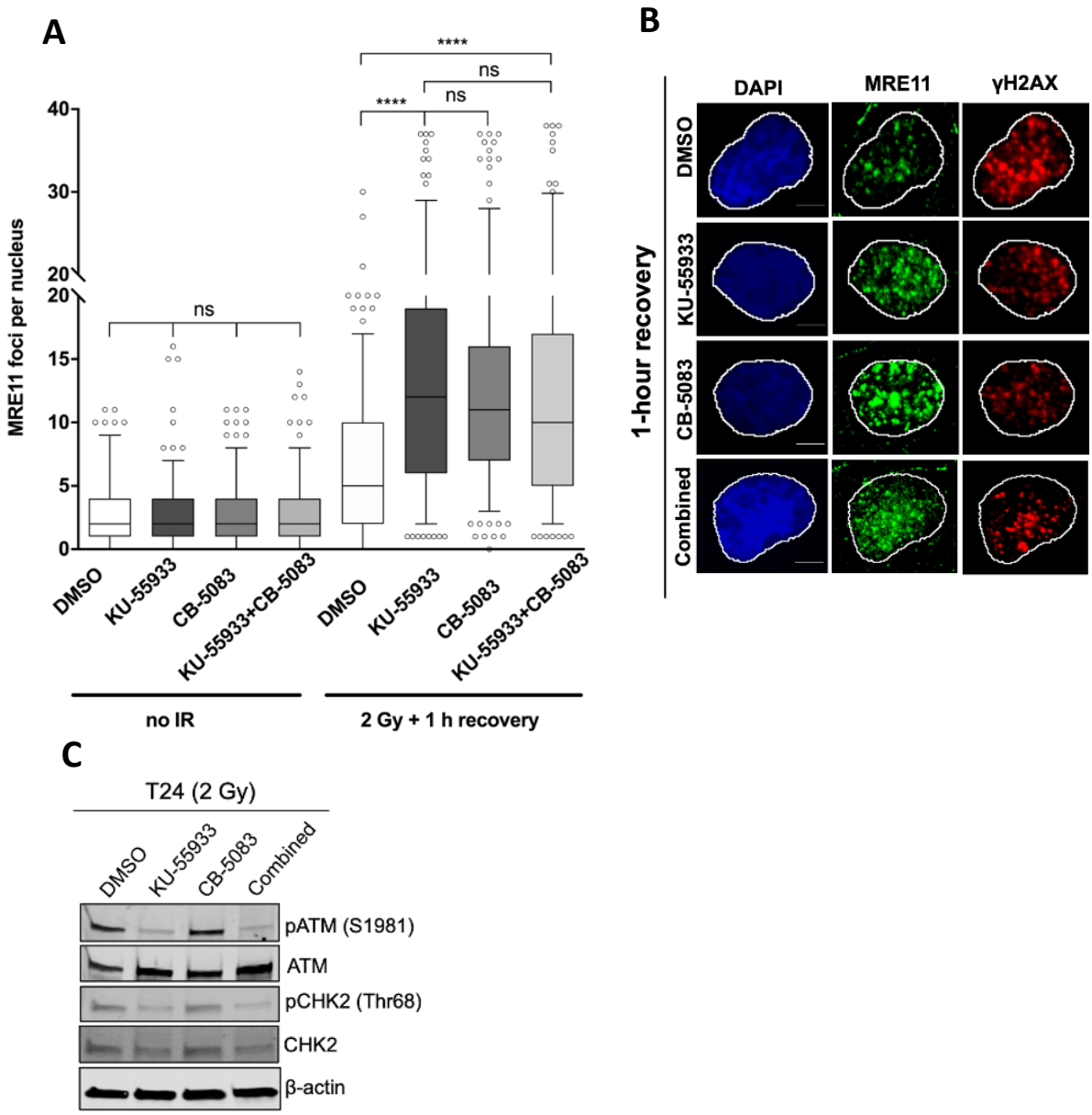


Figure 46 ATM inhibition causes MRE11 accumulation on sites of DNA damage similarly to p97 inhibition.

(A, B) Quantifications (A) and representative images (B) of the number of MRE11 foci at 1 hour after recovery from 2 Gy IR in T24 cells. **(C)** Western Blot showing inhibition of ATM by phospho-ATM (S1981) and phospho-CHK2 (Thr68). Data in (A) is presented as box plot with interquartile ranges shown, and values beyond the 5th and 95th percentiles are shown as individual points and analysed by Kruskal-Wallis test with Dunn's multiple comparisons. At least 60 individual cells were counted per repeat and condition; n = 3 independent experiments. NS, not significant; **** $p<0.0001$. Scale bar: 5µm.

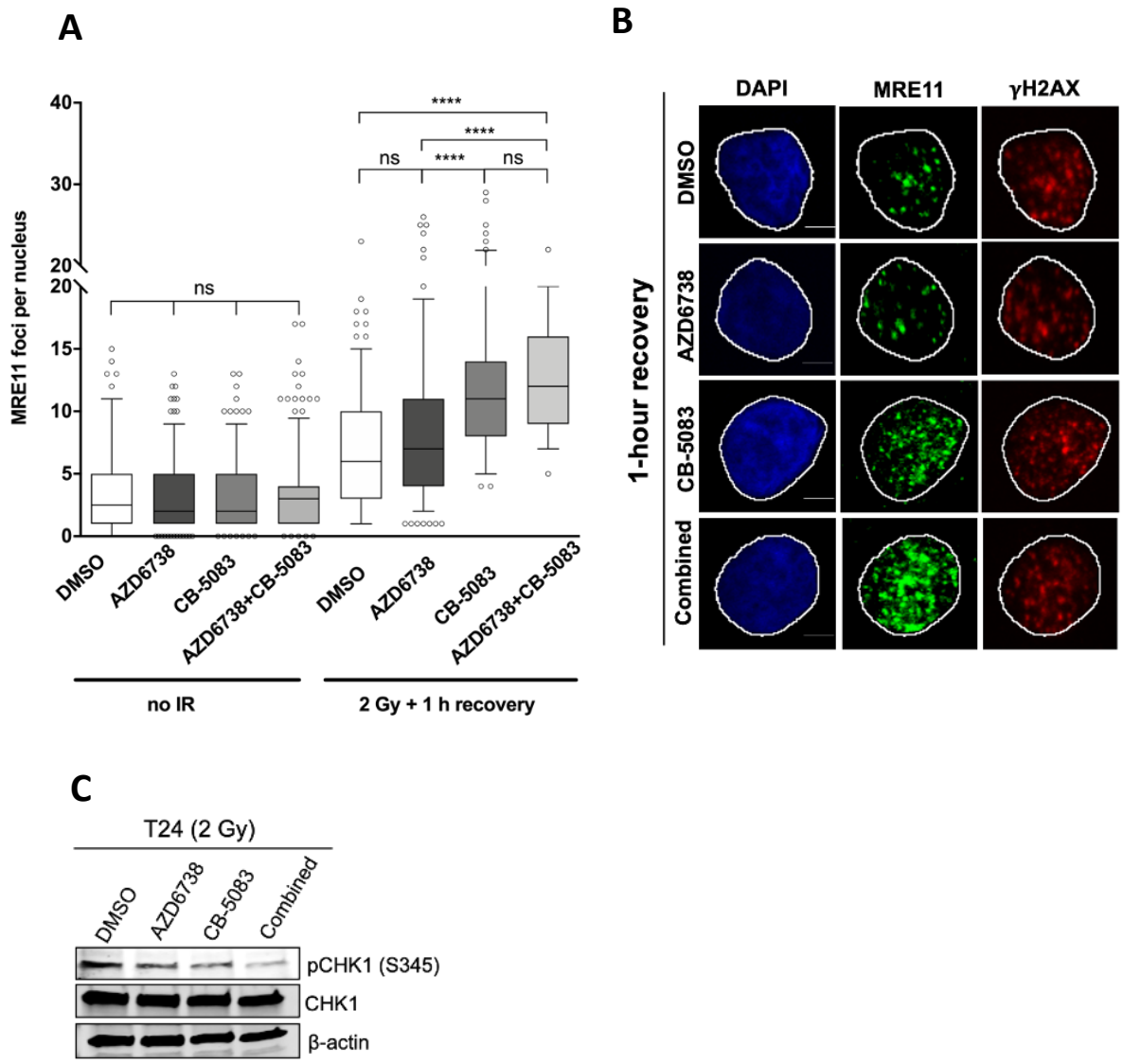


Figure 47 ATR inhibition does not cause MRE11 accumulation on sites of DNA damage compared to p97 inhibition.

(A, B) Quantifications (A) and representative images (B) of the number of MRE11 foci at 1 hour after recovery from 2 Gy IR in T24 cells. (C) Western Blot showing inhibition of ATR by phospho-CHK1 (S345). Beta-actin is loading control. Data in (A) is presented as box plot with interquartile ranges shown, and values beyond the 5th and 95th percentiles are shown as individual points and analysed by Kruskal-Wallis test with Dunn's multiple comparisons. At least 60 individual cells were counted per repeat and condition; n=3 independent experiments. NS, not significant; **** $p<0.0001$. Scale bar: 5µm.

To study how inhibition of DNA-PK regulates MRE11 accumulation upon IR-induced DNA damage, T24 cells were treated with the DNA-PK inhibitor NU7441, and MRE11 accumulation was observed in the nucleus upon 2 Gy IR and over 24 hours of recovery. In line with ATM inhibition, DNA-PK inhibition led to a significant increase of MRE11 accumulation in IRIF compared to DMSO control cells over 24 hours of recovery from IR. There was no further accumulation observed when p97 inhibition was combined with DNA-PK inhibition, suggesting that both DNA-PK and p97 act in the same pathway in regulating MRE11 (Figure 48 A and B). To further confirm the effect of DNA-PK inhibitors, the number of γH2AX foci were determined in DNA-PK-inhibited and p97-inhibited cells over 24 hours after 2 Gy IR. As previously shown for p97 inactivation, CB-5083 caused a DSB repair delay by an increased number of γH2AX foci at 24 hours after DNA damage (Figure 49 A and B). In contrast, DNA-PK inhibition caused an early increase in the number of γH2AX foci visible after 1 hour of recovery from IR, persisting over 24 hours of recovery (Figure 49 A and B), in line with previously published results (Fok et al., 2019, Willoughby et al., 2020).

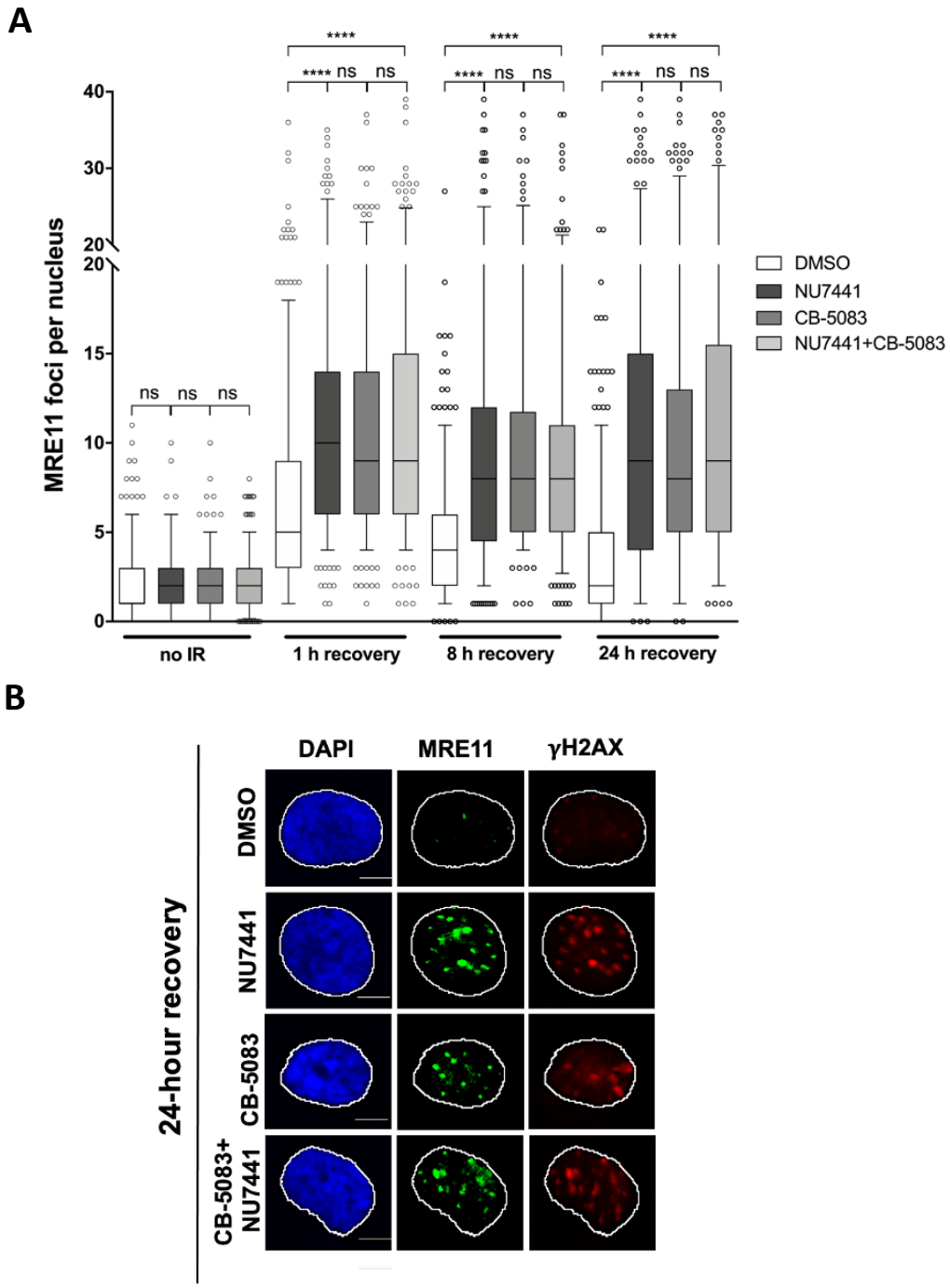


Figure 48 DNA-PK inhibition causes MRE11 accumulation on sites of DNA damage similarly to p97 inhibition.

(A, B) Quantifications (A) and representative images (B) of the number of MRE11 foci over 24 hours after recovery from 2 Gy IR in T24 cells. Data in (A) is presented as box plot with interquartile ranges shown, and values beyond the 5th and 95th percentiles are shown as individual points and analysed by Kruskal-Wallis test with Dunn's multiple comparisons. At least 60 individual cells were counted per repeat and condition; n=3 independent experiments. NS, not significant; **** p<0.0001. Scale bar: 5µm.

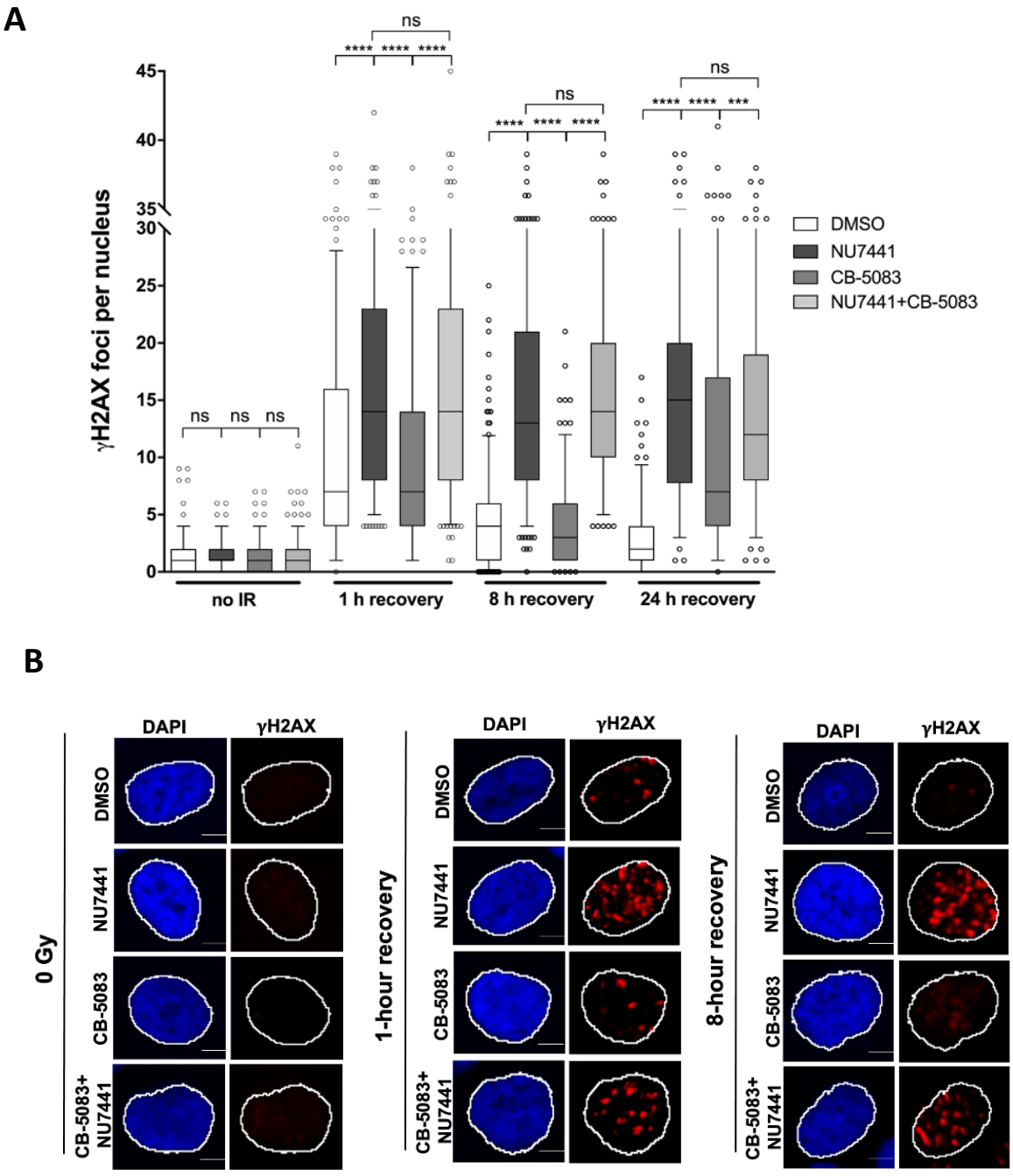


Figure 49 Inhibition of DNA-PK causes early accumulation of the DNA damage marker γH2AX and DSB repair delay after 24 hours of recovery from IR.

(A, B) Quantifications (A) and representative images (B) of the number of γH2AX foci over 24 hours after recovery from 2 Gy IR in T24 cells. Data in (A) is presented as box plot with interquartile ranges shown, and values beyond the 5th and 95th percentiles are shown as individual points and analysed by Kruskal-Wallis test with Dunn's multiple comparisons. At least 60 individual cells were counted per repeat and condition; n=3 independent experiments. NS, not significant; **** $p<0.0001$. Scale bar: 5µm.

In conclusion, there is an ATM- and DNA-PK-dependent but ATR-independent effect of p97-mediated regulation of MRE11 accumulation on DNA damage sites. Both ATM and DNA-PK are acting in the same pathway as p97 in the regulation of MRE11 as combined inhibition of p97 and ATM or DNA-PK did not lead to any further changes of MRE11 accumulation on DNA damage sites compared to inhibition of p97 or the two kinases alone.

The ATM-dependent regulation of MRE11 retention on DNA damage is in line with previous literature that has shown two ATM-dependent MRE11 phosphorylation sites (Serine 676/678) to be important for its removal from chromatin. In cells where these phospho-sites were mutated from Serine 676/678 to Alanine 676/678, MRE11 accumulates on chromatin, leading to excessive DNA end resection and defective HR repair (Kijas et al., 2015). In summary, these results indicate that IR-induced ATM signalling regulates p97-mediated MRE11 removal from DNA damage sites, which is in line with previously identified ATM-dependent regulation of MRE11 retention on chromatin. In addition to phosphorylating MRE11, ATM also phosphorylates p97 at Serine 784 upon DNA damage, which enhances its chromatin-related protein degradation and is needed for DNA damage response and cell survival (Zhu et al., 2020, Livingstone et al., 2005). Future studies could also determine to what extent MRE11 retention on DNA damage sites is dependent on ATM-mediated phosphorylation of p97 at Serine 784.

DNA-dependent protein kinase (DNA-PK) contains the p97-binding motif VIM and interacts with p97 in the cytoplasm. It is therefore considered as one of the potential p97's substrates (Jiang et al., 2013). Although the function of this interaction is unclear, our recent mass spectrometry screen of the p97 interactome upon IR identified DNA-PK as one of the most abundant interactors of p97 on chromatin (unpublished data). DNA-PK is also amongst one of the first factors recruited to DSB sites, and DNA-PK inhibitors are in clinical trials for cancer therapy in combination with IR (https://clinicaltrials.gov; trial number NCT02316197) (Fok et al., 2019). These results are in agreement with previously published work showing that inhibiting DNA-PK causes an increase in DNA double-strand breaks after IR compared to control cells (Willoughby et al., 2020).

In future work, it would be important to identify whether phosphorylation of the MRN complex components by both ATM and DNA-PK is necessary for the recruitment of downstream E3 ligases and whether upstream phosphorylation events affect MRN ubiquitination in general. It would also be interesting to determine how phosphorylation of the MRN complex affects IR sensitivity in combination with p97 inactivation.

Finally, ATR inhibition is synthetic lethal with the inhibition of the ATM signalling axis (Kwok et al., 2016, Kwok et al., 2015). The results from this chapter demonstrated that ATM inhibition resulted in MRE11 accumulation upon IR-induced DNA damage similarly to p97 inhibition, whereas ATR inhibition did not result in MRE11 accumulation under the same conditions. Furthermore, the recently developed p97 ATPase inhibitor CB-5339 has been shown to target ATM signalling (Roux et al., 2021). It would therefore be interesting to explore the potential synthetic lethal effects between p97 inhibitors in combination with ATR inhibitors.

Chapter 7: p97-mediated MRE11 regulation affects cell killing after IR *in vitro* and *in vivo*

The heightened dependency of cancer cells on the UPS system for survival makes tumour cells vulnerable to inhibition of protein degradation pathways (Guang et al., 2019). Several drugs targeting the UPS are either currently in clinical trials or FDA approved, including ubiquitinating and deubiquitinating enzyme inhibitors, p97 inhibitors and inhibitors of the proteasome (Wu et al., 2020). Various classes of p97 inhibitors exist, but only the D2 ATPase targeting small molecule inhibitors CB-5083 and CB-5339 have shown efficacy *in vivo* and been taken into Phase I clinical trials (Anderson et al., 2015, Tang et al., 2019, Zhou et al., 2015, Roux et al., 2021). However, CB-5083 and CB-5339 have not been widely studied in combination with radiotherapy (Roux et al., 2021). The work in this thesis is based on a collaboration between labs interested in finding therapeutic targets in combination with IR for the treatment of bladder cancer. To better understand the involvement of p97 in bladder cancer and in the DDR in combination with radiotherapy, p97 expression levels were studied in bladder cancer tissue sections and the effects of p97 inhibition on radiosensitisation were studied in bladder cancer cell lines. To understand the p97 system in relation to the MRN complex, the extent to which cell survival upon p97 inhibition and IR depends on MRE11 was also determined.

7.1. Inhibition of p97 radiosensitises cancer cells *in vitro*

As shown previously in this thesis, p97 controls MRE11-mediated DNA end resection and thereby DNA DSB repair pathway choice. Therefore, it was hypothesised that inhibition of p97 by CB-5083 in combination with IR leads to sustained DNA damage due to compromised HR repair and increased mutagenic alternative SSA repair, causing radiosensitisation that could be exploitable clinically. It has been previously shown that p97 knockdown radiosensitises U2OS osteosarcoma cells (Meerang et al., 2011). Furthermore, inhibiting p97 causes apoptosis and decreases overall cell survival in a variety of cancer cell lines as well as *in vivo* tumour models (Anderson et al., 2015, Le Moigne et al., 2017, Roux et al., 2021). To determine whether CB-5083 similarly radiosensitises bladder cancer cells, T24 and RT112 cell lines were given different doses of IR (0, 2, 4 and 6 Gy) and recovered over 8-12 days. Firstly, RT112 and T24 cells were treated with various concentrations of CB-5083 to determine the IC10 and IC50 concentrations of the drug after 6 hours of treatment (Figure 50 A-C), where IC10 and IC50 are the drug concentrations at which 90% and 50% of the cells survive, respectively. Inhibiting p97 increased radiosensitivity in T24 and RT112 cell lines over a range of IR doses (Figure 51 A and B). Six hours of CB-5083 exposure with either IC10 (T24: 1 μM; RT112: 1 μM) or IC50 (T24: 6 μM; RT112: 10 μM) concentrations was sufficient to induce radiosensitisation in the selected cell lines. Additionally, clonogenic assays using T24 cells and the MRE11 inhibitor Mirin (IC10 ≈18 μM; 24-hour treatment) in combination with p97 inhibition (IC10: 1 μM, 6-hour treatment) after IR demonstrated that Mirin rescues the radiosensitisation phenotype of CB-5083 (Figure 52 A-B), supporting previous findings which demonstrated excessive MRE11-mediated DNA end resection and decreased HR in p97-inhibited conditions. The phenotype of p97 and MRE11 co-inhibition rescuing cell survival after IR was further shown in p97-depleted cells combined with small hairpin RNA (shRNA)-mediated knockdown of MRE11 (Figure 53 A and B). Overall, the results of these experiments show that inhibiting p97 with the small molecule inhibitor CB-5083 induces radiosensitisation in bladder cancer cells, and this could be further tested in xenograft mouse models to see if similar effects are seen *in vivo*.

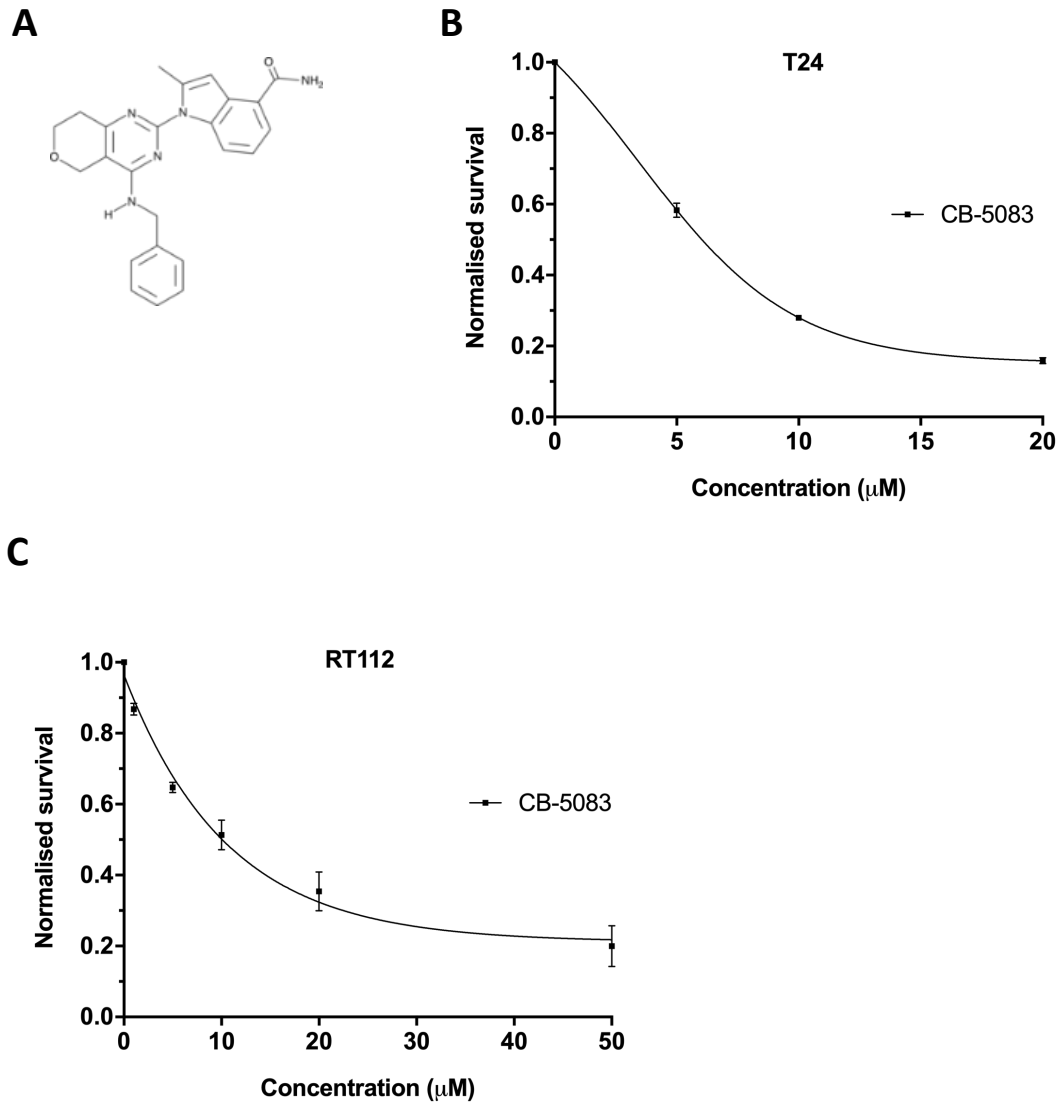


Figure 50 Determining IC10 and IC50 concentrations of CB-5083 upon 6 hours of treatment of T24 and RT112 bladder cancer cells.

(**A**) Chemical structure of CB-5083. (**B**) Survival of T24 and RT112 (**C**) bladder cancer cell lines after treatment with indicated concentrations of CB-5083 (dissolved in DMSO) over 6 hours to determine IC10 (T24: 1 µM; RT112: 1 µM) and IC50 (T24: 6 µM; RT112: 10 µM) concentrations. After treatment, cells were cultured for 8-12 days to allow colonies to form. All values were normalised to the negative DMSO control (indicated as 0 µM drug on the graphs), where the concentration of DMSO was the same as with the highest concentration used with the drug. Graphs are representative of 3 independent biological experiments across 3 technical replicates. Error bars represent +/- SEM.

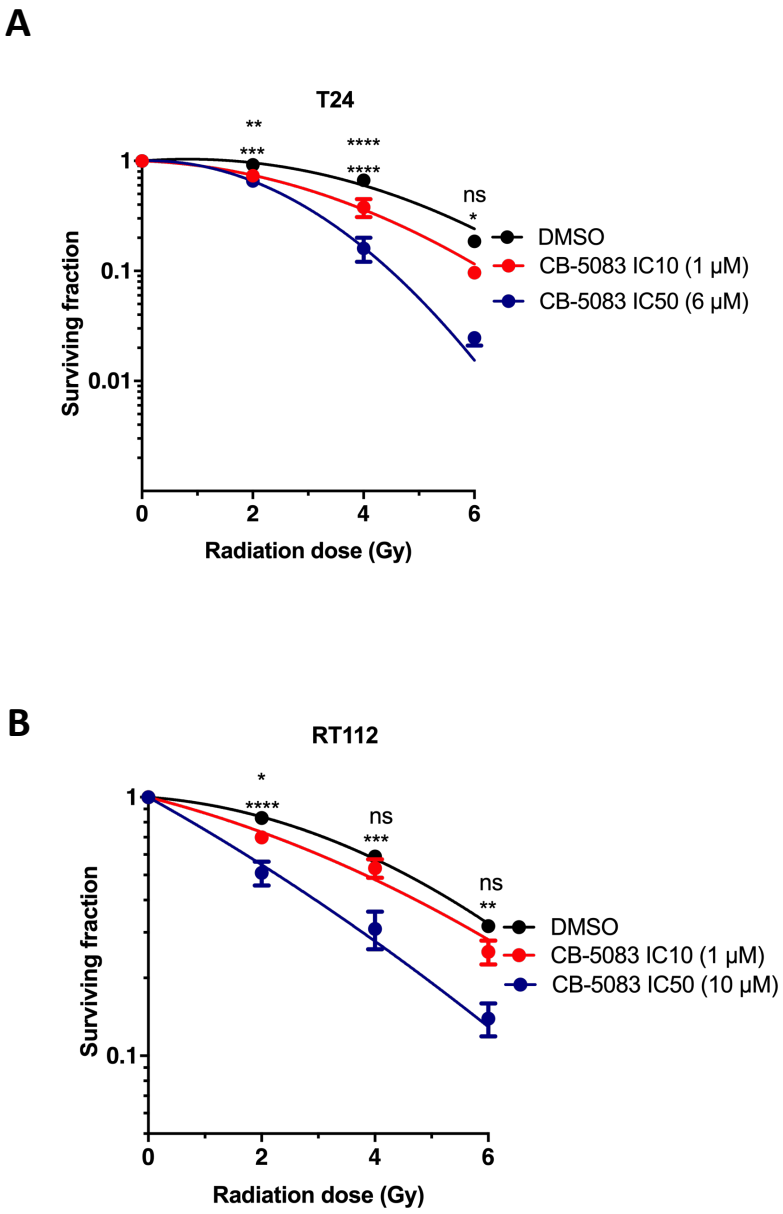
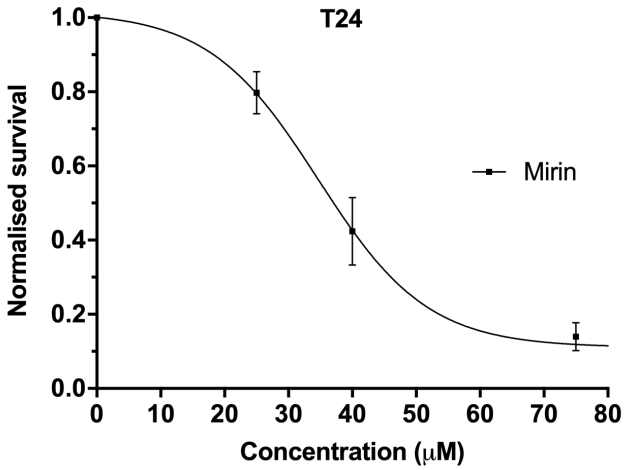


Figure 51 CB-5083 radiosensitises T24 and RT112 bladder cancer cell lines.
A) Linear quadratic (LQ) survival curves of T24 and (**B**) RT112 cells treated with 0, 2, 4 or 6 Gy IR either in combination with CB-5083 IC10 (T24: 1 µM and RT112: 1 µM), IC50 (T24: 6 µM and RT112: 10 µM), or with IR alone. DMSO was used as a negative control. After treatment, cells were cultured for 8-12 days to allow colonies to form. Graphs are representative of 3 independent biological experiments in triplicates. Statistical analysis: Two-way ANOVA, where NS, not significant; * p≤0.05; ** p≤0.01; *** p≤0.001; **** p≤0.0001. The upper row of significance stars represents IC10 compared to DMSO control, whereas the row below represents IC50 in comparison to DMSO. Error bars represent +/- SEM.

A



B

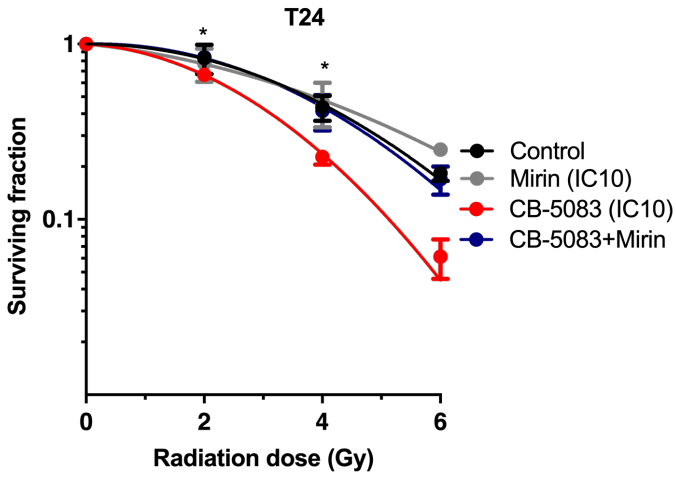


Figure 52 MRE11 inactivation by Mirin rescues the radiosensitivity phenotype induced by CB-5083.

A) Normalised survival of T24 cells after treatment with indicated concentrations of the MRE11 complex inhibitor Mirin (dissolved in DMSO) to determine IC10 (≈18 μM) and IC50 (37 μM) after 24 hours of treatment and 8-12 days of recovery. Data is normalised to DMSO control (indicated as 0 μM drug on the graphs), where the concentration of DMSO was the same as with the highest concentration used with the drug. The graph represents 3 biological repeats with 3 technical replicates. Error bars indicate +/- SEM. **B)** Surviving fraction of T24 cells upon indicated doses of IR and treatment with DMSO control, CB-5083, Mirin, or both. Figures are representative of 3 individual biological experiments in triplicate. Statistical analysis: Two-way ANOVA, comparing between CB-5083 and CB-5083+Mirin. Statistical significance: * p≤0.05. Error bars represent +/- SEM.

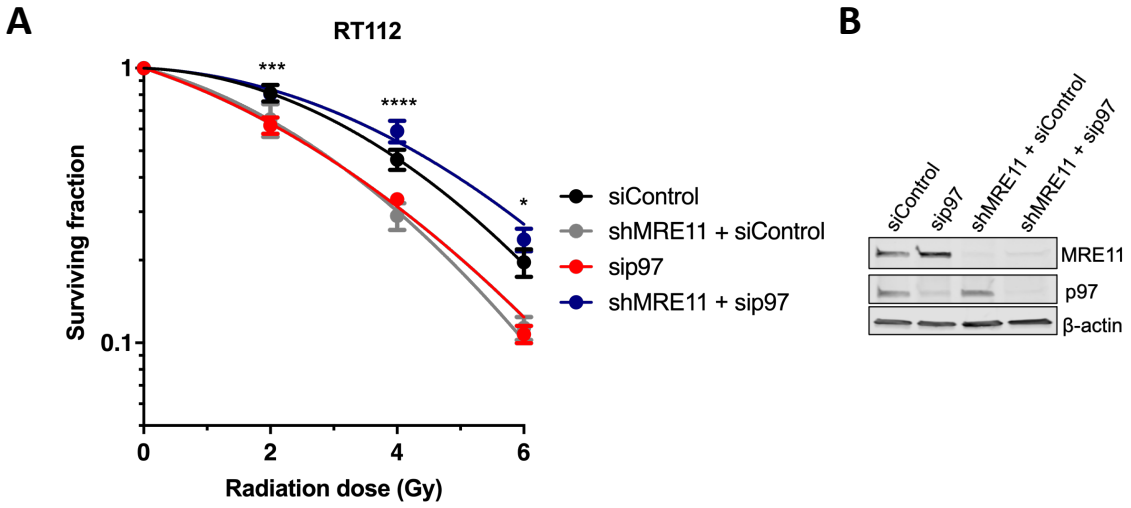


Figure 53 MRE11 inactivation by shRNA rescues the radiosensitivity phenotype induced by siRNA-mediated p97 depletion.

A) Surviving fraction of RT112 cells upon indicated doses of IR and treatment with siRNA control, siRNA against p97 (10 nM) and stable shRNA knockdown of MRE11, or both. After treatment, cells were cultured for 8-12 days to allow colonies to form. Results are representative of 3 individual biological experiments in triplicate. Statistical analysis: Two-way ANOVA, comparing between sip97 and sip97+shMRE11. Statistical significance: * $p \leq 0.05$; *** $p \leq 0.001$; **** $p \leq 0.0001$. Error bars represent +/- SEM. **B)** Western Blot confirming successful knockdown of p97 and MRE11. Beta-actin is loading control.

7.2. p97 is more highly expressed in invasive than papillary bladder cancer

Using data from The Cancer Genome Atlas (TCGA) (Tang et al., 2017), our group found significantly higher p97 gene expression across different tumour types compared to corresponding normal tissues (Kilgas et al., 2021), including in muscle-invasive bladder cancer (tumours n=404; normal tissue=28). Consequently, our group found that high tumour p97 expression levels were significantly correlated with poorer disease-specific survival (DSS) following cystectomy (p=0.05) (Kilgas et al., 2021). These results led us to study p97 expression levels in bladder cancer tissue samples to see whether the gene overexpression changes seen in TCGA analysis correlate to p97 overexpression at a protein level.

Immunohistochemical staining of tissue samples from 27 patients with high-grade non-muscle invasive bladder cancer (NMIBC) with invasion to the lamina propria (pT1G3 stage) showed higher protein expression levels of p97 in invasive tissue areas compared to papillary areas (Figure 54 A-C). The staining intensity was determined by H-score, comparing both nuclear and cytoplasmic staining between papillary and invasive regions. The average H-score difference in cytoplasmic staining was 3-fold between papillary and invasive areas: H-scores of 55 and 158, respectively. The average nuclear H-scores in papillary and invasive regions were 4.3 and 25.3, respectively. The nuclear staining pattern showed lower overall H-scores compared to cytoplasmic staining, however the difference between papillary and invasive areas in the nuclei was 6-fold. The observed increase in the nuclear p97 expression in invasive areas indicates the importance of nuclear p97 functions and could be a compensatory response to increased protein stress within the nuclei of invasive cells compared to papillary cells. Overall, these data demonstrate that more invasive areas of bladder cancer tissue have higher levels of p97 protein expression compared to non-invasive papillary tissue from the same patients. However, as the patient numbers are relatively small, a larger sample size is needed to draw more general conclusions on p97 expression and pathological progression of bladder cancer.

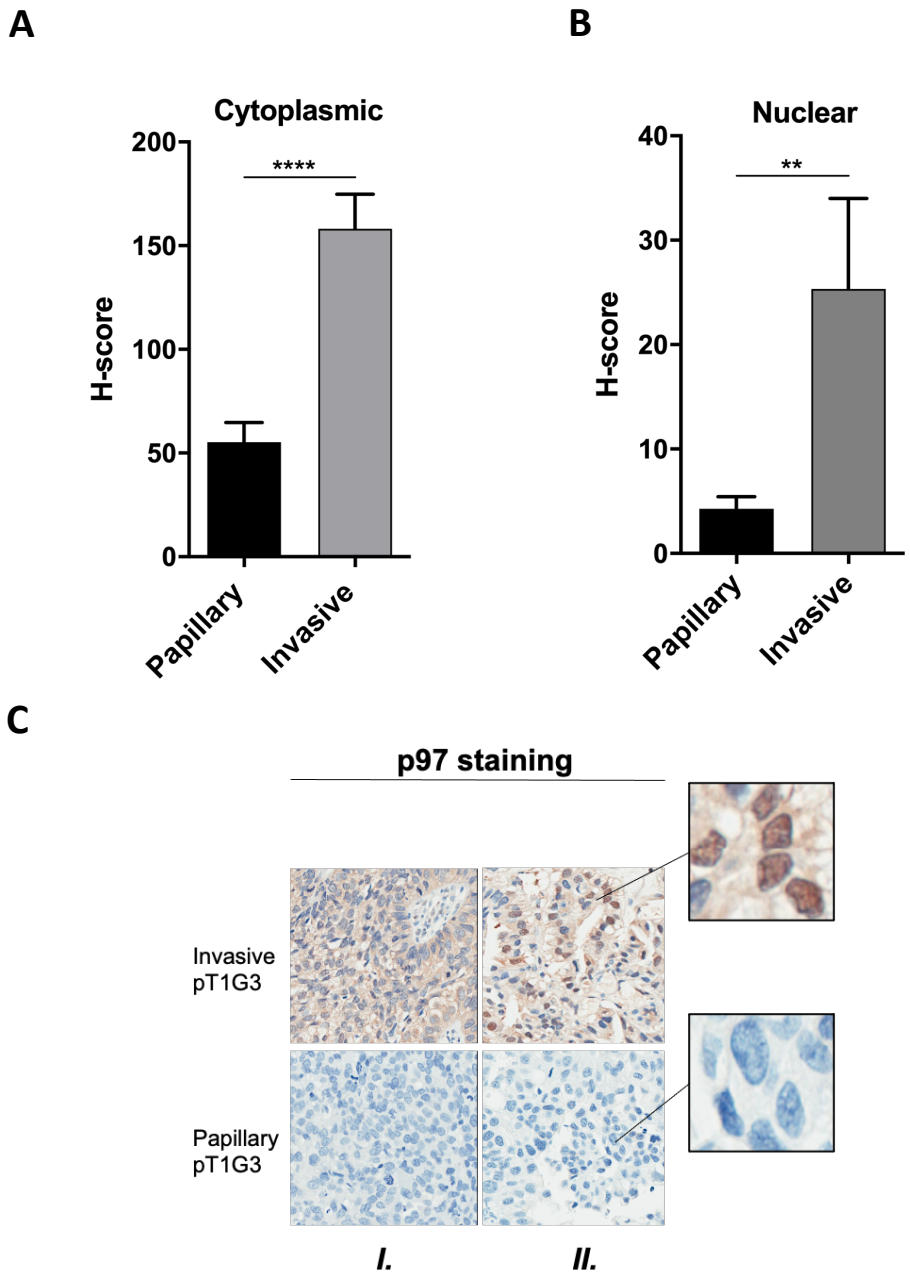


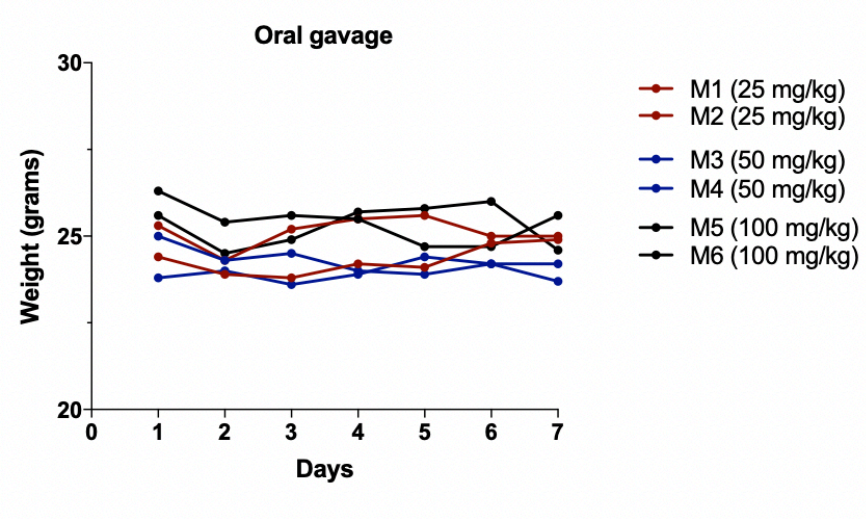
Figure 54 Cytoplasmic and nuclear expression levels of p97 in papillary and invasive bladder cancer tissue sections.

Tumour tissue samples from 27 patients with NMIBC with invasion to the lamina propria were stained with p97 antibody. Cytoplasmic **(A)** and nuclear **(B)** p97 H-scores in papillary and invasive regions. Data represented as mean H-score +/- SEM. Statistical analysis: Mann-Whitney U-test: ** $p<0.01$ and **** $p<0.0001$. **C)** Tissue staining examples from two patients marked as "*I*" and "*II*". Invasive pT1G3 areas are shown in the upper row and papillary regions are located below. Nuclear staining examples are represented as cropped zoomed images of the original images shown. The cytoplasmic and nuclear invasive and papillary areas are representative of the highest and the lowest nuclear staining intensity, respectively.

7.3. The p97 inhibitor CB-5083 is well-tolerated *in vivo*

Given the radiosensitisation effects of CB-5083 *in vitro*, the radiosensitising effect of CB-5083 was assessed *in vivo* using RT112-derived superficial flank xenografts in CD-1 nude mice. For this purpose, dose escalation studies were carried out to determine the safety profile of the drug in CD-1 nude mice after either oral gavage or intraperitoneal (IP) injections. Six 6-7-week-old mice were divided into 3 treatment groups, and two mice received either 25 mg/kg, 50 mg/kg or 100 mg/kg CB-5083 (in suspension of 5% DMSO and 0.5% methylcellulose) by oral gavage. Figure 55 A shows weight changes in mice over a week after a single oral dose of CB-5083. The chosen doses have been previously tested *in vivo* by oral gavage (Anderson et al., 2015). Consistent with previous studies, these doses were well-tolerated in CD-1 nude mice by oral gavage. To study the effects of CB-5083 given intraperitoneally, five 6-7-week-old mice were assigned into two treatment groups, where 2 mice received 25 mg/kg CB-5083 and 3 mice received 50 mg/kg CB-5083 (diluted in 5% DMSO, 0.5% methylcellulose and 1% Tween-80 in ddH_2O) (Figure 55 B). These doses were well-tolerated via IP injections, as there were no significant weight changes over a course of a week in these mice. Additionally, mice showed no visible changes in behaviour or general well-being. Overall, these results confirm that the drug is well-tolerated in the *in vivo* mouse model tested and at these doses tested. No specific experiments were conducted to assess eye toxicity in mice over the experimental period.

A



B

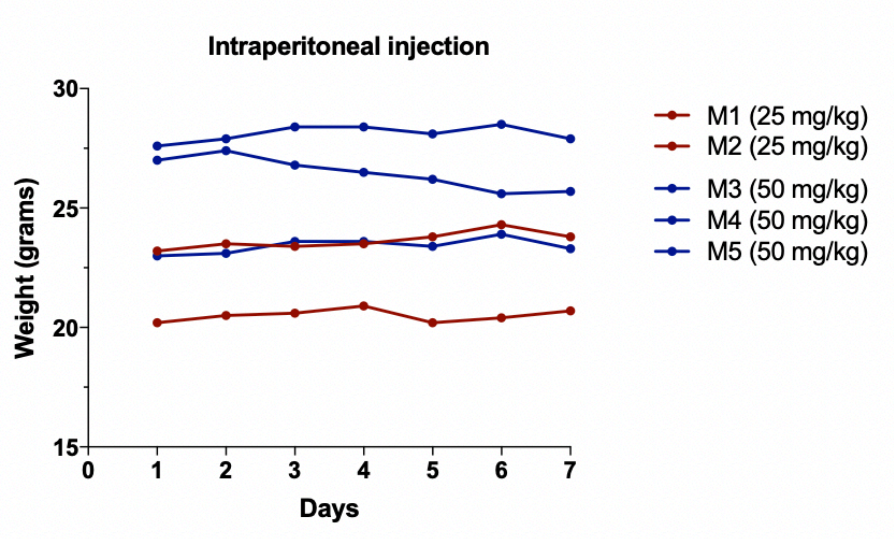


Figure 55 A single oral dose or IP injection of CB-5083 is well-tolerated in CD-1 nude mice.

A) Oral gavage dose escalation studies in CD-1 nude mice. The graph demonstrates combined weight changes in 6-7-week-old CD-1 nude mice after a single oral dose of 25 mg/kg, 50 mg/kg or 100 mg/kg of CB-5083 (n=2 mice per group). M1 – Mouse 1; M2 – Mouse 2. **B)** Intraperitoneal (IP) injection dose escalation studies in CD-1 nude mice. The graph shows weight changes of 6-7-week-old CD-1 nude mice after a single intraperitoneal injection of CB-5083 at 25 mg/kg (n=3 mice) or 50 mg/kg (n=2 mice). M1 – Mouse 1; M2 – Mouse 2; M3 – Mouse 3.

7.4. The p97 inhibitor CB-5083 suppresses tumour growth *in vivo*

Previous *in vivo* studies on CB-5083 have focused on its effects as a single agent in tumour growth suppression, but not as a potential radiosensitiser. Having demonstrated the radiosensitising effect of CB-5083 in two separate bladder cancer cell lines, its radiosensitising effects were studied on *in vivo* superficial flank RT112 bladder cancer xenografts. In a previous study, the uptake of CB-5083 (25 mg/kg CB-5083) was studied in plasma, tumour and several tissues, of CD-1 nude mice after 6 hours of treatment (Kilgas et al., 2021). The mean tumour uptake of CB-5083 was 25 µM, which was significantly higher than the mean concentration in plasma (5 µM). Furthermore, the drug concentrations in bladder, kidney and liver were significantly higher than in plasma (* $p<0.05$) (Kilgas et al., 2021).

Having shown a good uptake of the drug in tumour tissues, CD-1 nude mice bearing RT112 xenograft tumours (n=8 per group) were divided into 4 treatment groups: the control group with no treatment, the drug-only group (a single injection of CB-5083 at 25 mg/kg), radiotherapy-only group (6 Gy IR, single fraction) and the combined therapy of a single injection of CB-5083 and a single fraction of radiotherapy at 6 Gy (Figure 56). The time to reach the size for the start of the treatment (50 mm^3) did not significantly differ between the treatment groups (Appendices: Figure 60 A). The combined group showed significant tumour growth inhibition at day 8 compared to the rest of the groups, after which a positive trend continued. Additionally, the time to treble tumour volume was significantly different between the combined therapy and the control group, but not between combined group and the IR or drug-alone groups (Appendices: Figure 60 B).

A

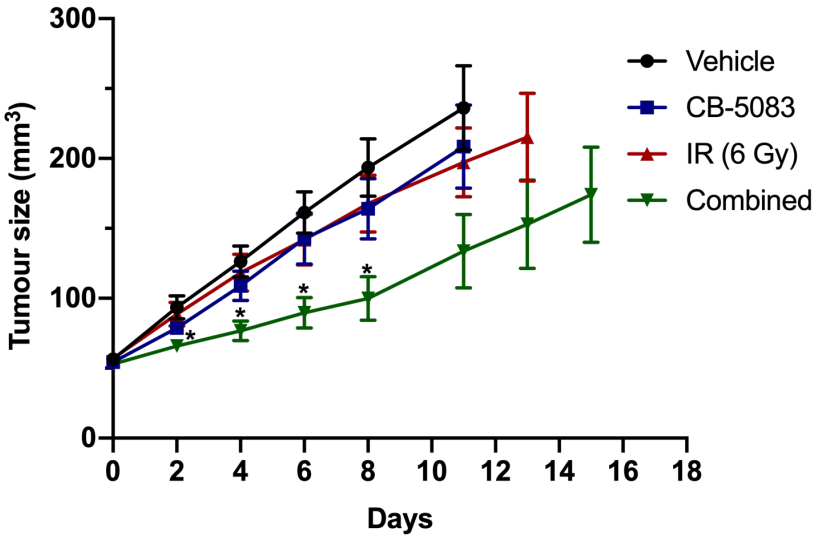


Figure 56 CB-5083 radiosensitising effects *in vivo*.
A) CD-1 nude mice (n=8 per group) were divided into four groups: control (no treatment), single intraperitoneal injection of CB-5083 (25 mg/kg), radiotherapy (6 Gy, single fraction) and combined therapy of CB-5083 (25 mg/kg) and radiotherapy (6 Gy). RT112 bladder cancer cells were injected subcutaneously into the flank of CD-1 nude mice and tumour growth was measured three times a week. The treatments were initiated once tumours reached 50 mm^3. Statistical analysis: One-way ANOVA with Dunnett's multiple comparisons: *$p<0.05$. The work was done by Dr Salome Paillas. Susan Kilgas aided with parts of the experiment and data analysis.

In conclusion, the work from this chapter demonstrates that p97 acts as an effective radiosensitising agent in selected bladder cancer cell lines, and this is dependent on MRE11 activity as both Mirin-mediated MRE11 inhibition as well as shMRE11 treatment in combination with p97 inactivation rescued cell survival after IR. When putting this in the context of previous findings, both in this thesis and in the literature, p97 inhibition alone causes radiosensitivity most likely due to downregulation of HR as well as NHEJ pathways (Singh et al., 2019, Meerang et al., 2011). The cell survival rescue with MRE11 inactivation, either by inhibition or shRNA-mediated knockdown, could lead to restoration of NHEJ, which was further studied in previous chapters by showing that p97 inactivation leads to NHEJ factor 53BP1 recruitment defects that were fully rescued by an addition of the MRE11 complex inhibitor Mirin. It would be interesting to study this through GFP-based reporter assays to have a quantitative readout of NHEJ and study whether the combination of p97 and MRE11 inhibition restores p97 inhibition related decreased in NHEJ efficiency upon DSB induction.

When comparing Mirin treatment and shMRE11 treatments, shMRE11-mediated knockdown of MRE11 on its own caused increased radiosensitivity as expected. Previously, several publications have demonstrated that MRE11 knockdown in mammalian cells leads to increased radiosensitivity (Takeda et al., 2016, Buis et al., 2008, Na et al., 2021). However, when compared to Mirin-treated cells in the conditions and cell line used in this study, no Mirin-induced radiosensitivity was observed. This is unexpected as MRE11 nuclease activity is necessary for cell survival in mammalian cells (Buis et al., 2008, Williams et al., 2008b, Wang et al., 2021). However, it could be proposed that this is because of the specific cell line (T24 cells) used, which had a relatively high concentration of IC50 (37 μM) after 24 hours of treatment and 8-12 days of colony formation (Figure 52A). Furthermore, IC10 concentration was used for radiosensitivity assays, which might have not been enough to see a radiosensitising effect under these specific conditions. Further studies should confirm this in a few other cell lines under similar conditions, where first IC10 and IC50 are determined over a 24-hour time period, and then radiosensitivity assays are conducted with both IC10 and IC50 concentrations to see whether Mirin alone leads to radiosensitivity.

Other reasons for induced radiosensitivity after p97 inhibition might be its overexpression and over-reliance on it by cancer cells. Results from IHC analyses in NMIBC (HGT1) patient samples were consistent with previous literature showing p97 overexpression in tumours (Yamamoto et al., 2004b; Valle et al., 2011; Yamamoto et al., 2004a), specifically in more invasive areas compared to papillary areas. This overexpression demonstrates the need for cancer cells to upregulate the UPS for survival while not affecting normal cells to the same extent under physiological conditions (Adams, 2004). In the future, it would be interesting to study more patient samples and differentiate between p97 expression levels in patients who did progress to metastatic disease compared to patients that did not. This would give us further correlative data between the severity of the disease and p97 expression levels. Due to the limited number of patient samples in this study these specific changes could not be compared.

Having demonstrated that a single injection of CB-5083 (25 mg/kg) in combination with a single dose of IR (6 Gy) can slow tumour growth *in vivo*, our lab also studied the associated acute normal tissue toxicity of p97 in combination with IR in CD-1 nude mice (Kilgas et al., 2021). In bladder cancer patients, radiosensitising agents can often be associated with additional toxicity to radiotherapy and are therefore not well-tolerated (Choudhury et al., 2011; James et al., 2012; Hoskin et al., 2010). Therefore, our group further studied the effects of adding intraperitoneal CB-5083 at 25 mg/kg on acute radiation-induced intestinal toxicity using an intestinal crypt assay as previously described (Groselj et al., 2018). There was no further loss of intestinal crypts in the combined group of IR (10-14 Gy) and CB-5083, which indicate that CB-5083 is not associated with acute intestinal tissue toxicity when combined with IR in the specific context studied. In future, *in vivo* effects of CB5083 on tumour radiosensitisation and associated acute tissue toxicity could be studied using the p97 second generation ATPase inhibitor that has been recently taken into clinical trials, CB-5339. Furthermore, in addition to acute toxicity, studies on long-term tissue toxicity to surrounding normal tissues would be needed when evaluating the potential of CB-5339 as a potential radiosensitising agent. The work in this thesis did not assess potential eye toxicity after a single dose of CB-5083, which, in the light of new evidence from a Phase I clinical trial (https://clinicaltrials.gov trial numbers NCT02243917 and NCT0223598), would

be an important aspect to monitor in the future. This would be especially important when studying long-term tissue toxicity.

Finally, future *in vivo* studies should also look at various doses of CB-5339 under different treatment regimens, where radiotherapy could be administered in fractions and the drug given over several days with rest periods. Thereby it would more closely mimic the clinic as well as give us a better understand of whether it can induce durable radiosensitising effects. The specific drug treatment regimens have previously been outlined in a publication describing CB-5083 as a single agent to treat solid and haematological tumours (Anderson et al., 2015, Roux et al., 2021).

Chapter 8: Discussion

The work presented in this thesis demonstrates that the AAA-type ATPase p97 regulates MRE11 accumulation on chromatin and on DNA damage sites, which affects DNA DSB repair pathway choice. The results of this thesis demonstrate that: (1) p97 interacts with all the MRN complex components: (2) inactivation of p97 causes MRE11 chromatin accumulation and subsequent excessive MRE11-mediated DNA end resection; (3) the MRE11-mediated excessive end resection causes a DSB repair pathway change from HR to SSA; (4) inhibition of p97 or its siRNA-mediated knockdown radiosensitises cancer cells in an MRE11-dependent manner.

The importance of maintaining MRE11 homeostasis on DNA damage sites has been outlined in various studies showing that insufficient MRE11 nuclease activity compromises error-free HR repair (Jachimowicz et al., 2019, Buis et al., 2008), whereas its excessive accumulation causes pathological DNA repair, degradation of nascent DNA strands, and genome instability syndromes (Hashimoto et al., 2010, Schlacher et al., 2011). In line with these observations, the work in thesis demonstrates that p97 inactivation leads to a decrease in “error-free” HR-mediated repair and an increase in mutagenic single strand-annealing (SSA), which ultimately leads to cancer cell radiosensitisation and cell death that is largely mediated by MRE11 nuclease activity.

The interaction between the MRN complex and p97 was first identified in two independent mass spectrometry screens from Prof Kristijan Ramadan’s and Prof Anne Kiltie’s labs that looked for either p97 chromatin interaction partners upon IR or MRE11 interaction partners upon IR, respectively. Both screens identified the MRN complex as one of the most prominent complexes interacting with p97, and the MRE11-based mass spectrometry screen further demonstrated that the number of p97 peptides in complex with MRE11 was similar to the number of peptides of the two MRE11 complex components, RAD50 and NBS1 (Kilgas et al., 2021). These data obtained from screens were further confirmed by immunoprecipitation and indicated that p97 could be a necessary factor regulating the MRN complex (Kilgas et al., 2021). A proposed model of p97-mediated regulation of MRE11 upon DNA damage is summarised in Figure 57. These results are in the context of

previously demonstrated p97-dependent regulation of KU on DSB sites (van den Boom et al., 2016).

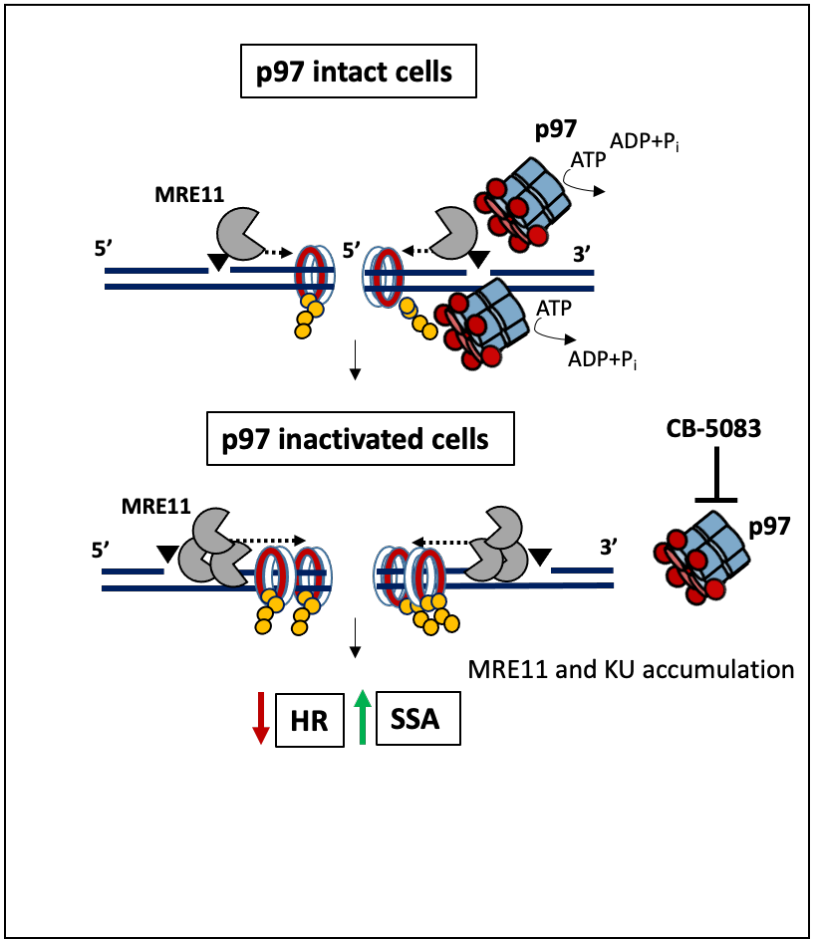


Figure 57 Model of p97-mediated MRE11 removal from DNA damage and consequent regulation of DSB repair pathway choice after IR.
Top: Cells with intact p97 function can efficiently remove both the Ku complex and MRE11 from DNA damage, thereby promoting physiological HR repair with appropriate DNA end resection. Bottom: When p97 is inactivated, both Ku70/80 and MRE11 accumulate on DNA damage, and MRE11's hyper-resection leads to excessive stretches of ssDNA, which cannot act as appropriate HR substrates, downregulating HR-mediated repair and upregulating mutagenic SSA, resulting in IR sensitivity. Figure adapted from (Kilgas et al., 2021).

8.1. p97-dependent regulation of DSB repair through MRN disassembly

Since simultaneous inactivation of p97 and MRE11 restores normal DNA end resection and cell survival upon radiation, it could be proposed that this is mediated through inhibiting end resection and subsequent restoration of NHEJ-mediated DSB repair. This is supported by the observations that inactivation of MRE11 completely restores the NHEJ factor 53BP1 recruitment to DNA damage in p97-inactivated cells. A similar cell survival restoration concept based on DSB repair pathway choice is observed in the context of 53BP1 loss in BRCA1-deficient cells, where BRCA1 deficiency on its own causes HR defects and PARP inhibitor sensitivity, whereas a simultaneous loss of the NHEJ factor 53BP1 restores DNA end resection and subsequent HR, rescuing cell survival and causing PARP inhibitor resistance (Bouwman et al., 2010, Cao et al., 2009, Bunting et al., 2010). Furthermore, it has been shown that decreased recruitment of the anti-resection factors 53BP1 and REV7 to sites of IR-induced foci forms a permissive environment for DNA end resection, which is in line with our observations (Xu et al., 2015).

It has been shown that inactivation of p97 and its co-factor complex Ufd1-Npl4 lead to Ku complex retention on DNA damage, which promotes NHEJ over HR (van den Boom et al., 2016). This suggests that p97-dependent regulation of MRE11 accumulation on DNA damage sites could be an indirect effect of Ku retention on DNA damage. However, the work in this thesis demonstrates that p97 regulates MRE11 in a Ku-independent manner, as MRE11 retention on sites of IR-induced DNA damage was not affected upon Ku80 depletion. Additionally, the p97-inactivation induced 53BP1 recruitment defect was found to be independent of Ku but dependent of MRE11, as MRE11 inactivation completely restored 53BP1 recruitment to DNA damage sites. The full restoration of 53BP1 recruitment in p97-depeleted cells upon inactivation of MRE11 suggests that MRE11 accumulation could act as a physical barrier to 53BP1 recruitment or promote resection-dependent repair that is antagonistic to NHEJ mediated by 53BP1 and the Shieldin complex. Furthermore, the excessive resection phenotypes caused by p97 inactivation were only rescued by MRE11 inactivation and not by inactivation of the downstream long-range nuclease EXO1, further demonstrating that excessive end resection is MRE11 specific. However, future studies should determine the dependency of this MRE11-mediated excessive end resection on the DNA2/BLM pathway, which is a distinct pathway from

EXO1-mediated resection. Overall, the findings in this thesis demonstrate that p97 forms a functional complex with the MRN complex that is regulated separately from previously described Ku70/80 axis, and this process directly regulates DSB repair pathway choice.

8.2. Post-translational modifications in the disassembly of MRN complex

In addition to the MRN complex, p97 is known to disassemble the MCM replicative helicase complex (Maric et al., 2014, Moreno et al., 2014), which could resemble the proposed mechanism of p97-dependent MRN disassembly. Both protein complexes are large oligomeric DNA-bound ring structures (Lammens et al., 2011, Moreno et al., 2014), so it can be assumed that both require ATPase activity to be removed from chromatin. However, there is a gap of knowledge in the field regarding the mechanism of ubiquitin-dependent disassembly of the MRN complex upon IR. For example, it is unknown which ubiquitin ligases are responsible for MRN complex ubiquitination and which subunits are ubiquitinated. It is also not understood which of the over 40 known p97-related co-factors bridge p97 to the MRN complex. Furthermore, it is unknown how upstream PTMs affect downstream ubiquitination. For example, it is recognised that protein phosphorylation often acts as a recruitment signal for ubiquitination (Hunter, 2007), and MRE11-focused phosphorylation is specifically important for its removal from chromatin (Kijas et al., 2015). ATM-dependent phosphorylation of MRE11 at serine 676 and 678 causes its removal from chromatin and mutating these phospho-sites to alanine leads to similar phenotypes as p97 inhibition in combination with IR: MRE11 accumulation on chromatin, excessive DNA end resection, compromised HR-mediated repair and increased mutagenic SSA repair (Kijas et al., 2015). Therefore, it could be speculated that these upstream events are connected to downstream p97-mediated MRE11 removal from chromatin, and that MRE11 phosphorylation acts as a recruitment signal for specific E3 ligases and p97-associated co-factors that lead to the ubiquitin-dependent disassembly of the MRN complex.

Chemical inhibition of ATM and DNA-PK, but not ATR, led to MRE11 accumulation on DNA damage sites, demonstrating pathway specificity and suggesting that both DNA-PK and ATM could regulate either p97 and/or MRE11 phosphorylation, thereby affecting MRE11 accumulation on DNA damage sites after IR. These results need to be further validated by using stably expressing MRE11 phospho-defective and -mimetic variants in MRE11-null

background to study DNA-PK and ATM-dependency in the MRN disassembly pathway. After having identified how DNA-PK and ATM affect phospho-MRE11 accumulation on chromatin upon DNA damage, it could be studied whether MRE11 phosphorylation affects downstream ubiquitination and whether this is associated with protein extraction and degradation. Furthermore, it could be determined how both phosphorylation and ubiquitination of the MRN complex regulate IR sensitivity.

8.3. Potential clinical applications of targeting the p97 system in cancer therapy

Many drugs are currently being evaluated in clinical trials that target the UPS system, including the p97 small molecule ATPase inhibitor CB-5339 (Roux et al., 2021, LaPlante and Zhang, 2021). CB-5339 is a second-generation small molecule p97 ATPase inhibitor and was developed to be more specific than the previous p97 ATPase inhibitor CB-5083, which was associated with normal tissue toxicity in Phase I clinical trials (Roux et al., 2021). Our findings that inhibiting p97 causes radiosensitivity in bladder cancer cell lines and suppresses tumour growth *in vivo* without significant acute normal tissue toxicity supports previous studies showing heightened dependency of the UPS in the survival of different types of cancers (Kilgas et al., 2021, Tokheim et al., 2021). Furthermore, pT1G3 bladder cancer patient samples analysed in this thesis confirmed higher p97 cytoplasmic and nuclear expression in invasive areas compared to non-invasive papillary areas. These results are also in line with our TCGA p97 gene expression analysis across a variety of different cancers, which demonstrate significantly upregulated p97 gene expression in tumours when compared to normal tissue (Kilgas et al., 2021). When studying the molecular mechanism of cell survival after ionising radiation, it was interesting to observe that the radiosensitivity phenotype was completely rescued upon MRE11 inactivation in p97-inhibited or -depleted cells. This suggests a restoration of DNA DSB repair pathways that were previously downregulated. Indeed, in addition to decreasing HR, depletion of p97 is known to also downregulate NHEJ (Singh et al., 2019, Meerang et al., 2011), which is likely restored upon MRE11 inactivation as it led to the complete restoration of 53BP1 recruitment as well as control levels of DNA end resection. It would be interesting to test the specificity of this mechanisms in cell survival context by also inactivating downstream nucleases such as EXO1 and DNA2 and observing whether their inactivation can rescue p97

inhibition-induced radiosensitivity. In terms of gene expression analysis, the p97 TCGA dataset could be overlapped with the MRE11 expression dataset to determine to what extent p97 overexpression correlates with MRE11-related DNA damage repair functions, and to what extent proteostasis-related functions play a role.

Even though two p97 inhibitors, CB-5083 and CB-5339, have been taken into phase I clinical trials, only CB-5339 is currently being evaluated due to off-target eye toxicity found in patients treated with CB-5083 (https://clinicaltrials.gov trial numbers NCT02243917 and NCT0437264) (Arshavsky et al., 2002, Roux et al., 2021, Tang et al., 2019). The next-generation p97 inhibitor CB-5339 has been shown to be more specific and have no off-target effects connected to CB-5083 (Roux et al., 2021). However, given that p97 has pleiotropic effects both in the nucleus and the cytoplasm, and acts in the regulation of protein balance in almost every organelle, it is not surprising that p97 inhibitors used in patients have shown undesirable off-target effects (Meerang et al., 2011, Torrecilla et al., 2017). It is therefore important to identify specific p97-related co-factors that are associated with the regulation of specific molecular pathways. In the context of the work shown in this thesis, identification of potential E3 ubiquitin ligases and p97 co-factors that are associated with MRN disassembly after DNA damage holds promise to also identify relevant targetable components within the UPS, regulating p97-mediated DSB repair pathway choice in a more controlled manner without affecting all the functions of p97.

Chapter 9: Future work

Currently, there is a knowledge gap in the field regarding the mechanism of ubiquitin-dependent disassembly of the MRN complex upon IR. A collaboration between Prof Anne Kiltie's and Prof Kristijan Ramadan's labs showed that the p97 co-factor SPRTN-dependent inactivation of the MRN complex by MRE11 cleavage correlates with significantly better disease-specific survival of urinary bladder cancer patients after radiotherapy compared to patients who received cystectomy (Choudhury et al., 2010, Na et al., 2021). Thus, understanding how the MRN complex is regulated by the p97 system in a more specific manner has potential to identify targets for radiosensitising cancer therapies. It is known that ATM-dependent MRE11 phosphorylation is necessary for MRE11 removal, however it is unclear how upstream phosphorylation interplays with downstream ubiquitination that results in MRN complex disassembly. Furthermore, knowing which subunits of the complex are ubiquitinated by which E3 ligases and which p97 co-factors bridge ubiquitinated MRN to p97 will help us identify enzymatic targets in the pathway that would have more specificity than inhibition of p97 alone. These questions can be answered by high-throughput proteomic approaches coupled to biochemical validation.

During the writing of this thesis, a collaboration was started between Prof Kristijan Ramadan's and Prof Benedikt Kessler's labs to identify E3 ligases and p97 co-factors involved in the MRN complex ubiquitination. For this, individual MRN complex components were cloned into APEX-2 peroxidase-expressing plasmids to establish stable HEK293 FRT T-REX inducible cell lines. These cells can then be exposed to IR and treated with biotin-phenol and H_2O_2 to induce biotin-phenoxyl radicals, resulting in the biotinylation of nearby electron-rich amino acids. This technique allows the creation of a proteomic map of the MRN complex and its interacting proteins after DNA damage, identifying both strong and weak/transient interaction partners (Rhee et al., 2013, Gupta et al., 2018). The biotinylated proteins will be isolated from nuclear factions and analysed by non-labelled quantitative mass spectrometry.

From the APEX-2 screen, candidate E3 ligases and p97 cofactors can be confirmed by a variety of methods such as immunoprecipitation (+/-IR), cycloheximide (CHX) protein

stability assays (with or without IR), and immunofluorescence-based microscopy after IR. Furthermore, it could be determined how the identified E3 ligase(s) and p97 cofactor(s) affect the ubiquitination status of the MRN complex and whether these interactions are IR-inducible. Proximity ligation assays can also be used to localise interactions between the MRN complex and the identified E3 ubiquitin ligases as well as p97 co-factors. It would also be interesting to study how the inactivation of identified factors affects DNA end resection by ssDNA assays such as the quantitative single molecule analysis of resection tracks (SMART) assay and the semi-quantitative BrdU assay under non-denaturing conditions (Cruz-Garcia et al., 2014, Kilgas et al., 2021). The effects of inactivating specific E3 ligases and p97 co-factors on DSB repair pathway choice can be studied by FACS-based reporter assays, which would allow us to determine to what extent are these potential candidates involved in the regulation of MRE11-mediated DNA end resection. Furthermore, it could be studied how the inactivation of identified E3 ligases and p97 co-factors affect cancer cell radiosensitisation across a panel of different cancer cell lines and be determined whether radiosensitisation is dependent on the catalytic activity of the candidate E3 ligase. An alternative approach to a mass spectrometry-based screening would be to do a functional genomic CRISPR-Cas9 screen to determine potential E3 ligases for the MRN complex relevant in cancer. For instance, a recently published CRISPR-Cas9 screen of the human ubiquitin pathways uncovered several E3 ligases and DUBs whose loss sensitises cells to various inhibitors used in targeting cancer, including inhibitors of the cell cycle progression, cytoskeletal integrity, metabolism, and intracellular transport (Hundley et al., 2021).

Finally, to understand why phosphorylation of the MRN complex is important for its subsequent disassembly from chromatin and how this is connected to p97, it would be necessary to study whether chemical inhibition of upstream DDR kinases affects the recruitment of p97, downstream E3 ligases and p97 co-factors after IR as well as how phosphorylation affects the MRN complex ubiquitination and their consequent association with p97. Furthermore, it should be determined how these PTMs on the MRN complex regulate IR sensitivity by cell survival assays.

Overall, the p97 system is an attractive target in cancer therapy and small molecule inhibitors of p97 ATPase activity have been developed for clinical studies. As p97 is a

pleiotropic protein with crucial cytoplasmic and nuclear functions in the maintenance of cellular homeostasis, discovering new targetable enzymes in specific p97-coordinated pathways would allow us to control p97 in a more specific way and thereby decrease chances of developing side-effects associated with p97 inactivation.

Appendices

Table 2 Table of antibodies and reagents used, their sources and catalogue numbers.

REAGENT or RESOURCE	SOURCE	IDENTIFIER
Antibodies		
BrdU Mouse monoclonal (dilution 1:300)	BD Biosciences	Cat# 347580
Phospho-Histone H2A.X (Ser139) Mouse monoclonal (dilution: IF: 1:500)	Millipore	Cat# 2739172
Phospho-Histone H2A.X (Ser139) Rabbit polyclonal (dilution: IF: 1:500)	Cell Signaling	Cat# 2577
RPA70/RPA1 Rabbit polyclonal (dilution: IF: 1:300)	Cell Signaling	Cat# 2267
P97/VCP Rabbit polyclonal (dilution: WB: 1:1,000; IHC: 1:2,000)	Proteintech	Cat# 10736-1-AP
53BP1 Rabbit polyclonal (dilution: IF: 1:250)	Cell Signaling	Cat# 4937
RAD51 Mouse monoclonal (dilution: IF: 1:100)	Santa Cruz	Cat# 398587
RAD52 Mouse monoclonal (dilution: IF: 1:100)	Santa Cruz	Cat# 365341
RAD50 Mouse monoclonal (dilution: WB: 1,1000; IF: 1:200)	Abcam	Cat# 89
MRE11 Rabbit polyclonal (dilution: WB: 1:1,000; IF: 1:200)	Abcam	Cat# 33125
MRE11 Mouse monoclonal (dilution: WB: 1:1,000; IF: 1:200)	Abcam	Cat# ab214
L3MBTL1 Rabbit polyclonal (dilution: WB: 1:1000)	Abcam	Cat# ab51880
MAD2B Mouse monoclonal (dilution: IF: 1:200)	BD Biosciences	Cat# 612266
NBS1 Mouse monoclonal (dilution: WB: 1:1,000)	BD Biosciences	Cat# 611870
CHK1 Rabbit polyclonal (dilution: WB: 1:1,000)	Abcam	Cat# ab47574
Phospho-CHK1 Rabbit polyclonal (S345) (dilution: WB: 1:1,000)	Abcam	Cat# ab58567
ATM Mouse monoclonal (dilution: WB: 1:1,000)	Novus Biologicals	Cat# 2C1
Phospho-ATM Mouse monoclonal (S1981) (dilution: WB: 1:1,000)	Cell Signaling	Cat# 4526
CHK2 Rabbit polyclonal (dilution: WB: 1:1,000)	Abcam	Cat# ab47433
Phospho-CHK2 (Thr68) Rabbit monoclonal (dilution: WB: 1:1,000)	Cell Signaling	Cat#2197
Vinculin Mouse monoclonal (dilution: WB: 1:1,000)	Abcam	Cat# ab18058
Lamin A/C Mouse monoclonal (dilution: WB: 1:1,000)	Cell Signaling	Cat# 4777
Histone H2B Rabbit monoclonal (dilution: WB: 1:1,000)	Cell Signaling	Cat# 12364
Alexa Fluor 488 Rabbit polyclonal (dilution: IF: 1:500)	Thermo Fisher Scientific	Cat# A-11034
Alexa Fluor 488 Mouse polyclonal (dilution: IF: 1:500)	Thermo Fisher Scientific	Cat# A-21202
Alexa Fluor 568 Rabbit polyclonal (dilution: IF: 1:500)	Thermo Fisher Scientific	Cat# A-11011
Alexa Fluor 568 Mouse polyclonal (dilution: IF: 1:500)	Thermo Fisher Scientific	Cat# A-10037
RPA32/RPA2 (phospho S4+S8) rabbit polyclonal (dilution: IF: 1:300)	Abcam	Cat# ab87277
KU80 Mouse monoclonal (dilution: WB: 1:1,000)	Abcam	Cat# 119935

Lamin B1 Rabbit polyclonal (dilution: WB: 1:1,000)	Thermo Fisher Scientific	Cat# PA5-19468
Mouse 800 secondary (dilution: WB: 1:10,000)	LI-COR	Cat# 925-32210
Rabbit 680 secondary (dilution: WB: 1:10,000)	LI-COR	Cat# 925-68021
β-actin Mouse monoclonal (dilution: WB: 1:1,000)	Thermo Fisher Scientific	Cat# AM4302
β-actin Rabbit (13E5) monoclonal (dilution: WB: 1:1,000)	Cell Signaling	Cat# 4970
Control Rabbit IgG (dilution: WB: 1:1,000)	Non-commercial	Kristijan Ramadan Lab
Rabbit IgG (HRP conjugated) Goat polyclonal (dilution: WB: 1:10,000)	Sigma-Aldrich	Cat# A9169
Mouse IgG (HRP conjugated) Rabbit polyclonal (dilution: WB: 1:10,000)	Sigma-Aldrich	Cat# A9044
Goat anti-Rabbit IgG (H+L) Secondary Antibody, Biotin (dilution: IHC: 1:10,000)	Thermo Fisher Scientific	Cat# 65-6140
Biological samples		
Bladder cancer human tumour samples (HGT1)	Oxford Radcliffe Biobank	http://orb.ndcls.ox.ac.uk
Chemicals, peptides, and recombinant proteins		
Avidin	Vector labs	Cat# SP-2001
Biotin	Vector labs	Cat# SP-2001
3,3’-Diaminobenzidine (DAB)	Vector labs	Cat# SK-4100
Dibutyl phthalate polystyrene xylene (DPX)	Sigma-Aldrich	Cat#1005790500
Harris’ haematoxylin	Sigma-Aldrich	Cat#HHS32-1L
5’-Bromo-2’-deoxyuridine (BrdU)	Sigma-Aldrich	Cat# B5002
5-Ethynyl-2’-deoxyuridine (EdU)	Thermo Fisher Scientific	Cat# A10044
Cycloheximide	Sigma-Aldrich	Cat# C1988
Benzonase	Millipore	Cat# 71205
Doxycycline	PanReac AppliChem	Cat# A2951,0025
Puromycin	Thermo Fisher Scientific	Cat# A1113802
Hoechst 3325	Sigma-Aldrich	Cat# 23491-45-4
RNase A (10 mg/mL)	Thermo Fisher Scientific	Cat# EN0531
ProLong Diamond antifade with DAPI	Thermo Fisher Scientific	Cat# P36962
cOmplete™, Mini, EDTA-free Protease Inhibitor Cocktail	Roche	Cat# 11836170001
Intercept® (PBS) Blocking Buffer	LI-COR	Cat# 927-70001
Sequencing Grade Modified Trypsin	Promega	Cat# V5111
Bovine Serum Albumin (BSA)	Sigma-Aldrich	Cat# 9048-46-8
Fetal Bovine Serum (FBS)	Thermo Fisher Scientific	Cat# 11573397
Trypsin-EDTA (0.25%)	Thermo Fisher Scientific	Cat# 25200072
Sodium azide 0.1 M solution	Sigma-Aldrich	Cat# 08591

Radio-immunoprecipitation Assay (RIPA) buffer	Thermo Fisher Scientific	Cat#89901
Fisher Bioreagents™ Phosphatase Inhibitor Cocktail I	Thermo Fisher Scientific	Cat# 12821650
Pierce™ Protease Inhibitor Mini Tablets, EDTA-free	Thermo Fisher Scientific	Cat# A32955
Bicinchoninic acid assay (BCA)	Thermo Fisher Scientific	Cat#23225
Lipofectamine RNAiMAX	Thermo Fisher Scientific	Cat# 13778-150
Lipofectamine 3000	Thermo Fisher Scientific	Cat# L3000008
QIAGEN maxiprep kit	QIAGEN	Cat# 12362
FuGENE Transfection Reagent	Promega	Cat# E2311
jetPRIME Transfection Reagent	Polyplus-transfection	Cat# 114-01
Opti-MEM reduced serum medium	Thermo Fisher Scientific	Cat# 11058021
CB-5083	MedChem Express	Cat# HY-12861
Mirin	Sigma-Aldrich	Cat# M9948
PFM01	Tocris	Cat# 6222
PFM39	Sigma-Aldrich	Cat# SML1839
Dimethyl sulfoxide (DMSO)	Sigma-Aldrich	Cat# D2650
Methanol	Thermo Fisher Scientific	Cat# 67-56-1
Methyl cellulose	Thermo Fisher Scientific	Cat# 155496
Nitrocellulose membrane	Thermo Fisher Scientific	Cat# 88018
N-Ethylmaleimide (NEM)	Sigma-Aldrich	Cat# EE3876-25G
Tween-20	Sigma-Aldrich	Cat# P7949
Tween-80	Sigma-Aldrich	Cat# 9005-65-6
Puromycin	Gibco	Cat# A11138-03
G-418	Sigma-Aldrich	Cat# 108321-42-2
Gefitinib	Sigma-Aldrich	Cat# SML1657
Matrigel	BD Biosciences	Cat# 356237
Phosphate buffered saline (PBS)	Gibco	Cat# 10010023
20X Transfer buffer	Bio-Rad	Cat# 10026938
10X Running buffer (Tris/Glycine/SDS)	Bio-Rad	Cat# 1610772
Sodium Dodecyl Sulphate (SDS)	Sigma-Aldrich	Cat# 151-21-3
Laemmli 2X concentrate	Sigma-Aldrich	Cat# S3401
Antibody diluent	LI-COR	Cat# 927-75001
Hydroxyurea (HU)	Sigma	Cat# H8627
Triton X-100	Sigma-Aldrich	Cat# T8787
4-(2-hydroxyethyl)-1-piperazineethanesulfonic acid (HEPES)	Sigma-Aldrich	Cat# H4034
Sucrose	Sigma-Aldrich	Cat# S0389
Glycerol	Sigma-Aldrich	Cat# 56-81-5

Skimmed milk powder	Sigma-Aldrich	Cat# 70166
Magnesium Chloride ($MgCl_2$)	Thermo Fisher Scientific	Cat# AM9530G
Sodium chloride (NaCl)	Sigma-Aldrich	Cat# S5150
Potassium chloride (KCl)	Sigma-Aldrich	Cat# 231-211-8
Sodium bicarbonate ($NaHCO_3$)	Sigma-Aldrich	Cat#144-55-8
Magnesium sulphate ($MgSO_4$)	Sigma-Aldrich	Cat#7487-88-9
Hydrogen peroxide (H_2O_2) (30% solution)	Thermo Fisher Scientific	Cat# 7722-84-1
Lithium carbonate (Li. $_2$CO. $_3$)	Sigma-Aldrich	Cat#554-13-2
Crystal violet powder	Sigma-Aldrich	Cat# 548-62-9
SOC outgrowth medium	NEB	Cat# B9020S
Xylene	Thermo Fisher Scientific	Cat#1330-20-7
Normal goat serum	Agilent	Cat# X090710-8
EDTA	Thermo Fisher Scientific	Cat# 15575020
EGTA	Sigma-Aldrich	Cat# 67-42-5
Tris hydrochloride (Tris-HCl)	Sigma-Aldrich	Cat# 1185-53-1
Formaldehyde 36% (39% w/v)	VWR	Cat# 50-00-0
Click-IT EdU Alexa Fluor 647 imaging kit	Thermo Fisher Scientific	Cat# C10340
Click-IT EdU Alexa Fluor 555 imaging kit	Thermo Fisher Scientific	Cat# C10338
McCoy's 5A Medium	Thermo Fisher Scientific	Cat# 16600082
Trypan blue solution	Thermo Fisher Scientific	Cat#15250061
Pierce Anti-HA Magnetic Beads	Thermo Fisher Scientific	Cat# 88836
Dynabeads™ Protein A	Thermo Fisher Scientific	Cat# 10002D
Portein A magnetic beads	NEB	Cat# S1425S
Dynabeads™ Protein G	Thermo Fisher Scientific	Cat# 10003D
Strep-Tactin® Sepharose® 50% suspension beads	IBA Life Sciences	Cat# 2-1201-010
MagStrep "type3" XT beads	IBA Life Sciences	Cat# 2-4090-002
SuperSignal™ West Pico PLUS Chemiluminescent Substrate	Thermo Fisher Scientific	Cat# 34579
Deposited data		
ProteomeXchange Consortium	PRIDE	PXD016279
Experimental models: cell lines		
Human: T-24	German Collection of Microorganisms and Cell Cultures (DSMZ)	DSMZ No 376

Human: RT112	German Collection of Microorganisms and Cell Cultures (DSMZ)	DSMZ No 418
Human: HEK293	ATCC	Cat# 300192/p777_HEK293
Human: DR-GFP U2OS	Laboratory of Dr Timothy Humphrey (Ahrabi et al., 2016)	N/A
Human: SA-GFP U2OS	Laboratory of Dr. Pavel Janscak (Paliwal et al., 2014)	N/A
RT112 (shMRE11)	Laboratory of Prof Anne E Kiltie (Na et al., 2021)	N/A
Experimental models: organisms/strains		
CD-1 nude mice (Female)	Charles River Laboratories	Strain Code: 086 (Homozygous)
Oligonucleotides		
siRNA_Control (proprietary sequence) (final concentration: 10-40 nM, depending on targeting siRNAs used)	QIAGEN	Cat# 1027280
siRNA_RAD51 (5'- AAGGGAATTAGTGAAGCCAAA-3') (final concentration: 10 nM)	QIAGEN	Cat# SI02663682
siRNA_RAD52 (5'-AAGGATGGTTCATATCATGAA-3') (final concentration: 10 nM)	QIAGEN	Cat# SI03035123
siRNA_MRE11 (5'GAGCAUAACUCCAUAAGUA(dT)(dT)-3') (final concentration: 20 nM)	Thermo Fisher Scientific	Cat# 10620310
siRNA_XRCC5/siKU80 (5'-GCAUGGAUGUGAUUCAACA-3') (final concentration: 20 nM)	Dharmacon	Cat# 7520
siRNA_p97 (5'-UUCUGUUUGAGAAUGGCUGUU-3') (final concentration: 20 nM)	Thermo Fisher Scientific	Cat# 10620310
siRNA_p97_2 (5'-AACAGCCAUUCUCAAACAGAA-3') (final concentration: 20 nM)	QIAGEN	N/A
siRNA_L3MBT1 (5'-AAGCGAGUAUAAGCC-3') (final concentration: 40 nM)	Microsynth	N/A
siRNA_L3MBT1_2 (5'-CCAGGCAGUCACUCA-3') (final concentration: 40 nM)	Micorynth	N/A
shMRE11_foward (5'-GAT CCG AAC CTG GTC CCA GAG GAG TTC AAG AGA CTC CTC TGG GAC CAG GTT CTT TTT TGG AAA-3')	Laboratory of Prof Anne E Kiltie	N/A

shMRE11_reverse (5’ 5’-AGC TTT TCC AAA AAA GAA CCT GGT CCC AGA GGA GTC TCT TGA ACT CCT CTG GGA CCA GGT TCG-3’)	Laboratory of Prof Anne E Kiltie	N/A
Recombinant DNA		
pcDNA3.3 N-term HA-MRE11	Laboratory of Prof Anne E Kiltie (Nicholson et al., 2017)	N/A
pcDNA5-p97-EQ-Myc-Strep	Laboratory of Prof Kristijan Ramadan (Meerang et al., 2011)	N/A
Software and algorithms		
Prism 8	GraphPad Software	https://www.graphpad.com
Fiji	NIH	https://imagej.net/Fiji/Downloads
FlowJo v10	FlowJo	https://www.flowjo.com/solutions/flowjo/downloads
Image Studio Lite 5.2	LI-COR	https://www.licor.com/bio/image-studio-lite/download
Omega FLUOstar	BMG Labtech	https://www.bmglabtech.com/omega-series/
UCSC Xena	University of California, Santa Cruz	https://www.biorxiv.org/content/10.1101/326470v6
Proteome Discoverer Software	Thermo Fisher Scientific	https://thermo.flexnetoperations.com/control/thmo/login
MASCOT 2.3	Matrix Science Inc	http://www.matrixscience.com/
PRIDE	Wellcome Genome Campus, Hinxton, Cambridgeshire	https://www.ebi.ac.uk/pride/archive/
Other		
Round cover glasses; 9 mm; thickness: No. 1	VWR	Cat# 631-0169
6-well plate, round	Thermo Fisher Scientific	Cat# 174901
T75 flasks	Thermo Fisher Scientific	Cat# 156499
4-20% SDS-PAGE precast gels (10-well)	Bio-Rad	Cat#4561096
Forceps	Sigma-Aldrich	Cat# F3767
Kimwipes	Thermo Fisher Scientific	Cat# 06-666

Superfrost Plus Microscope Slides	Thermo Fisher Scientific	Cat #22-037-246
Magnetic rack for IPs	Thermo Fisher Scientific	Cat ##12321D
GSR D1 gamma irradiator	Gamma-Service Medical GmbH	N/A
Zeiss 710 confocal microscope	Zeiss	N/A
Nikon Ni-E epifluorescent microscope	Nikon	N/A
Aperio ScanScope™ CS2 scanner	Leica Biosystems	N/A
LI-COR imaging system	Odyssey	N/A
NanoDrop Spectrophotometer	Thermo Fisher Scientific	Cat# ND-ONE-W

A

MRE11-HA pull-down Mascot output (significance threshold p<0.001)			
Description	**Score**	**No. of significant sequences**	**emPAI**
MRE11	419	9	0.59
RAD50	269	10	0.28
NBS1	247	5	0.25
VCP/p97	228	5	0.23

Figure 58 Related to Figure 13. Mass spectrometry screen of the MRE11 interactome.

Abundance of MRE11 interaction partners based on SILAC quantifications identifies RAD50, NBS1 and p97 with similar abundance. The experiments were conducted by Dr Judith Nicholson from Prof Anne Kiltie's group.

A

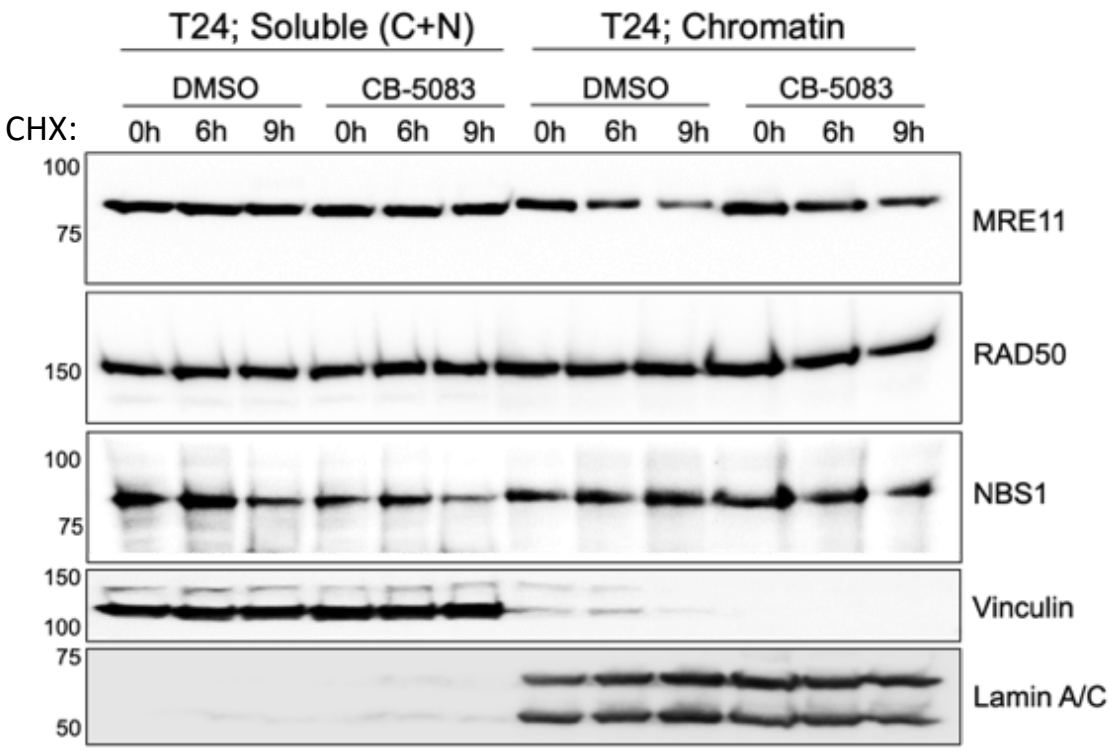
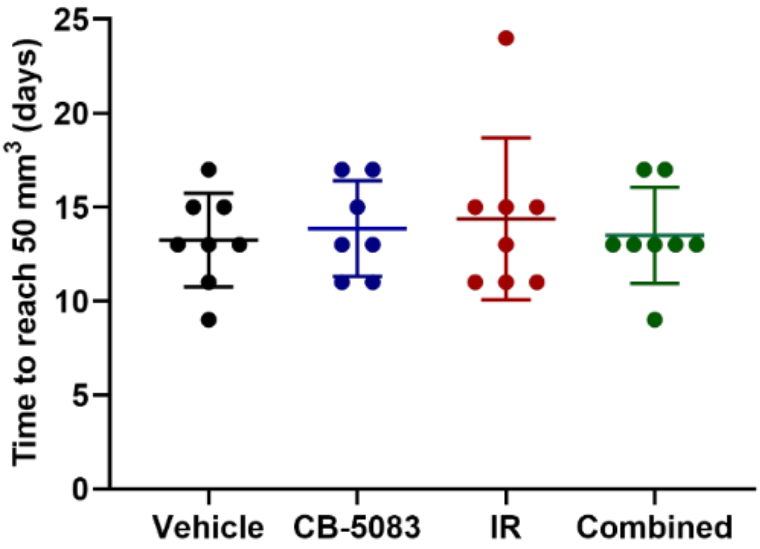


Figure 59 Sub-fractionation blot of a CHX chase of the MRN complex upon p97 inhibition. T24 cells treated with CHX with or without CB-5083 upon 10 Gy IR. Soluble and insoluble fractions were run on the same gel. Vinculin serves as loading control for the soluble fraction. Lamin A/C serves as a loading control for chromatin fraction; n=3 independent experiments. Abbreviations: C+N indicates cytoplasm and nucleoplasm fractions. These data were created and analysed by Dr Abhay Narayan Singh from Prof Kristijan Ramadan's group.

A



B

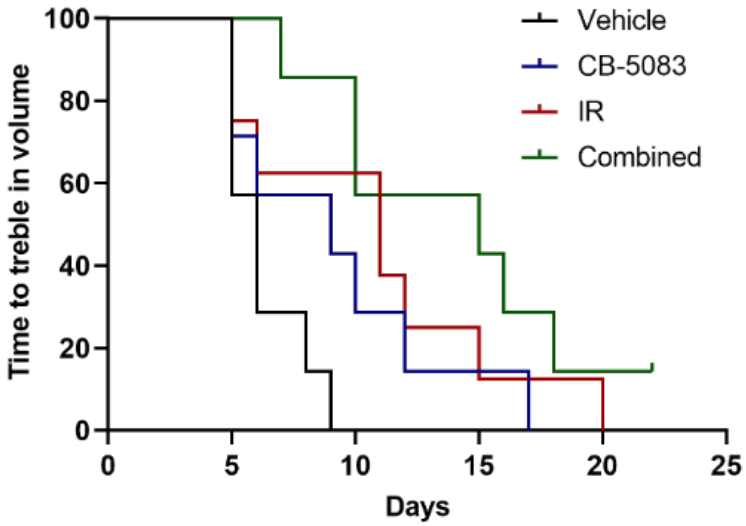


Figure 60 Related to Figure 55. CB-5083 effects *in vivo.*

A) Time (in days) to reach 50 mm^3 in tumour size for individual CD-1 nude mice with RT112 superficial xenografts implanted into the flank. No significant difference was observed between treatment groups. Statistical analysis: One-way ANOVA. **B**) Kaplan-Meier survival curve of CD-1 nude mice with RT112 xenografts (N=8 mice per group) showing the time (days) to treble in tumour volume. This data was generated and analysed by Dr Salome Paillas. Susan Kilgas helped with parts of the experiment and data analysis for tumour growth curves.

References

Acharya, P., Liao, M., Engel, J. C. & Correia, M. A. 2011. Liver cytochrome P450 3A endoplasmic reticulum-associated degradation: a major role for the p97 AAA ATPase in cytochrome P450 3A extraction into the cytosol. J Biol Chem, 286, 3815-28.

Acs, K., Luijsterburg, M. S., Ackermann, L., Salomons, F. A., Hoppe, T. & Dantuma, N. P. 2011. The AAA-ATPase VCP/p97 promotes 53BP1 recruitment by removing L3MBTL1 from DNA double-strand breaks. Nat Struct Mol Biol, 18, 1345-50.

Aguilera, A. & Garcia-Muse, T. 2012. R loops: from transcription byproducts to threats to genome stability. Mol Cell, 46, 115-24.

Ahrabi, S., Sarkar, S., Pfister, S. X., Pirovano, G., Higgins, G. S., Porter, A. C. & Humphrey, T. C. 2016. A role for human homologous recombination factors in suppressing microhomology-mediated end joining. Nucleic Acids Res, 44, 5743-57.

Al-Minawi, A. Z., Saleh-Gohari, N. & Helleday, T. 2008. The ERCC1/XPF endonuclease is required for efficient single-strand annealing and gene conversion in mammalian cells. Nucleic Acids Res, 36, 1-9.

Alexandru, G., Graumann, J., Smith, G. T., Kolawa, N. J., Fang, R. & Deshaies, R. J. 2008. UBXD7 binds multiple ubiquitin ligases and implicates p97 in HIF1alpha turnover. Cell, 134, 804-16.

Alizadeh, E., Sanz, A. G., Garcia, G. & Sanche, L. 2013. Radiation Damage to DNA: The Indirect Effect of Low Energy Electrons. J Phys Chem Lett, 4, 820-825.

Alsbeih, G., Al-Hadyan, K. & Al-Harbi, N. 2008. Assessment of carriers' frequency of a novel MRE11 mutation responsible for the rare ataxia telangiectasia-like disorder. Genet Test, 12, 387-9.

Altan, B., Yokobori, T., Ide, M., Bai, T., Yanoma, T., Kimura, A., Kogure, N., Suzuki, M., Bao, P., Mochiki, E., Ogata, K., Handa, T., Kaira, K., Nishiyama, M., Asao, T., Oyama, T. & Kuwano, H. 2016. High Expression of MRE11-RAD50-NBS1 Is Associated with Poor Prognosis and Chemoresistance in Gastric Cancer. Anticancer Res, 36, 5237-5247.

Anand, R., Jasrotia, A., Bundschuh, D., Howard, S. M., Ranjha, L., Stucki, M. & Cejka, P. 2019. NBS1 promotes the endonuclease activity of the MRE11-RAD50 complex by sensing CtIP phosphorylation. EMBO J, 38.

Anand, R., Ranjha, L., Cannavo, E. & Cejka, P. 2016. Phosphorylated CtIP Functions as a Co-factor of the MRE11-RAD50-NBS1 Endonuclease in DNA End Resection. Mol Cell, 64, 940-950.

Anand, R. P., Lovett, S. T. & Haber, J. E. 2013. Break-induced DNA replication. Cold Spring Harb Perspect Biol, 5, a010397.

Anderson, D. J., Le Moigne, R., Djakovic, S., Kumar, B., Rice, J., Wong, S., Wang, J., Yao, B., Valle, E., Kiss Von Soly, S., Madriaga, A., Soriano, F., Menon, M. K., Wu, Z. Y., Kampmann, M., Chen, Y., Weissman, J. S., Aftab, B. T., Yakes, F. M., Shawver, L., Zhou, H. J., Wustrow, D. & Rolfe, M. 2015. Targeting the AAA ATPase p97 as an Approach to Treat Cancer through Disruption of Protein Homeostasis. Cancer Cell, 28, 653-665.

Andres, S. N. & Williams, R. S. 2017. CtIP/Ctp1/Sae2, molecular form fit for function. DNA Repair (Amst), 56, 109-117.

Arshavsky, V. Y., Lamb, T. D. & Pugh, E. N., Jr. 2002. G proteins and phototransduction. Annu Rev Physiol, 64, 153-87.

Assenmacher, N. & Hopfner, K. P. 2004. MRE11/RAD50/NBS1: complex activities. Chromosoma, 113, 157-66.

Audebert, M., Salles, B. & Calsou, P. 2004. Involvement of poly(ADP-ribose) polymerase-1 and XRCC1/DNA ligase III in an alternative route for DNA double-strand breaks rejoining. J Biol Chem, 279, 55117-26.

Bai, Y., Wang, W., Li, S., Zhan, J., Li, H., Zhao, M., Zhou, X. A., Li, S., Li, X., Huo, Y., Shen, Q., Zhou, M., Zhang, H., Luo, J., Sung, P., Zhu, W. G., Xu, X. & Wang, J. 2019. C1QBP Promotes Homologous Recombination by Stabilizing MRE11 and Controlling the Assembly and Activation of MRE11/RAD50/NBS1 Complex. Mol Cell, 75, 1299-1314 e6.

Barazzuol, L., Jena, R., Burnet, N. G., Meira, L. B., Jeynes, J. C., Kirkby, K. J. & Kirkby, N. F. 2013. Evaluation of poly (ADP-ribose) polymerase inhibitor ABT-888 combined with radiotherapy and temozolomide in glioblastoma. Radiat Oncol, 8, 65.

Bartkova, J., Tommiska, J., Oplustilova, L., Aaltonen, K., Tamminen, A., Heikkinen, T., Mistrik, M., Aittomaki, K., Blomqvist, C., Heikkila, P., Lukas, J., Nevanlinna, H. & Bartek, J. 2008. Aberrations of the MRE11-RAD50-NBS1 DNA damage sensor complex in human breast cancer: MRE11 as a candidate familial cancer-predisposing gene. Mol Oncol, 2, 296-316.

Bays, N. W., Gardner, R. G., Seelig, L. P., Joazeiro, C. A. & Hampton, R. Y. 2001. Hrd1p/Der3p is a membrane-anchored ubiquitin ligase required for ER-associated degradation. Nat Cell Biol, 3, 24-9.

Becker, J. R., Clifford, G., Bonnet, C., Groth, A., Wilson, M. D. & Chapman, J. R. 2021. BARD1 reads H2A lysine 15 ubiquitination to direct homologous recombination. Nature, 596, 433-437.

Begg, A. C., Stewart, F. A. & Vens, C. 2011. Strategies to improve radiotherapy with targeted drugs. Nat Rev Cancer, 11, 239-53.

Bekker-Jensen, S., Lukas, C., Kitagawa, R., Melander, F., Kastan, M. B., Bartek, J. & Lukas, J. 2006. Spatial organization of the mammalian genome surveillance machinery in response to DNA strand breaks. J Cell Biol, 173, 195-206.

Bekker-Jensen, S. & Mailand, N. 2010. Assembly and function of DNA double-strand break repair foci in mammalian cells. DNA Repair (Amst), 9, 1219-28.

Berkovich, E., Monnat, R. J., Jr. & Kastan, M. B. 2007. Roles of ATM and NBS1 in chromatin structure modulation and DNA double-strand break repair. Nat Cell Biol, 9, 683-90.

Bhargava, R., Onyango, D. O. & Stark, J. M. 2016. Regulation of Single-Strand Annealing and its Role in Genome Maintenance. Trends Genet, 32, 566-575.

Bian, L., Meng, Y., Zhang, M. & Li, D. 2019. MRE11-RAD50-NBS1 complex alterations and DNA damage response: implications for cancer treatment. Mol Cancer, 18, 169.

Binette, J., Dube, M., Mercier, J., Halawani, D., Latterich, M. & Cohen, E. A. 2007. Requirements for the selective degradation of CD4 receptor molecules by the human immunodeficiency virus type 1 Vpu protein in the endoplasmic reticulum. Retrovirology, 4, 75.

Blackstock, A. W., Mornex, F., Partensky, C., Descos, L., Case, L. D., Melin, S. A., Levine, E. A., Mishra, G., Limentani, S. A., Kachnic, L. A. & Tepper, J. E. 2006. Adjuvant gemcitabine and concurrent radiation for patients with resected pancreatic cancer: a phase II study. Br J Cancer, 95, 260-5.

Bodnar, N. O. & Rapoport, T. A. 2017. Molecular Mechanism of Substrate Processing by the Cdc48 ATPase Complex. Cell, 169, 722-735 e9.

Bouwman, P., Aly, A., Escandell, J. M., Pieterse, M., Bartkova, J., Van Der Gulden, H., Hiddingh, S., Thanasoula, M., Kulkarni, A., Yang, Q., Haffty, B. G., Tommiska, J., Blomqvist, C., Drapkin, R., Adams, D. J., Nevanlinna, H., Bartek, J., Tarsounas, M., Ganesan, S. & Jonkers, J. 2010. 53BP1 loss rescues BRCA1 deficiency and is associated with triple-negative and BRCA-mutated breast cancers. Nat Struct Mol Biol, 17, 688-95.

Brandman, O., Stewart-Ornstein, J., Wong, D., Larson, A., Williams, C. C., Li, G. W., Zhou, S., King, D., Shen, P. S., Weibezahn, J., Dunn, J. G., Rouskin, S., Inada, T., Frost, A. & Weissman, J. S. 2012. A ribosome-bound quality control complex triggers degradation of nascent peptides and signals translation stress. Cell, 151, 1042-54.

Brandt, S., Samartzis, E. P., Zimmermann, A. K., Fink, D., Moch, H., Noske, A. & Dedes, K. J. 2017. Lack of MRE11-RAD50-NBS1 (MRN) complex detection occurs frequently in low-grade epithelial ovarian cancer. BMC Cancer, 17, 44.

Bressan, D. A., Baxter, B. K. & Petrini, J. H. 1999. The Mre11-Rad50-Xrs2 protein complex facilitates homologous recombination-based double-strand break repair in Saccharomyces cerevisiae. Mol Cell Biol, 19, 7681-7.

Broderick, R., Nieminuszczy, J., Baddock, H. T., Deshpande, R., Gileadi, O., Paull, T. T., Mchugh, P. J. & Niedzwiedz, W. 2016. EXD2 promotes homologous recombination by facilitating DNA end resection. Nat Cell Biol, 18, 271-280.

Brodsky, J. L. 2012. Cleaning up: ER-associated degradation to the rescue. Cell, 151, 1163-7.

Brown, J. M., Carlson, D. J. & Brenner, D. J. 2014. The tumor radiobiology of SRS and SBRT: are more than the 5 Rs involved? Int J Radiat Oncol Biol Phys, 88, 254-62.

Bryant, H. E., Schultz, N., Thomas, H. D., Parker, K. M., Flower, D., Lopez, E., Kyle, S., Meuth, M., Curtin, N. J. & Helleday, T. 2005. Specific killing of BRCA2-deficient tumours with inhibitors of poly(ADP-ribose) polymerase. Nature, 434, 913-7.

Buchberger, A., Schindelin, H. & Hanzelmann, P. 2015. Control of p97 function by cofactor binding. FEBS Lett, 589, 2578-89.

Buckley, A. M., Lynam-Lennon, N., O'neill, H. & O'sullivan, J. 2020. Targeting hallmarks of cancer to enhance radiosensitivity in gastrointestinal cancers. Nat Rev Gastroenterol Hepatol, 17, 298-313.

Buis, J., Wu, Y., Deng, Y., Leddon, J., Westfield, G., Eckersdorff, M., Sekiguchi, J. M., Chang, S. & Ferguson, D. O. 2008. Mre11 nuclease activity has essential roles in DNA repair and genomic stability distinct from ATM activation. Cell, 135, 85-96.

Bunting, S. F., Callen, E., Wong, N., Chen, H. T., Polato, F., Gunn, A., Bothmer, A., Feldhahn, N., Fernandez-Capetillo, O., Cao, L., Xu, X., Deng, C. X., Finkel, T., Nussenzweig, M., Stark, J. M. & Nussenzweig, A. 2010. 53BP1 inhibits homologous recombination in Brca1-deficient cells by blocking resection of DNA breaks. Cell, 141, 243-54.

Bursavich, M. G., Parker, D. P., Willardsen, J. A., Gao, Z. H., Davis, T., Ostanin, K., Robinson, R., Peterson, A., Cimbora, D. M., Zhu, J. F. & Richards, B. 2010. 2-Anilino-4-aryl-1,3-thiazole inhibitors of valosin-containing protein (VCP or p97). Bioorg Med Chem Lett, 20, 1677-9.

Cancer Genome Atlas Research, N., Weinstein, J. N., Collisson, E. A., Mills, G. B., Shaw, K. R., Ozenberger, B. A., Ellrott, K., Shmulevich, I., Sander, C. & Stuart, J. M. 2013. The Cancer Genome Atlas Pan-Cancer analysis project. Nat Genet, 45, 1113-20.

Cannavo, E. & Cejka, P. 2014. Sae2 promotes dsDNA endonuclease activity within Mre11-Rad50-Xrs2 to resect DNA breaks. Nature, 514, 122-5.

Cao, L., Xu, X., Bunting, S. F., Liu, J., Wang, R. H., Cao, L. L., Wu, J. J., Peng, T. N., Chen, J., Nussenzweig, A., Deng, C. X. & Finkel, T. 2009. A selective requirement for 53BP1 in the biological response to genomic instability induced by Brca1 deficiency. Mol Cell, 35, 534-41.

Carr, A. M., Paek, A. L. & Weinert, T. 2011. DNA replication: failures and inverted fusions. Semin Cell Dev Biol, 22, 866-74.

Carvajal-Garcia, J., Cho, J. E., Carvajal-Garcia, P., Feng, W., Wood, R. D., Sekelsky, J., Gupta, G. P., Roberts, S. A. & Ramsden, D. A. 2020. Mechanistic basis for microhomology identification and genome scarring by polymerase theta. Proc Natl Acad Sci U S A, 117, 8476-8485.

Ceccaldi, R., Rondinelli, B. & D'andrea, A. D. 2016. Repair Pathway Choices and Consequences at the Double-Strand Break. Trends Cell Biol, 26, 52-64.

Cejka, P. 2015. DNA End Resection: Nucleases Team Up with the Right Partners to Initiate Homologous Recombination. J Biol Chem, 290, 22931-8.

Cerosaletti, K. & Concannon, P. 2004. Independent roles for nibrin and Mre11-Rad50 in the activation and function of Atm. J Biol Chem, 279, 38813-9.

Cerosaletti, K., Wright, J. & Concannon, P. 2006. Active role for nibrin in the kinetics of atm activation. Mol Cell Biol, 26, 1691-9.

Chang, E. Y., Tsai, S., Aristizabal, M. J., Wells, J. P., Coulombe, Y., Busatto, F. F., Chan, Y. A., Kumar, A., Dan Zhu, Y., Wang, A. Y., Fournier, L. A., Hieter, P., Kobor, M. S., Masson, J. Y. & Stirling, P. C. 2019. MRE11-RAD50-NBS1 promotes Fanconi Anemia R-loop suppression at transcription-replication conflicts. Nat Commun, 10, 4265.

Chapman, J. R., Sossick, A. J., Boulton, S. J. & Jackson, S. P. 2012a. BRCA1-associated exclusion of 53BP1 from DNA damage sites underlies temporal control of DNA repair. J Cell Sci, 125, 3529-34.

Chapman, J. R., Taylor, M. R. & Boulton, S. J. 2012b. Playing the end game: DNA double-strand break repair pathway choice. Mol Cell, 47, 497-510.

Chen, R. & Wold, M. S. 2014. Replication protein A: single-stranded DNA's first responder: dynamic DNA-interactions allow replication protein A to direct single-strand DNA intermediates into different pathways for synthesis or repair. Bioessays, 36, 1156-61.

Choi, E. J., Cho, B. J., Lee, D. J., Hwang, Y. H., Chun, S. H., Kim, H. H. & Kim, I. A. 2014. Enhanced cytotoxic effect of radiation and temozolomide in malignant glioma cells: targeting PI3K-AKT-mTOR signaling, HSP90 and histone deacetylases. BMC Cancer, 14, 17.

Chou, D. M., Adamson, B., Dephoure, N. E., Tan, X., Nottke, A. C., Hurov, K. E., Gygi, S. P., Colaiacovo, M. P. & Elledge, S. J. 2010. A chromatin localization screen reveals poly (ADP ribose)-regulated recruitment of the repressive polycomb and NuRD complexes to sites of DNA damage. Proc Natl Acad Sci U S A, 107, 18475-80.

Chou, T. F., Li, K., Frankowski, K. J., Schoenen, F. J. & Deshaies, R. J. 2013. Structure-activity relationship study reveals ML240 and ML241 as potent and selective inhibitors of p97 ATPase. ChemMedChem, 8, 297-312.

Choudhury, A., Nelson, L. D., Teo, M. T., Chilka, S., Bhattarai, S., Johnston, C. F., Elliott, F., Lowery, J., Taylor, C. F., Churchman, M., Bentley, J., Knowles, M. A., Harnden, P., Bristow, R. G., Bishop, D. T. & Kiltie, A. E. 2010. MRE11 expression is predictive of

cause-specific survival following radical radiotherapy for muscle-invasive bladder cancer. Cancer Res, 70, 7017-26.
Ciccia, A. & Elledge, S. J. 2010. The DNA damage response: making it safe to play with knives. Mol Cell, 40, 179-204.
Connelly, J. C., De Leau, E. S. & Leach, D. R. 1999. DNA cleavage and degradation by the SbcCD protein complex from Escherichia coli. Nucleic Acids Res, 27, 1039-46.
Cook, P. J., Ju, B. G., Telese, F., Wang, X., Glass, C. K. & Rosenfeld, M. G. 2009. Tyrosine dephosphorylation of H2AX modulates apoptosis and survival decisions. Nature, 458, 591-6.
Cruz-Garcia, A., Lopez-Saavedra, A. & Huertas, P. 2014. BRCA1 accelerates CtIP-mediated DNA-end resection. Cell Rep, 9, 451-9.
Cui, F. B., Li, R. T., Liu, Q., Wu, P. Y., Hu, W. J., Yue, G. F., Ding, H., Yu, L. X., Qian, X. P. & Liu, B. R. 2014. Enhancement of radiotherapy efficacy by docetaxel-loaded gelatinase-stimuli PEG-Pep-PCL nanoparticles in gastric cancer. Cancer Lett, 346, 53-62.
Daley, J. M., Niu, H., Miller, A. S. & Sung, P. 2015. Biochemical mechanism of DSB end resection and its regulation. DNA Repair (Amst), 32, 66-74.
Damiola, F., Pertesi, M., Oliver, J., Le Calvez-Kelm, F., Voegele, C., Young, E. L., Robinot, N., Forey, N., Durand, G., Vallee, M. P., Tao, K., Roane, T. C., Williams, G. J., Hopper, J. L., Southey, M. C., Andrulis, I. L., John, E. M., Goldgar, D. E., Lesueur, F. & Tavtigian, S. V. 2014. Rare key functional domain missense substitutions in MRE11A, RAD50, and NBN contribute to breast cancer susceptibility: results from a Breast Cancer Family Registry case-control mutation-screening study. Breast Cancer Res, 16, R58.
Dantuma, N. P., Acs, K. & Luijsterburg, M. S. 2014. Should I stay or should I go: VCP/p97-mediated chromatin extraction in the DNA damage response. Exp Cell Res, 329, 9-17.
Davis, E. J., Lachaud, C., Appleton, P., Macartney, T. J., Nathke, I. & Rouse, J. 2012. DVC1 (C1orf124) recruits the p97 protein segregase to sites of DNA damage. Nat Struct Mol Biol, 19, 1093-100.
Deng, C., Brown, J. A., You, D. & Brown, J. M. 2005. Multiple endonucleases function to repair covalent topoisomerase I complexes in Saccharomyces cerevisiae. Genetics, 170, 591-600.
Deng, S. K., Gibb, B., De Almeida, M. J., Greene, E. C. & Symington, L. S. 2014. RPA antagonizes microhomology-mediated repair of DNA double-strand breaks. Nat Struct Mol Biol, 21, 405-12.
Desai-Mehta, A., Cerosaletti, K. M. & Concannon, P. 2001. Distinct functional domains of nibrin mediate Mre11 binding, focus formation, and nuclear localization. Mol Cell Biol, 21, 2184-91.
Deshaies, R. J. 2014. Proteotoxic crisis, the ubiquitin-proteasome system, and cancer therapy. BMC Biol, 12, 94.
Deshpande, R. A., Lee, J. H., Arora, S. & Paull, T. T. 2016. Nbs1 Converts the Human Mre11/Rad50 Nuclease Complex into an Endo/Exonuclease Machine Specific for Protein-DNA Adducts. Mol Cell, 64, 593-606.
Dev, H., Chiang, T. W., Lescale, C., De Krijger, I., Martin, A. G., Pilger, D., Coates, J., Sczaniecka-Clift, M., Wei, W., Ostermaier, M., Herzog, M., Lam, J., Shea, A., Demir, M., Wu, Q., Yang, F., Fu, B., Lai, Z., Balmus, G., Belotserkovskaya, R., Serra, V., O'connor, M. J., Bruna, A., Beli, P., Pellegrini, L., Caldas, C., Deriano, L., Jacobs, J. J. L., Galanty, Y. & Jackson, S. P. 2018. Shieldin complex promotes DNA end-joining

and counters homologous recombination in BRCA1-null cells. Nat Cell Biol, 20, 954-965.

Dewan, M. Z., Galloway, A. E., Kawashima, N., Dewyngaert, J. K., Babb, J. S., Formenti, S. C. & Demaria, S. 2009. Fractionated but not single-dose radiotherapy induces an immune-mediated abscopal effect when combined with anti-CTLA-4 antibody. Clin Cancer Res, 15, 5379-88.

Digweed, M. & Sperling, K. 2004. Nijmegen breakage syndrome: clinical manifestation of defective response to DNA double-strand breaks. DNA Repair (Amst), 3, 1207-17.

Dikic, I., Wakatsuki, S. & Walters, K. J. 2009. Ubiquitin-binding domains - from structures to functions. Nat Rev Mol Cell Biol, 10, 659-71.

Dobrynin, G., Popp, O., Romer, T., Bremer, S., Schmitz, M. H., Gerlich, D. W. & Meyer, H. 2011. Cdc48/p97-Ufd1-Npl4 antagonizes Aurora B during chromosome segregation in HeLa cells. J Cell Sci, 124, 1571-80.

Doil, C., Mailand, N., Bekker-Jensen, S., Menard, P., Larsen, D. H., Pepperkok, R., Ellenberg, J., Panier, S., Durocher, D., Bartek, J., Lukas, J. & Lukas, C. 2009. RNF168 binds and amplifies ubiquitin conjugates on damaged chromosomes to allow accumulation of repair proteins. Cell, 136, 435-46.

Dupre, A., Boyer-Chatenet, L. & Gautier, J. 2006. Two-step activation of ATM by DNA and the Mre11-Rad50-Nbs1 complex. Nat Struct Mol Biol, 13, 451-7.

Duursma, A. M., Driscoll, R., Elias, J. E. & Cimprich, K. A. 2013. A role for the MRN complex in ATR activation via TOPBP1 recruitment. Mol Cell, 50, 116-22.

Edelmann, M. J., Nicholson, B. & Kessler, B. M. 2011. Pharmacological targets in the ubiquitin system offer new ways of treating cancer, neurodegenerative disorders and infectious diseases. Expert Rev Mol Med, 13, e35.

Escribano-Diaz, C., Orthwein, A., Fradet-Turcotte, A., Xing, M., Young, J. T., Tkac, J., Cook, M. A., Rosebrock, A. P., Munro, M., Canny, M. D., Xu, D. & Durocher, D. 2013. A cell cycle-dependent regulatory circuit composed of 53BP1-RIF1 and BRCA1-CtIP controls DNA repair pathway choice. Mol Cell, 49, 872-83.

Fagan-Solis, K. D., Simpson, D. A., Kumar, R. J., Martelotto, L. G., Mose, L. E., Rashid, N. U., Ho, A. Y., Powell, S. N., Wen, Y. H., Parker, J. S., Reis-Filho, J. S., Petrini, J. H. J. & Gupta, G. P. 2020. A P53-Independent DNA Damage Response Suppresses Oncogenic Proliferation and Genome Instability. Cell Rep, 30, 1385-1399 e7.

Farmer, H., Mccabe, N., Lord, C. J., Tutt, A. N., Johnson, D. A., Richardson, T. B., Santarosa, M., Dillon, K. J., Hickson, I., Knights, C., Martin, N. M., Jackson, S. P., Smith, G. C. & Ashworth, A. 2005. Targeting the DNA repair defect in BRCA mutant cells as a therapeutic strategy. Nature, 434, 917-21.

Feng, L. & Chen, J. 2012. The E3 ligase RNF8 regulates KU80 removal and NHEJ repair. Nat Struct Mol Biol, 19, 201-6.

Feng, L., Li, N., Li, Y., Wang, J., Gao, M., Wang, W. & Chen, J. 2015. Cell cycle-dependent inhibition of 53BP1 signaling by BRCA1. Cell Discov, 1, 15019.

Fielden, J., Wiseman, K., Torrecilla, I., Li, S., Hume, S., Chiang, S. C., Ruggiano, A., Narayan Singh, A., Freire, R., Hassanieh, S., Domingo, E., Vendrell, I., Fischer, R., Kessler, B. M., Maughan, T. S., El-Khamisy, S. F. & Ramadan, K. 2020. TEX264 coordinates p97- and SPRTN-mediated resolution of topoisomerase 1-DNA adducts. Nat Commun, 11, 1274.

Fievet, A., Bellanger, D., Valence, S., Mobuchon, L., Afenjar, A., Giuliano, F., Dubois D'enghien, C., Parfait, B., Pedespan, J. M., Auger, N., Rieunier, G., Collet, A., Burglen,

L., Stoppa-Lyonnet, D. & Stern, M. H. 2019. Three new cases of ataxia-telangiectasia-like disorder: No impairment of the ATM pathway, but S-phase checkpoint defect. Hum Mutat, 40, 1690-1699.

Fink, L. S., Lerner, C. A., Torres, P. F. & Sell, C. 2010. Ku80 facilitates chromatin binding of the telomere binding protein, TRF2. Cell Cycle, 9, 3798-806.

Fok, J. H. L., Ramos-Montoya, A., Vazquez-Chantada, M., Wijnhoven, P. W. G., Follia, V., James, N., Farrington, P. M., Karmokar, A., Willis, S. E., Cairns, J., Nikkila, J., Beattie, D., Lamont, G. M., Finlay, M. R. V., Wilson, J., Smith, A., O'connor, L. O., Ling, S., Fawell, S. E., O'connor, M. J., Hollingsworth, S. J., Dean, E., Goldberg, F. W., Davies, B. R. & Cadogan, E. B. 2019. AZD7648 is a potent and selective DNA-PK inhibitor that enhances radiation, chemotherapy and olaparib activity. Nat Commun, 10, 5065.

Foster, S. S., Balestrini, A. & Petrini, J. H. 2011. Functional interplay of the Mre11 nuclease and Ku in the response to replication-associated DNA damage. Mol Cell Biol, 31, 4379-89.

Fradet-Turcotte, A., Canny, M. D., Escribano-Diaz, C., Orthwein, A., Leung, C. C., Huang, H., Landry, M. C., Kitevski-Leblanc, J., Noordermeer, S. M., Sicheri, F. & Durocher, D. 2013. 53BP1 is a reader of the DNA-damage-induced H2A Lys 15 ubiquitin mark. Nature, 499, 50-4.

Franz, A., Ackermann, L. & Hoppe, T. 2014. Create and preserve: proteostasis in development and aging is governed by Cdc48/p97/VCP. Biochim Biophys Acta, 1843, 205-15.

Franz, A., Orth, M., Pirson, P. A., Sonneville, R., Blow, J. J., Gartner, A., Stemmann, O. & Hoppe, T. 2011. CDC-48/p97 coordinates CDT-1 degradation with GINS chromatin dissociation to ensure faithful DNA replication. Mol Cell, 44, 85-96.

Franz, A., Pirson, P. A., Pilger, D., Halder, S., Achuthankutty, D., Kashkar, H., Ramadan, K. & Hoppe, T. 2016. Chromatin-associated degradation is defined by UBXN-3/FAF1 to safeguard DNA replication fork progression. Nat Commun, 7, 10612.

Fullbright, G., Rycenga, H. B., Gruber, J. D. & Long, D. T. 2016. p97 Promotes a Conserved Mechanism of Helicase Unloading during DNA Cross-Link Repair. Mol Cell Biol, 36, 2983-2994.

Garcia, V., Phelps, S. E., Gray, S. & Neale, M. J. 2011. Bidirectional resection of DNA double-strand breaks by Mre11 and Exo1. Nature, 479, 241-4.

Ghezraoui, H., Oliveira, C., Becker, J. R., Bilham, K., Moralli, D., Anzilotti, C., Fischer, R., Deobagkar-Lele, M., Sanchiz-Calvo, M., Fueyo-Marcos, E., Bonham, S., Kessler, B. M., Rottenberg, S., Cornall, R. J., Green, C. M. & Chapman, J. R. 2018. 53BP1 cooperation with the REV7-shieldin complex underpins DNA structure-specific NHEJ. Nature, 560, 122-127.

Goodarzi, A. A., Noon, A. T., Deckbar, D., Ziv, Y., Shiloh, Y., Lobrich, M. & Jeggo, P. A. 2008. ATM signaling facilitates repair of DNA double-strand breaks associated with heterochromatin. Mol Cell, 31, 167-77.

Gottlich, B., Reichenberger, S., Feldmann, E. & Pfeiffer, P. 1998. Rejoining of DNA double-strand breaks in vitro by single-strand annealing. Eur J Biochem, 258, 387-95.

Goy, A., Younes, A., Mclaughlin, P., Pro, B., Romaguera, J. E., Hagemeister, F., Fayad, L., Dang, N. H., Samaniego, F., Wang, M., Broglio, K., Samuels, B., Gilles, F., Sarris, A. H., Hart, S., Trehu, E., Schenkein, D., Cabanillas, F. & Rodriguez, A. M. 2005. Phase

II study of proteasome inhibitor bortezomib in relapsed or refractory B-cell non-Hodgkin's lymphoma. J Clin Oncol, 23, 667-75.
Gravel, S., Chapman, J. R., Magill, C. & Jackson, S. P. 2008. DNA helicases Sgs1 and BLM promote DNA double-strand break resection. Genes Dev, 22, 2767-72.
Grootjans, J., Kaser, A., Kaufman, R. J. & Blumberg, R. S. 2016. The unfolded protein response in immunity and inflammation. Nat Rev Immunol, 16, 469-84.
Groselj, B., Ruan, J. L., Scott, H., Gorrill, J., Nicholson, J., Kelly, J., Anbalagan, S., Thompson, J., Stratford, M. R. L., Jevons, S. J., Hammond, E. M., Scudamore, C. L., Kerr, M. & Kiltie, A. E. 2018. Radiosensitization In Vivo by Histone Deacetylase Inhibition with No Increase in Early Normal Tissue Radiation Toxicity. Mol Cancer Ther, 17, 381-392.
Guang, M. H. Z., Kavanagh, E. L., Dunne, L. P., Dowling, P., Zhang, L., Lindsay, S., Bazou, D., Goh, C. Y., Hanley, C., Bianchi, G., Anderson, K. C., O'gorman, P. & Mccann, A. 2019. Targeting Proteotoxic Stress in Cancer: A Review of the Role that Protein Quality Control Pathways Play in Oncogenesis. Cancers (Basel), 11.
Gupta, R., Somyajit, K., Narita, T., Maskey, E., Stanlie, A., Kremer, M., Typas, D., Lammers, M., Mailand, N., Nussenzweig, A., Lukas, J. & Choudhary, C. 2018. DNA Repair Network Analysis Reveals Shieldin as a Key Regulator of NHEJ and PARP Inhibitor Sensitivity. Cell, 173, 972-988 e23.
Gurvich, N., Perna, F., Farina, A., Voza, F., Menendez, S., Hurwitz, J. & Nimer, S. D. 2010. L3MBTL1 polycomb protein, a candidate tumor suppressor in del(20q12) myeloid disorders, is essential for genome stability. Proc Natl Acad Sci U S A, 107, 22552-7.
Haber, J. E. 1998. The many interfaces of Mre11. Cell, 95, 583-6.
Halazonetis, T. D., Gorgoulis, V. G. & Bartek, J. 2008. An oncogene-induced DNA damage model for cancer development. Science, 319, 1352-5.
Hanahan, D. & Weinberg, R. A. 2011. Hallmarks of cancer: the next generation. Cell, 144, 646-74.
Harrison, L. B., Chadha, M., Hill, R. J., Hu, K. & Shasha, D. 2002. Impact of tumor hypoxia and anemia on radiation therapy outcomes. Oncologist, 7, 492-508.
Hartsuiker, E., Neale, M. J. & Carr, A. M. 2009. Distinct requirements for the Rad32(Mre11) nuclease and Ctp1(CtIP) in the removal of covalently bound topoisomerase I and II from DNA. Mol Cell, 33, 117-23.
Hartsuiker, E., Vaessen, E., Carr, A. M. & Kohli, J. 2001. Fission yeast Rad50 stimulates sister chromatid recombination and links cohesion with repair. EMBO J, 20, 6660-71.
Hashimoto, Y., Ray Chaudhuri, A., Lopes, M. & Costanzo, V. 2010. Rad51 protects nascent DNA from Mre11-dependent degradation and promotes continuous DNA synthesis. Nat Struct Mol Biol, 17, 1305-11.
He, Y. J., Meghani, K., Caron, M. C., Yang, C., Ronato, D. A., Bian, J., Sharma, A., Moore, J., Niraj, J., Detappe, A., Doench, J. G., Legube, G., Root, D. E., D'andrea, A. D., Drane, P., De, S., Konstantinopoulos, P. A., Masson, J. Y. & Chowdhury, D. 2018. DYNLL1 binds to MRE11 to limit DNA end resection in BRCA1-deficient cells. Nature, 563, 522-526.
Heidelberger, J. B., Voigt, A., Borisova, M. E., Petrosino, G., Ruf, S., Wagner, S. A. & Beli, P. 2018. Proteomic profiling of VCP substrates links VCP to K6-linked ubiquitylation and c-Myc function. EMBO Rep, 19.
Heikkinen, K., Rapakko, K., Karppinen, S. M., Erkko, H., Knuutila, S., Lundan, T., Mannermaa, A., Borresen-Dale, A. L., Borg, A., Barkardottir, R. B., Petrini, J. & Winqvist, R. 2006.

RAD50 and NBS1 are breast cancer susceptibility genes associated with genomic instability. Carcinogenesis, 27, 1593-9.
Hellevik, T. & Martinez-Zubiaurre, I. 2014. Radiotherapy and the tumor stroma: the importance of dose and fractionation. Front Oncol, 4, 1.
Hemion, C., Flammer, J. & Neutzner, A. 2014. Quality control of oxidatively damaged mitochondrial proteins is mediated by p97 and the proteasome. Free Radic Biol Med, 75, 121-8.
Herdendorf, T. J., Albrecht, D. W., Benkovic, S. J. & Nelson, S. W. 2011. Biochemical characterization of bacteriophage T4 Mre11-Rad50 complex. J Biol Chem, 286, 2382-92.
Hershko, A. & Ciechanover, A. 1998. The ubiquitin system. Annu Rev Biochem, 67, 425-79.
Hideshima, T., Bradner, J. E., Wong, J., Chauhan, D., Richardson, P., Schreiber, S. L. & Anderson, K. C. 2005. Small-molecule inhibition of proteasome and aggresome function induces synergistic antitumor activity in multiple myeloma. Proc Natl Acad Sci U S A, 102, 8567-72.
Hoa, N. N., Shimizu, T., Zhou, Z. W., Wang, Z. Q., Deshpande, R. A., Paull, T. T., Akter, S., Tsuda, M., Furuta, R., Tsutsui, K., Takeda, S. & Sasanuma, H. 2016. Mre11 Is Essential for the Removal of Lethal Topoisomerase 2 Covalent Cleavage Complexes. Mol Cell, 64, 1010.
Hollien, J. & Weissman, J. S. 2006. Decay of endoplasmic reticulum-localized mRNAs during the unfolded protein response. Science, 313, 104-7.
Hopfner, K. P., Craig, L., Moncalian, G., Zinkel, R. A., Usui, T., Owen, B. A., Karcher, A., Henderson, B., Bodmer, J. L., Mcmurray, C. T., Carney, J. P., Petrini, J. H. & Tainer, J. A. 2002. The Rad50 zinc-hook is a structure joining Mre11 complexes in DNA recombination and repair. Nature, 418, 562-6.
Huang, S., Peet, C. R., Saker, J., Li, C., Armstrong, E. A., Kragh, M., Pedersen, M. W. & Harari, P. M. 2013. Sym004, a novel anti-EGFR antibody mixture, augments radiation response in human lung and head and neck cancers. Mol Cancer Ther, 12, 2772-81.
Huang, Z., Wu, Y., Zhou, X., Xu, J., Zhu, W., Shu, Y. & Liu, P. 2014. Efficacy of therapy with bortezomib in solid tumors: a review based on 32 clinical trials. Future Oncol, 10, 1795-807.
Huertas, P. & Jackson, S. P. 2009. Human CtIP mediates cell cycle control of DNA end resection and double strand break repair. J Biol Chem, 284, 9558-65.
Hundley, F. V., Sanvisens Delgado, N., Marin, H. C., Carr, K. L., Tian, R. & Toczyski, D. P. 2021. A comprehensive phenotypic CRISPR-Cas9 screen of the ubiquitin pathway uncovers roles of ubiquitin ligases in mitosis. Mol Cell, 81, 1319-1336 e9.
Hunter, N. 2015. Meiotic Recombination: The Essence of Heredity. Cold Spring Harb Perspect Biol, 7.
Hunter, T. 2007. The age of crosstalk: phosphorylation, ubiquitination, and beyond. Mol Cell, 28, 730-8.
Ikeda, H. O., Sasaoka, N., Koike, M., Nakano, N., Muraoka, Y., Toda, Y., Fuchigami, T., Shudo, T., Iwata, A., Hori, S., Yoshimura, N. & Kakizuka, A. 2014. Novel VCP modulators mitigate major pathologies of rd10, a mouse model of retinitis pigmentosa. Sci Rep, 4, 5970.
Indig, F. E., Partridge, J. J., Von Kobbe, C., Aladjem, M. I., Latterich, M. & Bohr, V. A. 2004. Werner syndrome protein directly binds to the AAA ATPase p97/VCP in an ATP-dependent fashion. J Struct Biol, 146, 251-9.

Ismail, I. H., Gagne, J. P., Genois, M. M., Strickfaden, H., Mcdonald, D., Xu, Z., Poirier, G. G., Masson, J. Y. & Hendzel, M. J. 2015. The RNF138 E3 ligase displaces Ku to promote DNA end resection and regulate DNA repair pathway choice. Nat Cell Biol, 17, 1446-57.

Ivanov, E. L., Sugawara, N., Fishman-Lobell, J. & Haber, J. E. 1996. Genetic requirements for the single-strand annealing pathway of double-strand break repair in Saccharomyces cerevisiae. Genetics, 142, 693-704.

Jachimowicz, R. D., Beleggia, F., Isensee, J., Velpula, B. B., Goergens, J., Bustos, M. A., Doll, M. A., Shenoy, A., Checa-Rodriguez, C., Wiederstein, J. L., Baranes-Bachar, K., Bartenhagen, C., Hertwig, F., Teper, N., Nishi, T., Schmitt, A., Distelmaier, F., Ludecke, H. J., Albrecht, B., Kruger, M., Schumacher, B., Geiger, T., Hoon, D. S. B., Huertas, P., Fischer, M., Hucho, T., Peifer, M., Ziv, Y., Reinhardt, H. C., Wieczorek, D. & Shiloh, Y. 2019. UBQLN4 Represses Homologous Recombination and Is Overexpressed in Aggressive Tumors. Cell, 176, 505-519 e22.

Jackson, S. P. & Bartek, J. 2009. The DNA-damage response in human biology and disease. Nature, 461, 1071-8.

Jackson, S. P. & Durocher, D. 2013. Regulation of DNA damage responses by ubiquitin and SUMO. Mol Cell, 49, 795-807.

Jazayeri, A., Balestrini, A., Garner, E., Haber, J. E. & Costanzo, V. 2008. Mre11-Rad50-Nbs1-dependent processing of DNA breaks generates oligonucleotides that stimulate ATM activity. EMBO J, 27, 1953-62.

Ji, Z., Li, H., Peterle, D., Paulo, J. A., Ficarro, S. B., Wales, T. E., Marto, J. A., Gygi, S. P., Engen, J. R. & Rapoport, T. A. 2021. Translocation of polyubiquitinated protein substrates by the hexameric Cdc48 ATPase. Mol Cell.

Jiang, N., Shen, Y., Fei, X., Sheng, K., Sun, P., Qiu, Y., Larner, J., Cao, L., Kong, X. & Mi, J. 2013. Valosin-containing protein regulates the proteasome-mediated degradation of DNA-PKcs in glioma cells. Cell Death Dis, 4, e647.

Jiang, X., Zhang, B., Zhou, Z., Meng, L., Sun, Z., Xu, Y., Xu, Q., Yuan, A., Yu, L., Qian, H., Wu, J., Hu, Y. & Liu, B. 2017. Enhancement of radiotherapy efficacy by pleiotropic liposomes encapsulated paclitaxel and perfluorotributylamine. Drug Deliv, 24, 1419-1428.

Jin, C., Zhu, X., Huang, X., Gong, T., Wei, Z. & You, J. 2022. Efficacy and safety of PD-1/PD-L1 and CTLA-4 immune checkpoint inhibitors in colorectal cancer: a meta-analysis. J Comp Eff Res, 11, 203-212.

Jungmichel, S. & Stucki, M. 2010. MDC1: The art of keeping things in focus. Chromosoma, 119, 337-49.

Keeney, S., Giroux, C. N. & Kleckner, N. 1997. Meiosis-specific DNA double-strand breaks are catalyzed by Spo11, a member of a widely conserved protein family. Cell, 88, 375-84.

Kerr, M., Scott, H. E., Groselj, B., Stratford, M. R., Karaszi, K., Sharma, N. L. & Kiltie, A. E. 2014. Deoxycytidine kinase expression underpins response to gemcitabine in bladder cancer. Clin Cancer Res, 20, 5435-45.

Khanna, K. K. & Jackson, S. P. 2001. DNA double-strand breaks: signaling, repair and the cancer connection. Nat Genet, 27, 247-54.

Khanolkar, R. C., Zhang, C., Al-Fatyan, F., Lawson, L., Depasquale, I., Meredith, F. M., Muller, F., Nicolson, M., Dahal, L. N., Abu-Eid, R., Rajpara, S., Barker, R. N., Ormerod, A. D. & Ward, F. J. 2021. TGFbeta2 Induces the Soluble Isoform of CTLA-4 - Implications

for CTLA-4 Based Checkpoint Inhibitor Antibodies in Malignant Melanoma. Front Immunol, 12, 763877.
Kijas, A. W., Lim, Y. C., Bolderson, E., Cerosaletti, K., Gatei, M., Jakob, B., Tobias, F., Taucher-Scholz, G., Gueven, N., Oakley, G., Concannon, P., Wolvetang, E., Khanna, K. K., Wiesmuller, L. & Lavin, M. F. 2015. ATM-dependent phosphorylation of MRE11 controls extent of resection during homology directed repair by signalling through Exonuclease 1. Nucleic Acids Res, 43, 8352-67.
Kilgas, S., Singh, A. N., Paillas, S., Then, C. K., Torrecilla, I., Nicholson, J., Browning, L., Vendrell, I., Konietzny, R., Kessler, B. M., Kiltie, A. E. & Ramadan, K. 2021. p97/VCP inhibition causes excessive MRE11-dependent DNA end resection promoting cell killing after ionizing radiation. Cell Rep, 35, 109153.
Kilkenny, C., Browne, W. J., Cuthill, I. C., Emerson, M. & Altman, D. G. 2012. Improving bioscience research reporting: the ARRIVE guidelines for reporting animal research. Osteoarthritis Cartilage, 20, 256-60.
Kim, J. A., Kruhlak, M., Dotiwala, F., Nussenzweig, A. & Haber, J. E. 2007. Heterochromatin is refractory to gamma-H2AX modification in yeast and mammals. J Cell Biol, 178, 209-18.
Kim, J. H., Grosbart, M., Anand, R., Wyman, C., Cejka, P. & Petrini, J. H. J. 2017. The Mre11-Nbs1 Interface Is Essential for Viability and Tumor Suppression. Cell Rep, 18, 496-507.
Kim, J. W. & Lee, I. J. 2021. Exploring the mythical abscopal effect: Radiation and programmed cell death protein 1 (PD-1) blockade for hepatocellular carcinoma. Clin Mol Hepatol, 27, 103-106.
Kim, M. S., Machida, Y., Vashisht, A. A., Wohlschlegel, J. A., Pang, Y. P. & Machida, Y. J. 2013. Regulation of error-prone translesion synthesis by Spartan/C1orf124. Nucleic Acids Res, 41, 1661-8.
Kirchner, P., Bug, M. & Meyer, H. 2013. Ubiquitination of the N-terminal region of caveolin-1 regulates endosomal sorting by the VCP/p97 AAA-ATPase. J Biol Chem, 288, 7363-72.
Kohnken, R., Kodigepalli, K. M. & Wu, L. 2015. Regulation of deoxynucleotide metabolism in cancer: novel mechanisms and therapeutic implications. Mol Cancer, 14, 176.
Komander, D. & Rape, M. 2012. The ubiquitin code. Annu Rev Biochem, 81, 203-29.
Kotsantis, P., Silva, L. M., Irmscher, S., Jones, R. M., Folkes, L., Gromak, N. & Petermann, E. 2016. Increased global transcription activity as a mechanism of replication stress in cancer. Nat Commun, 7, 13087.
Krastev, D. B., Li, S., Sun, Y., Wicks, A. J., Hoslett, G., Weekes, D., Badder, L. M., Knight, E. G., Marlow, R., Pardo, M. C., Yu, L., Talele, T. T., Bartek, J., Choudhary, J. S., Pommier, Y., Pettitt, S. J., Tutt, A. N. J., Ramadan, K. & Lord, C. J. 2022. The ubiquitin-dependent ATPase p97 removes cytotoxic trapped PARP1 from chromatin. Nat Cell Biol, 24, 62-73.
Kuo, C. Y., Li, X., Stark, J. M., Shih, H. M. & Ann, D. K. 2016. RNF4 regulates DNA double-strand break repair in a cell cycle-dependent manner. Cell Cycle, 15, 787-98.
Kwok, M., Davies, N., Agathanggelou, A., Smith, E., Oldreive, C., Petermann, E., Stewart, G., Brown, J., Lau, A., Pratt, G., Parry, H., Taylor, M., Moss, P., Hillmen, P. & Stankovic, T. 2016. ATR inhibition induces synthetic lethality and overcomes chemoresistance in TP53- or ATM-defective chronic lymphocytic leukemia cells. Blood, 127, 582-95.

Kwok, M., Davies, N., Agathanggelou, A., Smith, E., Petermann, E., Yates, E., Brown, J., Lau, A. & Stankovic, T. 2015. Synthetic lethality in chronic lymphocytic leukaemia with DNA damage response defects by targeting the ATR pathway. Lancet, 385 Suppl 1, S58.

Lammens, K., Bemeleit, D. J., Mockel, C., Clausing, E., Schele, A., Hartung, S., Schiller, C. B., Lucas, M., Angermuller, C., Soding, J., Strasser, K. & Hopfner, K. P. 2011. The Mre11:Rad50 structure shows an ATP-dependent molecular clamp in DNA double-strand break repair. Cell, 145, 54-66.

Langerak, P., Mejia-Ramirez, E., Limbo, O. & Russell, P. 2011. Release of Ku and MRN from DNA ends by Mre11 nuclease activity and Ctp1 is required for homologous recombination repair of double-strand breaks. PLoS Genet, 7, e1002271.

Laplante, G. & Zhang, W. 2021. Targeting the Ubiquitin-Proteasome System for Cancer Therapeutics by Small-Molecule Inhibitors. Cancers (Basel), 13.

Le Moigne, R., Aftab, B. T., Djakovic, S., Dhimolea, E., Valle, E., Murnane, M., King, E. M., Soriano, F., Menon, M. K., Wu, Z. Y., Wong, S. T., Lee, G. J., Yao, B., Wiita, A. P., Lam, C., Rice, J., Wang, J., Chesi, M., Bergsagel, P. L., Kraus, M., Driessen, C., Kiss Von Soly, S., Yakes, F. M., Wustrow, D., Shawver, L., Zhou, H. J., Martin, T. G., 3rd, Wolf, J. L., Mitsiades, C. S., Anderson, D. J. & Rolfe, M. 2017. The p97 Inhibitor CB-5083 Is a Unique Disrupter of Protein Homeostasis in Models of Multiple Myeloma. Mol Cancer Ther, 16, 2375-2386.

Lee, J. H. & Paull, T. T. 2005. ATM activation by DNA double-strand breaks through the Mre11-Rad50-Nbs1 complex. Science, 308, 551-4.

Lee, K. J., Saha, J., Sun, J., Fattah, K. R., Wang, S. C., Jakob, B., Chi, L., Wang, S. Y., Taucher-Scholz, G., Davis, A. J. & Chen, D. J. 2016. Phosphorylation of Ku dictates DNA double-strand break (DSB) repair pathway choice in S phase. Nucleic Acids Res, 44, 1732-45.

Lengsfeld, B. M., Rattray, A. J., Bhaskara, V., Ghirlando, R. & Paull, T. T. 2007. Sae2 is an endonuclease that processes hairpin DNA cooperatively with the Mre11/Rad50/Xrs2 complex. Mol Cell, 28, 638-51.

Lessel, D., Vaz, B., Halder, S., Lockhart, P. J., Marinovic-Terzic, I., Lopez-Mosqueda, J., Philipp, M., Sim, J. C., Smith, K. R., Oehler, J., Cabrera, E., Freire, R., Pope, K., Nahid, A., Norris, F., Leventer, R. J., Delatycki, M. B., Barbi, G., Von Ameln, S., Hogel, J., Degoricija, M., Fertig, R., Burkhalter, M. D., Hofmann, K., Thiele, H., Altmuller, J., Nurnberg, G., Nurnberg, P., Bahlo, M., Martin, G. M., Aalfs, C. M., Oshima, J., Terzic, J., Amor, D. J., Dikic, I., Ramadan, K. & Kubisch, C. 2014. Mutations in SPRTN cause early onset hepatocellular carcinoma, genomic instability and progeroid features. Nat Genet, 46, 1239-44.

Leung, J. W., Agarwal, P., Canny, M. D., Gong, F., Robison, A. D., Finkelstein, I. J., Durocher, D. & Miller, K. M. 2014. Nucleosome acidic patch promotes RNF168- and RING1B/BMI1-dependent H2AX and H2A ubiquitination and DNA damage signaling. PLoS Genet, 10, e1004178.

Li, H., Liu, Z. Y., Wu, N., Chen, Y. C., Cheng, Q. & Wang, J. 2020. PARP inhibitor resistance: the underlying mechanisms and clinical implications. Mol Cancer, 19, 107.

Li, Y. & Seto, E. 2016. HDACs and HDAC Inhibitors in Cancer Development and Therapy. Cold Spring Harb Perspect Med, 6.

Liang, L., Deng, L., Nguyen, S. C., Zhao, X., Maulion, C. D., Shao, C. & Tischfield, J. A. 2008. Human DNA ligases I and III, but not ligase IV, are required for microhomology-

mediated end joining of DNA double-strand breaks. Nucleic Acids Res, 36, 3297-310.
Lieber, M. R., Ma, Y., Pannicke, U. & Schwarz, K. 2003. Mechanism and regulation of human non-homologous DNA end-joining. Nat Rev Mol Cell Biol, 4, 712-20.
Lilley, B. N. & Ploegh, H. L. 2005. Multiprotein complexes that link dislocation, ubiquitination, and extraction of misfolded proteins from the endoplasmic reticulum membrane. Proc Natl Acad Sci U S A, 102, 14296-301.
Liu, C., Srihari, S., Cao, K. A., Chenevix-Trench, G., Simpson, P. T., Ragan, M. A. & Khanna, K. K. 2014. A fine-scale dissection of the DNA double-strand break repair machinery and its implications for breast cancer therapy. Nucleic Acids Res, 42, 6106-27.
Livingstone, M., Ruan, H., Weiner, J., Clauser, K. R., Strack, P., Jin, S., Williams, A., Greulich, H., Gardner, J., Venere, M., Mochan, T. A., Ditullio, R. A., Jr., Moravcevic, K., Gorgoulis, V. G., Burkhardt, A. & Halazonetis, T. D. 2005. Valosin-containing protein phosphorylation at Ser784 in response to DNA damage. Cancer Res, 65, 7533-40.
Lo, K. W., Kan, H. M., Chan, L. N., Xu, W. G., Wang, K. P., Wu, Z., Sheng, M. & Zhang, M. 2005. The 8-kDa dynein light chain binds to p53-binding protein 1 and mediates DNA damage-induced p53 nuclear accumulation. J Biol Chem, 280, 8172-9.
Loehrer, P. J., Sr., Feng, Y., Cardenes, H., Wagner, L., Brell, J. M., Cella, D., Flynn, P., Ramanathan, R. K., Crane, C. H., Alberts, S. R. & Benson, A. B., 3rd 2011. Gemcitabine alone versus gemcitabine plus radiotherapy in patients with locally advanced pancreatic cancer: an Eastern Cooperative Oncology Group trial. J Clin Oncol, 29, 4105-12.
Lord, C. J. & Ashworth, A. 2012. The DNA damage response and cancer therapy. Nature, 481, 287-94.
Lukas, J., Lukas, C. & Bartek, J. 2011. More than just a focus: The chromatin response to DNA damage and its role in genome integrity maintenance. Nat Cell Biol, 13, 1161-9.
Luo, G., Yao, M. S., Bender, C. F., Mills, M., Bladl, A. R., Bradley, A. & Petrini, J. H. 1999. Disruption of mRad50 causes embryonic stem cell lethality, abnormal embryonic development, and sensitivity to ionizing radiation. Proc Natl Acad Sci U S A, 96, 7376-81.
Machida, Y., Kim, M. S. & Machida, Y. J. 2012. Spartan/C1orf124 is important to prevent UV-induced mutagenesis. Cell Cycle, 11, 3395-402.
Magadan, J. G., Perez-Victoria, F. J., Sougrat, R., Ye, Y., Strebel, K. & Bonifacino, J. S. 2010. Multilayered mechanism of CD4 downregulation by HIV-1 Vpu involving distinct ER retention and ERAD targeting steps. PLoS Pathog, 6, e1000869.
Magnaghi, P., D'alessio, R., Valsasina, B., Avanzi, N., Rizzi, S., Asa, D., Gasparri, F., Cozzi, L., Cucchi, U., Orrenius, C., Polucci, P., Ballinari, D., Perrera, C., Leone, A., Cervi, G., Casale, E., Xiao, Y., Wong, C., Anderson, D. J., Galvani, A., Donati, D., O'brien, T., Jackson, P. K. & Isacchi, A. 2013. Covalent and allosteric inhibitors of the ATPase VCP/p97 induce cancer cell death. Nat Chem Biol, 9, 548-56.
Mahajan, K. N., Nick Mcelhinny, S. A., Mitchell, B. S. & Ramsden, D. A. 2002. Association of DNA polymerase mu (pol mu) with Ku and ligase IV: role for pol mu in end-joining double-strand break repair. Mol Cell Biol, 22, 5194-202.
Mailand, N., Bekker-Jensen, S., Faustrup, H., Melander, F., Bartek, J., Lukas, C. & Lukas, J. 2007. RNF8 ubiquitylates histones at DNA double-strand breaks and promotes assembly of repair proteins. Cell, 131, 887-900.

Makharashvili, N., Arora, S., Yin, Y., Fu, Q., Wen, X., Lee, J. H., Kao, C. H., Leung, J. W., Miller, K. M. & Paull, T. T. 2018. Sae2/CtIP prevents R-loop accumulation in eukaryotic cells. Elife, 7.

Makharashvili, N., Tubbs, A. T., Yang, S. H., Wang, H., Barton, O., Zhou, Y., Deshpande, R. A., Lee, J. H., Lobrich, M., Sleckman, B. P., Wu, X. & Paull, T. T. 2014. Catalytic and noncatalytic roles of the CtIP endonuclease in double-strand break end resection. Mol Cell, 54, 1022-33.

Malkova, A. & Ira, G. 2013. Break-induced replication: functions and molecular mechanism. Curr Opin Genet Dev, 23, 271-9.

Mansour, W. Y., Rhein, T. & Dahm-Daphi, J. 2010. The alternative end-joining pathway for repair of DNA double-strand breaks requires PARP1 but is not dependent upon microhomologies. Nucleic Acids Res, 38, 6065-77.

Mari, P. O., Florea, B. I., Persengiev, S. P., Verkaik, N. S., Bruggenwirth, H. T., Modesti, M., Giglia-Mari, G., Bezstarosti, K., Demmers, J. A., Luider, T. M., Houtsmuller, A. B. & Van Gent, D. C. 2006. Dynamic assembly of end-joining complexes requires interaction between Ku70/80 and XRCC4. Proc Natl Acad Sci U S A, 103, 18597-602.

Maric, M., Maculins, T., De Piccoli, G. & Labib, K. 2014. Cdc48 and a ubiquitin ligase drive disassembly of the CMG helicase at the end of DNA replication. Science, 346, 1253596.

Mateos-Gomez, P. A., Gong, F., Nair, N., Miller, K. M., Lazzerini-Denchi, E. & Sfeir, A. 2015. Mammalian polymerase theta promotes alternative NHEJ and suppresses recombination. Nature, 518, 254-7.

Mcvey, M., Khodaverdian, V. Y., Meyer, D., Cerqueira, P. G. & Heyer, W. D. 2016. Eukaryotic DNA Polymerases in Homologous Recombination. Annu Rev Genet, 50, 393-421.

Meerang, M., Ritz, D., Paliwal, S., Garajova, Z., Bosshard, M., Mailand, N., Janscak, P., Hubscher, U., Meyer, H. & Ramadan, K. 2011. The ubiquitin-selective segregase VCP/p97 orchestrates the response to DNA double-strand breaks. Nat Cell Biol, 13, 1376-82.

Meray, R. K. & Lansbury, P. T., Jr. 2007. Reversible monoubiquitination regulates the Parkinson disease-associated ubiquitin hydrolase UCH-L1. J Biol Chem, 282, 10567-75.

Messner, S., Altmeyer, M., Zhao, H., Pozivil, A., Roschitzki, B., Gehrig, P., Rutishauser, D., Huang, D., Caflisch, A. & Hottiger, M. O. 2010. PARP1 ADP-ribosylates lysine residues of the core histone tails. Nucleic Acids Res, 38, 6350-62.

Mevissen, T. E. T. & Komander, D. 2017. Mechanisms of Deubiquitinase Specificity and Regulation. Annu Rev Biochem, 86, 159-192.

Meyer, H., Bug, M. & Bremer, S. 2012. Emerging functions of the VCP/p97 AAA-ATPase in the ubiquitin system. Nat Cell Biol, 14, 117-23.

Mi, Y., Shao, Z., Vang, J., Kaidar-Person, O. & Wang, A. Z. 2016. Application of nanotechnology to cancer radiotherapy. Cancer Nanotechnol, 7, 11.

Mimitou, E. P. & Symington, L. S. 2008. Sae2, Exo1 and Sgs1 collaborate in DNA double-strand break processing. Nature, 455, 770-4.

Mimitou, E. P. & Symington, L. S. 2010. Ku prevents Exo1 and Sgs1-dependent resection of DNA ends in the absence of a functional MRX complex or Sae2. EMBO J, 29, 3358-69.

Mole, R. H. 1953. Whole body irradiation; radiobiology or medicine? Br J Radiol, 26, 234-41.

Moreau, S., Ferguson, J. R. & Symington, L. S. 1999. The nuclease activity of Mre11 is required for meiosis but not for mating type switching, end joining, or telomere maintenance. Mol Cell Biol, 19, 556-66.

Moreno, S. P., Bailey, R., Campion, N., Herron, S. & Gambus, A. 2014. Polyubiquitylation drives replisome disassembly at the termination of DNA replication. Science, 346, 477-81.

Munoz, M. C., Laulier, C., Gunn, A., Cheng, A., Robbiani, D. F., Nussenzweig, A. & Stark, J. M. 2012. RING finger nuclear factor RNF168 is important for defects in homologous recombination caused by loss of the breast cancer susceptibility factor BRCA1. J Biol Chem, 287, 40618-28.

Myler, L. R., Gallardo, I. F., Soniat, M. M., Deshpande, R. A., Gonzalez, X. B., Kim, Y., Paull, T. T. & Finkelstein, I. J. 2017. Single-Molecule Imaging Reveals How Mre11-Rad50-Nbs1 Initiates DNA Break Repair. Mol Cell, 67, 891-898 e4.

Na, J., Newman, J. A., Then, C. K., Syed, J., Vendrell, I., Torrecilla, I., Ellermann, S., Ramadan, K., Fischer, R. & Kiltie, A. E. 2021. SPRTN protease-cleaved MRE11 decreases DNA repair and radiosensitises cancer cells. Cell Death Dis, 12, 165.

Nakamura, K., Kogame, T., Oshiumi, H., Shinohara, A., Sumitomo, Y., Agama, K., Pommier, Y., Tsutsui, K. M., Tsutsui, K., Hartsuiker, E., Ogi, T., Takeda, S. & Taniguchi, Y. 2010. Collaborative action of Brca1 and CtIP in elimination of covalent modifications from double-strand breaks to facilitate subsequent break repair. PLoS Genet, 6, e1000828.

Nakamura, K., Saredi, G., Becker, J. R., Foster, B. M., Nguyen, N. V., Beyer, T. E., Cesa, L. C., Faull, P. A., Lukauskas, S., Frimurer, T., Chapman, J. R., Bartke, T. & Groth, A. 2019. H4K20me0 recognition by BRCA1-BARD1 directs homologous recombination to sister chromatids. Nat Cell Biol, 21, 311-318.

Neale, M. J., Pan, J. & Keeney, S. 2005. Endonucleolytic processing of covalent protein-linked DNA double-strand breaks. Nature, 436, 1053-7.

Nicholson, J., Jevons, S. J., Groselj, B., Ellermann, S., Konietzny, R., Kerr, M., Kessler, B. M. & Kiltie, A. E. 2017. E3 Ligase cIAP2 Mediates Downregulation of MRE11 and Radiosensitization in Response to HDAC Inhibition in Bladder Cancer. Cancer Res, 77, 3027-3039.

Nicolette, M. L., Lee, K., Guo, Z., Rani, M., Chow, J. M., Lee, S. E. & Paull, T. T. 2010. Mre11-Rad50-Xrs2 and Sae2 promote 5' strand resection of DNA double-strand breaks. Nat Struct Mol Biol, 17, 1478-85.

Nimonkar, A. V., Genschel, J., Kinoshita, E., Polaczek, P., Campbell, J. L., Wyman, C., Modrich, P. & Kowalczykowski, S. C. 2011. BLM-DNA2-RPA-MRN and EXO1-BLM-RPA-MRN constitute two DNA end resection machineries for human DNA break repair. Genes Dev, 25, 350-62.

Nimonkar, A. V., Ozsoy, A. Z., Genschel, J., Modrich, P. & Kowalczykowski, S. C. 2008. Human exonuclease 1 and BLM helicase interact to resect DNA and initiate DNA repair. Proc Natl Acad Sci U S A, 105, 16906-11.

Noordermeer, S. M. & Van Attikum, H. 2019. PARP Inhibitor Resistance: A Tug-of-War in BRCA-Mutated Cells. Trends Cell Biol, 29, 820-834.

Nussenzweig, A., Chen, C., Da Costa Soares, V., Sanchez, M., Sokol, K., Nussenzweig, M. C. & Li, G. C. 1996. Requirement for Ku80 in growth and immunoglobulin V(D)J recombination. Nature, 382, 551-5.

O'connor, M. J. 2015. Targeting the DNA Damage Response in Cancer. Mol Cell, 60, 547-60.

O'connor, O. A., Wright, J., Moskowitz, C., Muzzy, J., Macgregor-Cortelli, B., Stubblefield, M., Straus, D., Portlock, C., Hamlin, P., Choi, E., Dumetrescu, O., Esseltine, D., Trehu, E., Adams, J., Schenkein, D. & Zelenetz, A. D. 2005. Phase II clinical experience with the novel proteasome inhibitor bortezomib in patients with indolent non-Hodgkin's lymphoma and mantle cell lymphoma. J Clin Oncol, 23, 676-84.

Ochs, F., Somyajit, K., Altmeyer, M., Rask, M. B., Lukas, J. & Lukas, C. 2016. 53BP1 fosters fidelity of homology-directed DNA repair. Nat Struct Mol Biol, 23, 714-21.

Oh, J., Al-Zain, A., Cannavo, E., Cejka, P. & Symington, L. S. 2016. Xrs2 Dependent and Independent Functions of the Mre11-Rad50 Complex. Mol Cell, 64, 405-415.

Oronsky, B. T., Knox, S. J. & Scicinski, J. 2011. Six degrees of separation: the oxygen effect in the development of radiosensitizers. Transl Oncol, 4, 189-98.

Paillas, S., Then, C. K., Kilgas, S., Ruan, J. L., Thompson, J., Elliott, A., Smart, S. & Kiltie, A. E. 2020. The Histone Deacetylase Inhibitor Romidepsin Spares Normal Tissues While Acting as an Effective Radiosensitizer in Bladder Tumors in Vivo. Int J Radiat Oncol Biol Phys, 107, 212-221.

Paliwal, S., Kanagaraj, R., Sturzenegger, A., Burdova, K. & Janscak, P. 2014. Human RECQ5 helicase promotes repair of DNA double-strand breaks by synthesis-dependent strand annealing. Nucleic Acids Res, 42, 2380-90.

Palmeri, S., Rufa, A., Pucci, B., Santarnecchi, E., Malandrini, A., Stromillo, M. L., Mandala, M., Rosini, F., De Stefano, N. & Federico, A. 2013. Clinical course of two Italian siblings with ataxia-telangiectasia-like disorder. Cerebellum, 12, 596-9.

Paull, T. T. 2018. 20 Years of Mre11 Biology: No End in Sight. Mol Cell, 71, 419-427.

Paull, T. T. & Gellert, M. 1998. The 3' to 5' exonuclease activity of Mre 11 facilitates repair of DNA double-strand breaks. Mol Cell, 1, 969-79.

Paull, T. T. & Gellert, M. 1999. Nbs1 potentiates ATP-driven DNA unwinding and endonuclease cleavage by the Mre11/Rad50 complex. Genes Dev, 13, 1276-88.

Pauwels, B., Korst, A. E., Lardon, F. & Vermorken, J. B. 2005. Combined modality therapy of gemcitabine and radiation. Oncologist, 10, 34-51.

Pearl, L. H., Schierz, A. C., Ward, S. E., Al-Lazikani, B. & Pearl, F. M. 2015. Therapeutic opportunities within the DNA damage response. Nat Rev Cancer, 15, 166-80.

Pei, H., Zhang, L., Luo, K., Qin, Y., Chesi, M., Fei, F., Bergsagel, P. L., Wang, L., You, Z. & Lou, Z. 2011. MMSET regulates histone H4K20 methylation and 53BP1 accumulation at DNA damage sites. Nature, 470, 124-8.

Piccirillo, R. & Goldberg, A. L. 2012. The p97/VCP ATPase is critical in muscle atrophy and the accelerated degradation of muscle proteins. EMBO J, 31, 3334-50.

Pleasure, I. T., Black, M. M. & Keen, J. H. 1993. Valosin-containing protein, VCP, is a ubiquitous clathrin-binding protein. Nature, 365, 459-62.

Quennet, V., Beucher, A., Barton, O., Takeda, S. & Lobrich, M. 2011. CtIP and MRN promote non-homologous end-joining of etoposide-induced DNA double-strand breaks in G1. Nucleic Acids Res, 39, 2144-52.

Ramadan, K. 2012. p97/VCP- and Lys48-linked polyubiquitination form a new signaling pathway in DNA damage response. Cell Cycle, 11, 1062-9.

Ramadan, K., Bruderer, R., Spiga, F. M., Popp, O., Baur, T., Gotta, M. & Meyer, H. H. 2007. Cdc48/p97 promotes reformation of the nucleus by extracting the kinase Aurora B from chromatin. Nature, 450, 1258-62.

Raman, M., Havens, C. G., Walter, J. C. & Harper, J. W. 2011. A genome-wide screen identifies p97 as an essential regulator of DNA damage-dependent CDT1 destruction. Mol Cell, 44, 72-84.

Ramanathan, H. N. & Ye, Y. 2012. The p97 ATPase associates with EEA1 to regulate the size of early endosomes. Cell Res, 22, 346-59.

Ramsden, D. A., Carvajal-Garcia, J. & Gupta, G. P. 2022. Mechanism, cellular functions and cancer roles of polymerase-theta-mediated DNA end joining. Nat Rev Mol Cell Biol, 23, 125-140.

Ray Chaudhuri, A., Callen, E., Ding, X., Gogola, E., Duarte, A. A., Lee, J. E., Wong, N., Lafarga, V., Calvo, J. A., Panzarino, N. J., John, S., Day, A., Crespo, A. V., Shen, B., Starnes, L. M., De Ruiter, J. R., Daniel, J. A., Konstantinopoulos, P. A., Cortez, D., Cantor, S. B., Fernandez-Capetillo, O., Ge, K., Jonkers, J., Rottenberg, S., Sharan, S. K. & Nussenzweig, A. 2016. Replication fork stability confers chemoresistance in BRCA-deficient cells. Nature, 535, 382-7.

Reaper, P. M., Griffiths, M. R., Long, J. M., Charrier, J. D., Maccormick, S., Charlton, P. A., Golec, J. M. & Pollard, J. R. 2011. Selective killing of ATM- or p53-deficient cancer cells through inhibition of ATR. Nat Chem Biol, 7, 428-30.

Reginato, G., Cannavo, E. & Cejka, P. 2017. Physiological protein blocks direct the Mre11-Rad50-Xrs2 and Sae2 nuclease complex to initiate DNA end resection. Genes Dev, 31, 2325-2330.

Rey, S., Schito, L., Koritzinsky, M. & Wouters, B. G. 2017. Molecular targeting of hypoxia in radiotherapy. Adv Drug Deliv Rev, 109, 45-62.

Rhee, H. W., Zou, P., Udeshi, N. D., Martell, J. D., Mootha, V. K., Carr, S. A. & Ting, A. Y. 2013. Proteomic mapping of mitochondria in living cells via spatially restricted enzymatic tagging. Science, 339, 1328-1331.

Riballo, E., Kuhne, M., Rief, N., Doherty, A., Smith, G. C., Recio, M. J., Reis, C., Dahm, K., Fricke, A., Krempler, A., Parker, A. R., Jackson, S. P., Gennery, A., Jeggo, P. A. & Lobrich, M. 2004. A pathway of double-strand break rejoining dependent upon ATM, Artemis, and proteins locating to gamma-H2AX foci. Mol Cell, 16, 715-24.

Richardson, P. G., Sonneveld, P., Schuster, M. W., Irwin, D., Stadtmauer, E. A., Facon, T., Harousseau, J. L., Ben-Yehuda, D., Lonial, S., Goldschmidt, H., Reece, D., San-Miguel, J. F., Blade, J., Boccadoro, M., Cavenagh, J., Dalton, W. S., Boral, A. L., Esseltine, D. L., Porter, J. B., Schenkein, D., Anderson, K. C. & Assessment of Proteasome Inhibition for Extending Remissions, I. 2005. Bortezomib or high-dose dexamethasone for relapsed multiple myeloma. N Engl J Med, 352, 2487-98.

Ritz, D., Vuk, M., Kirchner, P., Bug, M., Schutz, S., Hayer, A., Bremer, S., Lusk, C., Baloh, R. H., Lee, H., Glatter, T., Gstaiger, M., Aebersold, R., Weihl, C. C. & Meyer, H. 2011. Endolysosomal sorting of ubiquitylated caveolin-1 is regulated by VCP and UBXD1 and impaired by VCP disease mutations. Nat Cell Biol, 13, 1116-23.

Rodriguez-Martin, B., Alvarez, E. G., Baez-Ortega, A., Zamora, J., Supek, F., Demeulemeester, J., Santamarina, M., Ju, Y. S., Temes, J., Garcia-Souto, D., Detering, H., Li, Y., Rodriguez-Castro, J., Dueso-Barroso, A., Bruzos, A. L., Dentro, S. C., Blanco, M. G., Contino, G., Ardeljan, D., Tojo, M., Roberts, N. D., Zumalave, S., Edwards, P. a. W., Weischenfeldt, J., Puiggros, M., Chong, Z., Chen, K., Lee, E. A., Wala, J. A., Raine, K., Butler, A., Waszak, S. M., Navarro, F. C. P., Schumacher, S. E., Monlong, J., Maura, F., Bolli, N., Bourque, G., Gerstein, M., Park, P. J., Wedge, D. C., Beroukhim, R., Torrents, D., Korbel, J. O., Martincorena, I., Fitzgerald, R. C., Van Loo,

P., Kazazian, H. H., Burns, K. H., Group, P. S. V. W., Campbell, P. J., Tubio, J. M. C. & Consortium, P. 2020. Pan-cancer analysis of whole genomes identifies driver rearrangements promoted by LINE-1 retrotransposition. Nat Genet, 52, 306-319.

Rodriguez-Ruiz, M. E., Rodriguez, I., Garasa, S., Barbes, B., Solorzano, J. L., Perez-Gracia, J. L., Labiano, S., Sanmamed, M. F., Azpilikueta, A., Bolanos, E., Sanchez-Paulete, A. R., Aznar, M. A., Rouzaut, A., Schalper, K. A., Jure-Kunkel, M. & Melero, I. 2016. Abscopal Effects of Radiotherapy Are Enhanced by Combined Immunostimulatory mAbs and Are Dependent on CD8 T Cells and Crosspriming. Cancer Res, 76, 5994-6005.

Rothkamm, K. & Lobrich, M. 2003. Evidence for a lack of DNA double-strand break repair in human cells exposed to very low x-ray doses. Proc Natl Acad Sci U S A, 100, 5057-62.

Roux, B., Vaganay, C., Vargas, J. D., Alexe, G., Benaksas, C., Pardieu, B., Fenouille, N., Ellegast, J. M., Malolepsza, E., Ling, F., Sodaro, G., Ross, L., Pikman, Y., Conway, A. S., Tang, Y., Wu, T., Anderson, D. J., Le Moigne, R., Zhou, H. J., Luciano, F., Hartigan, C. R., Galinsky, I., Deangelo, D. J., Stone, R. M., Auberger, P., Schenone, M., Carr, S. A., Guirouilh-Barbat, J., Lopez, B., Khaled, M., Lage, K., Hermine, O., Hemann, M. T., Puissant, A., Stegmaier, K. & Benajiba, L. 2021. Targeting acute myeloid leukemia dependency on VCP-mediated DNA repair through a selective second-generation small-molecule inhibitor. Sci Transl Med, 13.

Sanchez, A., Reginato, G. & Cejka, P. 2021. Crossover or non-crossover outcomes: tailored processing of homologous recombination intermediates. Curr Opin Genet Dev, 71, 39-47.

Sartori, A. A., Lukas, C., Coates, J., Mistrik, M., Fu, S., Bartek, J., Baer, R., Lukas, J. & Jackson, S. P. 2007. Human CtIP promotes DNA end resection. Nature, 450, 509-14.

Sasagawa, Y., Higashitani, A., Urano, T., Ogura, T. & Yamanaka, K. 2012. CDC-48/p97 is required for proper meiotic chromosome segregation via controlling AIR-2/Aurora B kinase localization in Caenorhabditis elegans. J Struct Biol, 179, 104-11.

Sasazawa, Y., Kanagaki, S., Tashiro, E., Nogawa, T., Muroi, M., Kondoh, Y., Osada, H. & Imoto, M. 2012. Xanthohumol impairs autophagosome maturation through direct inhibition of valosin-containing protein. ACS Chem Biol, 7, 892-900.

Sasset, L., Petris, G., Cesaratto, F. & Burrone, O. R. 2015. The VCP/p97 and YOD1 Proteins Have Different Substrate-dependent Activities in Endoplasmic Reticulum-associated Degradation (ERAD). J Biol Chem, 290, 28175-28188.

Savic, V., Yin, B., Maas, N. L., Bredemeyer, A. L., Carpenter, A. C., Helmink, B. A., Yang-Iott, K. S., Sleckman, B. P. & Bassing, C. H. 2009. Formation of dynamic gamma-H2AX domains along broken DNA strands is distinctly regulated by ATM and MDC1 and dependent upon H2AX densities in chromatin. Mol Cell, 34, 298-310.

Schlacher, K., Christ, N., Siaud, N., Egashira, A., Wu, H. & Jasin, M. 2011. Double-strand break repair-independent role for BRCA2 in blocking stalled replication fork degradation by MRE11. Cell, 145, 529-42.

Schuberth, C. & Buchberger, A. 2008. UBX domain proteins: major regulators of the AAA ATPase Cdc48/p97. Cell Mol Life Sci, 65, 2360-71.

Schwertman, P., Bekker-Jensen, S. & Mailand, N. 2016. Regulation of DNA double-strand break repair by ubiquitin and ubiquitin-like modifiers. Nat Rev Mol Cell Biol, 17, 379-94.

Seki, M., Marini, F. & Wood, R. D. 2003. POLQ (Pol theta), a DNA polymerase and DNA-dependent ATPase in human cells. Nucleic Acids Res, 31, 6117-26.

Senra, J. M., Telfer, B. A., Cherry, K. E., Mccrudden, C. M., Hirst, D. G., O'connor, M. J., Wedge, S. R. & Stratford, I. J. 2011. Inhibition of PARP-1 by olaparib (AZD2281) increases the radiosensitivity of a lung tumor xenograft. Mol Cancer Ther, 10, 1949-58.

Shamanna, R. A., Lu, H., De Freitas, J. K., Tian, J., Croteau, D. L. & Bohr, V. A. 2016. WRN regulates pathway choice between classical and alternative non-homologous end joining. Nat Commun, 7, 13785.

Shen, M., Schmitt, S., Buac, D. & Dou, Q. P. 2013. Targeting the ubiquitin-proteasome system for cancer therapy. Expert Opin Ther Targets, 17, 1091-108.

Shibata, A., Conrad, S., Birraux, J., Geuting, V., Barton, O., Ismail, A., Kakarougkas, A., Meek, K., Taucher-Scholz, G., Lobrich, M. & Jeggo, P. A. 2011. Factors determining DNA double-strand break repair pathway choice in G2 phase. EMBO J, 30, 1079-92.

Shibata, A., Moiani, D., Arvai, A. S., Perry, J., Harding, S. M., Genois, M. M., Maity, R., Van Rossum-Fikkert, S., Kertokalio, A., Romoli, F., Ismail, A., Ismalaj, E., Petricci, E., Neale, M. J., Bristow, R. G., Masson, J. Y., Wyman, C., Jeggo, P. A. & Tainer, J. A. 2014. DNA double-strand break repair pathway choice is directed by distinct MRE11 nuclease activities. Mol Cell, 53, 7-18.

Simsek, D., Brunet, E., Wong, S. Y., Katyal, S., Gao, Y., Mckinnon, P. J., Lou, J., Zhang, L., Li, J., Rebar, E. J., Gregory, P. D., Holmes, M. C. & Jasin, M. 2011. DNA ligase III promotes alternative nonhomologous end-joining during chromosomal translocation formation. PLoS Genet, 7, e1002080.

Singh, A. N., Oehler, J., Torrecilla, I., Kilgas, S., Li, S., Vaz, B., Guerillon, C., Fielden, J., Hernandez-Carralero, E., Cabrera, E., Tullis, I. D., Meerang, M., Barber, P. R., Freire, R., Parsons, J., Vojnovic, B., Kiltie, A. E., Mailand, N. & Ramadan, K. 2019. The p97-Ataxin 3 complex regulates homeostasis of the DNA damage response E3 ubiquitin ligase RNF8. EMBO J, 38, e102361.

Situ, Y., Chung, L., Lee, C. S. & Ho, V. 2019. MRN (MRE11-RAD50-NBS1) Complex in Human Cancer and Prognostic Implications in Colorectal Cancer. Int J Mol Sci, 20.

So, A., Le Guen, T., Lopez, B. S. & Guirouilh-Barbat, J. 2017. Genomic rearrangements induced by unscheduled DNA double strand breaks in somatic mammalian cells. FEBS J, 284, 2324-2344.

Soniat, M. M., Myler, L. R., Kuo, H. C., Paull, T. T. & Finkelstein, I. J. 2019. RPA Phosphorylation Inhibits DNA Resection. Mol Cell, 75, 145-153 e5.

Spitz, D. R., Buettner, G. R., Petronek, M. S., St-Aubin, J. J., Flynn, R. T., Waldron, T. J. & Limoli, C. L. 2019. An integrated physico-chemical approach for explaining the differential impact of FLASH versus conventional dose rate irradiation on cancer and normal tissue responses. Radiother Oncol, 139, 23-27.

Stark, J. M., Pierce, A. J., Oh, J., Pastink, A. & Jasin, M. 2004. Genetic steps of mammalian homologous repair with distinct mutagenic consequences. Mol Cell Biol, 24, 9305-16.

Steel, G. G., Mcmillan, T. J. & Peacock, J. H. 1989. The 5Rs of radiobiology. Int J Radiat Biol, 56, 1045-8.

Stewart, G. S., Panier, S., Townsend, K., Al-Hakim, A. K., Kolas, N. K., Miller, E. S., Nakada, S., Ylanko, J., Olivarius, S., Mendez, M., Oldreive, C., Wildenhain, J., Tagliaferro, A., Pelletier, L., Taubenheim, N., Durandy, A., Byrd, P. J., Stankovic, T., Taylor, A. M. &

Durocher, D. 2009. The RIDDLE syndrome protein mediates a ubiquitin-dependent signaling cascade at sites of DNA damage. Cell, 136, 420-34.
Stiff, T., O'driscoll, M., Rief, N., Iwabuchi, K., Lobrich, M. & Jeggo, P. A. 2004. ATM and DNA-PK function redundantly to phosphorylate H2AX after exposure to ionizing radiation. Cancer Res, 64, 2390-6.
Stracker, T. H., Theunissen, J. W., Morales, M. & Petrini, J. H. 2004. The Mre11 complex and the metabolism of chromosome breaks: the importance of communicating and holding things together. DNA Repair (Amst), 3, 845-54.
Stucki, M. & Jackson, S. P. 2006. gammaH2AX and MDC1: anchoring the DNA-damage-response machinery to broken chromosomes. DNA Repair (Amst), 5, 534-43.
Sun, Y., Jiang, X., Chen, S., Fernandes, N. & Price, B. D. 2005. A role for the Tip60 histone acetyltransferase in the acetylation and activation of ATM. Proc Natl Acad Sci U S A, 102, 13182-7.
Swatek, K. N., Usher, J. L., Kueck, A. F., Gladkova, C., Mevissen, T. E. T., Pruneda, J. N., Skern, T. & Komander, D. 2019. Insights into ubiquitin chain architecture using Ub-clipping. Nature, 572, 533-537.
Takeda, S., Hoa, N. N. & Sasanuma, H. 2016. The role of the Mre11-Rad50-Nbs1 complex in double-strand break repair-facts and myths. J Radiat Res, 57 Suppl 1, i25-i32.
Taleei, R., Weinfeld, M. & Nikjoo, H. 2011. A kinetic model of single-strand annealing for the repair of DNA double-strand breaks. Radiat Prot Dosimetry, 143, 191-5.
Tang, W. K., Odzorig, T., Jin, W. & Xia, D. 2019. Structural Basis of p97 Inhibition by the Site-Selective Anticancer Compound CB-5083. Mol Pharmacol, 95, 286-293.
Tang, Z., Li, C., Kang, B., Gao, G., Li, C. & Zhang, Z. 2017. GEPIA: a web server for cancer and normal gene expression profiling and interactive analyses. Nucleic Acids Res, 45, W98-W102.
Tay, C. Y., Cai, P., Setyawati, M. I., Fang, W., Tan, L. P., Hong, C. H., Chen, X. & Leong, D. T. 2014. Nanoparticles strengthen intracellular tension and retard cellular migration. Nano Lett, 14, 83-8.
Taylor, A. M., Groom, A. & Byrd, P. J. 2004. Ataxia-telangiectasia-like disorder (ATLD)-its clinical presentation and molecular basis. DNA Repair (Amst), 3, 1219-25.
Taylor, E. B. & Rutter, J. 2011. Mitochondrial quality control by the ubiquitin-proteasome system. Biochem Soc Trans, 39, 1509-13.
Tokheim, C., Wang, X., Timms, R. T., Zhang, B., Mena, E. L., Wang, B., Chen, C., Ge, J., Chu, J., Zhang, W., Elledge, S. J., Brown, M. & Liu, X. S. 2021. Systematic characterization of mutations altering protein degradation in human cancers. Mol Cell, 81, 1292-1308 e11.
Torrecilla, I., Oehler, J. & Ramadan, K. 2017. The role of ubiquitin-dependent segregase p97 (VCP or Cdc48) in chromatin dynamics after DNA double strand breaks. Philos Trans R Soc Lond B Biol Sci, 372.
Torres, E. M., Dephoure, N., Panneerselvam, A., Tucker, C. M., Whittaker, C. A., Gygi, S. P., Dunham, M. J. & Amon, A. 2010. Identification of aneuploidy-tolerating mutations. Cell, 143, 71-83.
Trujillo, K. M. & Sung, P. 2001. DNA structure-specific nuclease activities in the Saccharomyces cerevisiae Rad50*Mre11 complex. J Biol Chem, 276, 35458-64.
Trujillo, K. M., Yuan, S. S., Lee, E. Y. & Sung, P. 1998. Nuclease activities in a complex of human recombination and DNA repair factors Rad50, Mre11, and p95. J Biol Chem, 273, 21447-50.

Truong, L. N., Li, Y., Shi, L. Z., Hwang, P. Y., He, J., Wang, H., Razavian, N., Berns, M. W. & Wu, X. 2013. Microhomology-mediated End Joining and Homologous Recombination share the initial end resection step to repair DNA double-strand breaks in mammalian cells. Proc Natl Acad Sci U S A, 110, 7720-5.

Tsukamoto, Y., Mitsuoka, C., Terasawa, M., Ogawa, H. & Ogawa, T. 2005. Xrs2p regulates Mre11p translocation to the nucleus and plays a role in telomere elongation and meiotic recombination. Mol Biol Cell, 16, 597-608.

Twomey, E. C., Ji, Z., Wales, T. E., Bodnar, N. O., Ficarro, S. B., Marto, J. A., Engen, J. R. & Rapoport, T. A. 2019. Substrate processing by the Cdc48 ATPase complex is initiated by ubiquitin unfolding. Science, 365.

Twyman-Saint Victor, C., Rech, A. J., Maity, A., Rengan, R., Pauken, K. E., Stelekati, E., Benci, J. L., Xu, B., Dada, H., Odorizzi, P. M., Herati, R. S., Mansfield, K. D., Patsch, D., Amaravadi, R. K., Schuchter, L. M., Ishwaran, H., Mick, R., Pryma, D. A., Xu, X., Feldman, M. D., Gangadhar, T. C., Hahn, S. M., Wherry, E. J., Vonderheide, R. H. & Minn, A. J. 2015. Radiation and dual checkpoint blockade activate non-redundant immune mechanisms in cancer. Nature, 520, 373-7.

Uematsu, N., Weterings, E., Yano, K., Morotomi-Yano, K., Jakob, B., Taucher-Scholz, G., Mari, P. O., Van Gent, D. C., Chen, B. P. & Chen, D. J. 2007. Autophosphorylation of DNA-PKCS regulates its dynamics at DNA double-strand breaks. J Cell Biol, 177, 219-29.

Urick, M. E., Chung, E. J., Shield, W. P., 3rd, Gerber, N., White, A., Sowers, A., Thetford, A., Camphausen, K., Mitchell, J. & Citrin, D. E. 2011. Enhancement of 5-fluorouracil-induced in vitro and in vivo radiosensitization with MEK inhibition. Clin Cancer Res, 17, 5038-47.

Van De Ven, A. L., Tangutoori, S., Baldwin, P., Qiao, J., Gharagouzloo, C., Seitzer, N., Clohessy, J. G., Makrigiorgos, G. M., Cormack, R., Pandolfi, P. P. & Sridhar, S. 2017. Nanoformulation of Olaparib Amplifies PARP Inhibition and Sensitizes PTEN/TP53-Deficient Prostate Cancer to Radiation. Mol Cancer Ther, 16, 1279-1289.

Van Den Boom, J., Kueck, A. F., Kravic, B., Muschenborn, H., Giesing, M., Pan, D., Kaschani, F., Kaiser, M., Musacchio, A. & Meyer, H. 2021. Targeted substrate loop insertion by VCP/p97 during PP1 complex disassembly. Nat Struct Mol Biol, 28, 964-971.

Van Den Boom, J. & Meyer, H. 2018. VCP/p97-Mediated Unfolding as a Principle in Protein Homeostasis and Signaling. Mol Cell, 69, 182-194.

Van Den Boom, J., Wolf, M., Weimann, L., Schulze, N., Li, F., Kaschani, F., Riemer, A., Zierhut, C., Kaiser, M., Iliakis, G., Funabiki, H. & Meyer, H. 2016. VCP/p97 Extracts Sterically Trapped Ku70/80 Rings from DNA in Double-Strand Break Repair. Mol Cell, 64, 189-198.

Van Nifterik, K. A., Van Den Berg, J., Stalpers, L. J., Lafleur, M. V., Leenstra, S., Slotman, B. J., Hulsebos, T. J. & Sminia, P. 2007. Differential radiosensitizing potential of temozolomide in MGMT promoter methylated glioblastoma multiforme cell lines. Int J Radiat Oncol Biol Phys, 69, 1246-53.

Vaz, B., Halder, S. & Ramadan, K. 2013. Role of p97/VCP (Cdc48) in genome stability. Front Genet, 4, 60.

Verma, R., Oania, R., Fang, R., Smith, G. T. & Deshaies, R. J. 2011. Cdc48/p97 mediates UV-dependent turnover of RNA Pol II. Mol Cell, 41, 82-92.

Verma, R., Oania, R. S., Kolawa, N. J. & Deshaies, R. J. 2013. Cdc48/p97 promotes degradation of aberrant nascent polypeptides bound to the ribosome. Elife, 2, e00308.

Walter, P. & Ron, D. 2011. The unfolded protein response: from stress pathway to homeostatic regulation. Science, 334, 1081-6.

Waltes, R., Kalb, R., Gatei, M., Kijas, A. W., Stumm, M., Sobeck, A., Wieland, B., Varon, R., Lerenthal, Y., Lavin, M. F., Schindler, D. & Dork, T. 2009. Human RAD50 deficiency in a Nijmegen breakage syndrome-like disorder. Am J Hum Genet, 84, 605-16.

Wang, H., Li, Y., Truong, L. N., Shi, L. Z., Hwang, P. Y., He, J., Do, J., Cho, M. J., Li, H., Negrete, A., Shiloach, J., Berns, M. W., Shen, B., Chen, L. & Wu, X. 2014. CtIP maintains stability at common fragile sites and inverted repeats by end resection-independent endonuclease activity. Mol Cell, 54, 1012-21.

Wang, H., Mu, X., He, H. & Zhang, X. D. 2018. Cancer Radiosensitizers. Trends Pharmacol Sci, 39, 24-48.

Wang, M., Wu, W., Wu, W., Rosidi, B., Zhang, L., Wang, H. & Iliakis, G. 2006. PARP-1 and Ku compete for repair of DNA double strand breaks by distinct NHEJ pathways. Nucleic Acids Res, 34, 6170-82.

Wang, Q., Li, L. & Ye, Y. 2008. Inhibition of p97-dependent protein degradation by Eeyarestatin I. J Biol Chem, 283, 7445-54.

Wang, Y. Y., Hung, A. C., Lo, S., Hsieh, Y. C. & Yuan, S. F. 2021. MRE11 as a molecular signature and therapeutic target for cancer treatment with radiotherapy. Cancer Lett, 514, 1-11.

Wight, J. C., Hawkes, E. A., Berlangieri, S. U., Khor, R. & Grigg, A. P. 2018. An abscopal effect may augment PD-1 inhibition in refractory classical Hodgkin lymphoma. Leuk Lymphoma, 59, 2749-2751.

Williams, B. R., Prabhu, V. R., Hunter, K. E., Glazier, C. M., Whittaker, C. A., Housman, D. E. & Amon, A. 2008a. Aneuploidy affects proliferation and spontaneous immortalization in mammalian cells. Science, 322, 703-9.

Williams, R. S., Moncalian, G., Williams, J. S., Yamada, Y., Limbo, O., Shin, D. S., Groocock, L. M., Cahill, D., Hitomi, C., Guenther, G., Moiani, D., Carney, J. P., Russell, P. & Tainer, J. A. 2008b. Mre11 dimers coordinate DNA end bridging and nuclease processing in double-strand-break repair. Cell, 135, 97-109.

Willoughby, C. E., Jiang, Y., Thomas, H. D., Willmore, E., Kyle, S., Wittner, A., Phillips, N., Zhao, Y., Tudhope, S. J., Prendergast, L., Junge, G., Lourenco, L. M., Finlay, M. R. V., Turner, P., Munck, J. M., Griffin, R. J., Rennison, T., Pickles, J., Cano, C., Newell, D. R., Reeves, H. L., Ryan, A. J. & Wedge, S. R. 2020. Selective DNA-PKcs inhibition extends the therapeutic index of localized radiotherapy and chemotherapy. J Clin Invest, 130, 258-271.

Wong, A. D., Ye, M., Ulmschneider, M. B. & Searson, P. C. 2015. Quantitative Analysis of the Enhanced Permeation and Retention (EPR) Effect. PLoS One, 10, e0123461.

Wright, W. D. & Heyer, W. D. 2014. Rad54 functions as a heteroduplex DNA pump modulated by its DNA substrates and Rad51 during D loop formation. Mol Cell, 53, 420-32.

Wu, H. Q., Baker, D. & Ovaa, H. 2020. Small molecules that target the ubiquitin system. Biochem Soc Trans, 48, 479-497.

Wu, J., Huen, M. S., Lu, L. Y., Ye, L., Dou, Y., Ljungman, M., Chen, J. & Yu, X. 2009. Histone ubiquitination associates with BRCA1-dependent DNA damage response. Mol Cell Biol, 29, 849-60.

Wu, W., Sato, K., Koike, A., Nishikawa, H., Koizumi, H., Venkitaraman, A. R. & Ohta, T. 2010. HERC2 is an E3 ligase that targets BRCA1 for degradation. Cancer Res, 70, 6384-92.

Wu, Y., Kantake, N., Sugiyama, T. & Kowalczykowski, S. C. 2008. Rad51 protein controls Rad52-mediated DNA annealing. J Biol Chem, 283, 14883-92.

Xiao, Y. & Weaver, D. T. 1997. Conditional gene targeted deletion by Cre recombinase demonstrates the requirement for the double-strand break repair Mre11 protein in murine embryonic stem cells. Nucleic Acids Res, 25, 2985-91.

Xie, A., Hartlerode, A., Stucki, M., Odate, S., Puget, N., Kwok, A., Nagaraju, G., Yan, C., Alt, F. W., Chen, J., Jackson, S. P. & Scully, R. 2007. Distinct roles of chromatin-associated proteins MDC1 and 53BP1 in mammalian double-strand break repair. Mol Cell, 28, 1045-57.

Xie, A., Kwok, A. & Scully, R. 2009. Role of mammalian Mre11 in classical and alternative nonhomologous end joining. Nat Struct Mol Biol, 16, 814-8.

Xu, G., Chapman, J. R., Brandsma, I., Yuan, J., Mistrik, M., Bouwman, P., Bartkova, J., Gogola, E., Warmerdam, D., Barazas, M., Jaspers, J. E., Watanabe, K., Pieterse, M., Kersbergen, A., Sol, W., Celie, P. H. N., Schouten, P. C., Van Den Broek, B., Salman, A., Nieuwland, M., De Rink, I., De Ronde, J., Jalink, K., Boulton, S. J., Chen, J., Van Gent, D. C., Bartek, J., Jonkers, J., Borst, P. & Rottenberg, S. 2015. REV7 counteracts DNA double-strand break resection and affects PARP inhibition. Nature, 521, 541-544.

Xue, L., Blythe, E. E., Freiberger, E. C., Mamrosh, J. L., Hebert, A. S., Reitsma, J. M., Hess, S., Coon, J. J. & Deshaies, R. J. 2016. Valosin-containing protein (VCP)-Adaptor Interactions are Exceptionally Dynamic and Subject to Differential Modulation by a VCP Inhibitor. Mol Cell Proteomics, 15, 2970-86.

Yamaguchi-Iwai, Y., Sonoda, E., Sasaki, M. S., Morrison, C., Haraguchi, T., Hiraoka, Y., Yamashita, Y. M., Yagi, T., Takata, M., Price, C., Kakazu, N. & Takeda, S. 1999. Mre11 is essential for the maintenance of chromosomal DNA in vertebrate cells. EMBO J, 18, 6619-29.

Yates, L. A., Aramayo, R. J., Pokhrel, N., Caldwell, C. C., Kaplan, J. A., Perera, R. L., Spies, M., Antony, E. & Zhang, X. 2018. A structural and dynamic model for the assembly of Replication Protein A on single-stranded DNA. Nat Commun, 9, 5447.

Ye, Y., Meyer, H. H. & Rapoport, T. A. 2001. The AAA ATPase Cdc48/p97 and its partners transport proteins from the ER into the cytosol. Nature, 414, 652-6.

Ye, Y., Meyer, H. H. & Rapoport, T. A. 2003. Function of the p97-Ufd1-Npl4 complex in retrotranslocation from the ER to the cytosol: dual recognition of nonubiquitinated polypeptide segments and polyubiquitin chains. J Cell Biol, 162, 71-84.

Ye, Y., Shibata, Y., Yun, C., Ron, D. & Rapoport, T. A. 2004. A membrane protein complex mediates retro-translocation from the ER lumen into the cytosol. Nature, 429, 841-7.

Ye, Y., Tang, W. K., Zhang, T. & Xia, D. 2017. A Mighty "Protein Extractor" of the Cell: Structure and Function of the p97/CDC48 ATPase. Front Mol Biosci, 4, 39.

Yeung, H. O., Kloppsteck, P., Niwa, H., Isaacson, R. L., Matthews, S., Zhang, X. & Freemont, P. S. 2008. Insights into adaptor binding to the AAA protein p97. Biochem Soc Trans, 36, 62-7.

Yi, P., Higa, A., Taouji, S., Bexiga, M. G., Marza, E., Arma, D., Castain, C., Le Bail, B., Simpson, J. C., Rosenbaum, J., Balabaud, C., Bioulac-Sage, P., Blanc, J. F. & Chevet, E. 2012. Sorafenib-mediated targeting of the AAA(+) ATPase p97/VCP leads to disruption of the secretory pathway, endoplasmic reticulum stress, and hepatocellular cancer cell death. Mol Cancer Ther, 11, 2610-20.

Yin, Y., Seifert, A., Chua, J. S., Maure, J. F., Golebiowski, F. & Hay, R. T. 2012. SUMO-targeted ubiquitin E3 ligase RNF4 is required for the response of human cells to DNA damage. Genes Dev, 26, 1196-208.

You, Z., Chahwan, C., Bailis, J., Hunter, T. & Russell, P. 2005. ATM activation and its recruitment to damaged DNA require binding to the C terminus of Nbs1. Mol Cell Biol, 25, 5363-79.

Yousefzadeh, M. J. & Wood, R. D. 2013. DNA polymerase POLQ and cellular defense against DNA damage. DNA Repair (Amst), 12, 1-9.

Zaki, B. I., Suriawinata, A. A., Eastman, A. R., Garner, K. M. & Bakhoum, S. F. 2014. Chromosomal instability portends superior response of rectal adenocarcinoma to chemoradiation therapy. Cancer, 120, 1733-42.

Zatreanu, D., Robinson, H. M. R., Alkhatib, O., Boursier, M., Finch, H., Geo, L., Grande, D., Grinkevich, V., Heald, R. A., Langdon, S., Majithiya, J., Mcwhirter, C., Martin, N. M. B., Moore, S., Neves, J., Rajendra, E., Ranzani, M., Schaedler, T., Stockley, M., Wiggins, K., Brough, R., Sridhar, S., Gulati, A., Shao, N., Badder, L. M., Novo, D., Knight, E. G., Marlow, R., Haider, S., Callen, E., Hewitt, G., Schimmel, J., Prevo, R., Alli, C., Ferdinand, A., Bell, C., Blencowe, P., Bot, C., Calder, M., Charles, M., Curry, J., Ekwuru, T., Ewings, K., Krajewski, W., Macdonald, E., Mccarron, H., Pang, L., Pedder, C., Rigoreau, L., Swarbrick, M., Wheatley, E., Willis, S., Wong, A. C., Nussenzweig, A., Tijsterman, M., Tutt, A., Boulton, S. J., Higgins, G. S., Pettitt, S. J., Smith, G. C. M. & Lord, C. J. 2021. Poltheta inhibitors elicit BRCA-gene synthetic lethality and target PARP inhibitor resistance. Nat Commun, 12, 3636.

Zehir, A., Benayed, R., Shah, R. H., Syed, A., Middha, S., Kim, H. R., Srinivasan, P., Gao, J., Chakravarty, D., Devlin, S. M., Hellmann, M. D., Barron, D. A., Schram, A. M., Hameed, M., Dogan, S., Ross, D. S., Hechtman, J. F., Delair, D. F., Yao, J., Mandelker, D. L., Cheng, D. T., Chandramohan, R., Mohanty, A. S., Ptashkin, R. N., Jayakumaran, G., Prasad, M., Syed, M. H., Rema, A. B., Liu, Z. Y., Nafa, K., Borsu, L., Sadowska, J., Casanova, J., Bacares, R., Kiecka, I. J., Razumova, A., Son, J. B., Stewart, L., Baldi, T., Mullaney, K. A., Al-Ahmadie, H., Vakiani, E., Abeshouse, A. A., Penson, A. V., Jonsson, P., Camacho, N., Chang, M. T., Won, H. H., Gross, B. E., Kundra, R., Heins, Z. J., Chen, H. W., Phillips, S., Zhang, H., Wang, J., Ochoa, A., Wills, J., Eubank, M., Thomas, S. B., Gardos, S. M., Reales, D. N., Galle, J., Durany, R., Cambria, R., Abida, W., Cercek, A., Feldman, D. R., Gounder, M. M., Hakimi, A. A., Harding, J. J., Iyer, G., Janjigian, Y. Y., Jordan, E. J., Kelly, C. M., Lowery, M. A., Morris, L. G. T., Omuro, A. M., Raj, N., Razavi, P., Shoushtari, A. N., Shukla, N., Soumerai, T. E., Varghese, A. M., Yaeger, R., Coleman, J., Bochner, B., Riely, G. J., Saltz, L. B., Scher, H. I., Sabbatini, P. J., Robson, M. E., Klimstra, D. S., Taylor, B. S., Baselga, J., Schultz, N., Hyman, D. M., Arcila, M. E., Solit, D. B., Ladanyi, M. & Berger, M. F. 2017. Mutational landscape of metastatic cancer revealed from prospective clinical sequencing of 10,000 patients. Nat Med, 23, 703-713.

Zeman, M. K. & Cimprich, K. A. 2014. Causes and consequences of replication stress. Nat Cell Biol, 16, 2-9.

Zhang, H., Wang, Q., Kajino, K. & Greene, M. I. 2000. VCP, a weak ATPase involved in multiple cellular events, interacts physically with BRCA1 in the nucleus of living cells. DNA Cell Biol, 19, 253-63.

Zhang, P., Wang, L., Rodriguez-Aguayo, C., Yuan, Y., Debeb, B. G., Chen, D., Sun, Y., You, M. J., Liu, Y., Dean, D. C., Woodward, W. A., Liang, H., Yang, X., Lopez-Berestein, G., Sood, A. K., Hu, Y., Ang, K. K., Chen, J. & Ma, L. 2014. miR-205 acts as a tumour radiosensitizer by targeting ZEB1 and Ubc13. Nat Commun, 5, 5671.

Zhou, H. J., Wang, J., Yao, B., Wong, S., Djakovic, S., Kumar, B., Rice, J., Valle, E., Soriano, F., Menon, M. K., Madriaga, A., Kiss Von Soly, S., Kumar, A., Parlati, F., Yakes, F. M., Shawver, L., Le Moigne, R., Anderson, D. J., Rolfe, M. & Wustrow, D. 2015. Discovery of a First-in-Class, Potent, Selective, and Orally Bioavailable Inhibitor of the p97 AAA ATPase (CB-5083). J Med Chem, 58, 9480-97.

Zhou, Y., Caron, P., Legube, G. & Paull, T. T. 2014. Quantitation of DNA double-strand break resection intermediates in human cells. Nucleic Acids Res, 42, e19.

Zhou, Z. X., Zhang, M. J., Peng, X., Takayama, Y., Xu, X. Y., Huang, L. Z. & Du, L. L. 2013. Mapping genomic hotspots of DNA damage by a single-strand-DNA-compatible and strand-specific ChIP-seq method. Genome Res, 23, 705-15.

Zhu, C., Rogers, A., Asleh, K., Won, J., Gao, D., Leung, S., Li, S., Vij, K. R., Zhu, J., Held, J. M., You, Z., Nielsen, T. O. & Shao, J. 2020. Phospho-Ser(784)-VCP Is Required for DNA Damage Response and Is Associated with Poor Prognosis of Chemotherapy-Treated Breast Cancer. Cell Rep, 31, 107745.

Zhu, J., Petersen, S., Tessarollo, L. & Nussenzweig, A. 2001. Targeted disruption of the Nijmegen breakage syndrome gene NBS1 leads to early embryonic lethality in mice. Curr Biol, 11, 105-9.

Zhu, Z., Chung, W. H., Shim, E. Y., Lee, S. E. & Ira, G. 2008. Sgs1 helicase and two nucleases Dna2 and Exo1 resect DNA double-strand break ends. Cell, 134, 981-94.

List of publications

1. **Kilgas, S**., Kiltie, A. E. & Ramadan, K. 2021. Immunofluorescence microscopy-based detection of ssDNA foci by BrdU in mammalian cells – *STAR Protoc*, 25, 100978.
2. **Kilgas, S**., Singh, A. N., Paillas, S., Then, C. K., Torrecilla, I., Nicholson, J., Browning, L., Vendrell, I., Konietzny, R., Kessler, B. M., Kiltie, A. E. & Ramadan, K. 2021. p97/VCP inhibition causes excessive MRE11-dependent DNA end resection promoting cell killing after ionizing radiation. *Cell Rep,* 35**,** 109153.
3. Ruggiano, A.***** and Vaz, B.***, Kilgas, S**., Popovic, M., Rodriguez-Berriguete, G., Singh, A. N., Higgins, G. S., Kiltie, A. E. & Ramadan, K. 2020. SPRTN protease and SUMOylation coordinate DNA-protein crosslink repair to prevent genome instability – *Cell Rep,* 37, 110080.
4. Paillas, S., Then, C. K**., Kilgas, S**., Ruan, J. L., Thompson, J., Elliott, A., Smart, S. & Kiltie, A. E. 2020. The Histone Deacetylase Inhibitor Romidepsin Spares Normal Tissues While Acting as an Effective Radiosensitizer in Bladder Tumors in Vivo. *Int J Radiat Oncol Biol Phys,* 107**,** 212-221.
5. Singh, A. N.***** and Oehler, J.*****, Torrecilla, I., **Kilgas, S**., Li, S., Vaz, B., Guerillon, C., Fielden, J., Hernandez-Carralero, E., Cabrera, E., Tullis, I. D., Meerang, M., Barber, P. R., Freire, R., Parsons, J., Vojnovic, B., Kiltie, A. E., Mailand, N. & Ramadan, K. 2019. The p97- Ataxin 3 complex regulates homeostasis of the DNA damage response E3 ubiquitin ligase RNF8. *EMBO J,* 38**,** e102361.